Pattern Formation and Branching in Morphogen-Controlled Interface Growth

Dissertation
zur Erlangung des akademischen Grades
Doctor rerum naturalium

vorgelegt
dem Bereich Mathematik und Naturwissenschaften
der Technischen Universität Dresden

von
Christian Hanauer

Technische Universität Dresden
Max-Planck-Institut für Physik komplexer Systeme

Dresden, 2023

Eingereicht am 21.12.2023
Verteidigt am 17.05.2024

Gutachter:
Prof. Dr. Frank Jülicher
Prof. Dr. Karsten Kruse

Abstract

During animal development numerous organs with functions ranging from fluid transport to signal propagation develop into highly branched shapes and forms. To ensure organ function, the formation of their geometrical and topological as well as size-dependent properties is crucial. For example, organ geometry serves to maximize exchange area with its surroundings and organ topology controls the response to fluctuations and damage. Most importantly, organ size and proportion need to scale throughout animal growth to meet the demands of increasing body size. However, how organ geometry and topology are established and scaled in a self-organized manner, remains poorly understood. In this thesis, we present a novel theoretical framework to study the self-organized growth and scaling of branched organs. In this framework, we represent the organ outline by an infinitely thin interface and consider morphogen-controlled interface evolution in growing domains. We demonstrate that an instability in interface motion can lead to the self-organized formation of complex branched morphologies and show how the interplay between interface motion, morphogen dynamics, and domain growth controls the geometrical, topological, and size-dependent properties of the resulting structures.

To understand the formation of branched structures from instabilities in morphogen-controlled interface growth, we first consider a range of different interface growth scenarios in non-growing domains. In a first approach, we present a stochastic lattice model with interface growth driven by a morphogen concentration gradient. We find a range of branched morphologies extending from self-similar fractal structures to almost circular structures with only a few branches depending on the morphogen gradient length scale. We present the Euler characteristic as an example of a topological invariant and employ it to introduce topological constraints into interface growth, leading to the formation of tree-like structures. In a second approach, we study a continuum model for morphogen-controlled interface growth. In this model, the interface has a constant tendency to grow and is inhibited by morphogen concentration. Additionally, we take into account a curvature dependency of interface growth, which leads to an effective stabilization of interface motion at small length scales. We identify branch distance and thickness as key morphological properties and discuss their regulation. We relate branch distance regulation to the

interplay of destabilization from morphogen inhibition and stabilization from the curvature dependency of interface growth and explain branch thickness regulation in terms of mutual branch inhibition. By considering interface instability in different scenarios, we overall demonstrate the robustness of our approach.

Finally, we apply our theoretical framework to study the branching morphogenesis of the planarian gut. The planarian gut is a highly branched organ that spans the entire organism and is responsible for the delivery of nutrients to the planarian body. Planarians undergo massive body size changes of more than one order of magnitude in organism length and thus constitute an ideal model organism to study the growth and scaling of branched organs. We reconsider our continuum model and include novel features needed to account for the organization of the planarian gut. We take into account external guiding cues that alter the orientation of branches and, most importantly, consider branching morphogenesis in a growing domain. We demonstrate that our model can account for the geometrical and topological properties of the gut and show that gut scaling can arise from to the interplay of branch growth and organism growth.

Overall, we present a novel theoretical framework to study the growth and scaling of branched organs. In this framework, we demonstrate the self-organized formation of branched morphologies from instabilities in morphogen-controlled interface growth and show how the interplay of interface motion, morphogen dynamics, and system size determine geometry, topology, and size-dependent properties of the resulting structures.

Zusammenfassung

In der Entwicklung von Tieren formen sich zahlreiche Organe mit Funktionen von Fluidtransport bis zu Signalweiterleitung, zu hochgradig verzweigten Strukturen. Um die Funktion dieser Organe zu gewährleisten, sind deren geometrischen, topologischen und größenabhängigen Eigenschaften entscheidend. Die Organgeometrie zum Beispiel dient zur Maximierung der Austauschoberfläche mit der Umgebung und die Organtopologie bestimmt das Verhalten bei Fluktuationen und Beschädigungen. Vor allem müssen Organgröße und -proportion mit der Körpergröße skalieren, um den Anforderungen zunehmender Körpergröße gerecht zu werden. Wie sich jedoch die Geometrie und Topologie von Organen in selbstorganisierter Art und Weise herausbildet und mit der Körpergröße skaliert, ist nur wenig verstanden. In dieser Arbeit stellen wir eine neue Theorie vor, um das selbstorganisierte Wachstum und Skalieren von verzweigten Organen zu untersuchen. In dieser Theorie stellen wir die Organoberfläche durch eine dünne Grenzfläche dar und betrachten die morphogengesteuerte Grenzflächendynamik in wachsenden Domänen. Wir zeigen, dass eine Instabilität in der Grenzflächenbewegung zur selbstorganisierten Bildung von komplexen, verzweigten Strukturen führen kann und wie das Zusammenspiel von Grenzflächenwachstum, Morphogendynamik und Domänenwachstum die geometrischen, topologischen und größenabhängigen Eigenschaften der resultierenden Strukturen steuert.

Um die Bildung von verzweigten Strukturen aufgrund von Instabilitäten in morphogengesteuertem Grenzflächenwachstum zu verstehen, betrachten wir zunächst eine Reihe unterschiedlicher Szenarien für Grenzflächenwachstum in nicht wachsenden Domänen. In einem ersten Ansatz stellen wir ein stochastisches Gittermodell vor, in dem das Grenzflächenwachstum von einem Morphogengradienten gesteuert wird. Wir finden in Abhängigkeit der Länge des Morphogengradienten eine Reihe verzweigter Morphologien, die von selbstähnlichen fraktalen Strukturen bis zu beinahe kreisförmigen Strukturen mit nur wenigen Verzweigungen reichen. Wir stellen die Euler-Charakteristik als ein Beispiel für eine topologische Invariante vor und benutzen sie, um topologische Einschränkungen in das Grenzfächenwachstum einzuführen, welche zur Bildung baumartiger Strukturen führen. In einem zweiten Ansatz stellen wir ein Kontinuumsmodell für morphogengesteuertes Grenzflächenwachstum vor. In diesem Modell besitzt die Grenzfläche eine konstante Wachs-

tumstendenz und wird von der Morphogenkonzentration inhibiert. Zusätzlich beziehen wir eine Krümmungsabhängigkeit des Grenzflächenwachstums mit ein, welches die Grenzflächenbewegung auf kleinen Längenskalen effektiv stabilisiert. Wir identifizieren den Zweigabstand und die Zweigdicke als morphologische Schlüsseleigenschaften und diskutieren deren Regulation. Wir setzen die Regulation des Zweigabstandes mit dem Zusammenspiel von Destabilisierung durch die Morphogeninhibierung und Stabilisierung durch die Krümmungsabhängigkeit des Grenzflächenwachstums in Verbindung und erklären die Zweigdicke durch die gegenseitige Inhibierung der Zweige. Durch das Betrachten von Grenzflächeninstabilitäten in verschiedenen Szenarien, zeigen wir insgesamt die Robustheit unseres Ansatzes.

Wir wenden unsere Theorie schließlich an, um die Morphogenese des Plattwurmdarms zu untersuchen. Der Plattwurmdarm ist ein hochgradig verzweigtes Organ, das den ganzen Organismus durchdringt und für die Versorgung des Plattwurmkörpers mit Nährstoffen verantwortlich ist. Plattwürmer erfahren Änderungen ihrer Körperlänge von bis zu einer Größenordnung und stellen daher einen idealen Modellorganismus zur Untersuchung von Wachstum und Skalierung verzweigter Organe dar. Wir betrachten wieder unser Kontinuumsmodell und fügen neue Bestandteile hinzu, die zur Beschreibung der Organisation des Plattwurmdarms benötigt werden. Wir ziehen Umgebungsreize in Betracht, welche die Orientierung von Zweigen verändern und betrachten die Morphogenese verzweigter Strukturen in einer wachsenden Domäne. Wir zeigen, dass unser Modell die geometrischen und topologischen Eigenschaften des Darmes korrekt wiedergibt und dass die Skalierung des Darmes aus dem Zusammenspiel von Zweigwachstum und Organismuswachstum entstehen kann.

Insgesamt präsentieren wir eine neue Theorie zur Untersuchung des Wachstums und Skalierens verzweigter Organe. In dieser Theorie demonstrieren wir die selbstorganisierte Bildung verzweigter Morphologien mittels Instabilitäten in morphogengesteuertem Grenzflächenwachstum und zeigen, wie das Zusammenspiel von Grenzflächenwachstum, Morphogendynamik und Systemgröße die Geometrie, Topologie und größenabhängigen Eigenschaften der resultierenden Strukturen bestimmt.

Acknowledgements

First and foremost I would like to thank Frank Jülicher for his scientific guidance and support throughout my PhD. I am grateful for his feedback on various aspects of my work and his availability for discussions despite his busy schedule. Special thanks also go to Efe Ilker for his constant availability for discussions, his out-of-the-box thinking, and memorable moments also outside the institute. I am grateful to Jochen Rink for providing the perspective of a biologist on my work and challenging me to communicate ideas and results in a non-technical way. I would also like to express my thanks to Amrutha Palavalli for sharing data on gut branching morphogenesis, inspiring discussions, and showing me around the lab during my visit in Göttingen.

I would like to thank the members of the biophysics division at PKS for a pleasant working atmosphere and for helpful feedback on my work in the internal and PhD seminar. In particular, I would like to thank Kartik Chhajed, Kathrin Laxhuber, Suganthan Senthilkumar, and Ali Tahaei for proofreading parts of this thesis. I acknowledge helpful feedback from the members of the lab of Jochen Rink and in particular I am thankful to Hanh Vu and James Cleland for providing gut images that sparked my interest in gut branching morphogenesis.

I would also like to acknowledge help from the non-scientific staff at PKS. Many thanks go to Ulrike Burkert for support in administrative issues and the organization of meetings with Frank and Jochen. Many thanks also go to the IT department at PKS. In particular, I would like to thank Hubert Scherrer-Paulus for keeping the cluster running and installing software whenever I needed it and Thomas Müller for Mac support.

Finally, I would like to thank my family for their continuous support throughout my life.

Contents

Chapter 1

Introduction

1.1 Development of living organisms

The development of living organisms is a fascinating process. Many life forms develop from a single fertilized egg into a multicellular organism consisting of billions of cells of various types [1–3]. To ensure correct development, numerous processes need to be coordinated and controlled. On the molecular scale, gene expression is regulated to ensure the formation of the correct proteins at the right place at the right time. Numerous cell divisions take place where at every round two daughter cells are formed each having a copy of the genetic material. Cells group to form intricate tissue and organ architectures that perform tasks ranging from digestion of food to excretion of waste and pumping of fluids. Overall, development is a prime example for the self-organization of a highly complex system from an initially simple state.

Despite the complexity of this process, four key developmental processes can be identified [1]. The most apparent of all developmental processes is probably growth. Growth refers to the increase of organism size during development and can be achieved in different ways. For example, the increase of organism size can take place via cell proliferation, i.e. repeated rounds of increase in cell size and subsequent division. Growth can also take place by cell enlargement or by accumulation of extracellular material. As the number of cells in the organism increases, tissue patterning becomes important. During development different regions with distinct cellular behavior are organized. For example, during embryonic development cells are recruited to different germ layers. These are regions of cells that give rise to specialized tissues in the adult organism, such as gut, muscle, or nervous system. Another example for tissue patterning is the establishment of the body plan. Bilaterally symmetric organisms possess an anterior-posterior axis and a dorsal-ventral axis that are set up during embryonic development. Closely related to tissue patterning

(a) Geometry (b) Topology

Figure 1.1: Morphogenesis: self-organization of complex spatio-temporal patterns (a) We show gut villi of the mouse intestine as an example for a pattern with an intricate geometry. Image shows immunostaining with VEGFR2/CD31 (green/red) as cell surface markers. Scale bar denotes 200 µm. (b) We show the vein network of a lemon leaf as an example of a pattern with intricate topology. Image shows an experiment in which a hole was cut into the main vein (black circle). Despite the hole, fluorescein (yellow) flows to regions behind the stem due to the topology of the network. Reproduced with permission from Refs. [11, 12]

is cell differentiation. The vertebrate body contains hundreds of different cell types such as epithelial cells, blood cells, or muscle cells [3]. Cell differentiation refers to the process by which cells adopt these distinct cell fates. Finally, organisms exhibit a great variety of forms and shapes. The generation of form is another key element of development, which we discuss next in more detail.

1.1.1 Morphogenesis: the emergence of geometry and topology

Morphogenesis, the generation of form in developing organisms, is a central aspect of development as is combines all of the aforementioned processes [1, 4]. As the organism grows, cells differentiate and form complex 3D organ and tissue architectures. A striking example is gastrulation, the process by which the blastula (a spheroidal arrangement of cells) transforms into the gastrula (a structure that contains three germ layers endoderm, mesoderm and ectoderm) during early embryonic development [3]. At the end of this process, the embryo has transformed from a single-layered to a multi-layered structure with different cell types and correctly oriented anterior-posterior axis. Other prominent examples include branching morphogenesis of numerous organs [5, 6], the formation of villi in the gut [7, 8], or the formation of cortical convolutions in the brain [9, 10].

The generation of form includes the specification of both geometry (length scales and size) and topology (connectivity) of objects [13]. For example, geometry plays a role for the growth of gut villi [7, 8]. Villi need to attain their characteristic finger-like shape and have

to be spaced correctly to ensure efficient nutrient absorption (Fig. 1.1a). Topology plays a role during branching morphogenesis as network topology influences transport properties (Fig. 1.1b). Tree-like networks yield optimal fluid transport [14–16], while networks with loops yield optimal transport for fluctuating loads and with respect to damage to parts of the network [12, 17].

Questions regarding the origin of geometry and topology of living organisms are old and date back to ancient Greeks [1]. Today it is acknowledged that a combination of chemical signals and mechanics organize the morphogenesis of living organisms [4, 18, 19]. For example, chemical substances can provide a length scale via a reaction-diffusion mechanism [4]. A substance that diffuses with diffusion constant D and undergoes degradation with rate k can form graded concentration profiles with a characteristic degradation length scale $\lambda = \sqrt{D/k}$. Also, signaling can influence topology. In some cases of branching morphogenesis, inhibitory signals are released that prevent different branches from merging [20].

Apart from simple, graded concentration profiles, complex, spatio-temporal geometries and topologies can be generated via instabilities [4]. The Turing-instability is a prominent example of such a pattern formation process and exemplifies how complex patterns can emerge from uniform initial states [21] (Fig. 1.2). In his seminal paper titled "The chemical basis of morphogenesis", Turing studied a minimal system comprising two chemical species that undergo diffusion and react with each other [22]. He showed that such a system exhibits rich pattern formation processes ranging from uniform states to oscillations and traveling waves. In particular, a standing wave (now known as Turing pattern) can be generated with a wavelength that emerges from the reaction-diffusion length scales of the chemical species. Key to the formation of such Turing patterns is a reaction network with

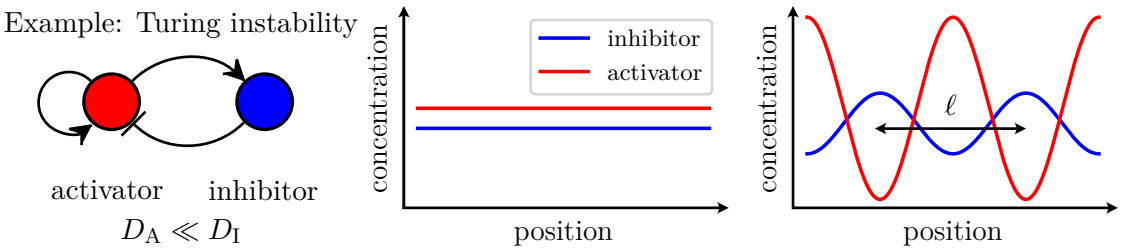

Figure 1.2: Instabilities as a mechanism for the self-organization of complex spatio-temporal patterns. We show the Turing instability as an example. The interaction of an activator (diffusion constant D_A) and an inhibitor (diffusion constant D_I) leads to the self-organized transition from a homogeneous to an inhomogeneous structure with a characteristic length scale ℓ.

short-ranged activation and long-ranged inhibition [23–25]. Turing patterns are discussed in the context of digit formation [26] or the stripes of zebrafish [27], to name just a few of the numerous examples. Apart from the Turing-instability, instabilities have also been discussed in the context of tissue mechanics [4]. For example, it was proposed that brain cortex folding arises from the relative growth of white (inner layer, slow growth) and gray matter (outer layer, fast growth) [9, 10].

In this thesis, we focus on the influence of chemical signals on morphogenesis. In the next section, we discuss a special class of chemical signals, called morphogens, and their role in development.

1.1.2 The role of morphogens in development

Morphogens and morphogen gradients are central to our understanding of development [1]. Morphogens are diffusable signaling molecules that determine cell division and differentiation in a concentration-dependent way [2]. Morphogens are produced in dedicated regions, spread in the tissue and undergo degradation. They form morphogen gradients, i.e. the morphogen distribution decreases away from the production region. We next highlight key experiments that elucidated the role of morphogens in development and then briefly discuss the formation of morphogen gradients.

The notion of gradients that influence developmental processes first appeared in the work of Morgan and Child at the beginning of the 20th century [28–30]. In his studies of the regenerative capabilities of Tubularia, Morgan noticed the phenomenon of polarity in his experiments as amputated tissue pieces correctly reestablished their body axes [31]. He explained this finding by introducing a hypothetical substance that spreads between the poles of the animal in a graded manner. While Child shared his views on the existence of such gradients, he interpreted them not in terms of "*formative substances*" [32] as Morgan, but in terms of a gradient in metabolic activity [33]. While the precise nature of gradients was under debate, the notion of gradients was born.

The experiments of Hilde Mangold and Hans Spemann mark the next important milestone in our understanding of how morphogens organize development [2, 34–37]. Mangold and Spemann studied newts at gastrulation stage. At this stage, the blastula (a spheroidal arrangement of cells) develops into the gastrula (a structure that contains endoderm, mesoderm, and ectoderm) [3]. In their experiments, they transplanted tissue from the dorsal side of the gastrula (so-called blastolip) to the ventral side of a gastrula of another embryo. Using embryos of newts with different pigmentation allowed them to distinguish host and donor cells. Interestingly, they observed that the transplanted cells remained blastopore

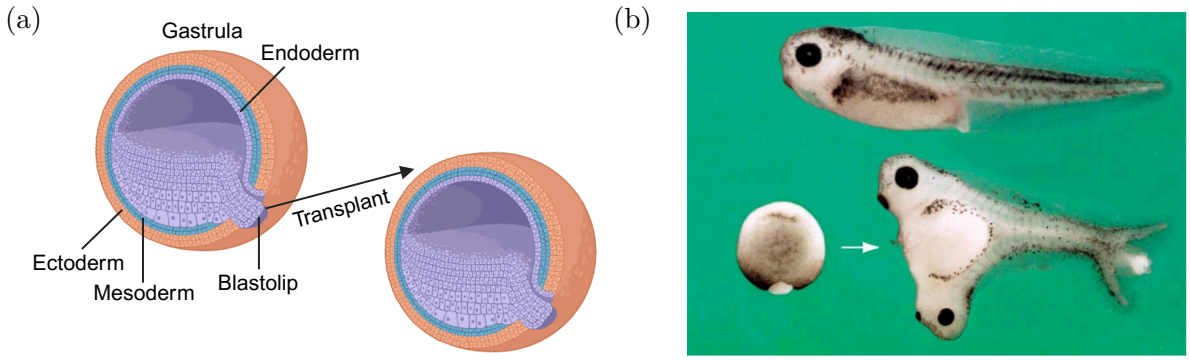

Figure 1.3: Spemann-Mangold experiment. (a) Tissue transplantation from blastolip of donor gastrula to host gastrula. (b) The Spemann-Mangold experiment in *Xenopus laevis*. Image shows wild-type animal (top) along with animal obtained from gastrula with transplanted tissue at same developmental stage. Reproduced with permission from Ref. [38, 39].

lip and even initiated gastrulation. A second embryo with correctly established anterior-posterior and dorsal-ventral axis formed and is attached ventrally to the embryo generated by the host tissue. Both embryos contain pigmented and unpigmented cells indicating that host cells adapted a fate they would not have chosen without the transplantation. Therefore, cell fate is not predetermined, but can induced by distinct organizer regions. The blastopore lip of the new embryo is nowadays known as Spemann organizer. Overall, the experiments of Spemann and Mangold demonstrated what is now known as the concept of induction. Signals released from specialized "organizer" regions influence the fate of cells in the surrounding tissue.

Lewis Wolpert then combined the ideas of "organizer" regions and morphogen gradients in his famous French flag model to explain how positional information can be generated [1, 2, 40] (Fig. 1.4). In this model, source cells produce morphogen that spreads in the tissue and is read out by target cells. Target cells are capable of exhibiting different concentration-dependent responses. In particular, Wolpert assumed that cell fate depends on whether certain concentration thresholds are reached. Thereby, one morphogen signal can give rise to multiple cell types in the tissue. Even though the concept of how a morphogen works, was now stated, a clear experimental demonstration was still lacking.

The first clear experimental demonstration of a morphogen was the Bicoid protein in *Drosophila* embryos [1, 29]. In a set of seminal experiments, Nüsslein-Volhard and colleagues elucidated the role of Bicoid protein for head formation in *Drosophila* embryos [42–44] and demonstrated a gradient of Bicoid [45, 46] (Fig. 1.5). They showed that Bicoid deficient embryos could not form a head, but head formation could be rescued by

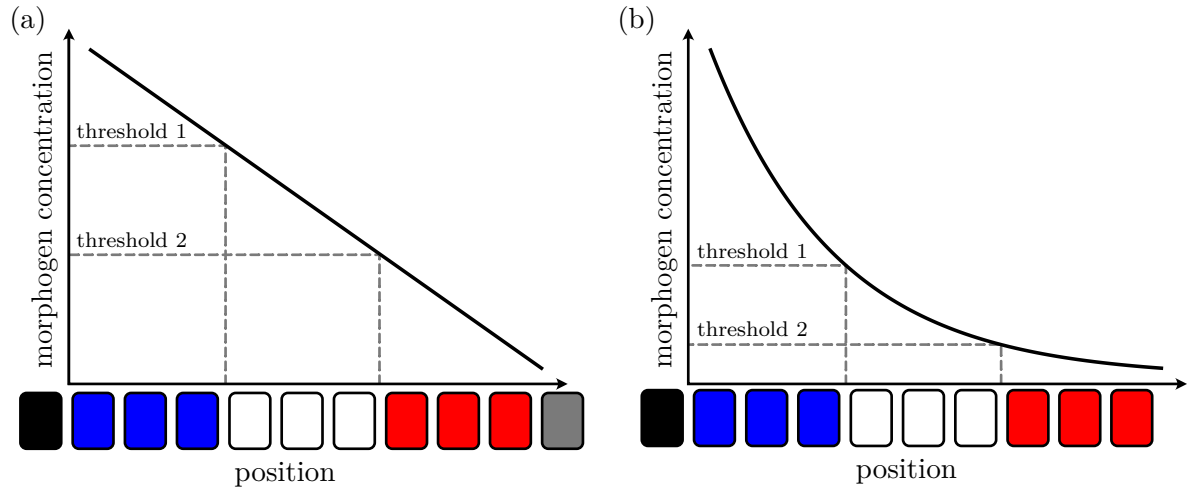

Figure 1.4: Morphogen-gradient generation and interpretation. (a) According to Crick's model, morphogen is produced in a source region (black) and degraded in a sink region (gray), which results in a linear concentration gradient. (b) Morphogen gradients can also be formed by production in a source region (black) and uniform degradation. According to the French flag model, cells in the tissue show a concentration-dependent behavior and adapt cell fates accordingly (color) in both scenarios of gradient formation. Figure based on Ref. [41].

adding Bicoid protein obtained from wild-type embryos. Most importantly, the injection site of Bicoid protein determined the position of head formation. This way a head located at the anterior pole and in the middle of the embryo could be formed. Even a second head could be induced by injecting Bicoid at the posterior region of a wild type embryo. Altogether, their results identified that Bicoid acts as a morphogen in *Drosophila* embryos and paved the way for the identification of more morphogens.

Over the years various other morphogens in a diverse set of tissues and organs in different organisms have been identified (see [41, 47] for an overview). Apart from patterning the fly embryo, morphogens are also involved in body axis formation in the fly wing. Here, an interplay of Hh and Dpp signaling patterns the anterior-posterior axis of the fly wing [48–52]. During gastrulation of *Xenopus* embryos, wnt patterns the anterior-posterior axis of the neural plate [53] and bmp organizes the dorsal-ventral axis in the zebrafish embryo [54], to name just a few of the numerous examples. Beyond setting up the body plan, morphogens also control the growth of tissues and organs [55]. For example, Dpp organizes the growth of fly wing and eye [56–58] and recent results suggest that bmp influences growth of the zebrafish pectoral fin [59]. In a later section, we explore the role of morphogens in branching morphogenesis. The widespread usage of morphogens to coordinate and control the development of tissues and organs highlights the importance

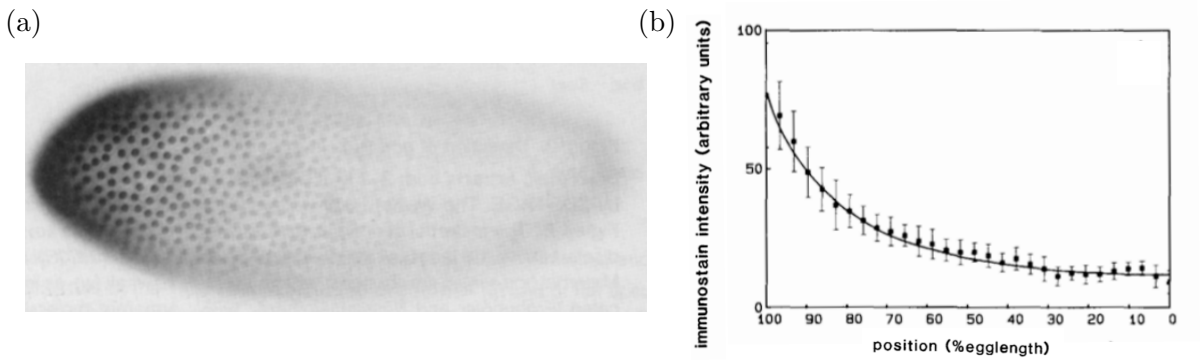

Figure 1.5: Bicoid gradient in *Drosophila* embryos. (a) Bicoid protein distribution in whole mount of wild-type embryos at syncytial blastoderm stage. (b) Quantification of the Bicoid gradient. Image shows anti-*bcd* immunostain intensity as function of position along anteroposterior axis averaged from 12 wild-type embryos. Error bars denote twofold standard deviation. Images adapted with permission from Ref. [45].

of the morphogen concept for understanding developmental processes.

The formation of morphogen gradients is crucial for providing positional information and therefore the control of development processes. Thus, much effort has been devoted to understand the mechanisms underlying the formation of morphogen gradients. Nowadays, morphogen gradients are thought to form by the interplay of transport, removal, and production [30, 47]. Both directional and non-directional as well as active and passive mechanisms contribute to the transport of morphogen [47, 60]. On small length and timescales (nm,ms), morphogen transport takes place by free, extracellular diffusion. By contrast, on the tissue scale (µm to mm) a range of different mechanisms affects transport. For example, morphogen can repeatedly attach and detach to receptors on the cell surface and parts of the extracellular matrix which overall hinders its motion. Moreover, morphogen transport can take place via transcytosis, i.e. morphogen can enter the cell, undergo intracellular transport, and subsequently leave the cell again. Also cytonemes, thin, actin-rich protrusions that extend from cells, contribute to morphogen motion [61]. Cytonemes can be employed by morphogen producing cells to transport morphogen to distant regions, but also the reverse process takes place and morphogen receiving cells use cytonemes to sense morphogen at distant locations [41]. Removal of morphogen takes place via degradation, immobilization, and also an effective removal of morphogen takes place due to dilution of morphogen concentration by cell division. Production takes place in distinct morphogen producing regions.

Despite the plethora of processes contributing to morphogen transport and removal, the formation of morphogen gradients can be described by reaction-diffusion models, where

transport takes place with an effective diffusion and degradation rate [29, 60]. Crick was the first to propose a reaction-diffusion model for morphogen gradient formation [62]. In his model, he studied the concentration of a morphogen subject to diffusion and uniform degradation together with a distinct morphogen production and degradation region. In 1D, the proposed model gives rise to linear gradients (Fig. 1.4a). Nowadays, the so-called synthesis-diffusion-degradation model (SDD) provides a minimal framework to study the morphogen gradient formation [30, 47]. In this model, morphogen gradients form from the interplay of diffusion with uniform degradation that takes place in the entire system. This approach gives rise to gradients of exponential shape with a characteristic length scale that increases for more diffusive morphogen species and with larger morphogen lifetime (Fig. 1.4b). The SDD model has been successfully employed to study morphogen gradient formation in the *Drosophila* wing imaginal disc and the zebrafish embryo [63, 64] and will also be an important cornerstone of our work.

1.1.3 Allometric scaling: the role of body size in biology

Body size is an important aspect of living organisms and thus also morphogenesis. While small crustaceans weigh only a few µg, blue whales have a body mass of roughly 10^5 kg. Thus, living organisms span a remarkable range of 14 orders of magnitude in terms of body mass [65–67]. Assuming that similar developmental processes form organisms at either side of this spectrum, this naturally raises the question of how differently sized animals are related. Are large organism just a scaled up version of smaller organisms and how are scale and proportion maintained during growth?

The term allometry describes the study of how biological features change with organism size [68–70]. This includes morphological features (e.g. organ and tissue size), physiological features (e.g. metabolic rate, energy storage) as well as ecological features (e.g. locomotion speed) [70, 71]. Four main classes of allometry are distinguished [68, 70]. Ontogenetic allometry studies the relationship between biological features and body size during growth of a species. Interspecies allometry compares features between different adult species, whereas intraspecies allometry compares features within different adult organisms of the same species. Phylogenetic allometry studies how biological features changed throughout evolution. In this thesis, we will study ontogenetic allometries.

We refer to the equations that describe the functional dependence of a biological feature with body size as allometric equations. Interestingly, it turns out that allometric equations often obey power laws of the form

$$y = y_0 x^{\alpha}, \tag{1.1}$$

where y denotes a biological feature and x denotes the body size of the organism [71, 72]. We refer to α as the scaling exponent and y_0 as the intercept.

Power laws of the form of Eq. (1.1) yield linear functions in double logarithmic coordinates which facilitates the interpretation of α and y_0 (Fig. 1.6) [70, 72]. The scaling exponent α measures how much a biological feature changes compared with changes in organism size. We distinguish isometric scaling ($\alpha = 1$) and allometric scaling ($\alpha \neq 1$). While for isometric scaling biological features change proportionally with organism size, this proportionality breaks down for allometric scaling. Note that the term "allometric" comes from the Greek word "alloios" meaning "different", expressing the disparity in growth of biological features and organism size [72]. We distinguish sublinear scaling ($\alpha < 1$) and superlinear scaling ($\alpha > 1$). For sublinear scaling, biological features change less than organism size. Conversely, for superlinear scaling, biological features change more than organism size. The proportionality factor y_0 sets the intercept of the linear function in double logarithmic coordinates. It therefore marks biological features at a particular reference organism size.

Scaling relations are ubiquitous in biology [71, 72]. For example, the surface area A of mammals scales with body mass M as $A \propto M^{2/3}$ [71, 73]. This is an example of how scaling relation can be rationalized by simple geometrical considerations. The scaling of metabolic rate P with body mass M as $P \propto M^{3/4}$ (known as Kleiber's law) is another prominent scaling relation [74]. Assuming that metabolic rate is proportional to surface area gives 2/3 as scaling exponent, which is in contradiction with the observed exponent. Thus, the derivation of the scaling exponent from geometrical consideration fails in this case. Instead, it was suggested that the distribution of nutrients is limited by exchange surfaces (e.g. vasculature) and the structure and scaling of exchanges surfaces gives rise metabolic scaling [75–77].

1.2 Development of branched structures: branching morphogenesis

Branching morphogenesis is a ubiquitous developmental process occurring in plants, animals, and even fungi on a large range of spatial scales [80, 81]. The term refers to the formation of branched morphologies by repeated rounds of branch initiation and extension. Branching manifests itself in different ways [80]. While some organisms have a branched body plan (e.g. trees and corals), other organisms possess a branched internal anatomy (e.g. lungs). Branched morphologies can fill the entire organism body (e.g. vasculature),

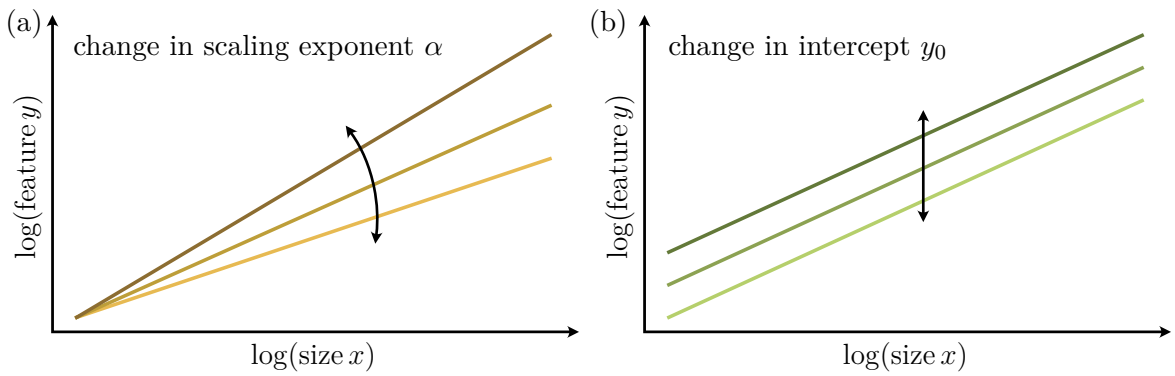

Figure 1.6: Allometric scaling of a general organismal feature y with body size x. Scaling relations of the form of Eq. (1.1) yield linear functions in a plot with logarithmic axes. (a) A change in scaling exponent α corresponds to a change in slope. (b) A change in y_0 corresponds to a change in the intercept of the corresponding linear function.

but can also be confined to a constrained region (e.g. lung). Branching can take place at the single cell level (dendrite of neuronal cells), but can also involve the collective migration of many cells (e.g. lungs). Branched morphologies also perform a variety of functions like the transport of fluids (vasculature) and gases to signal propagation (nervous network). While shape and functions are diverse, branching typically serves to maximize exchange area between compartments when space is limited. We find maximization of the exchange area in the respiratory organs (lungs, trachea), excretory organs (kidney) and exocrine glands (mammary gland, salivary gland) and the vasculature.

Morphogen gradients also play an important role during the formation of branched organs [5, 6, 82–85]. A set of local and global guiding cues ensure the correct formation and growth of branches. A system where this interplay is particularly well understood is the tracheal system of *Drosophila* (Fig. 1.7a) [86–88]. The tracheal system is the respiratory system of insects and transports air from openings in the insect body to the interior. It is an example of a stereotyped organ, meaning that branching occurs in a highly reproducible way and organ structure is similar in different organisms of the same species. The tracheal systems develops during embryogenesis from sac-like structures of the embryo. The growth factor branchless (Bnl, a member of the FGF family) is expressed in target tissue and acts as a chemoattractant. Tracheal cells sense Bnl via receptors called Breathless (Btl) and migrate towards the source of Bnl [89, 90]. Since tracheal cells are connected by adherens junctions, neighboring cells are pulled along with them causing the formation of an elongated tube. In response to high levels of Btl, receptors Delta/Notch signaling is triggered [91–93]. Cells with high levels of Btl have an increased Delta production,

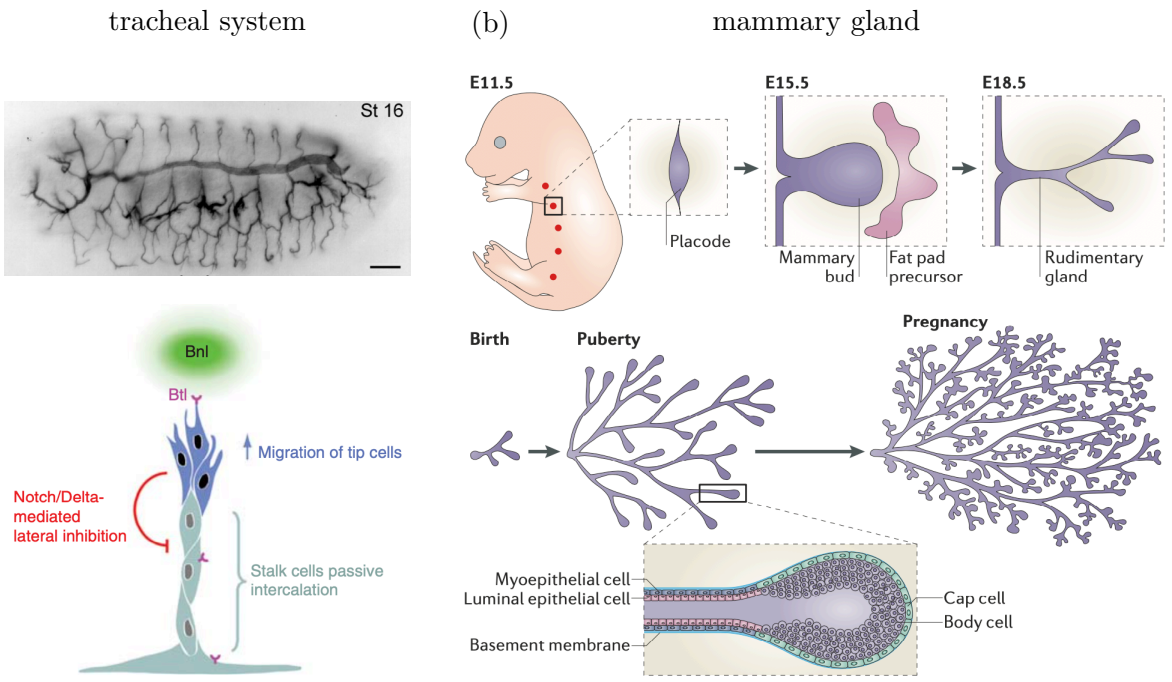

Figure 1.7: Examples of branching morphogenesis. (a) Top: Tracheal system in *Drosophila* embryo at stage 16. Scale bar denotes 25 µm. Bottom: Tip cells sense the growth factor Bnl via receptor Btl and migrate towards source of Bnl. Notch/Delta signaling causes the formation of a stalk. (b) The mouse mammary gland forms during embryonic, pubertal, and adult stages. In the embryonic stage, a rudimentary gland is formed that invades surrounding tissue during puberty. During pregnancy milk producing alveoli form. Reproduced with permission from Refs. [6, 78, 79]

which in turn induces Notch signaling in neighboring cells. Notch inhibits the tip cell fate thereby causing the formation of stalk. Overall, the tracheal system serves as an example of a stereotyped organ that forms under the influence of a chemoattractant.

In contrast to the tracheal system of *Drosophila*, the mammary gland is an example of a non-stereotyped organ that forms by chemorepulsion (Fig. 1.7b) [6, 79]. The mammary gland is a bilayered epithelial structure comprising inner luminal epithelial cells and basal myoepithelial cells forming ducts. The development of the mammary gland takes place during embryonic, pubertal, and adult stages. First, five placodes are formed during embryonic development that subsequently develop into a rudimentary branched structure. Then, the most striking change takes place during puberty when branches invade the surrounding tissue to form the mammary gland. Finally, during pregnancy milk-producing alveoli form. Interestingly, the mammary gland obtains its structure without any chemoattraction [83, 94–97], but instead relies on chemorepulsion. TGFβ, an inhibitor of branching morphogenesis, is produced by the mammary gland itself and forms

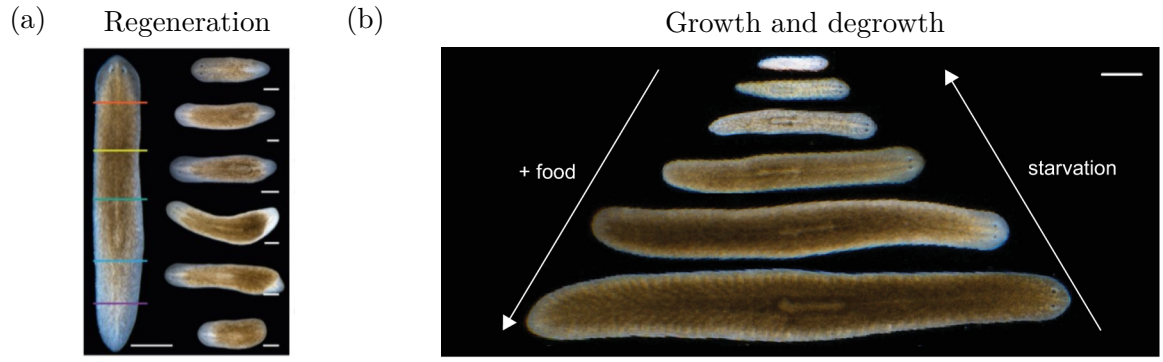

Figure 1.8: Growth, degrowth, and regeneration of planarians. (a) Planarians exhibit exceptional regenerative capabilities. Colored lines indicate the position of a cut. Regenerated tissue fragments from 14 d.p.a. Scale bar 500 µm. (b) Depending on food availability, planarians can grow and degrow. Scale bar 1 mm. Both images show the planarian species *Schmidtea mediterranea*. Reproduced with permission from Refs. [65, 101]

a gradient around branches, as demonstrated both *in vivo* and *in vitro* [82, 98]. TGFβ inhibits growth of ducts by either promoting the deposition of extracellular matrix around the mammary gland or by reducing the proliferation of basal cells [99, 100].

1.3 Planarians as a model system for organism scaling

Planarians are a group of flatworms that are mostly known for their exceptional abilities [102, 103]. For example, planarians are famous for their extraordinary regeneration capabilities (Fig. 1.8a). The planarian species *Schmidtea mediterranea* can regenerate missing body parts from (almost) arbitrarily small tissue fragments of any shape within approximately 14 days. This includes the *de-novo* formation and positioning of any missing body part, such as head or tail, and the restoration of size and proportion of the body [103]. These striking regenerative capabilities inspired John Graham Dalyell in 1814 to state that planarians "*...may almost be called immortal under the edge of the knife*" [104]. Besides their regenerative capabilities, planarians are also studied for their fluctuating body size (Fig. 1.8b). For example, the species *S. mediterranea* grows when food is available and shrinks during starvation (also called degrow) and in the process undergoes massive changes in body length (1-20 mm), body mass (0.1-20 mg), and also cell number ($10^4 - 10^7$) [65]. Beside these massive intraspecies size variations, planarians also offer a large range of interspecies size variation. Species at lake Baikal were reported to reach ∼100 mm and a species in Japan even reaches up to 1 m in body length [105].

The exceptional capabilities of planarians challenge existing ideas and concepts in developmental biology. For example, the existence of morphogen gradients spanning the entire organism length in planarians questions existing concepts for morphogen gradient formation. While a diffusion-degradation mechanism can generate morphogen gradients spanning the size of a tissue, novel concepts are needed to explain the formation of gradients spanning the entire organism [106]. Moreover, morphogen gradients in planarians have the ability to both scale with organism size and restore after an amputation event. While patterns in a Turing instability emerge in a self-organized way, they show a characteristic length scale and thus lack scaling with organism size. Inspired by morphogen gradients in planarians, a novel class of pattern forming mechanism was proposed that shows both scaling and self-organization [107]. In this thesis, we proceed in the same spirit and use the capabilities of planarians as inspiration to develop novel theoretical concepts. In particular, we use planarians as a model system to study growth and scaling of branched organs with the planarian gut as an example. Here, we now give an overview planarian anatomy including the planarian gut.

Planarians are part of the phylum Platyhelminthes (*platy*=flat; *helminthes*=worms) and constitute the clade Tricladida [105]. They are free-living organisms and live in both aquatic (salt- and freshwater) and terrestrial environments around the world. They have a bilaterally symmetric, flat body with anterior-posterior (distinct head and tail region) and dorso-ventral polarity (photoreceptors on the dorsal side). Despite their simple appearance they have a rich set of internal organ systems (Fig. 1.9).

The planarian gut is a highly branched organ that is responsible for the digestion of food and the delivery of nutrients to the body (Fig. 1.9,1). It spans the entire body and has a characteristic shape with one main branch in the anterior and two main branches in the posterior region [108]. The intestinal epithelium (gastrodermis) consists of three cell types [109–111]. The inner intestinal cell layer consists of phagocytes that absorb food particles for intracellular digestion and contain lipid droplets as well as glycogen and therefore contain part of the organismal energy storage. Goblet cells produce and secrete enzymes for digestion. Finally, the gut also possesses outer intestinal cells with so far unknown function [112]. The entire gut is enclosed by enteric muscle [113].

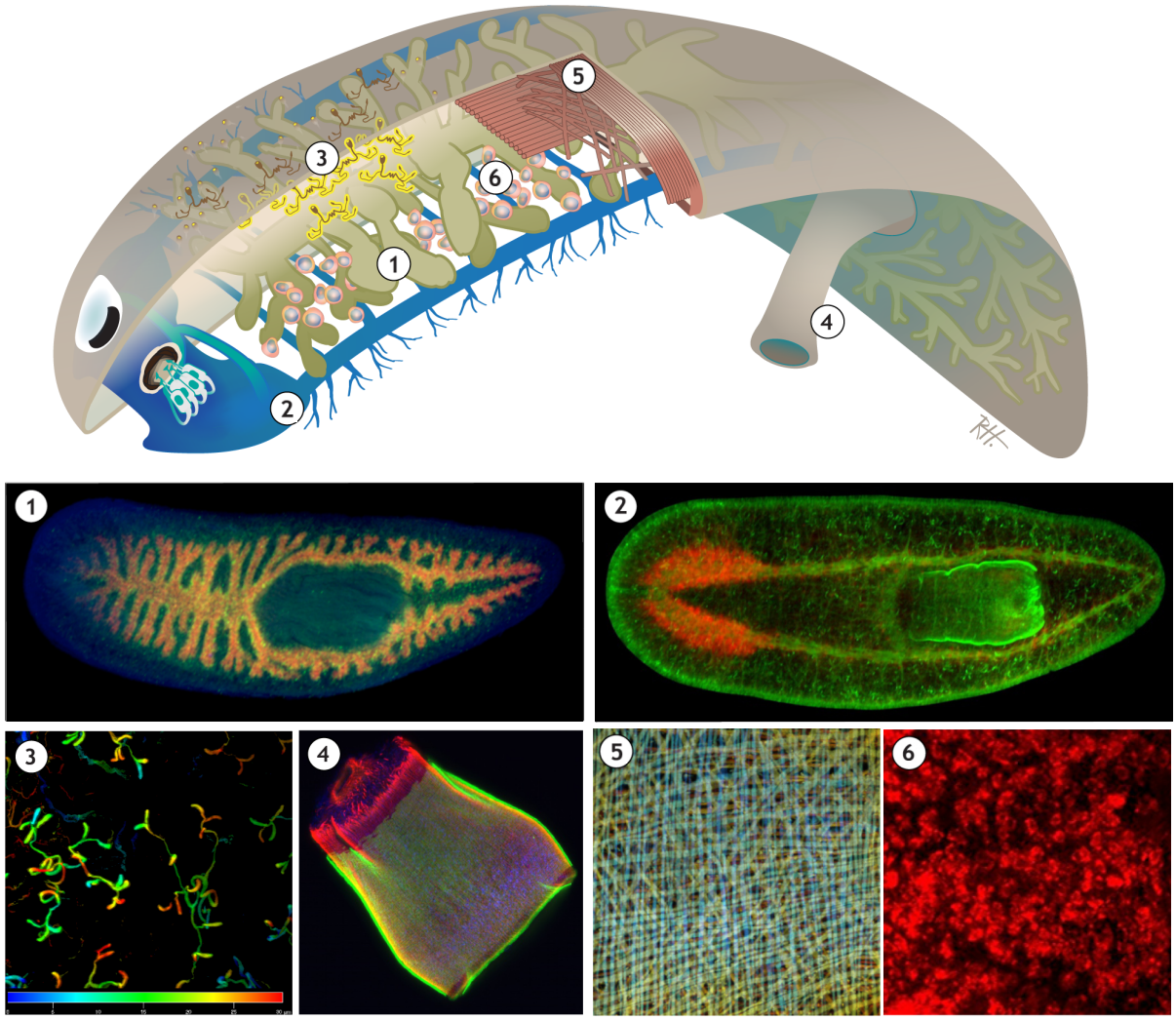

Figure 1.9: Planarian anatomy. Top: Sketch of planarian body anatomy. Bottom: Microscopy images of highlighted body regions. (1) The planarian gut (red, *Smed-porcupine-A*, green, *Smed-sufu in-situ* hybridization) along with the body outline (blue, nuclear counterstaining with DAPI). The gut is a highly branched organ responsible for food digestion. Empty region in the center of gut is the region the pharynx resides in. (2) Brain (red, *Smed-pc2 in-situ* hybridization), central nervous system, and pharynx (green, α-tubulin immunostaining). (3) Protonephridia (depth-coded confocal maximum projection of acetylated-tubulin immunostaining) are excretory organs distributed throughout the body. (4) The planarian pharynx is a muscular tube that can extrude upon food ingestion (red, phalloidin staining of muscle actin). (5) Pluripotent stem cells (red, confocal maximum projection of *piwi-1 in-situ* hybridization) are distributed throughout the body. (6) Planarians have a layer of longitudinal, diagonal, and horizontal oriented muscle fibers (depth-coded confocal maximum projection of 6G10 immunostaining). Staining details indicated in parentheses taken from Ref. [103]. Adapted with permission from Ref. [103].

Apart from the gut, planarians have a rich internal anatomy [103]. They have a brain connected with two ventral nerve cords and simple photoreceptors (Fig. 1.9,2). Protonephridia serve as a simple excretory organ (Fig. 1.9,3). The planarian pharynx is a muscular tube located on the ventral organism side and serves as the only body opening for both food ingestion and feces excretion (Fig. 1.9,4). The entire organism is surrounded by three layers of musculature with circular, longitudinal, and diagonal orientation [114, 115] (Fig. 1.9,5). The ventral side of the epidermis has cilia that are used for a gliding motion [116].

A key feature of planarian anatomy is their large population of pluripotent stem cells (called neoblasts) (Fig. 1.9,6) [117, 118]. Neoblasts are small, round cells (diameter 7-12 µm), that reside in the mesenchyme [103]. They constitute 10-20% of all cells and are the only cell type that can divide in the organism [119]. Thus, they are essential for the maintenance and regeneration of the planarian body. Under normal conditions they undergo division with a basal rate and renew all existing tissues. After feeding, neoblast division rate shortly increases, leading to an increase in organism size [120–122]. Irradiation with γ radiation blocks neoblast division and leads to the death of the organism [123, 124]. Interestingly, an organism can be rescued by transplanting a single stem cell from a healthy organism [125]. This experiment demonstrates that neoblast are pluripotent stem cells and highlights the importance of neoblasts for the regenerative capabilities of planarians.

A set of evolutionary conserved signaling pathways organizes the planarian body plan (Fig. 1.10) [103, 108]. For example, the Wnt signaling pathway organizes the anterior-posterior axis. Wnt shows graded activity along the anterior-posterior axis with highest activity in the tail and lowest activity in the head [126]. Activation of Wnt signaling leads to the transformation of a head into a tail and during regeneration at both poles tails form [127, 128]. Conversely, the inhibition of Wnt signaling leads to the transformation of a tail into a head (the animal forms a brain and eyes in the posterior region, only one instead of two main gut branches in posterior region) and during regeneration at both poles heads form [127, 129, 130]. The proteins Bmp4 and Admp ensure the organization of the dorso-ventral axis (BMP family) [131, 132]. In planarians *bmp4* is expressed at the dorsal pole and *admp* at the ventral pole of the organism. The knockdown of *bmp4* has striking consequences for the organism and leads to the formation of cilia on the dorsal epithelium [132]. Finally, the medio-lateral axis is controlled by the expression of *wnt5* and *slit* [133, 134]. Knockdown of *wnt5* leads to a phenotype with two additional pharynx placed next to the pharynx present in all wild-type animals and knockdown of *slit* leads to the fusion of photoreceptors on the organism midline.

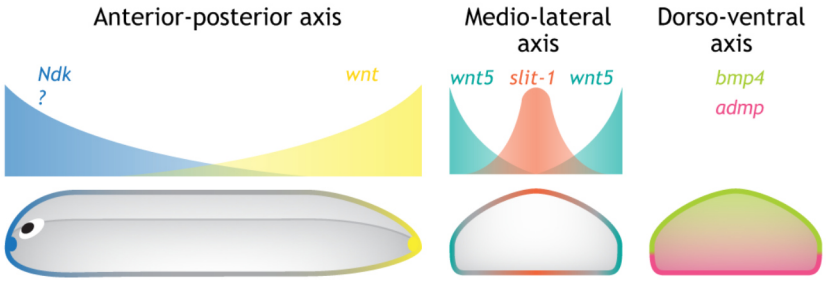

Figure 1.10: Morphogen signaling systems in planarians. We show the signaling activity of the main signaling pathways in planarians. Note that the shown signaling gradients are extrapolations from the respective gene expression pattern and do not reflect measurements. Reproduced with permission from Ref. [103].

1.4 Branching in physics: pattern formation in unstable interface growth

The formation of complex branched morphologies is not only a common process in biology, but also in many areas of physics [135–137]. Branched structures are observed in a wide class of systems including the solidification of a liquid from an undercooled melt, the flow of fluids through narrow channels, the aggregation of particles during electrodeposition, the growth of bacterial colonies, and also in dielectric breakdown (Fig. 1.11). While these systems seem diverse at first, their highly branched structure originates in a similar way. On an abstract level, all these systems can be described as the growth of an interface that separates two distinct regions (e.g. the liquid and solid phase in solidification). Any protrusion in this interface leads to an amplification of the growth rate of this protrusion and therefore leads to unstable interface evolution. Since the growth rate of this interface is controlled by a field that is determined by the Laplace equation (e.g. temperature in solidification), this class of pattern forming systems is called "Laplacian growth" [137, 138]. We now discuss the solidification of a pure liquid and diffusion-limited aggregation of particles as two paradigmatic examples of this broad class of pattern forming systems.

1.4.1 Solidification and the Mullins-Sekerka instability

The formation of complex interfacial patterns is a common process in crystal growth [135, 136, 144, 145]. Typical scenarios of crystallization include the growth of a solid from a pure undercooled liquid (e.g. freezing of water) or from a supersaturated solution (e.g. supersaturated solution of NH_4Cl). In both cases, crystallization starts from a nucleation seed and then the solid advances into the liquid while forming branched interfacial pat-

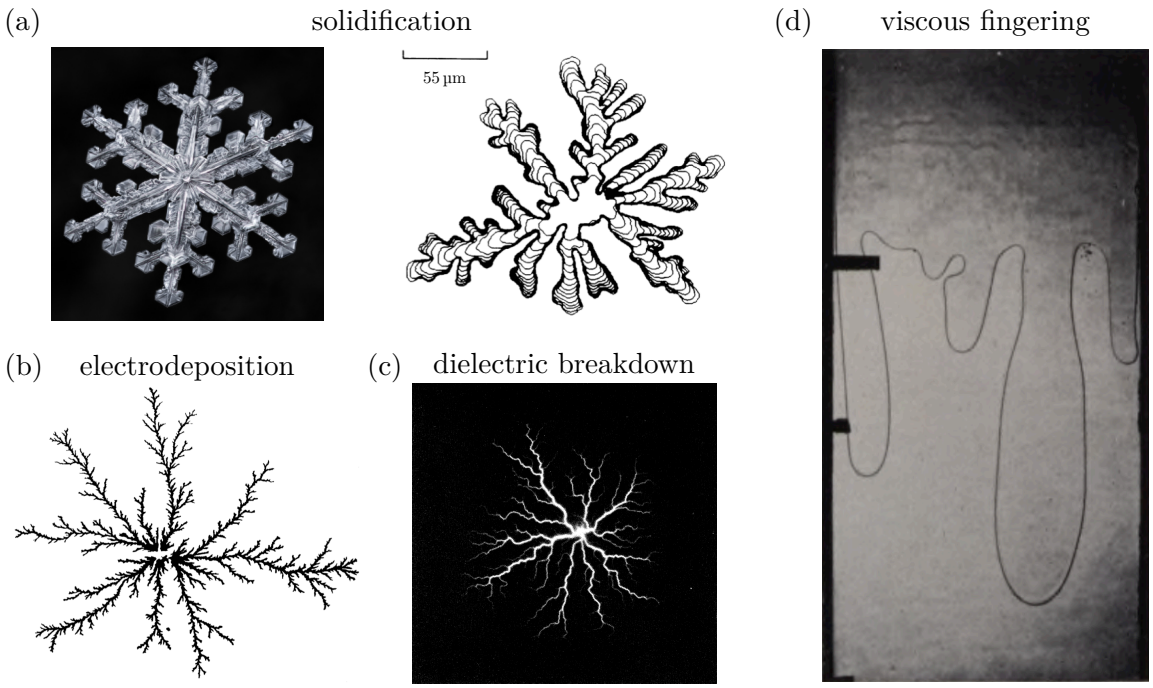

Figure 1.11: Pattern formation in unstable interface growth. (a) Left: Growth of a snowflake crystal as an example for solidification influenced by symmetry of its constituents. Right: Growth of a crystal from a supersaturated aqueous ammonium chloride solution between two glass plates as an example for solidification in a random environment as one of the glass plates has a rough surface. (b) Growth of zinc aggregates from aqueous solution of zinc sulfate. A carbon cathode is placed in the center of a zinc ring anode (diameter 17 cm) and a dc voltage applied. 2D aggregates grow along an interface of *n*-butyl acetate on the solution. (c) Time-integrated image of discharge pattern (Lichtenberg figure). An electrode was connected at the center of a thick glass plate that was grounded at the boundary. Upon applying a voltage pulse, a radial discharge pattern develops. (d) Viscous fingering pattern observed when a less viscous fluid (air) is injected into a more viscous fluid (glycerine). Reproduced with permission from Refs. [139–143]

terns. Here, we discuss the solidification from a pure undercooled liquid as an example to highlight key aspects for this class of pattern forming systems. The discussion of growth from a supersaturated solution is analogous and can be found in [135, 136].

We consider a scenario where a solid (s) phase is embedded in a liquid (l) phase [136]. The liquid phase is undercooled, i.e. it is at temperature $T < T_M$, where T_M is the melting temperature. As a simplification, we consider both phases to be separated by a sharp interface. In each phase, the temperature T_i is governed by the diffusion equation

$$\partial_t T_i = D_T^i \nabla^2 T_i, \tag{1.2}$$

where $i \in \{s, l\}$ labels the respective phase and D_T^i denotes the thermal diffusivity. This equation is complemented by appropriate boundary conditions depending on the specific scenario that is studied. At the interface, we can use energy conservation to arrive at an equation for the interface velocity v_n:

$$Lv_n = [D_T^s c_p^s (\boldsymbol{\nabla} T)_s - D_T^l c_p^l (\boldsymbol{\nabla} T)_l] \cdot \boldsymbol{n} \tag{1.3}$$

Here, L denotes the latent heat per unit volume, c_p^i denotes the specific heat per unit volume in the respective phase, and $\boldsymbol{n}$ denotes the interface normal vector. Eq. (1.3) balances the latent heat released upon solidification (left side) with the heat transported away from the interface into the two phases (right side). At the interface we use the Gibbs-Thomson relation

$$T = T_M \left(1 - \frac{\gamma \kappa}{L}\right) \tag{1.4}$$

as a boundary condition, which takes into account the dependency of the melting temperature on the interface curvature κ. The interface curvature κ is defined such that it is positive for a protrusion of the solid into the liquid phase and γ denotes the surface tension. Altogether, Eqs. (1.2)-(1.4) define a simple model for the growth of an interface by solidification. Note that solidification is an example of diffusion-limited growth since the rate of heat transport away from the interface determines the interface velocity (1.3). This has interesting consequences for the stability of the interface which we will discuss next.

To qualitatively understand the origin of unstable interface evolution in this model, we consider two scenarios of interface growth in a system with walls maintained at temperature $T < T_M$ [136]. In one scenario the solid is in contact with the walls and grows into a liquid with temperature $T > T_M$. In this scenario, interface growth is stable: Any protrusion of the interface results in a reduction of heat transport from the protrusion to the system wall and therefore in a reduction of protrusion velocity. The growth of protrusions is hindered and the interface gets smooth again. By contrast, the growth of a solid from the center of the system towards the system walls leads to unstable interface growth. Here, the formation of a protrusion leads to an increase of heat transport from the protrusion and thus to an increase of protrusion velocity. The growth of protrusions is promoted, leading to complex branched interfaces.

The diffusion-driven instability in solidification was first systematically studied by Mullins and Sekerka and is therefore today known as the Mullins-Sekerka instability [146, 147]. A similar instability with finger like protrusions (known as viscous fingering) can be observed

when a viscous fluid is pushed into a second more viscous fluid in a narrow, flat channel. Here, Saffman and Taylor elucidated the mechanism of the instability and therefore it is today known as Saffman-Taylor instability [140, 148]. Both systems serve as paradigmatic examples for the formation of branched interfaces.

While instabilities lead to highly branched structures, many other factors contribute to their overall morphology. For example, in solidification the anisotropy of the growing structure (e.g hexagonal symmetry of snowflakes) is closely related to the internal order of the substances forming it (e.g. molecular structure of water, Fig. 1.11a, left). More irregularly crystals can be formed if the growth process takes place in a "random environment". A crystal of NH_4Cl without apparent symmetry was grown between two glass plates, where one of the glass plates had a rough surface (Fig. 1.11,a, right) [139, 149]. Likewise, an anisotropy for patterns generated in viscous fingering can be induced by engraving a lattice structure on the glass plates confining the fluid motion in the experimental apparatus [150]. Thus, both the instability and external factors control the structure of branched patterns.

1.4.2 Diffusion-limited aggregation

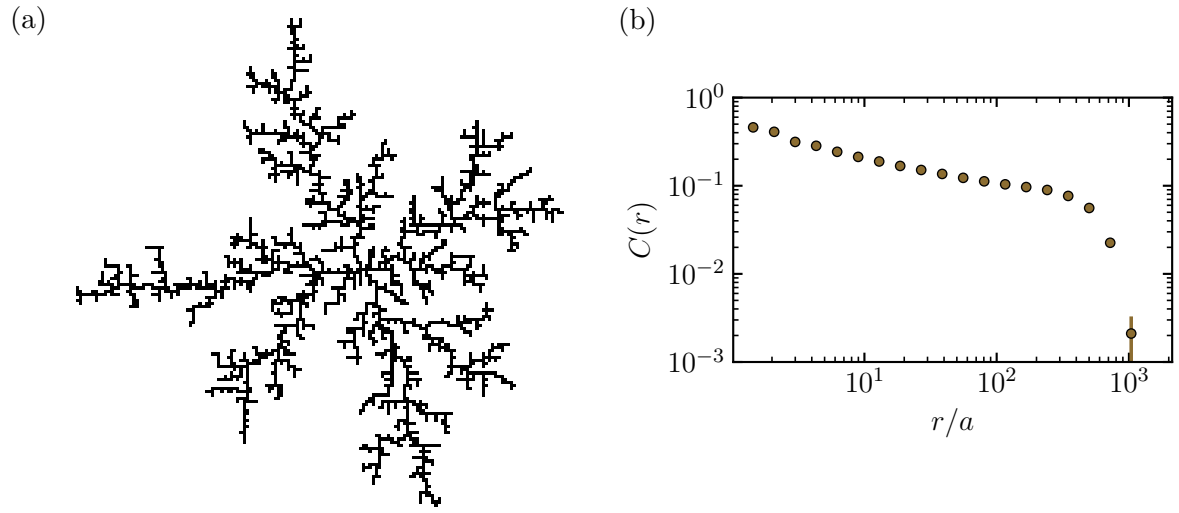

Figure 1.12: Unstable interface growth in diffusion-limited aggregation. (a) Example cluster of size $M = 2500$ generated by DLA. Simulation performed by the author. (b) Correlation function $C(r)$ for an ensemble of 12 aggregates of size $M = 50000$. We denote the size of a lattice site by a. Error bars denotes the standard deviation of the correlation function. Note that for the data shown here, the error bar size is smaller than the marker size.

The formation of clusters by irreversible aggregation of particles provides another important class of systems with complex interface growth. For example, in electrodeposition experiments a variety of interface morphologies can be bound [141, 151]. In these experiments, a cathode is placed in the center of a vat surrounded by a ring-like anode (e.g. Zn). Both anode and cathode are immersed in a solution (e.g. zinc sulfate $ZnSO_4$). Upon applying a dc voltage, the formation of highly branched structures can be observed (Fig. 1.11b).

In their seminal work, Witten and Sander developed a model to understand the structures observed in the irreversible aggregation of particles [152, 153]. In their model, now known as "diffusion-limited aggregation" (DLA), a random walker on a (square) lattice represents aggregating particles. Initially, a particle is placed as a nucleation seed in the center of the system and subsequently another particle is released at a random location at the system boundary. The particle performs a random walk until it reaches a site next to the cluster. In this case, the random walk is terminated and a new particle released. The random walk of a particle is also stopped, if a particle crosses the system boundary. The repeated execution of this process results in complex branching morphologies exhibiting self-similar fractal scaling (Fig. 1.12).

The formation of branching structures in DLA and solidification is closely related. To make this connection rigorously, we follow Witten and Sander and employ parallels between random walks and the diffusion equation [152, 153]. We introduce the probability $u(\boldsymbol{x}, k)$ that a random walker is at lattice site $\boldsymbol{x}$ at time step k. The probability $u(\boldsymbol{x}, k)$ satisfies the relation

$$u(\boldsymbol{x}, k+1) = \frac{1}{c} \sum_{\boldsymbol{l}} u(\boldsymbol{x} + \boldsymbol{l}, k), \tag{1.5}$$

where c denotes the number of neighbors of a lattice site. This equation expresses that a particle can be found at lattice site $\boldsymbol{x}$ at time step $k+1$ if it was at a neighboring lattice site $\boldsymbol{x}+\boldsymbol{l}$ at the previous time step and made a jump to $\boldsymbol{x}$. Eq.(1.5) is key to our discussion since we can use it to derive both the continuum limit of particle and interface motion. First, we can regard Eq. (1.5) as a discrete diffusion equation with boundary conditions $u = 1$ on the system boundary and $u = 0$ on the sites adjacent to the cluster. In the continuum limit, we find

$$\partial_t u = D \nabla^2 u \tag{1.6}$$

with diffusion constant D. Note that we can neglect the time derivative on the left hand site since particles are released one at a time and the quasistatic limit therefore holds. Next, we can derive the continuum limit of interface motion. From Eq. (1.5) we deduce

that the probability $v(\boldsymbol{x}, k)$ that a particle is added to the cluster satisfies

$$v(\boldsymbol{x}, k+1) = \frac{1}{c} \sum_{\boldsymbol{l}} u(\boldsymbol{x} + \boldsymbol{l}, k). \tag{1.7}$$

In the continuum limit, this gives for the normal velocity v_n of the interface of the cluster

$$v_n = D\boldsymbol{n} \cdot \boldsymbol{\nabla} u, \tag{1.8}$$

where $\boldsymbol{n}$ denotes the interface normal vector. Thus, we have derived the continuum limit of diffusion-limited aggregation given by Eq. (1.6) and (1.8).

With the continuum limit at hand, we can now discuss similarities and differences between models for diffusion-limited aggregation and solidification. In both cases, the interface grows by diffusion. In solidification, the diffusion of heat away from the interface determines the interface growth rate. The heat flux is largest at tips causing an instability of interface growth. In DLA, the diffusive motion of particles to the interface determines its growth. The arrival of particles at tips is largest, while valleys further inside of the cluster can be considered as screened. This leads to a self-amplification of the growth of tips in a similar way as for solidification. An important difference between both models is the lack of surface tension in DLA. This demonstrates the close connection between DLA and other surface growth models.

Over the years, many extensions and variants of DLA have been studied. Much effort has been devoted to approach the mean-field limit of DLA. For example, Nittmann developed a noise reduction technique where particles are only attached to the cluster once they have landed s times on the same perimeter site of the cluster [154]. This way, a transition from noisy structures (s small) to smooth structures with non-zero finger thickness (s large) could be demonstrated. To overcome the lack of surface tension in DLA, a curvature dependence was included into the attachment kinetics of random walkers. Vicsek and Tao used a curvature-dependent attachment probability [155, 156], while Kadanoff and Liang developed a method, where particles could detach and re-attach in a curvature-dependent manner [157, 158]. Variants of DLA have been applied to scenarios other than irreversible aggregation of particles. For example, Niemeyer developed the so-called dielectric-breakdown model to study self-similar structures observed in discharge patterns [142]. In this model, the analogy between the Laplace equation and the probability to find a random walker at a lattice site is used, cf. (1.5). Niemeyer solves the discrete Laplace equation for the electric potential and adds lattice sites to the cluster with a probability proportional to the gradient of the electric potential. This way, self-similar structures with

properties similar to discharge patterns can be generated.

1.5 Organization of this thesis

In this thesis, we study theoretically the self-organized formation of branched structures in biology. To this end, we combine the idea of morphogen-controlled growth of organs with the concept of self-organized formation of branched structures by unstable interface motion. Thus, we study instabilities and pattern formation in morphogen-controlled interface growth as a mechanism for the formation of branched structures in biology.

This thesis is broadly divided into two parts. In chapter 2 and 3, we first present minimal models for morphogen-controlled interface growth. We discuss how instabilities arise in interface motion and analyze the geometry and topology of the resulting interfacial patterns. In chapter 2, we present a lattice model for morphogen-controlled interface growth. In this model, interface growth takes place in a stochastic way with a rate determined by a concentration gradient. We relate our model to diffusion-limited aggregation and explain how an instability originates in analogy to DLA. We further discuss the statistical properties of the different branched structures the model gives rise to. Finally, we derive topology-preserving transition rates that allow us to control the topological properties of branched structures. Overall, chapter 2 presents a first example for an interface growth rule that exhibits an instability and allows us to study the limit of zero surface tension and finite noise of morphogen-controlled interface growth.

In chapter 3, we present a continuum model for morphogen-controlled interface growth. In contrast to chapter 2, we explicitly take into account surface tension in our description. We perform a linear stability analysis and discuss how an instability takes place in this model. Next, we go beyond the linear stability analysis and study the geometry and topology of interfacial patterns in the unstable parameter regime. We provide a brief introduction to the phase-field method and explain how it can be employed to numerically solve the interface equations. We combine simulations with analytically tractable special cases of our model to understand the geometrical and topological properties of resulting morphologies. Overall, chapter 3 presents a second example for an interface growth rule that exhibits an instability and allows us to study the limit of zero noise and finite surface tension of morphogen-controlled interface growth.

While the first part of this thesis served to understand basic principles of instabilities in morphogen-controlled interface growth, in the second part we apply the developed ideas and concepts together with colleagues from the MPINAT in Göttingen (Amrutha

Palavalli, Baiqun An from the lab of Jochen Rink) to study planarian gut morphogenesis. To this end, we first provide a quantitative analysis of the planarian gut in chapter 4. After presenting details of our quantification procedure, we discuss the geometrical and topological properties of the planarian gut. A particular focus lies on the size-dependent properties of the planarian gut, where we reveal how various gut features show power law scaling as a function of organism size.

In chapter 5, we present a model for the morphogen-controlled growth and scaling of the planarian gut. This model is based on our continuum description from chapter 3 and introduces novel concepts to account for the organization of the planarian gut. Since gut morphogenesis takes place in a growing organism, we include organism growth into our description. Inspired by branch orientation in the planarian gut, we introduce additional external guiding cues into the description to control branch orientation in our model. To understand the formation of branched patterns in this model, we first consider a non-growing system and discuss how branch distance, thickness, and orientation and also the symmetry of morphologies is controlled. Next, we study a growing system and study the size-dependency of resulting morphologies. We find that various properties of morphologies display power law scaling, which we rationalize by a minimal scaling argument. We finally compare model predictions with experimental data. We conclude this thesis with a discussion of our results and provide an outlook on future work in chapter 6.

Chapter 2

Geometry and topology of aggregates formed by morphogen-controlled growth

In this chapter, we combine the idea of morphogen-controlled growth of tissues and organs with concepts from diffusion-limited aggregation (DLA) to develop a minimal lattice model for morphogen-controlled branching morphogenesis. DLA is a central concept in unstable interface growth and has been employed to study electrodeposition, dielectric breakdown, or also viscous fingering [138]. Here, we present a stochastic lattice model of morphogen-controlled interface growth and demonstrate how highly branched morphologies are generated by an instability similar to the one in DLA. Motivated by the role of topology for branched structures in biology, we use the Euler characteristic as an example of a topological invariant to introduce constraints into the growth process and thereby generate tree-like aggregates.

This chapter is structured as follows. We first present our lattice model for morphogen controlled interface growth and relate it with DLA by considering the respective continuum limits. We demonstrate the generation of highly branched structures by an instability and discuss the statistical properties of resulting aggregates. In the second part of the chapter, we introduce the Euler characteristic and use it to introduce topological constraints into interface growth. We then discuss the statistical properties of the resulting morphologies. Finally, we provide an outlook on our approach and demonstrate how the incorporation of topological constraints into interface dynamics allows us to both grow and degrow aggregates. This might serve as a scenario to study the reversibility of interface growth processes in the future.

2.1 Stochastic lattice model of morphogen-controlled interface growth

2.1.1 General model setup

For simplicity, we consider a square lattice with N rows and columns and thus in total N^2 square lattice sites, where each lattice site is of length a. We label rows with index i and columns with index j and these indices thus satisfy

$$i = 0, \ldots, N-1 \tag{2.1a}$$

$$j = 0, \ldots, N-1. \tag{2.1b}$$

Each lattice site is equipped with an occupation number n_{ij} and a morphogen concentration c_{ij}. Occupation numbers are binary variables with $n_{ij} \in \{0, 1\}$. Morphogen concentrations c_{ij} are positive real numbers with $c_{ij} \geq 0$. We denote the set of all occupation numbers by $\{n_{ij}\}$ and likewise the set of all morphogen concentrations by $\{c_{ij}\}$. We refer to the set of all lattice sites with $n_{ij} = 1$ as "aggregate".

Due to the importance of local 3×3 neighborhoods for the definition of model dynamics, we provide a simplified notation for lattice site indices of such neighborhoods (Fig. 2.1). In particular, we use the mapping

$$r = Ni + j \qquad \text{with} \qquad r = 0, \ldots, N^2 - 1 \tag{2.2}$$

to number lattice sites with a single index r instead of labeling rows and columns with a pair of indices i, j. In this mapping, lattice sites are numbered in a row-major order, i.e. lattice sites are traversed and numbered along rows. We obtain a pair of indices i, j from a single index r by using the inverse of the mapping Eq. (2.2)

$$i = r/N \tag{2.3a}$$

$$j = r \bmod N, \tag{2.3b}$$

where "/" denotes integer division and "mod" denotes the modulo operation. Apart from the central lattice r in a neighborhood, we also provide a simplified notation for its neighbors. We denote the lattice site index of its four nearest neighbors by e_i. Likewise, we denote the lattice site index of its four next neighbors by d_i. In both cases, the index $i = 1, \ldots, 4$ labels the neighbors in a counterclockwise direction.

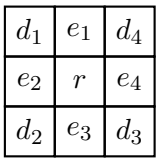

Figure 2.1: Notation for local 3×3 neighborhood around a lattice site r. We denote nearest neighbors by e_i and next neighbors by d_i, where we in both cases label neighbors by $i = 1, \ldots, 4$ in a counterclockwise direction.

2.1.2 Model dynamics

In our stochastic lattice model of branching morphogenesis, we study the coupled dynamics of occupation numbers $\{n_r\}$ and morphogen concentrations $\{c_r\}$ (Fig. 2.2a). The dynamics of occupation numbers is governed by the Master equation

$$\begin{aligned}\partial_t p(\{n_r\}, t) = &\sum_r [k_-^r n_r + k_+^r (1 - n_r)] p(n_0, \ldots, 1 - n_r, \ldots, n_{N-1}) \\ &- \sum_r [k_-^r n_r + k_+^r (1 - n_r)] p(n_0, \ldots, n_r, \ldots, n_{N-1}),\end{aligned} \tag{2.4}$$

which describes the stochastic transition of a single occupation number $n_r = 0 \to n_r = 1$ with growth rate k_+^r or $n_r = 1 \to n_r = 0$ with degrowth rate k_-^r. Here, we consider a special case of the dynamics described by Eq. (2.4) with transition rates

$$k_+^r = k_+^0 \sum_e (1 - n_r) n_{r+e} \frac{c_{r+e} - c_r}{a} \tag{2.5a}$$

$$k_-^r = k_-^0 \sum_e n_r (1 - n_{r+e}) \frac{c_{r+e} - c_r}{a}. \tag{2.5b}$$

Clearly, in both cases the (de)growth rate $k_\pm^r$ is determined by a morphogen gradient. Moreover, the terms $(1 - n_r)n_{r+e}$ and $n_r(1 - n_{r+e})$ ensure that transitions of occupation numbers take place only at interfaces, i.e. at lattice sites with a non-zero gradient of occupation number (Fig. 2.2b). While k_+^r is non-zero for empty lattice sites ($n_r = 0$) with any activated nearest neighbor ($n_{r+e} = 1$), k_-^r is non-zero for activated lattice sites ($n_r = 1$) with any empty nearest neighbor ($n_{r+e} = 0$). Thus, Eq. (2.4) and (2.5) describe an interface (de)growth process guided by a morphogen gradient. In both cases, the rate $k_\pm^0$ allows to adjust the overall rate of the process and therefore provides a timescale for this (de)growth process.

The dynamics of morphogen concentrations $\{c_r\}$ is governed by the reaction-diffusion equation

$$\partial_t c_r = D \bar{\nabla}^2 c_r - k(n_r) c_r + s(n_r), \tag{2.6}$$

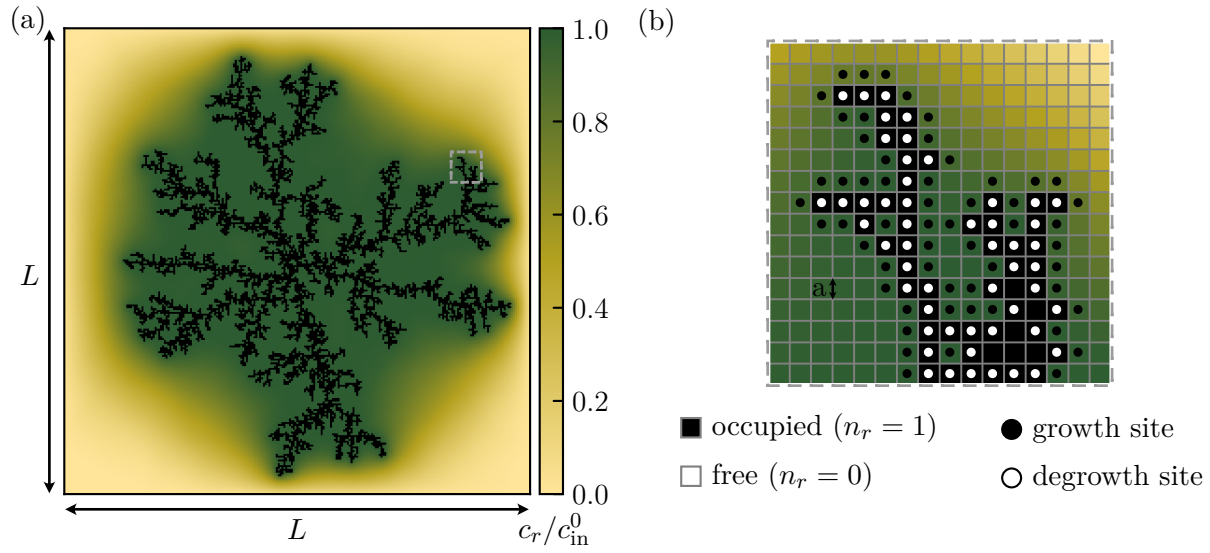

Figure 2.2: Lattice model for morphogen-controlled branching morphogenesis. (a) We consider a $N \times N$ square lattice with lattice constant a and system size $L = Na$. Each lattice site r carries an occupation number $n_r \in \{0, 1\}$ and a morphogen concentration c_r. We show an example aggregate formed according to Eq. (2.5) and Eq. (2.6) of size $M = 7500$ in the DLA-limit ($\lambda_{\text{in}}/a = 0.01$, $\lambda_{\text{out}}/L = 100$, $\Delta c = c^0_{\text{in}}$) displaying the characteristic, highly ramified structure. (b) Magnification of the dashed box in (a): We indicate potential growth sites (filled circles) and degrowth sites (empty circles). Note that topology-changing transitions are allowed according to the transition rates Eq. (2.5).

where we have used the discrete Laplacian operator

$$\bar{\nabla}^2 c_r = \frac{1}{a^2} \sum_e [c_{r+e} - c_r]. \tag{2.7}$$

These equations describe the diffusion of morphogen between lattice sites with diffusion constant D, the degradation with a rate $k(n_r)$, and the production with rate $s(n_r)$. For generality, we assumed that the degradation and production of morphogen can depend on the occupation number.

While Eq. (2.6) describes a general reaction diffusion process on a lattice, here we study a special case. For simplicity, we consider the quasistatic limit in which morphogen dynamics is much faster than the interface (de)growth dynamics. We therefore solve the case $\partial_t c_r = 0$ instead of the full dynamics defined by Eq. (2.6). Moreover, we consider the

degradation and production terms

$$k(n_r) = k_{\text{in}} n_r + k_{\text{out}}(1 - n_r) \tag{2.8}$$

$$s(n_r) = s_{\text{in}} n_r + s_{\text{out}}(1 - n_r). \tag{2.9}$$

Thus, degradation and production rates are constant, but in general different for regions inside ($n_r = 1$) and outside ($n_r = 0$) of aggregates. As a consequence, we have different reaction-diffusion lengths $\lambda_i = \sqrt{D/k_i}$ and characteristic morphogen concentrations $c_i^0 = s_i/k_i$ for inside and outside regions. In general, we have a non-zero difference Δc of characteristic morphogen concentrations between the inside and outside region, where $\Delta c = c_{\text{in}}^0 - c_{\text{out}}^0$. In our model we can study both the case of strong morphogen production inside ($\Delta c > 0$) and outside ($\Delta c < 0$) of aggregates. Here, we focus on the case of strong morphogen production inside the aggregate ($\Delta c > 0$), which corresponds to the case of morphogen that is produced in an organ diffuses in the organism and in this way guides organ growth.

In our model, we enforce zero occupation number ($n_r = 0$) and zero morphogen concentration ($c_r = 0$) at the system boundary, i.e. we have a morphogen sink at the boundary. As a simple scenario for pattern formation and in analogy to the situation studied in DLA, we initialize our system with a single occupied lattice site in the system center with zero concentration throughout the system.

To numerically obtain samples of the stochastic process defined by Eq. (2.4) and Eq. (2.5) together with the quasistatic limit of Eq. (2.6), we use the Gillespie algorithm [159–161]. Given a configuration of occupation numbers $\{n_r\}$ at a time t_0, we first obtain the corresponding concentration values $\{c_r\}$. In the quasistatic limit, the morphogen dynamics described by Eq. (2.6) and Eq. (2.7) constitute a system of M coupled linear equations that we can solve by using the conjugate gradient method [162]. Next, we use the rate α_r for a transition to take place at lattice site r to determine the overall transition rate α to leave the current state of the system:

$$\alpha = \sum_r \alpha_r \qquad\qquad \alpha_r = k_+^r + k_-^r \tag{2.10}$$

We use this to determine the time Δt to the next transition

$$\Delta t = t - t_0 = -\frac{\log \xi}{\alpha}, \tag{2.11}$$

where ξ is a uniformly distributed random number with $\xi \in [0, 1]$. The specific event that

will take place is determined according to

$$\sum_{s=0}^{r-1} \alpha_s < \zeta < \sum_{s=0}^{r} \alpha_s, \tag{2.12}$$

where ζ is another uniformly distributed random number with $\zeta \in [0, 1]$.

2.1.3 Relation to diffusion-limited aggregation

To compare our lattice model for branching morphogenesis with DLA, we consider the continuum limit of both models. In the continuum limit, the reaction-diffusion dynamics of the lattice model defined by Eq. (2.6) becomes

$$\partial_t c_i = D\nabla^2 c_i - k_i c_i + s_i, \tag{2.13}$$

where the index $i \in \{\text{in}, \text{out}\}$ labels regions inside and outside the aggregate. From the transition rate Eq. (2.5), we find that the normal velocity v_n of the interface separating the inside and outside region obeys

$$v_n = D^0_{\pm} \boldsymbol{n} \cdot \boldsymbol{\nabla} c, \tag{2.14}$$

where we have introduced the interface diffusion constant $D^0_{\pm} = k^0_{\pm} a$ and $\boldsymbol{n}$ denotes the interface normal vector. For a discussion of the continuum limit of DLA we refer the reader section 1.4.2 of the introduction chapter.

The continuum limit of our lattice model and DLA now allow us to discuss similarities and differences of both models. While in both cases the gradient of a diffusive field determines the growth of the aggregate, the models differ in the details of the dynamics and boundary conditions of the diffusive fields. In the lattice model, the morphogen concentration c constitutes the diffusive field and its dynamics is governed by the reaction diffusion equation Eq. (2.13) together with a fixed concentration at the system boundary. This allows us to consider different scenarios in which morphogen is predominantly produced on the aggregate and forms a gradient towards the boundary or the opposite case in which morphogen is predominantly produced on the boundary and forms a gradient towards the aggregate. In any case, the concentration fields have a characteristic length λ_{in} inside and λ_{out} outside of the aggregate. Moreover, the preferred concentration value $c^0_i = s_i/k_i$ in each region can be controlled by the ratio of production rate s_i and degradation rate k_i. In the case of DLA, the probability u to find a random walker constitutes the diffusive

field. The probability to find a random walker is governed by diffusive dynamics according to Eq. (1.6) together with the condition $u = 1$ at the system boundary (source of random walkers) and the condition $u = 0$ on the aggregate (sink of random walkers). In contrast to the lattice model, the number of random walker is conserved in DLA. Thus, a degradation rate and therefore a characteristic length scale is lacking. Overall, our lattice model is a versatile system to study the formation of interface patterns guided by a morphogen gradient. Note that we can recover the DLA dynamics with our lattice model ("DLA limit") in the limit of decoupled lattice sites on the aggregate ($\lambda_{\text{in}}/a \ll 1$ with $c_i^0 = \text{const}$) and vanishing degradation of morphogen outside of the aggregate ($\lambda_{\text{out}}/L \gg 1$).

The relation between our lattice model and DLA allows us to discuss if the lattice model exhibits unstable interface evolution. Witten and Sander performed a linear stability analysis for DLA and showed that the system can become unstable [152, 153]. An interface protrusion experiences a larger influx of random walkers than its flat surroundings and thus undergoes enhanced growth. Since protrusion growth further increases the influx of random walkers a positive feedback sets in, which leads to the formation of unstable interface morphologies. From this we conclude that our lattice model becomes unstable in the DLA-limit in a similar way. An interface protrusion experiences larger morphogen concentration gradients than its flat surroundings and thus undergoes enhanced growth. A positive feedback sets in, which leads to the formation of complex branched morphologies. Next, we numerically study our lattice model and confirm the unstable interface evolution in the DLA-limit. Additionally, we study the influence of coupled lattice sites ($\lambda_{\text{in}} \neq 0$) and non-vanishing morphogen degradation ($\lambda_{\text{out}}/L \ll 1$).

2.2 Geometry of aggregate morphologies

We next systematically studied the various interfacial patterns the lattice model gives rise to. To confirm the relation between our lattice model and DLA, we first considered the DLA-limit of the lattice model. In this limit, we find unstable interface evolution that gives rise to highly ramified morphologies with apparent similarity to DLA aggregates (Fig. 2.3a and b, left most). Next, we studied the influence of the diffusion-degradation length λ_{out} on aggregate morphology. To this end, we start with the DLA-limit and gradually increase λ_{out} while maintaining the remaining model parameters (Fig. 2.3a). We find a transition from highly branched morphologies ($\lambda_{\text{out}} \gg L$) to compact, almost circular shapes ($\lambda_{\text{out}} \ll L$). In the limit of strong morphogen degradation ($\lambda_{\text{out}} \ll L$), morphogen gradients at the interface are determined by the length scale λ_{out} only. As a

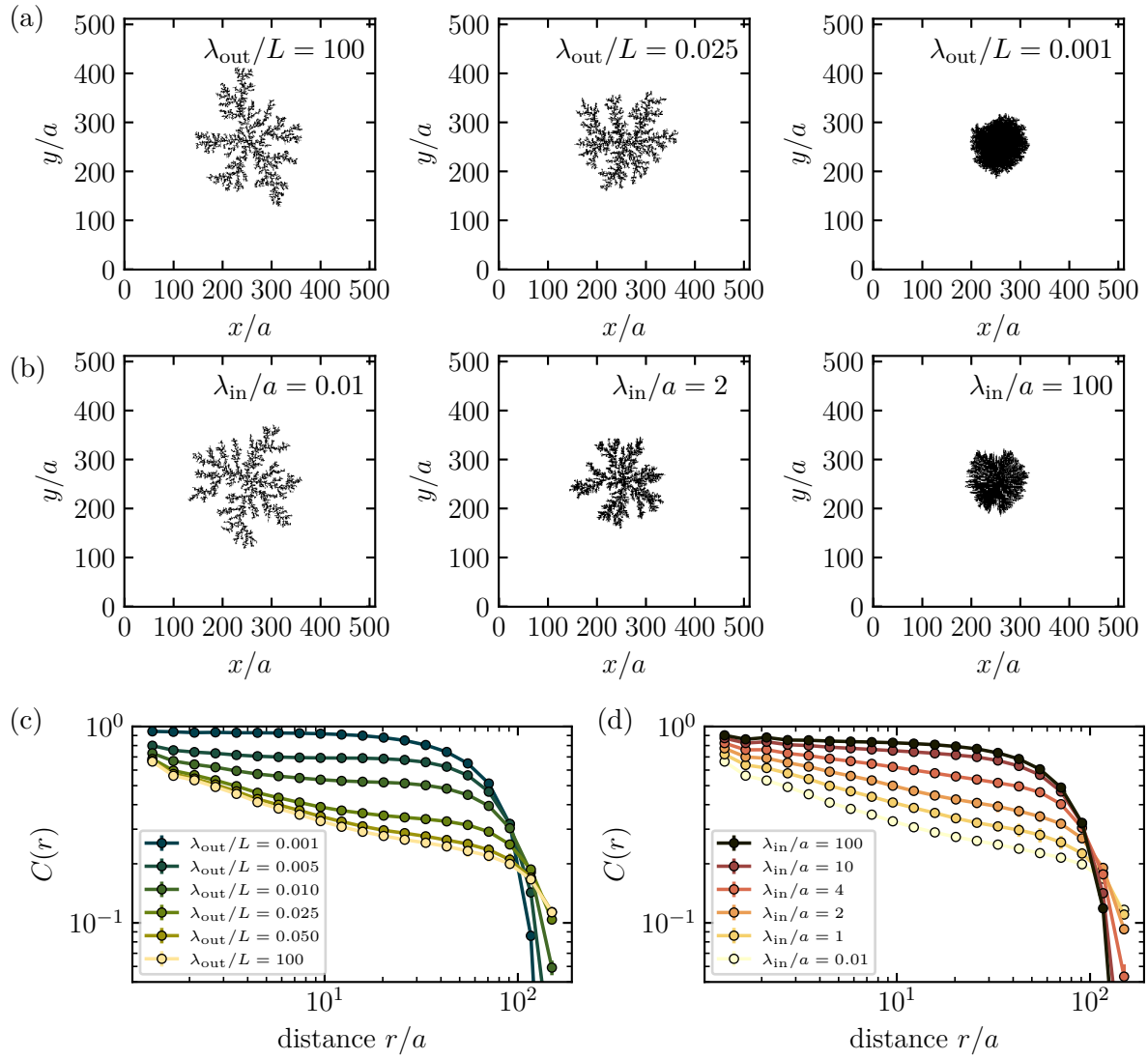

Figure 2.3: Aggregate morphologies and quantification of their statistical properties. (a) We show aggregates of size $M = 10000$ with $\lambda_{\text{in}}/a = 0.01$ for different values of λ_{out}. (b) We show aggregates of size $M = 10000$ with $\lambda_{\text{out}}/L = 100$ for different values of λ_{in}. (c,d) Quantification of statistical properties of aggregates with the two-point density-density correlation function $C(r)$ defined by Eq. (2.15). Error bars denote the standard deviation obtained from averaging the correlation function for $n = 16$ different aggregates, but are typically smaller than the marker size.

consequence, we find uniform growth rate along the interface which results in the reduction of the instability and the growth of a circular morphology. To study the influence of the diffusion-degradation length λ_{in} on aggregate morphology, we employ a similar strategy. We start with the DLA-limit and then gradually increase λ_{in} (Fig. 2.3b). Again, we find a transition from highly branched ($\lambda_{\text{in}} \ll a$) to compact morphologies ($\lambda_{\text{in}} \gg a$). In the limit of strong diffusion ($\lambda_{\text{in}} \gg a$), we again find uniform morphogen gradients at the interface resulting in the reduction of the instability and the growth of circular morphologies.

To quantify the statistical properties of the observed morphologies, we use the two-point density-density correlation function

$$C(r) = \langle \rho(\boldsymbol{r}_0)\rho(\boldsymbol{r}_0 + \boldsymbol{r}) \rangle_{|\boldsymbol{r}|=r}, \tag{2.15}$$

where $\langle \cdot \rangle$ denotes the average over all orientations and positions $\boldsymbol{r}_0$ [135, 163]. Intuitively, the correlation function $C(r)$ gives the probability to find two occupied lattice sites a distance r apart. To calculate the correlation function $C(r)$ of aggregates on a square lattice, we use the relation

$$C(r) = \lim_{\delta r \to 0} \frac{\mu(r, \delta r)}{V(r, \delta r)}, \tag{2.16}$$

where $\mu(r, \delta r)$ denotes the number of all pairs of occupied lattice sites within a shell of size $r - \delta r < r < r + \delta$ with $\delta r / r \ll 1$ and $V(r, \delta r)$ denotes the number of both occupied and unoccupied lattice sites in this shell [135].

We determined the correlation function $C(r)$ for the aggregate morphologies presented earlier (Fig. 2.3a,b) and found that the diffusion-degradation lengths λ_i overall control the qualitative behavior of $C(r)$. In particular, we distinguish two qualitatively different regimes of $C(r)$ depending on the relative size of the outside diffusion-degradation length λ_{out} to system size L and the relative size of inside diffusion-degradation length λ_{in} to lattice site size a (Fig. 2.3c,d). In the DLA-limit, we find that the behavior of the correlation function is well described by the power law

$$C(r) \propto r^{-\alpha} \tag{2.17}$$

with scaling exponent $\alpha = 0.27 \pm 0.03$. The scaling exponent was determined from a linear fit to the logarithmized correlation function obtained from $n = 16$ aggregates of size $M = 10000$ for the range $r < R_{\text{g}}$, where R_{g} denotes the radius of gyration. Thus, we found self-similar, fractal aggregates in this limit with a scaling exponent similar to the one found in DLA ($\alpha_{\text{DLA}} = 0.27$) [164]. Upon decreasing the diffusion-degradation length

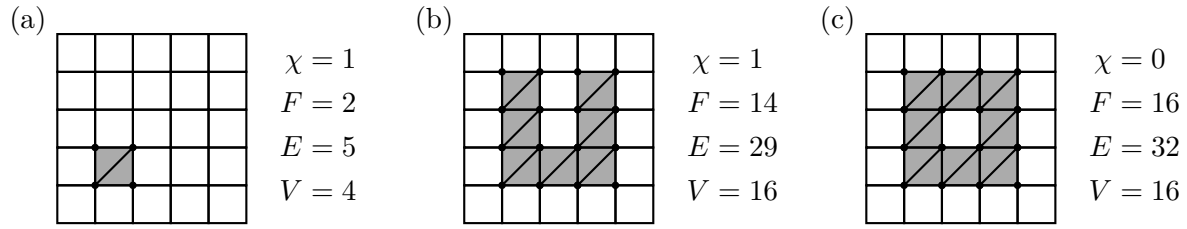

Figure 2.4: Calculation of the Euler characteristic χ on a square lattice. To determine the Euler characterisitic χ of an aggregate of non-zero occupation numbers, we first triangulate the aggregate by inserting a diagonal line for every lattice site with $n_r = 1$. Next, we determine the number of faces F (gray triangles), edges E (lines connecting vertices), and vertices V (circles on corner of triangles) of the triangulation and from this we calculate χ according to Eq. (2.18). The Euler characteristic provides information on the topology of the aggregate and in particular its topological changes. Since the aggregates in (a) and (b) have the same topology their Euler characteristic is the same. However, by placing an additional lattice site with $n_r = 1$ the topology of the aggregate changes and thus its Euler characteristic.

λ_{out}, we pass through an intermediate regime and finally find $C(r) = \text{const}$ ($\lambda_{\text{out}} \ll L$). In this regime, we found compact shapes and thus a homogeneous correlation function. Likewise, we find a transition from power law (DLA-limit) to homogeneous behavior of the correlation function for increasing values of the inside diffusion-degradation length λ_{in}. Note that for all of the regimes we find a sharp decrease in the correlation function for large values of r due to the finite size of the aggregates.

2.3 Topological control of stochastic interface growth

Given the importance of topology for the functioning of branched structures in biology, we naturally wondered how the topological properties of the generated aggregates can be controlled. Here, we present topology-preserving transition rates as a way to control aggregate topology. To define these transition rates, we use the Euler characteristic as a measure for aggregate morphology and allow only occupation number transitions that conserve the Euler characteristic. Here, we now first present how the Euler characteristic can be used to quantify aggregate morphology.

2.3.1 The Euler characteristic for a lattice

The classification of topological properties of objects is a well-studied problem in mathematics. Topological invariants, i.e. quantities that are invariant under smooth transfor-

mations of objects, have been established as an important concept for this classification [165–167]. For example, the Euler characteristic χ is an integer that provides a simple measure for the topology of an object and provides a classification of objects according to their topology. Conversely, topological changes of objects are the reflected by changes in χ. The Betti numbers b_i are another example of a topological invariant and provide a more fine-grained quantification of the topology of an object. While the zeroth Betti number b_0 is equal to the number of connected components C, the first Betti number provides the number of holes H in the object and in general the kth Betti number gives the number of k dimensional holes of an object. Given that Euler characteristic and Betti numbers both characterize the topology of an object it is hardly surprising that they are related. It can be shown that the Euler characteristic is the alternating sum of Betti numbers, which in the case of a 2D surface gives $\chi = C - H$ [168]. Overall, topological invariants such as the Euler characteristic or Betti numbers are a powerful tool to quantify the topology of objects. Due to its simplicity, we now focus on the Euler characteristic.

The Euler characteristic χ of a closed surface S is defined via a triangulation of S [166]. The triangulation consists of F faces, E edges, and V vertices and with this the Euler characteristic is defined as

$$\chi = F - E + V. \tag{2.18}$$

Note that the triangulation of S always exists given that the surface is closed. Moreover, it can be shown that Euler characteristic is independent of the chosen triangulation. Here, we consider only square lattices, which we triangulate by inserting a diagonal line into every lattice site.

To familiarize ourselves with the definition of the Euler characteristic and its calculation for regions of non-zero occupation numbers on a square lattice, we now determine the Euler characteristic for three different configurations of occupation numbers (Fig. 2.4). Clearly, configuration (a) and (b) share the same topology and thus their Euler characteristic is the same. By contrast, from (b) to (c) the topology and thus the Euler characteristic changes. Note that for the cases presented here the relation $\chi = C - H$ between Euler characteristic χ and the number of connected components C and holes H is useful. We can apply the relation to avoid counting the large amount of faces, edges, and vertices. Clearly, (a) and (b) have both $C = 1$ and $H = 0$ and thus $\chi = 1$. In (c), we still have $C = 1$, but now $H = 1$ and thus $\chi = 0$.

To evaluate the Euler characteristic for arbitrary configurations of occupation numbers $\{n_r\}$, we need a systematic method to determine the total number of faces F, edges E, and vertices V from a given set $\{n_r\}$. Here, we employ a strategy in which we first determine

the local number of faces F_r, the local number of edges E_r, and the local number of vertices V_r and from this obtain the total number of the respective quantity by summation over all lattice sites r:

$$F = \sum_r F_r \qquad E = \sum_r E_r \qquad V = \sum_r V_r \tag{2.19}$$

The calculation of the total number of faces from the local number of faces provides a simple example for this procedure. Since every square lattice site contains two triangular faces the local number of triangular faces is twice the occupation number n_r:

$$F_r = 2n_r \tag{2.20}$$

Clearly, the total number of faces is then given by the sum over the local number of faces. To calculate the total number of edges, we follow a similar strategy. However, in this case we need to distinguish different types of edges:

$$E_r = E_{1,r} + E_{2,r} + E_{3,r} \tag{2.21}$$

We first define the local number of edges $E_{1,r}$ that lie within a lattice site. Further, we define the local number of edges $E_{2,r}$ that lie at the border of a lattice site and are shared with an adjacent site and we also define the local number of edges $E_{3,r}$ that lie at the border of a lattice site, but are not shared with another site:

$$E_{1,r} = n_r \qquad E_{2,r} = \sum_i \frac{1}{2} n_r n_{e_i} \qquad E_{3,r} = \sum_i n_r (1 - n_{e_i}) \tag{2.22}$$

In every case, the local number of edges can be determined from the local configuration of occupation numbers (Fig. 2.5). Note that edges can occur in different orientations. To take into account every orientation, we perform a sum over all orientations i. In a similar way, we calculate the total number of vertices as the sum of local number of vertices:

$$V_r = V_{1,r} + V_{2,r} + V_{3,r} + V_{4,r} \tag{2.23}$$

We distinguish between the number of vertices $V_{n,r}$ that belong to n different lattice sites:

$$V_{1,r} = \sum_i n_r (1 - n_{e_i})(1 - n_{e_{i+1}}) \tag{2.24a}$$

$$V_{2,r} = \frac{1}{2}\sum_i n_r n_{e_i}(1-n_{e_{i+1}})(1-n_{d_i}) + n_r(1-n_{e_i})n_{e_{i+1}}(1-n_{d_i}) \tag{2.24b}$$

$$V_{3,r} = \frac{1}{3}\sum_i n_r(1-n_{e_i})n_{e_{i+1}}n_{d_i} + n_r n_{e_i}(1-n_{e_{i+1}})n_{d_i} + n_r n_{e_i} n_{e_{i+1}}(1-n_{d_i}) \tag{2.24c}$$

$$V_{4,r} = \frac{1}{4}\sum_i n_r n_{e_i} n_{e_{i+1}} n_{d_i} \tag{2.24d}$$

By adding up the total number of faces, edges, and vertices, we then find that the Euler characteristic is given by

$$\chi = \frac{1}{12}\sum_{r,i} n_r[3 - 2n_{e_i}n_{d_i} - 6n_{e_{i+1}} - 2n_{e_{i+1}}n_{d_i} + 4n_{e_i}n_{e_{i+1}} + 3n_{e_i}n_{e_{i+1}}n_{d_i}]. \tag{2.25}$$

Overall, this equation allows us to calculate the Euler characteristic for a arbitrary configurations of occupation numbers $\{n_r\}$. Interestingly, the Euler characteristic provides global information about the topology of a given configuration $\{n_r\}$, but can be calculated entirely from local information.

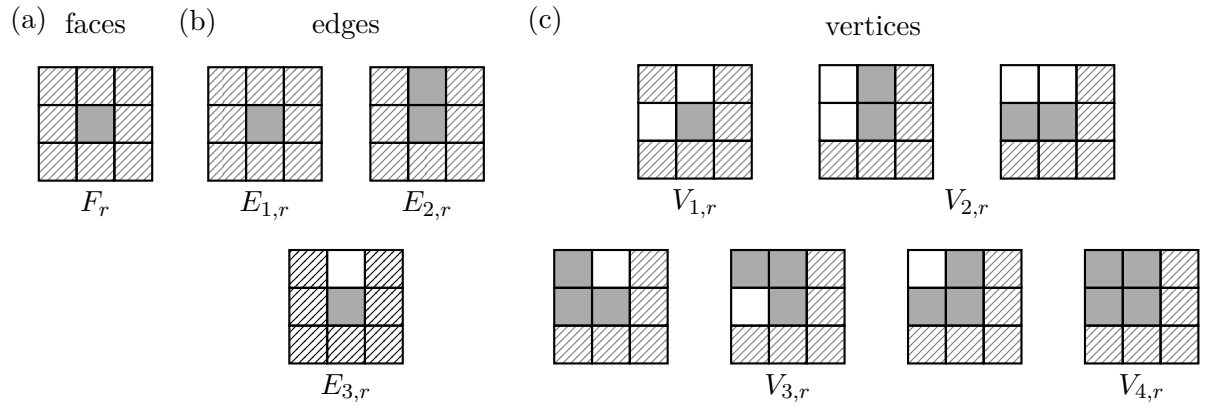

Figure 2.5: Definition of faces, edges, and vertices on a square lattice in terms of occupation numbers. The total number of faces F, edges E, and vertices V of an aggregate can be determined on the basis of local 3×3 neighborhoods. Lattice sites in this neighborhood can be occupied ($n_r = 1$, gray), free ($n_r = 0$, white), or the definition of an element is independent of the occupation number ($n_r \in \{0, 1\}$, lines). (a) Neighborhood corresponding to the definition of the local number of faces F_r. (b) We display the neighborhoods used to determine the number of edges $E_{1,r}$ belonging solely to one lattice site, the number edges $E_{2,r}$ shared between two occupied lattice sites, and the number of edges $E_{3,r}$ shared between occupied and free lattice site. (c) In a similar way, we display the configurations used to determine the number of vertices $V_{1,n}$ belonging to n occupied lattice sites. Note that in (b) and (c) also neighborhoods rotated by multiples of $\pi/2$ define the respective structure.

2.3.2 The Euler characteristic as a measure for topological changes

We next used our relation for χ to calculate the change of Euler characteristic $\Delta\chi$ given that a single occupation number at lattice site s is changed ($\Delta n_s = \pm 1$). To calculate the corresponding change in $\Delta\chi$ from Eq. (2.25), we need to determine the change of products of occupation numbers such as $\Delta(n_s n_t)$. We evaluate expressions of this form with the product rule like identity

$$\Delta(n_s n_t) = \Delta n_s n_t + n_s \Delta n_t \tag{2.26}$$

and analogously for expressions involving more than two occupation numbers. Note that higher order terms of the form $\Delta n_s \Delta n_t$ are lacking since we consider a process in which only one occupation number can be changed at a time.

We apply the product rule like identities to Eq. (2.25) and find after grouping terms according to their dependency on $\Delta n_r, \Delta n_{e_i}, \Delta n_{e_{i+1}}$, and Δn_{d_i} that $\Delta\chi$ is given by

$$\begin{aligned}\Delta\chi = \frac{1}{12}\sum_{r,i} \Delta n_r[\dots] + \Delta n_{e_i} \quad & (-2n_{d_i} + 4n_{e_{i+1}} + 3n_{e_{i+1}} n_{d_i}) n_r \\ & + \Delta n_{e_{i+1}} (-6 - 2n_{d_i} + 4n_{e_i} + 3n_{e_i} n_{d_i}) n_r \\ & + \Delta n_{d_i} \quad (-2n_{e_i} + 3n_{e_i} n_{e_{i+1}} - 2n_{e_{i+1}}) n_r,\end{aligned} \tag{2.27}$$

where "..." corresponds to the terms in square brackets in Eq. (2.25). This equation determines the total change in $\Delta\chi$ by summing the change in χ for every local, 3×3 neighborhood around lattice site r. The evaluation of the sum over r is straightforward since we have an occupation number change ($\Delta n_s = \pm 1$) only for lattice site s. After evaluating the sum in Eq. (2.27) we find

$$\Delta\chi = \Delta n_s \left[1 - \sum_i n_{e_i}(1 - n_{e_{i+1}} n_{d_i})\right] \tag{2.28}$$

for the change $\Delta\chi$ of the Euler characteristic. Thus, $\Delta\chi$ can be calculated from the occupation numbers in a local neighborhood around n_r.

To determine a simple criterion whether a change in occupation number leaves the topology invariant, we make use of Eq. (2.28). Given the change of a single lattice site ($\Delta n_s = \pm 1$), the topology remains invariant according to Eq. (2.28) if

$$\sum_i m_i = 1 \tag{2.29}$$

holds for a local neighborhood, where we have introduced $m_i = n_{e_i}(1 - n_{e_{i+1}} n_{d_i})$ as an

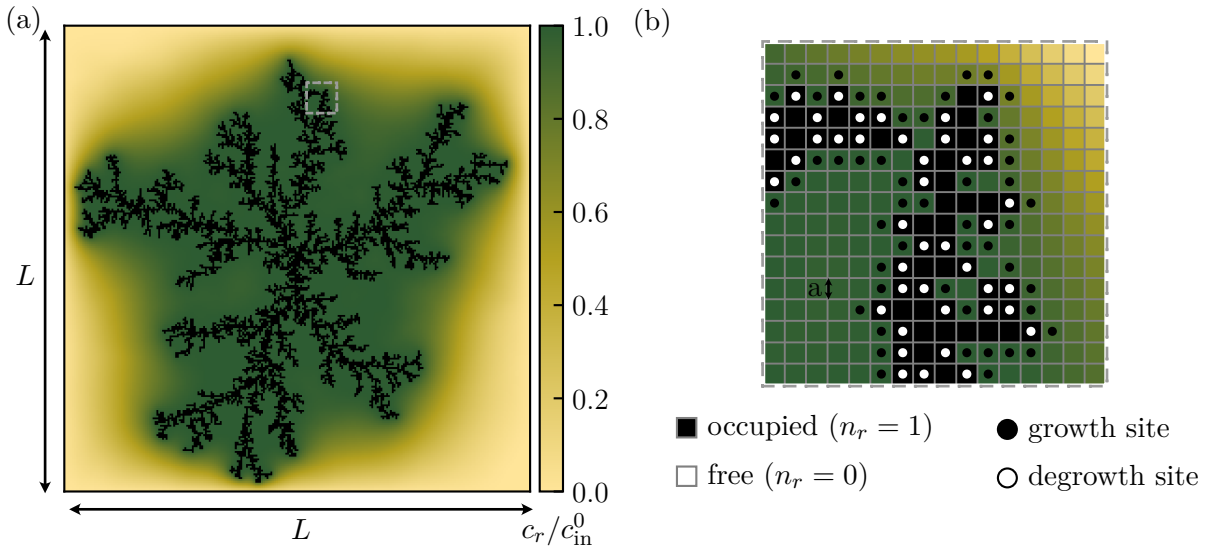

Figure 2.6: Lattice model for branching morphogenesis with topological constraints. (a) As before, we consider a $N \times N$ square lattice with lattice constant a and system size $L = Na$. We show an example aggregate of size $M = 7500$ formed with topological constraints according to Eq. (2.31) and Eq. (2.6) in the DLA-limit ($\lambda_{\mathrm{in}}/a = 0.01$, $\lambda_{\mathrm{out}}/L = 100$, $\Delta c = c_{\mathrm{in}}^0$). Due to the topological constraints imposed by the transition rates Eq. (2.31), loops are lacking in the aggregate. (b) Magnification of the dashed box in (a): We indicate potential growth sites (filled circles) and degrowth sites (empty circles). Note that topology-changing transitions are lacking.

abbreviation. Clearly, the sum of the four binary variables m_i is equal to one, given that exactly one of the m_i evaluates to one. To provide a simple, binary criterion if the local neighborhood fulfills Eq. (2.29), we use the logical xor function f

$$f(m_0, m_1, m_2, m_3) = m_0\bar{m}_1\bar{m}_2\bar{m}_3 + \bar{m}_0 m_1\bar{m}_2\bar{m}_3 + \bar{m}_0\bar{m}_1 m_2\bar{m}_3 + \bar{m}_0\bar{m}_1\bar{m}_2 m_3 \tag{2.30}$$

with four arguments, where the bar denotes the operation $\bar{m}_i = 1 - m_i$. The function in Eq. (2.30) evaluates to 1, provided that exactly one of its arguments is 1 (similar to the logical "xor" function with two arguments).

We can use criterion Eq. (2.30) to finally define the topology-preserving ($\Delta\chi = 0$) transition rates

$$k_+^E = k_+^0 \sum_e (1 - n_r) n_{r+e} f(m_0, m_1, m_2, m_3) \frac{c_{r+e} - c_r}{a} \tag{2.31a}$$

$$k_-^E = k_-^0 \sum_e n_r (1 - n_{r+e}) f(m_0, m_1, m_2, m_3) \frac{c_{r+e} - c_r}{a}. \tag{2.31b}$$

According to this relation, we find non-zero transition rates only for topology-preserving occupation number changes, which results in the growth of tree-like aggregates (Fig. 2.6).

2.3.3 Tree-like aggregates

We studied the influence of the diffusion-degradation lenghts λ_i on aggregate morphology and find behavior similar to the case without topology-preserving transition rates. As before, we find a transition from highly branched to circular morphologies for decreasing values of λ_{out} (Fig. 2.7a) and for increasing values of λ_{in} (Fig. 2.7b) along with the corresponding transition from power law scaling to homogeneous behavior in the correlation function (Fig. 2.7c,d).

While the statistical properties of aggregates grown with and without topological constraints are similar, differences become apparent when the growth of an aggregate is followed by its degrowth. To this end, we generated an aggregate in the DLA-limit without taking into account topological constraints. Next, we use the generated aggregate as an initial condition and study its degrowth with $k_-^0 = -k_+^0$. We find that as the size of the aggregate decreases, branches disconnect from the main part of the aggregate (Fig. 2.8a, highlighted by arrows). Next, we generated an aggregate in the DLA-limit with taking into account topological constraints and subsequently studied its degrowth. By contrast, no branches disconnect from the main part of the aggregate. Thus, the transition rates Eq. (2.31) allow us to study tree-like aggregates and its degrowth.

2.4 Summary and discussion

In this chapter, we have presented a minimal lattice model for morphogen-controlled branching morphogenesis. In this model, we combine the idea of morphogen-controlled growth of tissues and organs with concepts from DLA. In DLA, highly branched morphologies originate from an instability in the underlying interface growth process. Here, we demonstrate how a similar instability leads to the formation of highly branched morphologies in morphogen-controlled interface growth. We study the geometrical properties of the resulting structures and additionally demonstrate how the topology of structures can be controlled.

At the center of our study lies a stochastic lattice model. We consider a square lattice with system size L, where lattice sites of size a are equipped with a binary occupation number n_r that indicates the presence or absence of a cell belonging to a hypothetical organ. Occupation number transitions take place stochastically with a rate determined

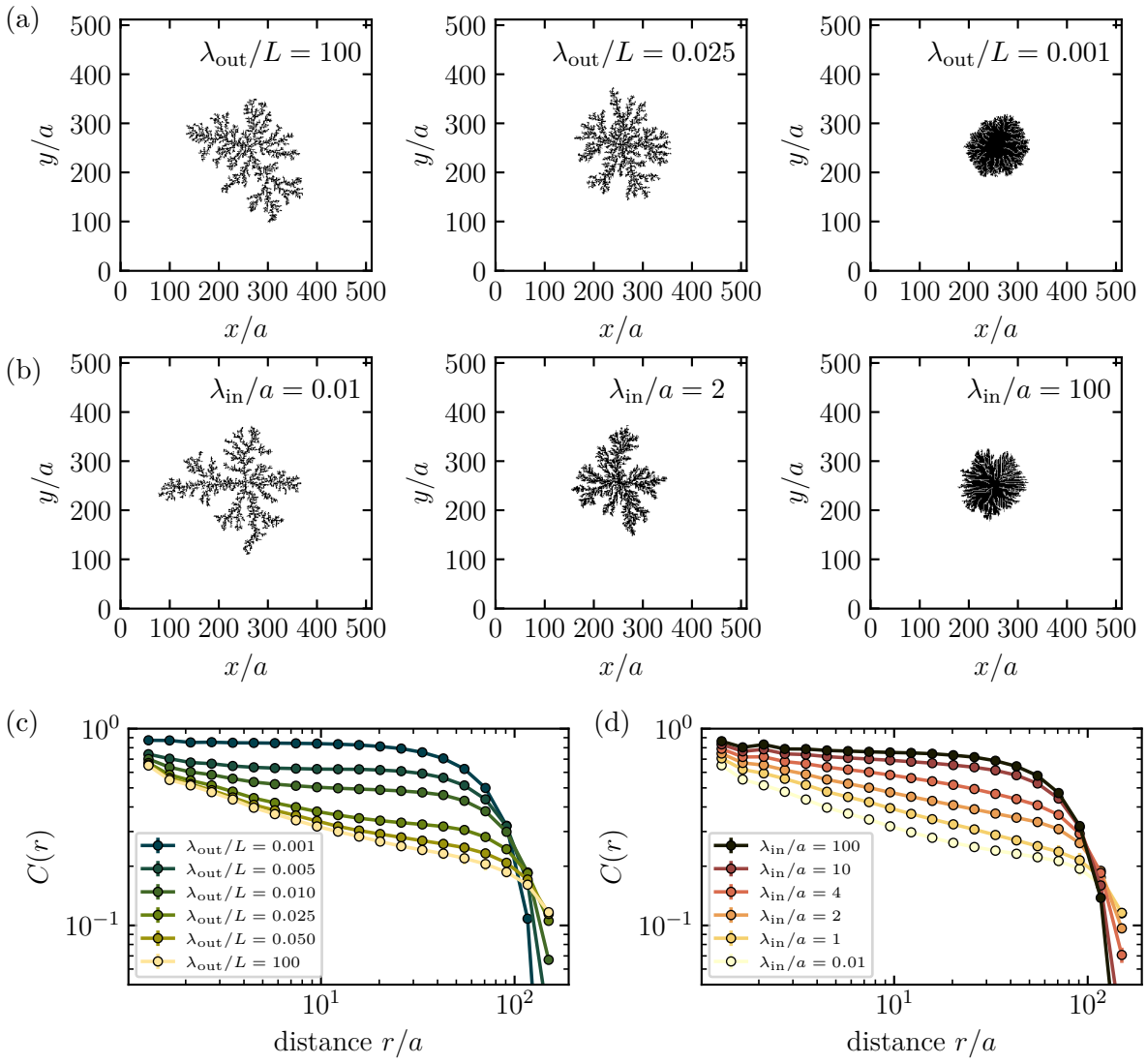

Figure 2.7: Tree-like aggregate morphologies and quantification of their statistical properties. (a) We show aggregates of size $M = 10000$ with $\lambda_{\text{in}}/a = 0.01$ for different values of λ_{out}. (b) We show aggregates of size $M = 10000$ with $\lambda_{\text{out}}/L = 100$ for different values of λ_{in}. (c,d) Quantification of statistical properties of aggregates with the two-point density-density correlation function $C(r)$ defined by Eq. (2.15). Error bars denote the standard deviation obtained from averaging the correlation function for $n = 16$ different aggregates, but are typically smaller than the marker size.

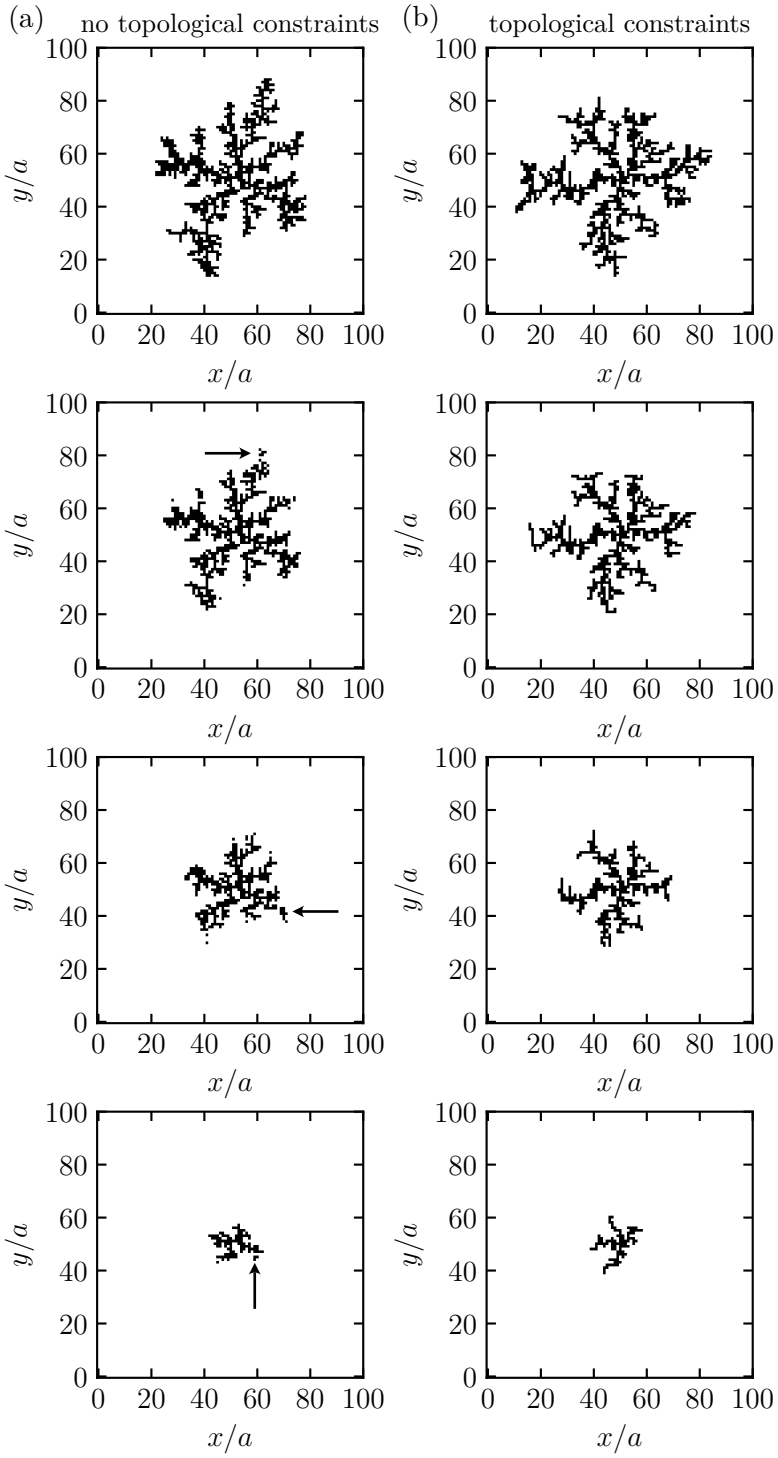

Figure 2.8: Growth and degrowth of (tree-like) aggregates in the DLA-limit. (a) We consider an aggregate formed without topology-preserving transition rates in the DLA-limit. We use this aggregate as an initial condition to our model and subsequently study its the degrowth also without topology-preserving transition rates. We indicate disconnected branches (black arrows). (b) We consider an aggregate formed with topology-preserving transition rates in the DLA-limit. We use this as an initial condition to our model and study its degrowth with topology-preserving transition rates. M denotes aggregate size. In (a,b), we show the aggregate sizes $M = 1000, 700, 400, 100$ (from top to bottom).

by a morphogen gradient and represent organ growth. We denote the morphogen concentration at each lattice site by c_r and assume a minimal reaction-diffusion process for the morphogen dynamics. Morphogen shows (effectively) free diffusion and undergoes region-dependent degradation and production. We consider the case of strong morphogen production in the "in" region and, as a result, find a morphogen gradient from the inside to the outside region of the system. Gradients have diffusion-degradation lengths λ_{in} and λ_{out}.

To understand the relation between DLA and our lattice model, we compared the respective continuum limits. In both models, we find that the growth of aggregates is controlled by the gradient of a field that obeys the diffusion equation, but the precise dynamics of the diffusive field and its boundary conditions differ. Our lattice model recovers DLA dynamics in the limit of decoupled lattice sites ($\lambda_{\text{in}}/a \ll 1$ while $c^0_{\text{in}} = \text{const}$) and vanishing degradation rate outside ($\lambda_{\text{out}}/L \gg 1$).

We next studied the interface dynamics numerically. Most importantly, we find that in the DLA-limit an instability occurs that leads to the formation of highly branched morphologies. The growth of an interface protrusion results in an increase in morphogen gradient and thus an increase in interface growth. A positive feedback sets in that leads to unstable interface growth. This mechanism is shared with DLA and thus is at the center of the formation of branched morphologies in both models. Next, we studied the influence of the diffusion-degradation lengths on morphologies. To this end, we started with the DLA limit and gradually increased the diffusion-degradation length λ_{out} and find a transition from highly branched ($\lambda_{\text{out}}/L \gg 1$) to almost circular morphologies ($\lambda_{\text{out}}/L \ll 1$). Similarly, we gradually increased the diffusion-degradation length λ_{in} and observed a similar transition from highly branched ($\lambda_{\text{in}}/a \ll 1$) to almost circular morphologies ($\lambda_{\text{in}}/a \gg 1$). In each case, the change in morphology is accompanied by a corresponding change in correlation function. We observe a transition from a self-similar power law correlation function (DLA-limit) to homogeneous correlation function. In the DLA-limit, the growth of branched morphologies is governed by the instability. Upon leaving the DLA limit ($\lambda_{\text{out}}/L \ll 1$ or $\lambda_{\text{in}}/a \gg 1$), we find uniform gradients along the interface, leading to uniform growth rates and the formation of circular morphologies.

A key novelty of our approach lies in the control of the topological properties of formed structures. We use the Euler characteristic as an example of a topological invariant to introduce topological constraints into interface growth and thus derive topology-preserving transition rates. As a result, we can demonstrate the growth of tree-like (loopless) branched morphologies with similar statistical properties to the conventional structures.

Our work complements previous studies on the formation of branched morphologies in

DLA. DLA and variations of it were employed to study patterns arising in electrodeposition [141] or fractal viscous fingering [169, 170]. In particular, Niemeyer et al. used a similar approach to generate branched structures observed in dielectric breakdown [142]. They generated highly branched morphologies by obtaining the electric potential from a solution of the Laplace equation and updating lattice sites based on the gradient of the electric potential. Here, we generalize this approach by introducing the additional length scales λ_{in} and λ_{out} in the problem. Additionally, we introduce topological constraints into the transition rates and demonstrate the formation of tree-like aggregates. We "rethink" DLA and show how it can be used to develop a model for the growth of branched morphologies in a biological context. We envision that the model presented here serves as a starting point for a quantitative study of e.g. retina vessels [171–173] or neuronal branching [174–176]. Our work also opens up various directions for more theoretical research. For example, the growth and degrowth of aggregates naturally raises questions regarding the irreversibility of this growth process. Additionally, we wonder if we can obtain fluctuating, steady-state structures by alternating growth and degrowth steps. Finally, it might be useful to develop the Euler characteristic also for other connectivities (considering diagonal neighbors on a square lattice also as connection) and for other lattice geometries (triangular, hexagonal).

A drawback of the approach presented here (and also DLA) lies in the difficulty to leave the strong-noise, low surface tension limit in a controlled way. For example, in studies on DLA an effective surface tension was introduce by including a curvature-dependent growth probability [155, 156] or by including curvature-dependent attachment and reattachment rules [157, 158]. However, these approaches suffer from the difficulty to define curvature on a lattice. Noise-reduction techniques were introduced in which particles must land several times on a perimeter site of the aggregate before it attaches. However, how exactly to perform the noise-reduction is ambiguous and different techniques lead to vastly different overall structures [154, 177]. In the next chapter, we present a model for morphogen-controlled branching morphogenesis that allows us to study the low noise and finite surface tension limit.

Chapter 3

Morphogen-controlled branching morphogenesis and growth

In this chapter, we study morphogen-controlled growth of an interface as a model for branching morphogenesis. We show how complex, branched morphologies can arise in a self-organized way from an instability in interface motion. Moreover, we explain the control of the geometrical and topological properties of the resulting branched morphologies from the interplay between interface growth and morphogen dynamics.

We first present our continuum model for branching morphogenesis and growth. We perform a linear stability of a flat moving interface and show how an instability can take place in this scenario. Next, we study interface growth beyond the linear regime. We present the phase field method as a numerical tool to study interface motion and explore various interface morphologies and their characteristics. We identify branch distance and thickness as key parameters of branched morphologies and discuss simple, analytically tractable scenarios of interface motion to understand branch distance and thickness regulation.

3.1 Continuum model for morphogen-controlled interface growth

We first present our continuum model for morphogen-controlled branching morphogenesis (Fig. 3.1a). In this model, we study the growth of a hypothetical organ guided by the concentration of a morphogen. For simplicity, we consider a 2D setting and divide the system into a region inside ("in") and outside ("out") the tissue. The interface between both regions is mathematically described by the curve $\boldsymbol{R}$.

We assume that the motion of the interface $\boldsymbol{R}$ takes place in normal direction with

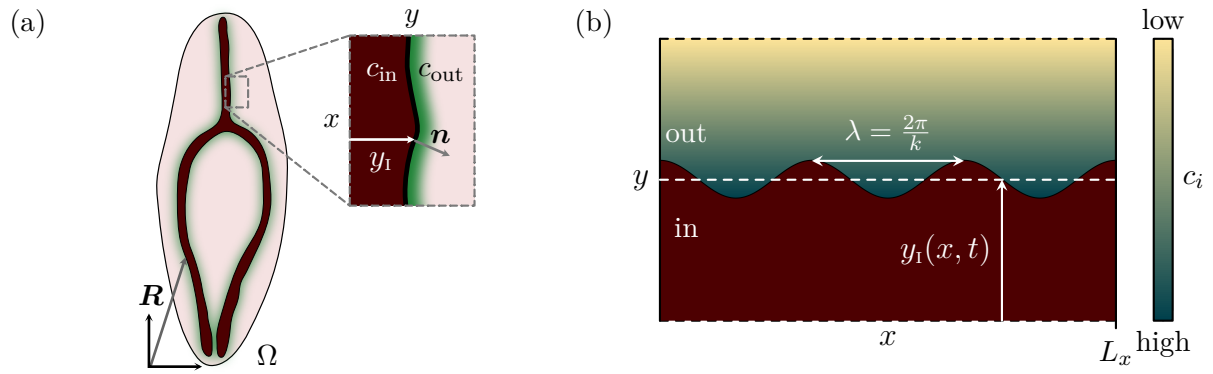

Figure 3.1: Morphogen-controlled branching morphogenesis. (a) In our model, we study the growth of an organ (brown) under the influence of a morphogen (green). As an example, we here show the planarian gut. We denote the system by Ω. We represent the organ outline by an interface vector $\boldsymbol{R}$ with interface normal $\boldsymbol{n}$. We denote the morphogen concentration inside and outside the organ by c_{in} and c_{out}, respectively. (b) We study the motion of an interface in an infinitely long rectangular system of width L_x as a minimal scenario to understand the pattern formation in our model. In the linear stability analysis, we study the growth of perturbations with wavelength λ and corresponding wavevector k.

normal velocity v_n according to

$$\partial_t \boldsymbol{R} = v_n \boldsymbol{n} \tag{3.1a}$$

$$v_n = \chi(c) - \beta\kappa, \tag{3.1b}$$

where $\boldsymbol{n}$ denotes the interface normal vector and κ the interface curvature which is positive for an outward protrusion and negative for an inward protrusion. The normal velocity of the interface motion lies at the heart of our model and is key to the pattern formation in this system. We assume that interface motion is in general morphogen-controlled as expressed by the term $\chi(c)$ and additionally depends on interface curvature. Due to the dependency of interface growth on curvature, outwards protrusions experience a negative velocity, and inwards protrusion a positive velocity. As a result, the interface has a tendency to reach a flattened configuration and is effectively stabilized. We denote the strength of coupling between interface and its curvature by β. For the dependency χ of interface motion on morphogen concentration, we make the choice

$$\chi(c) = v_0 - \gamma c, \tag{3.2}$$

which expresses the tendency of the interface to grow with velocity v_0 and the inhibition of interface growth by the presence of morphogen at the interface with inhibition strength

γ.

We assume that a minimal reaction-diffusion system governs the dynamics of the morphogen concentration c_i

$$\partial_t c_i = D\nabla^2 c_i - k_i c_i + s_i, \tag{3.3}$$

where the index $i \in \{\text{in}, \text{out}\}$ labels whether the morphogen concentration belongs to the inside or outside region of the organ. According to Eq. (3.3), morphogen diffuses with effective diffusion constant D and undergoes degradation and production with rate k_i and s_i, respectively. This dynamics describes the formation of morphogen gradients with a preferred concentration value $c_i^0 = s_i/k_i$ and degradation length $\lambda_i = \sqrt{D/k_i}$ in the inside and outside region, respectively. In particular, our model describes situations with a concentration difference $\Delta c = c_{\text{in}} - c_{\text{out}}$ between the preferred concentration values c_i^0 and allows us to study scenarios where morphogen production in the inside ($\Delta c > 0$) or outside ($\Delta c < 0$) region dominates. Here, we focus on the case where morphogen is predominantly produced in the organ ($\Delta c > 0$) and inhibits organ growth. Finally, we use the two boundary conditions at the interface $\boldsymbol{R}$

$$c_{\text{in}}(\boldsymbol{R}) = c_{\text{out}}(\boldsymbol{R}) \tag{3.4a}$$

$$\boldsymbol{n} \cdot \boldsymbol{\nabla} c_{\text{in}}(\boldsymbol{R}) = \boldsymbol{n} \cdot \boldsymbol{\nabla} c_{\text{out}}(\boldsymbol{R}). \tag{3.4b}$$

The conditions at the system boundary depend on the type of problem that is studied and we leave them for now unspecified. Overall, we think that this model captures key effects responsible for morphogen-controlled branching morphogenesis.

To understand pattern formation in this system, we study the motion of a flat interface in an infinitely long rectangular system Ω with $x \in [0, L_x]$ and $y \in [-\infty, \infty]$ (Fig. 3.1b). This scenario will allow us to study when an instability in interface motion is initiated and what time and length scales govern this instability. For the motion of an interface in a rectangular system the interface vector $\boldsymbol{R}$ can be written as

$$\boldsymbol{R}(x,t) = x\boldsymbol{e}_x + y_{\text{I}}(x,t)\boldsymbol{e}_y, \tag{3.5}$$

with the corresponding interface normal vector (oriented out of the interface)

$$\boldsymbol{n} = \frac{-\partial_x y_{\text{I}} \boldsymbol{e}_x + \boldsymbol{e}_y}{\sqrt{1 + (\partial_x y_{\text{I}})^2}}. \tag{3.6}$$

In both cases, y_{I} denotes the y coordinate of the interface position and from the time

derivative of Eq. (3.5) we can deduce $\partial_t y_\mathrm{I} = \partial_t \boldsymbol{R} \cdot \boldsymbol{e}_y$ for the dynamics of the interface position. By employing our definition of the interface dynamics in Eq. (3.1), we find

$$\partial_t y_\mathrm{I} = v_n \frac{1}{\sqrt{1 + (\partial_x y_\mathrm{I})^2}}. \tag{3.7}$$

In addition to the boundary conditions at the interface given by Eq. (3.4), we require that concentration gradients at infinity vanish as expressed by

$$\lim_{y \to \pm\infty} \partial_y c_i(x, y) = 0. \tag{3.8}$$

Additionally, we use periodic boundary conditions at the left and right side of our system.

3.2 Morphological instability of a moving front in an infinitely long system

3.2.1 Stationary state

Transformation to moving frame

The stationary state of the system defined by equation Eq. (3.1) and Eq. (3.3) is a planar interface moving with constant velocity v in y-direction accompanied by a stationary concentration profile $\bar{c}_i(y)$. To determine the interface velocity and the corresponding concentration profile, we transform the system from a resting reference frame to a reference frame co-moving with the interface. Mathematically, this transformation is expressed by

$$\begin{aligned} (x, y, t) &\to (\tilde{x}, \tilde{y}, \tilde{t}) \\ \tilde{x} &= x \\ \tilde{y} &= y - vt \\ \tilde{t} &= t. \end{aligned} \tag{3.9}$$

The transformed morphogen concentration $\tilde{c}$ obeys $\tilde{c}(\tilde{x}, \tilde{y}, \tilde{t}) = c(x, y, t)$ and the transformed interface position $\tilde{y}_\mathrm{I}$ obeys $\tilde{y}_\mathrm{I}(\tilde{x}, \tilde{t}) = y_\mathrm{I}(x, t) - vt$. We can evaluate their temporal and spatial derivatives in the moving frame and find

$$\begin{aligned} \frac{\partial y_\mathrm{I}}{\partial t} &= \frac{\partial \tilde{y}_\mathrm{I}}{\partial t} + v & \qquad \frac{\partial c}{\partial x} &= \frac{\partial \tilde{c}}{\partial \tilde{x}} \\ \frac{\partial c}{\partial t} &= \frac{\partial \tilde{c}}{\partial \tilde{t}} - v\frac{\partial \tilde{c}}{\partial \tilde{y}} & \qquad \frac{\partial c}{\partial y} &= \frac{\partial \tilde{c}}{\partial \tilde{y}}. \end{aligned} \tag{3.10}$$

Therefore, the dynamics in the moving reference frame reads

$$\partial_t y_\mathrm{I} = v_n \frac{1}{\sqrt{1+(\partial_x y_\mathrm{I})^2}} - v \tag{3.11a}$$

$$\partial_t c_i - v\partial_y c_i = D\nabla^2 c_i - k_i c_i + s_i. \tag{3.11b}$$

Note that we have omitted the $\sim$ symbol for quantities in the co-moving reference frame for notational simplicity which we will continue in the rest of this chapter. As a consequence of the transformation to a co-moving frame, we obtain an additional advection term, which describes the relative motion between a stationary system and the moving interface. The transformed boundary conditions at the interface in the co-moving frame are

$$c_\mathrm{in}(x,0) = c_\mathrm{out}(x,0) \tag{3.12a}$$

$$\boldsymbol{n}\cdot\boldsymbol{\nabla} c_\mathrm{in}(x,0) = \boldsymbol{n}\cdot\boldsymbol{\nabla} c_\mathrm{out}(x,0), \tag{3.12b}$$

together with periodic boundary conditions at $x = 0, L_x$ and no-flux boundaries at $y \to \pm\infty$. Having defined the system dynamics in the co-moving frame, we can now determine the stationary state of the system.

Morphogen concentration

We first derive the stationary morphogen profile in the co-moving frame. The stationary morphogen profile $\bar{c}_i$ is defined by the stationary diffusion equation

$$0 = \nabla^2 \bar{c}_i + \frac{1}{\ell}\partial_y \bar{c}_i - \frac{1}{\lambda_i^2}\bar{c}_i + \frac{1}{\lambda_i^2} c_i^0, \tag{3.13}$$

where we have introduced the diffusion length ℓ and the degradation lengths λ_i

$$\ell = \frac{D}{v} \qquad\qquad \lambda_i^2 = \frac{D}{k_i} \tag{3.14}$$

along with the offset concentration $c_i^0 = s_i/k_i$. While the diffusion-length ℓ provides a measure for the length of concentration gradients in systems without degradation ($k_i = 0$), the diffusion-degradation lengths λ_i provide a measure for the length of concentration gradients in resting systems ($v = 0$). The offset concentrations c_i^0 provide a characteristic morphogen concentration that originates from the interplay of morphogen production and degradation.

To solve the stationary diffusion equation, we make the ansatz

$$\bar{c}_{\text{in}}(y) = \bar{A}e^{q_{\text{in}}y} + c^0_{\text{in}} \qquad \bar{c}_{\text{out}}(y) = \bar{B}e^{-q_{\text{out}}y} + c^0_{\text{out}}, \tag{3.15}$$

where $\bar{A}$ and $\bar{B}$ are constants that we determine from the boundary conditions Eq. (3.12) at the interface and q_i are the positive solutions of

$$0 = q_i^2 \pm \frac{1}{\ell} q_i - \frac{1}{\lambda_i^2}. \tag{3.16}$$

Note that we have chosen the ansatz such that $\bar{c}_{\text{in}}$ remains finite for $y \to -\infty$ and that $\bar{c}_{\text{out}}$ remains finite for $y \to +\infty$. Finally, the solutions c_i are

$$\bar{c}_{\text{in}}(y) = \bar{A}\exp\left[+\frac{y}{\ell_{\text{in}}}\right] + c^0_{\text{in}} \qquad \bar{c}_{\text{out}}(y) = \bar{B}\exp\left[-\frac{y}{\ell_{\text{out}}}\right] + c^0_{\text{out}} \tag{3.17}$$

with the constants

$$\bar{A} = -\Delta c \frac{\frac{\ell_{\text{in}}}{\ell_{\text{out}}}}{1 + \frac{\ell_{\text{in}}}{\ell_{\text{out}}}} \qquad \bar{B} = +\Delta c \frac{1}{1 + \frac{\ell_{\text{in}}}{\ell_{\text{out}}}}, \tag{3.18}$$

the difference between inside and outside offset concentration $\Delta c = c^0_{\text{in}} - c^0_{\text{out}}$ and the diffusion-degradation length ℓ_i defined by

$$\frac{1}{\ell_i} = \pm\frac{1}{2\ell} + \sqrt{\frac{1}{4\ell^2} + \frac{1}{\lambda_i^2}}. \tag{3.19}$$

Here, the positive sign corresponds to the "in" solution and the negative sign to the "out" solution. The diffusion-degradation length ℓ_i is composed of the diffusion length ℓ and degradation length λ_i and provides a measure for the length scale of concentration gradients in moving systems with non-zero degradation ($v \neq 0$, $k_i \neq 0$).

Let us now discuss the stationary morphogen profiles (Fig. 3.2a). The concentration profile in the in- and outside region is given by an exponential function with the diffusion-degradation length ℓ_i as a characteristic length scale. For $y \ll \ell_{\text{in}}$, the concentration c_{in} approaches c^0_{in}, while for $y \gg \ell_{\text{out}}$, the concentration c_{out} approaches c^0_{out}. The diffusion-degradation length scale ℓ_i is determined by the ratio $\text{Pe}_i = \lambda_i/\ell$, which constitutes a Péclet number. This is a non-dimensional number that characterizes the importance of diffusion and degradation for the formation of concentration gradients. In the regime of small Péclet number, the morphogen degradation dominates the system dynamics. In this regime, only the diffusion-degradation length scale plays a role and ℓ_i reduces to $\ell_i = \lambda_i$.

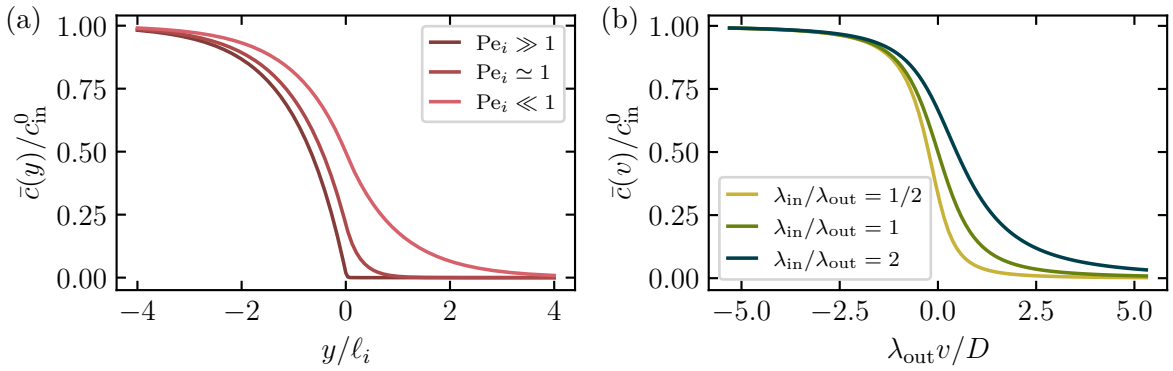

Figure 3.2: Stationary concentration profiles along a moving interface. (a) We show stationary concentration profiles $\bar{c}$ given by Eq. (3.17) as a function of position y for different values of the Péclet number $\mathrm{Pe}_i = \lambda_i/\ell$ (red). We normalize concentrations by the offset concentration c^0_{in} in the "in" region and rescale lengths by the diffusion-degradation length ℓ_i. (b) We show the stationary concentration $\bar{c}(v)$ at the interface position $y = 0$ given by Eq. (3.20) as a function of interface velocity v for different values of the inside degradation length λ_{in} (green).

By contrast, the dynamics is dominated by the interface motion in the regime of large Péclet number. Here, we find $\ell_{\mathrm{in}} = \ell$ and $\ell_{\mathrm{out}} \to \infty$. Due to the infinite length of the system, any position ahead of the interface ($y > 0$) has been exposed infinitely long to the production and degradation of morphogen and therefore has reached the value c_{out} without any spatial gradient. By contrast, positions behind the interface $y < 0$ have only been exposed for a finite amount of time to production and degradation of morphogen and therefore have not yet reached the offset concentration c_{in}.

From the general stationary concentration profile $\bar{c}$, we can now easily derive the concentration at the interface position $\bar{c}_{\mathrm{I}}$. An understanding of the concentration at the interface position is crucial as it determines the velocity of the stationary interface velocity. To obtain $\bar{c}_{\mathrm{I}}$, we set $y = 0$ in Eq. (3.17) and find:

$$\bar{c}_{\mathrm{I}}(v) = \Delta c \frac{1}{1 + \frac{\ell_{\mathrm{in}}}{\ell_{\mathrm{out}}}} + c^0_{\mathrm{out}} \tag{3.20}$$

As the stationary concentration profile in general, also the concentration value at the interface position is determined by the interplay of interface velocity and degradation length (Fig. 3.2b). For small velocities ($\mathrm{Pe}_i \ll 1$), the diffusion-degradation lengths ℓ_i reduce to the degradation lengths λ_i and thus $\bar{c}_{\mathrm{I}}$ is determined only by the degradation lengths for $v = 0$. By contrast, for large velocities ($\mathrm{Pe}_i \gg 1$), we find $\bar{c}_{\mathrm{I}} = c^0_{\mathrm{out}}$.

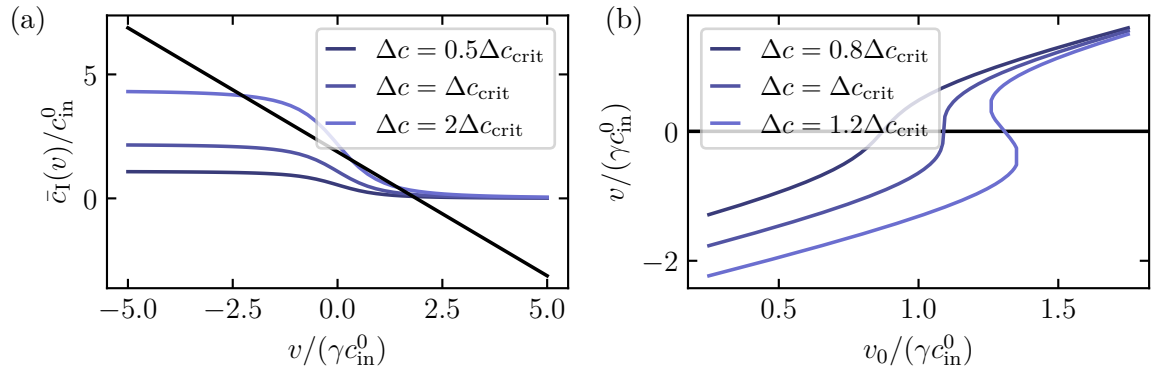

Figure 3.3: Stationary interface velocity. (a) We illustrate how the stationary velocity v of the interface is determined. We show the left hand side of Eq. (3.21), which is the morphogen concentration $\bar{c}_{\mathrm{I}}$ at the interface position as a function of interface velocity for different values of concentration difference Δc (blue). We additionally show the right hand side of the same equation which is a linear function with intercept v_0/γ and slope $-1/\gamma$ (black). (b) We show the stationary interface value v obtained from solutions of Eq. (3.21) for different values of concentration difference Δc.

Interface velocity

To obtain the stationary interface velocity v, we require $\partial_t y_{\mathrm{I}} = 0$ and find

$$\bar{c}_{\mathrm{I}}(v) = \frac{v_0}{\gamma} - \frac{1}{\gamma} v. \tag{3.21}$$

This equation constitutes an implicit relation for the interface velocity v. First, we graphically determine the number of solutions of this equation (Fig. 3.3a). Thus, we are seeking intersections of the concentration at the interface $\bar{c}_{\mathrm{I}}(v)$ with a linear function with offset v_0/γ and derivative $-1/\gamma$. If $\bar{c}'_{\mathrm{I}}(v=0)$ exceeds the slope of the linear function, we find exactly one solution, while we find up to three solutions (depending on the value of v_0) for the opposite case:

$$\bar{c}'_{\mathrm{I}}(v=0) < -\frac{1}{\gamma} : \text{up to three solutions} \tag{3.22a}$$

$$\bar{c}'_{\mathrm{I}}(v=0) \geq -\frac{1}{\gamma} : \text{exactly one solution} \tag{3.22b}$$

From the condition $c'_{\mathrm{I}}(v=0) = -1/\gamma$, we derive the value Δc_{crit} at which the transition from the regime of exactly one to up to three solutions occurs:

$$\Delta c_{\mathrm{crit}} = \frac{2D}{\gamma}\left(\frac{1}{\lambda_{\mathrm{in}}} + \frac{1}{\lambda_{\mathrm{out}}}\right) \tag{3.23}$$

Finally, we determine the solution of Eq. (3.21) numerically (Fig. 3.3b). For our purposes, we consider a parameter regime in this thesis with only one solution for the stationary interface velocity.

3.2.2 Stability analysis

Linearization at the stationary solution

We linearize the dynamical equations of the system given by Eq. (3.11) around the stationary interface position $\bar{y}_\mathrm{I} = 0$ and the stationary concentration profile $\bar{c}_i(y)$ by

$$y_\mathrm{I}(x,t) = \delta y_\mathrm{I}(x,t) \tag{3.24a}$$

$$c_i(x,y) = \bar{c}_i(y) + \delta c_i(x,y,t), \tag{3.24b}$$

where δy_I and δc_i denote small perturbations around the stationary interface position and concentration profile, respectively. The linearized interface and concentration dynamics then reads

$$\partial_t \delta y_\mathrm{I} = -\gamma[\partial_y \bar{c}(0)\delta y_\mathrm{I} + \delta c(0)] + \beta\partial_x^2 \delta y_\mathrm{I} \tag{3.25a}$$

$$\partial_t \delta c_i = D\nabla^2 \delta c_i + v\partial_y \delta c_i - k_i \delta c_i. \tag{3.25b}$$

Along with the dynamical equations of the system, we also linearize the boundary conditions given by Eq. (3.12) and find:

$$\delta c_\mathrm{in}(x,0) = \delta c_\mathrm{out}(x,0) \tag{3.26a}$$

$$\partial_y^2 \bar{c}_\mathrm{in}(x,0)\delta y_\mathrm{I} + \partial_y \delta c_\mathrm{in}(x,0) = \partial_y^2 \bar{c}_\mathrm{out}(x,0)\delta y_\mathrm{I} + \partial_y \delta c_\mathrm{out}(x,0) \tag{3.26b}$$

The linearized dynamical equations Eq. (3.25) together with the linearized boundary conditions Eq. (3.26) constitute a set of coupled linear differential equations that we now solve.

Determination of growth rates

Due to the translation invariance of the system in x-direction we make the ansatz

$$\delta y_\mathrm{I}(x) = \xi_k e^{ikx+\mu_k t} \tag{3.27a}$$

$$\delta c_i(x,y) = \delta c_{i,k}(y) e^{ikx+\mu_k t} \tag{3.27b}$$

for the interface perturbation δy_{I} and the concentration perturbation δc_i, where we have introduced the amplitudes ξ_k and $\delta c_{i,k}(y)$. We additionally introduced the wavevector k and the growth rate μ_k of a perturbation. According to our definition, an interface perturbation is amplified and thus the interface dynamics is unstable for $\mu_k > 0$, and we find stable interface dynamics for $\mu_k < 0$.

To determine the functional form of the amplitude $\delta c_{i,k}(y)$, we insert the ansatz for the concentration perturbation Eq. (3.27b) into the linearized concentration dynamics Eq. (3.25b). We find that the amplitudes obey

$$\delta c_{\mathrm{in},k} = c_k^{\mathrm{in}} e^{q_{\mathrm{in}} y} \tag{3.28a}$$

$$\delta c_{\mathrm{out},k} = c_k^{\mathrm{out}} e^{-q_{\mathrm{out}} y}, \tag{3.28b}$$

where q_{in} and q_{out} are the positive solutions of

$$0 = (\lambda_{\mathrm{in}} q)^2 - \frac{v}{D}\lambda_{\mathrm{in}}^2 q - \left((\lambda_{\mathrm{in}} k)^2 + 1 + \frac{\mu}{k_{\mathrm{in}}}\right) \tag{3.29a}$$

$$0 = (\lambda_{\mathrm{out}} q)^2 + \frac{v}{D}\lambda_{\mathrm{out}}^2 q - \left((\lambda_{\mathrm{out}} k)^2 + 1 + \frac{\mu}{k_{\mathrm{out}}}\right). \tag{3.29b}$$

Our sign convention in the argument of the exponential functions in Eq. (3.28) ensures that the solutions remain finite for $y \to \pm\infty$ in the respective region. To determine the prefactors c_k^{in} and c_k^{out}, we insert our ansatz for the concentration perturbation Eq. (3.27b) together with the concentration amplitude Eq. (3.28) into the linearized boundary conditions and find

$$c_k^{\mathrm{in}} = c_k^{\mathrm{out}} \tag{3.30a}$$

$$\xi_k[\partial_y^2 \bar{c}_{\mathrm{in}} - \partial_y^2 \bar{c}_{\mathrm{out}}] = -q_{\mathrm{out}} c_k^{\mathrm{out}} - q_{\mathrm{in}} c_k^{\mathrm{in}}. \tag{3.30b}$$

From this equation, we can determine c_k^i and thus we have fully specified the concentration perturbation $\delta c(x, y)$.

Finally, we determine the growth rates μ_k by inserting the ansatz for the interface perturbation Eq. (3.27a) into the linearized interface dynamics given by Eq. (3.25a) and find

$$\xi_k \mu_k = -\gamma[\partial_y \bar{c} \xi_k + \delta c(x, 0)] - \beta k^2 \xi_k. \tag{3.31}$$

We replace the interface amplitude ξ_k by Eq. (3.30) and use our previous results for the stationary concentration profile given by Eq. (3.17) and the perturbation of the mor-

phogen concentration given by Eq. (3.27b) to find that the growth rate of an interfacial perturbation is given by

$$\mu_k = \gamma\Delta c \frac{1}{\ell_{\text{out}} + \ell_{\text{in}}} \left[1 - \frac{\sqrt{1 + 4\left(\frac{\ell}{\lambda_{\text{out}}}\right)^2} + \sqrt{1 + 4\left(\frac{\ell}{\lambda_{\text{in}}}\right)^2}}{\sqrt{1 + 4\ell^2\left(\frac{\mu_k + k_{\text{out}}}{D} + k^2\right)} + \sqrt{1 + 4\ell^2\left(\frac{\mu_k + k_{\text{in}}}{D} + k^2\right)}} \right] - \beta k^2. \tag{3.32}$$

This constitutes an implicit equation for the growth rate μ_k that we will discuss next in more detail.

Analysis of the growth rates

We first analyze the quasistatic limit of the spectrum of growth rates. In this limit, we assume that morphogen dynamics is much faster than the dynamics of interface perturbations ($\mu_k/k_i \ll 1$) and, as a consequence, the morphogen concentration c_i can adapt instantaneously to any perturbation of the interface position. To find the growth rates μ_k in the quasistatic limit, we enforce $\partial_t c_i$ in Eq. (3.25b) and find

$$\mu_k = \gamma\Delta c \frac{1}{\ell_{\text{out}} + \ell_{\text{in}}} \left[1 - \frac{\sqrt{1 + 4\left(\frac{\ell}{\lambda_{\text{out}}}\right)^2} + \sqrt{1 + 4\left(\frac{\ell}{\lambda_{\text{in}}}\right)^2}}{\sqrt{1 + 4\ell^2\left(\frac{1}{\lambda_{\text{out}}^2} + k^2\right)} + \sqrt{1 + 4\ell^2\left(\frac{1}{\lambda_{\text{in}}^2} + k^2\right)}} \right] - \beta k^2. \tag{3.33}$$

In contrast to the general spectrum of growth rates in Eq. (3.32), we obtain an explicit relation for the growth rate μ_k, which allows us to discuss several key features of the instability.

Most importantly, we find that an instability can occur in interface motion. While for small values of morphogen inhibition γ, the system is stable, we find that for values larger than a critical inhibition γ_c, the system is unstable (Fig. 3.4a). To determine the critical value γ_c, we expand the growth rate given in Eq. (3.33) in a Taylor series up to second order. We find that zeroth and first order term are zero, leaving the second order term as the only non-zero term. The critical value γ_c is obtained from setting the slope of the expanded growth rates to zero at the origin according to $d\mu_k/dk|_{k=0} = 0$. From this, we find for the critical inhibition γ_c for the transition from stable to unstable interface behavior

$$\gamma_c = \frac{\beta}{\Delta c} \frac{1}{2\ell^2} \frac{\ell_{\text{in}} + \ell_{\text{out}}}{\left(\frac{2\ell}{\ell_{\text{in}}} - 1\right)\left(\frac{2\ell}{\ell_{\text{out}}} - 1\right)}. \tag{3.34}$$

Interestingly, we find that irrespective of inhibition strength a translation of the system

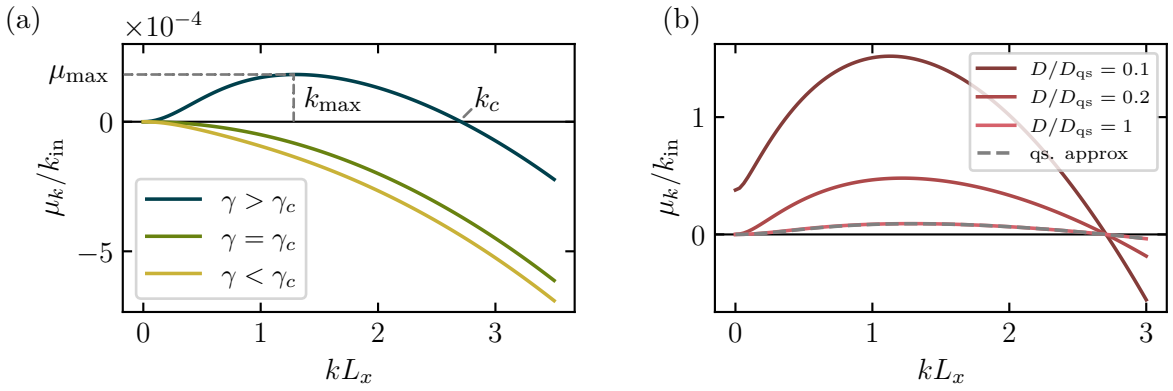

Figure 3.4: Growth rate spectrum. (a) We show the growth rate μ_k of an interface perturbation in the quasistatic limit given by Eq. (3.33) in the stable ($\gamma < \gamma_c$), critical ($\gamma = \gamma_c$), and unstable ($\gamma > \gamma_c$) regime. (b) We show the growth rate μ_k of interface perturbations obtained from the numerical solution of the implicit relation Eq. (3.32) for different values of the diffusion constant D while keeping ℓ and λ_i constant. D_{qs} denotes a reference diffusion constant. We additionally show the growth rate according to the quasistatic approximation Eq. (3.33) (gray dashed line).

(perturbation with $k = 0$) does not lead to an instability ($\mu = 0$ at $k = 0$). In the quasistatic limit, a translation of the interface is accompanied instantaneously by a corresponding translation of the morphogen concentration. Thus, $\mu(k = 0) = 0$ reflects the translation invariance of the system in the quasistatic limit.

The growth rate spectrum in the unstable regime exhibits a characteristic shape with zeros at $k = 0$ and $k_c > 0$ and a maximum in between at $k_{\max}$ (Fig. 3.4a). These special points can be used to define characteristic length scales via $k = 2\pi/\lambda$ that characterize the formation of unstable interfacial patterns. For example, we will later determine a measure for branch distance from $k_{\max}$. We use the limit $k_{\max}\ell \gg 1$ ("small velocity") and $k_{\max}\lambda_i \gg 1$ ("small branch distance") and find that $k_{\max}$ is given by

$$k_{\max}^3 = \frac{\gamma \Delta c}{\beta} \frac{1}{4\ell_{\text{in}}\ell_{\text{out}}}. \tag{3.35}$$

The zero k_c of the growth rate spectrum allows us to determine the instability of interface perturbations. While perturbations with $k < k_c$ are unstable, perturbations with $k > k_c$ are stable. To determine a relation for k_c, we use the approximations $k_c\ell \gg 1$ and $k_c\lambda_i \gg 1$ and find

$$k_c^2 = \frac{\gamma \Delta c}{\beta} \frac{1}{\ell_{\text{out}} + \ell_{\text{in}}}. \tag{3.36}$$

According to Eq. (3.33), the interface instability results from the competition of desta-

bilization from the inhibition of interface growth by a morphogen (positive first term) and the stabilization from the curvature dependency of interface growth (negative second term). The formation of a protrusion on a flat interface leads to a reduction of the morphogen concentration and inhibition at the protrusion tip. As a consequence, the protrusion experiences an increased growth rate compared to a flat interface. In the unstable regime, the stabilizing effect from the curvature dependency of interface growth is insufficient to compensate the increase of protrusion growth. The protrusion extends which leads to a further reduction of the morphogen concentration at its tip. We thus find a positive feedback between the decrease of morphogen concentration and the increase of protrusion growth, which eventually results in complex, branched interface morphologies.

In the quasistatic limit, the morphogen field adapts instantaneously to any perturbations of the interface. In general, however, a lag between interface perturbation and the morphogen dynamics can exist and lead to changes of the growth rate spectrum due to retardation effects (Fig. 3.4b). For example, when the quasistatic limit is violated we find that a flat interface is unstable against translations ($\mu_k > 0$ at $k = 0$). After a translation of the interface, the concentration field lags behind, which results in a reduction of morphogen concentration at the interface position, a corresponding reduction of inhibition, and thus an increase of interface growth.

3.3 Phase field model of morphogen-controlled interface growth

3.3.1 Introduction to the phase field method

To obtain solutions of our model for morphogen-controlled branching morphogenesis also in the nonlinear regime, we need a method for the numerical solution of the interface dynamics (3.1) along with the morphogen dynamics Eq. (3.3). Here, we use the phase field method, which is a versatile technique to treat problems of interface motion. It is an example of method in which the interface is represented implicitly and allows the treatment of topological changes of the interface. Additionally, it works easily in arbitrary dimensions and stands out due to its computational simplicity, as only a set of coupled reaction-diffusion equations has to be solved [178]. Other popular methods such as the level-set [179] or volume of fluid method [180] also represent interfaces in an implicit way, but are computationally more complex as advection equations have to be solved. The boundary-element method is an example of a method in which the interface is explicitly

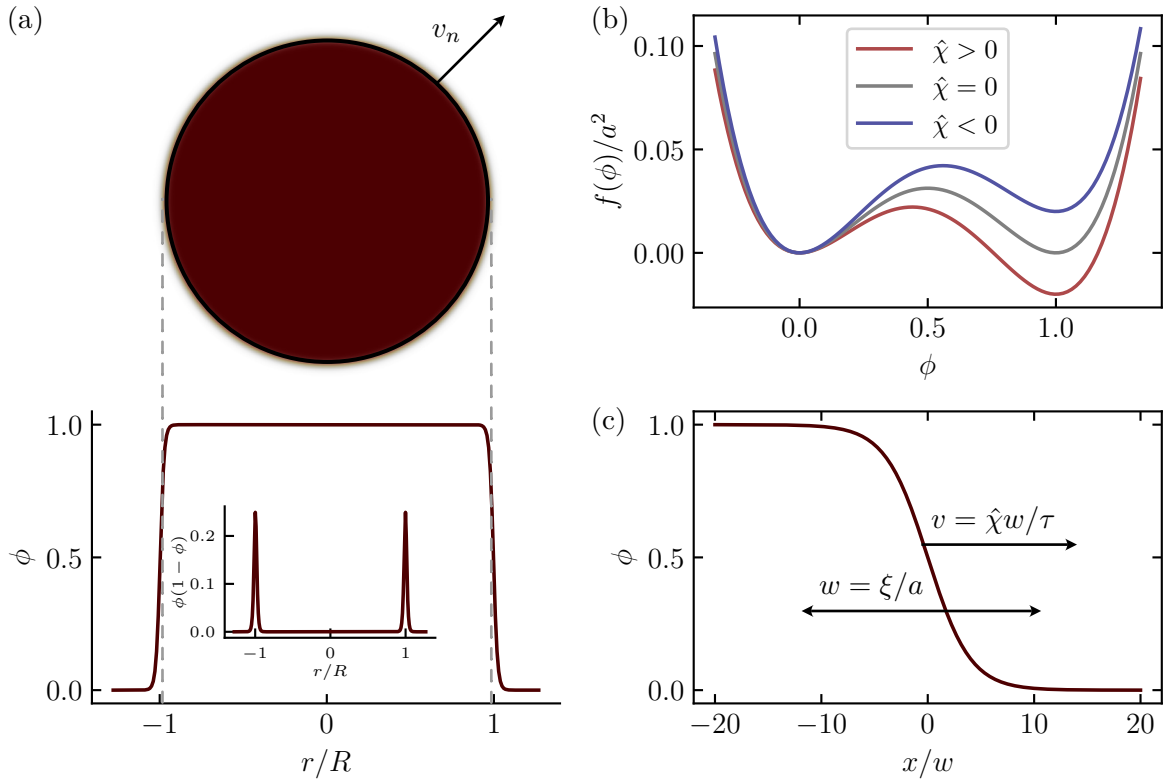

Figure 3.5: Phase field method for studying interface motion. (a) Top: We show a circular interface (black line) with radius R and moving with normal velocity v_n as a simple example of interface motion. Bottom: The phase field ϕ represents the interface in an implicit way. The function $\phi(1-\phi)$ peaks at the interface. (b) We show the energy density $f(\phi)$ given in Eq. (3.38) as a function of the phase field ϕ for different values of the bias $\hat{\chi}$. (c) We show the solution Eq. (3.42) of the Allen-Cahn equation in a 1D scenario as a function of the position x. The interface velocity v is given by the ratio of interface width w and time scale τ. The interface width w is given by the ratio of the energetic cost to form an interface ξ and a.

discretized. However, this approach suffers from the difficulty to account for topological changes of the interface and the computational cost for long and strongly curved interfaces is large [138, 181].

At the heart of the phase field method is the continuous order parameter like phase field $\phi(\boldsymbol{x}, t)$ that takes values $\phi \in [0, 1]$ (Fig. 3.5a). The phase field ϕ serves as a mathematical tool to implicitly represent the interface [178]. While the value $\phi = 1$ indicates the presence of organ, the value $\phi = 0$ indicates the absence of organ. Both regions are connected by a thin transition layer that we call the interface. By defining the dynamics of the order parameter ϕ, we thereby implicitly define the dynamics of the interface.

To derive the evolution equation of the phase field ϕ, we first define the energy $E[\phi]$ of a

given phase field configuration. The energy $E[\phi]$ is of Ginzburg-Landau type and defined by

$$E[\phi] = \int d\boldsymbol{x} \left[\frac{\xi^2}{2} (\boldsymbol{\nabla}\phi)^2 + f(\phi) \right]. \tag{3.37}$$

The first term denotes the energetic contribution of an interface and introduces an energetic cost of order ξ to form an interface between a region of $\phi = 1$ and $\phi = 0$. The second term denotes the bulk contribution (Fig. 3.5b)

$$f(\phi) = \frac{a^2}{2} f_{\mathrm{s}}(\phi) + \frac{\hat{\chi}}{6}\, f_{\mathrm{t}}(\phi) \tag{3.38}$$

of the energy and consists of a symmetric part f_{s} and tilting part f_{t} defined by

$$f_{\mathrm{s}}(\phi) = \phi^2(1-\phi)^2 \qquad\qquad f_{\mathrm{t}}(\phi) = \phi^2(2\phi - 3). \tag{3.39}$$

The parameters a and $\hat{\chi}$ allow us to control the relative importance of each energetic contribution and thus the interface dynamics. The symmetric part f_{s} is a double well potential with minima at $\phi = 0, 1$ that satisfy $f_{\mathrm{s}}(0) = f_{\mathrm{s}}(1) = 0$. Therefore, the symmetric part of the bulk energy defines two energetically preferred phases $\phi = 0, 1$. The tilting part f_{t} has minima at $\phi = 0, 1$ as well. However, we have constructed f_{t} such that $f_{\mathrm{t}}(0) = 0$ and $f_{\mathrm{t}}(1) = -1$, and therefore the phase $\phi = 1$ is energetically preferred by the tilting part f_{t}. From the properties of f_s and f_t, we can conclude that the bulk contribution f is a tilted double well potential with minima at $\phi = 0, 1$ and $f(0) = 0$ and $f(1) = -\hat{\chi}/6$. The parameter $\hat{\chi}$ allow us to control by how much the phase $\phi = 1$ is energetically preferred. To ensure the existence of minima at $\phi = 0, 1$, we require $|\hat{\chi}| < a^2$. Note that by using the energy function Eq. (3.37) along with the bulk contribution Eq. (3.38), we follow the convention presented in Ref. [178].

To derive the dynamics of the order parameter ϕ, we assume the relaxational dynamics

$$\tau \frac{\partial \phi}{\partial t} = -\frac{\delta E}{\delta \phi}. \tag{3.40}$$

According to this, the phase field develops into a configuration that minimizes energy E with a rate determined by the characteristic time scale τ [136, 178]. Upon performing the variational derivative in Eq. (3.40), we find that the time evolution of ϕ is governed by

$$\tau \frac{\partial \phi}{\partial t} = \xi^2 \nabla^2 \phi + 2a^2 \phi(1-\phi) \left(\phi - \frac{1}{2} + \frac{\hat{\chi}}{2a^2} \right), \tag{3.41}$$

which is known as the Allen-Cahn equation and central to the phase field method [178, 182]. To understand how Eq. (3.41) and in particular the parameters ξ, a, and τ determine interface dynamics and shape, we now study two minimal scenarios of interface motion.

We first consider a 1D system with boundary conditions $\phi(-\infty) = 1$ and $\phi(\infty) = 0$. In this system, Eq. (3.41) is solved by the interfacial profile of the form [178, 183]

$$\phi(x,t) = \frac{1}{2}\left[1 - \tanh\left(\frac{x - vt}{2w}\right)\right]. \tag{3.42}$$

Thus, the interfacial profile is described by a sigmoidal function, where energetic cost ξ to form interfaces between two phases of ϕ controls the interface width $w = \xi/a$ and $\hat{\chi}$ controls the interface velocity $v = \hat{\chi}\, w/\tau$ (Fig. 3.5c) [178]. The relations for interface velocity and width link the properties of the phase field with interface properties. Note that due to the finite width of ϕ the interface has the non-zero surface energy σ (also known as surface tension) [144, 178]. The surface energy is defined as the difference between total energy and bulk energy according to

$$\sigma = \int_{-\infty}^{\infty} dx \left[\frac{1}{2}(\partial_x \phi)^2 + f(\phi) - f(1)\right]. \tag{3.43}$$

We can rewrite this for the case of the energy Eq. (3.37) and the profile Eq. (3.42) to $\sigma = \xi^2 \int_{-\infty}^{\infty} dx (\partial_x \phi)^2$, which gives $\sigma = \xi^2/(6w)$. The surface tension is an important quantity and will be essential for the study of curved interfaces in 2D systems. We have thus established the connection between the parameters of the phase field energy with properties of the interface. Note that we can independently adjust interface thickness, surface tension, and propagation speed with the phase field parameters.

As a second minimal scenario of interface dynamics, we now consider the motion of a circular interface (Fig. 3.5a). This scenario allows us to study the influence of curvature on interface motion. To understand the interface dynamics in this case, we use the sharp interface limit of the Allen Cahn Eq. (3.41) instead of considering the full dynamics of ϕ as in the 1D case. By taking the limit of $w \to 0$ while the mobility $\mu = \tau/\xi^2$ and surface tension σ are held constant, we can find for the normal velocity v_n of an interface (see appendix B for a derivation)

$$v_n = \frac{1}{\mu}\left[\frac{\hat{\chi}}{6\sigma} - \frac{1}{R}\right], \tag{3.44}$$

where R denotes the radius of the circular interface [144, 184]. As before, we find that the energetic bias influences interface motion and can lead to a positive or negative contribu-

tion to interface velocity. Additionally, we find that the energetic cost to form an interface results in a negative contribution to interface velocity. Note that Eq. (3.44) reduces in the limit $R \to \infty$ to the result for the velocity of a flat interface that we have presented earlier.

In the next section, we present the phase field model corresponding to the continuum model presented in the previous section.

3.3.2 Phase field model for morphogen-controlled interface growth

In the phase field model that corresponds to our continuum model, we study the dynamics of the phase field ϕ and the morphogen concentration c described by the set of two coupled reaction-diffusion equations

$$\tau \frac{\partial \phi}{\partial t} = \xi^2 \nabla^2 \phi + 2a^2 \phi(1-\phi)\left(\phi - \frac{1}{2} + \frac{\hat{\chi}(c)}{2a^2}\right) \tag{3.45a}$$

$$\frac{\partial c}{\partial t} = D\nabla^2 c - k(\phi)c + s(\phi). \tag{3.45b}$$

As described in the previous section, the phase field equation describes interface motion in an implicit way, where the bias $\hat{\chi}$ determines the normal velocity of the interface. While we have so far considered a constant bias $\hat{\chi}$, we now consider a concentration-dependent bias in accordance with the growth rule Eq. (3.1):

$$\hat{\chi}(c) = \hat{v}_0 - \hat{\gamma} c(x, y) \tag{3.46}$$

Note that we denote quantities in the phase field model that have a counterpart in the continuum model with a hat symbol. To account for the region-dependency of morphogen degradation and production in the continuum model, we consider phase-field dependent degradation and production in the phase field model:

$$k(\phi) = k_{\text{in}}\phi + k_{\text{out}}(1-\phi) \tag{3.47a}$$

$$s(\phi) = s_{\text{in}}\phi + s_{\text{out}}(1-\phi) \tag{3.47b}$$

Clearly, in the inside region ($\phi = 1$), we find $k = k_{\text{in}}$, and in the outside region ($\phi = 0$), we find $k = k_{\text{out}}$ and similarly for the production term.

The phase field model is constructed in a way to match the sharp interface description in the limit of $w \to 0$ while mobility μ and surface tension σ are held constant. We present the details of the sharp interface limit in appendix B and here use Eq. (3.44) to find the

correspondence

$$v_0 = \frac{\xi/a}{\tau}\hat{v}_0 \qquad \gamma = \frac{\xi/a}{\tau}\hat{\gamma} \qquad \beta = \frac{\xi^2}{\tau} \tag{3.48}$$

between parameters in the continuum model and the phase field realization.

3.4 Geometry and topology of morphologies

To study pattern formation beyond the onset of instability, we use the phase field method to obtain numerical solutions of the continuum model. We consider a rectangular system of width L_x and length L_y with periodic boundary conditions $\phi(0, y) = \phi(L_x, y)$ along the left and right boundary and no-flux boundary conditions $\partial_y\phi(x, 0) = \partial_y\phi(x, L_y) = 0$ along the bottom and top boundary. We enforce the same boundary conditions for the morphogen concentration c. We initialize the system with a flat interface located at $y_\mathrm{I}(0)$ together with morphogen concentration $c(x, y) = 0$ in the entire system. To avoid boundary effects, we locate the initial interface position such that $y_\mathrm{I}(0) \gg \lambda_i$ for interfaces with velocity $v > 0$ and at $L_y - y_\mathrm{I}(0) \gg \lambda_i$ for interfaces with $v < 0$.

We consider an unstable parameter regime and find that after sufficiently long time ($\mu_\mathrm{max}t \gg 1$) a flat moving interface undergoes an instability and exhibits branching (Fig. 3.6). After a sufficiently long time the system reaches a space-filling configuration that we then quantify. Here, we provide a brief overview of our analysis and refer the reader to appendix C for a more detailed description. To analyze branch properties, we consider a row of the discretized phase field ϕ. We calculate the branch distance as the distance of branch midlines and branch thickness from the length of "in" regions.

3.4.1 Control of branch distance

To vary branch distance in a controlled way, we make use of results from the stability analysis. In the quasistatic limit, we find that the growth rate $\mu(k)$ of a perturbation with wavelength $\lambda = 2\pi/k$ has a maximum μ_max at a corresponding wavelength λ_max. As a result, perturbations with wavelength λ_max grow fastest and dominate the pattern formation process. We expect resulting patterns to have a characteristic length scale λ_max and thus use the fastest growing wavelength λ_max as a measure for branch distance d.

In the quasistatic limit, we obtained by additionally invoking the limit of small velocity ($k_\mathrm{max}\ell \gg 1$) and small branch distance ($k_\mathrm{max}\lambda_i \gg 1$) Eq. (3.35) as analytical expression for λ_max. Even though this relation is valid only in a well-defined limit, it allows us to

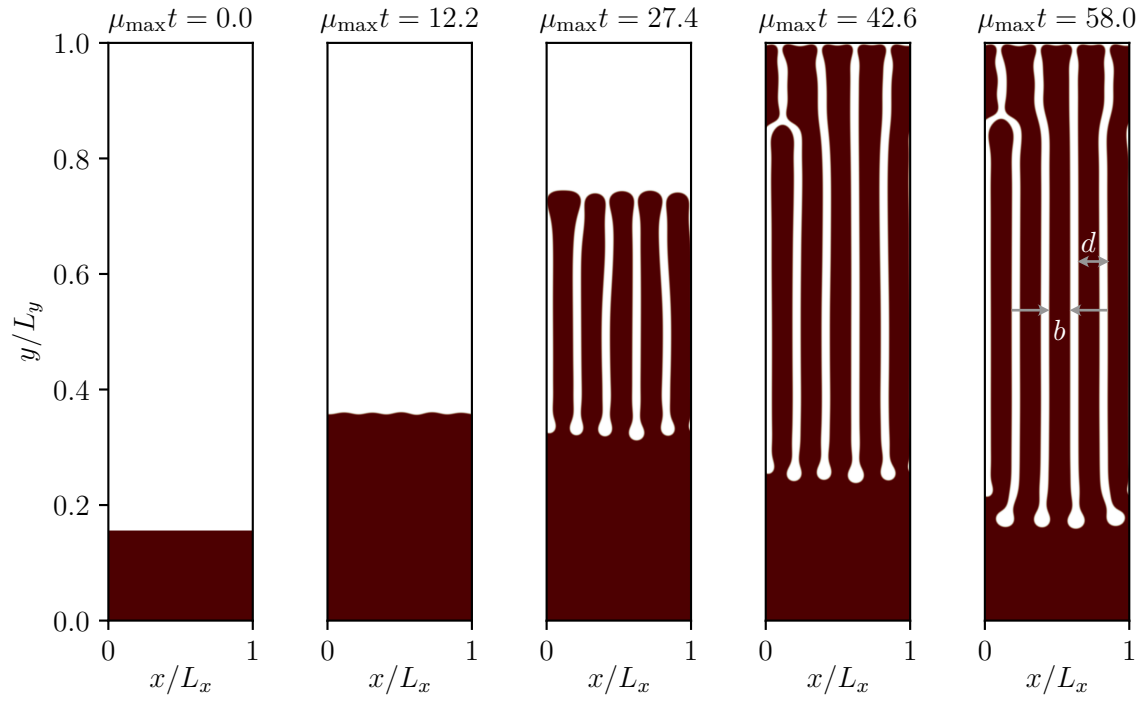

Figure 3.6: Interface evolution beyond the onset of instability. We study the instability of a flat moving interface in a rectangular domain of width L_x and length L_y. $\mu_{\max}$ denotes the maximal growth rate in Eq. (3.33). We additionally indicate branch distance d and the branch thickness b (gray arrows).

qualitatively discuss the dependency of $\lambda_{\max}$ and thus branch distance d on model parameters. According to Eq. (3.35), $\lambda_{\max}$ increases with β. The curvature dependency β of interface growth expresses the tendency of the system to relax back to a flat configuration after a perturbation and thus with increasing β branch distance increases.

To demonstrate how branch distance can be controlled in our model, we next studied the instability of a flat moving interface in a rectangular system with the phase field method. We use β as an example for a control parameter for branch distance, but note that any other of the previously mentioned parameters could take this role. To change β in the phase field model, we make use of the correspondence Eq. (3.48) between parameters in the continuum model and its implementation with the phase field method. We vary β by changing ξ and keeping the interface width constant by making a corresponding change in a. With this strategy, we study the effect of a ∼3fold change in β and find a corresponding ∼2fold change in terms of branch number, where we simply counted the number of branches along a horizontal direction in the system (Fig. 3.7a). To confirm this observation, we additionally quantified the branch distance in our simulations. We compare the

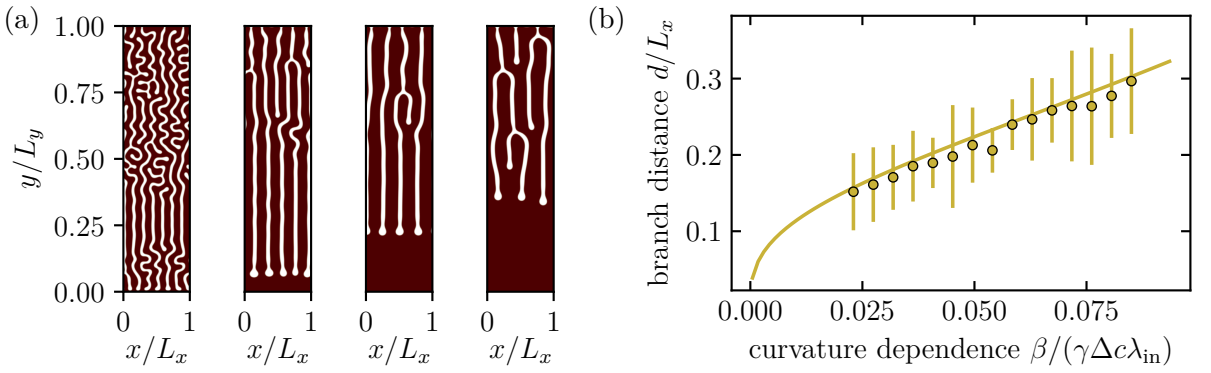

Figure 3.7: Control of branch distance. (a) We study the instability of a flat moving interface in a rectangular domain with width L_x and length L_y. We show morphologies obtained from the instability of a flat moving interface for different values of β. (b) We show the mean branch distance d extracted from simulations. Error bars denote the standard deviation. Additionally, we show the fastest growing wavelength λ_{max} (line) as a measure for branch distance d as a function of the curvature dependency β of interface growth. We numerically obtained λ_{max} from Eq. (3.33).

measured branch distance with the predicted branch distance from our relation for λ_{max} and find good agreement (Fig. 3.7b). Overall, we therefore identify λ_{max} as a measure and β as a control parameter for branch distance.

3.4.2 Control of branch thickness

The mutual inhibition of branches prevents them from growing into each other and therefore controls branch thickness. To understand this process in more detail, we now motivate a minimal, analytically tractable scenario for the interaction of branches. We consider an already formed branched morphology and focus on two branches that are aligned parallel to each other (Fig. 3.8a, inset). The boundaries of such branches are only slightly curved and thus they are well approximated by flat interfaces. Moreover, due to the symmetry of the problem, it is sufficient to consider only one of the branches in this scenario. With these simplifications we can study the interaction of branches by considering the position y_{I} of a flat interface in a system of size L (Fig. 3.8b). We relate the system size L to branch distance d by $d = 2L$ and we obtain the branch thickness b from the stationary position of the interface $\bar{y}_{\mathrm{I}}$ by $b = 2\bar{y}_{\mathrm{I}}$.

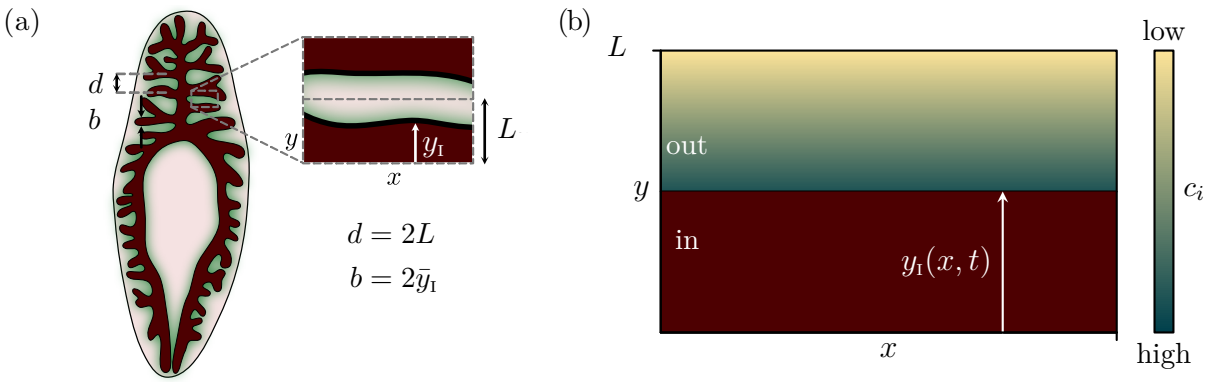

Figure 3.8: Minimal scenario to study branch thickness. (a) To understand what controls branch thickness, we study the mutual interaction of two branches. Due to the symmetry of the situation, we study only the interface position of one branch. We further consider the branch interface as flat. These simplifications allows us to infer branch thickness from the position y_I of a flat interface. (b) In our minimal scenario, the system size is related to branch distance by $d = 2L_y$ and we find the branch thickness from $b = 2\bar{y}_I$, where $\bar{y}_I$ denotes the stationary interface position.

The dynamics of interface position and morphogen concentration are governed by

$$\partial_t y_I = v_0 - \gamma c(y_I) \tag{3.49a}$$

$$\partial_t c_i = D\partial_y^2 c_i - k_i c_i + s_i, \tag{3.49b}$$

which is equivalent to the dynamics presented earlier in Eq. (3.1), except that the curvature-dependent term vanishes here since we consider a flat interface. The morphogen concentration further needs to satisfy that both concentration and concentration gradients at the interface match

$$c_{\text{in}}(y_I) = c_{\text{out}}(y_I) \qquad \partial_y c_{\text{in}}(y_I) = \partial_y c_{\text{out}}(y_I) \tag{3.50}$$

and we additionally require no-flux conditions

$$\partial_y c_{\text{in}}(x, 0) = 0 \qquad \partial_y c_{\text{out}}(x, L) = 0 \tag{3.51}$$

at the system boundary. Overall, we thus propose to reduce the problem of how branch thickness arises from the interaction of two branches to studying the stationary position $\bar{y}_I$ of a flat interface.

To obtain the stationary interface position and from this branch thickness, we now derive the stationary state of the system. We first determine the stationary concentration

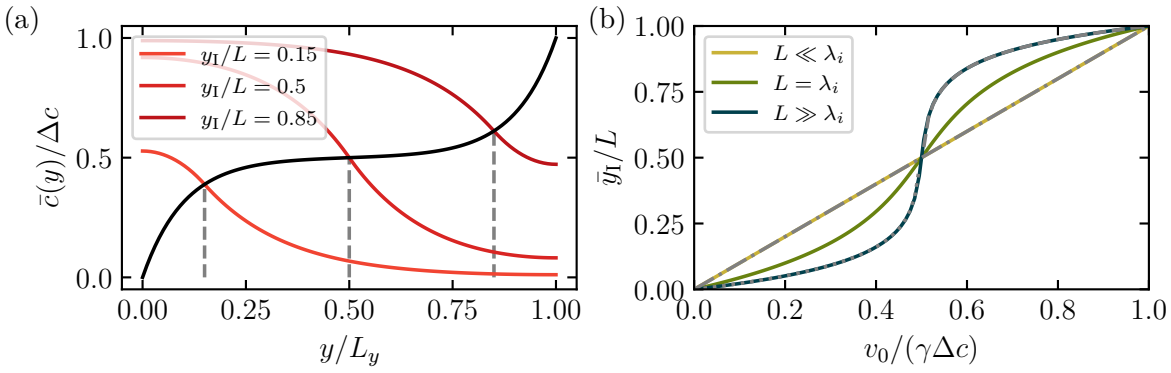

Figure 3.9: Stationary morphogen concentration profiles and interface position. (a) We show the stationary concentration profile $\bar{c}(y)$ (red lines) from Eq. (3.52) as a function of position y for different values of the interface position y_I (dashed gray lines). We additionally show the concentration value $\bar{c}_\mathrm{I}$ at the interface (black line). (b) We show the stationary interface position $\bar{y}_\mathrm{I}$ as a function of $v_0/(\gamma \Delta c)$ for different values of system size L. Additionally, we show the approximations in the limit of narrow branches given in Eq. (3.57) (gray dashed-dotted line), the limit of thin branches given in Eq. (3.58) (gray dotted line), and the limit of thick branches given in Eq. (3.59) (gray dashed line).

profile $\bar{c}_\mathrm{i}$ that is governed by the stationary reaction diffusion equation

$$0 = \partial_y^2 c_i - \frac{1}{\lambda_i^2} c_i + \frac{1}{\lambda_i^2} c_i^0, \tag{3.52}$$

where we have used the abbreviation of the degradation length $\lambda_i = \sqrt{D/k_i}$ and of the offset concentration $c_i^0 = s_i/k_i$. By making an exponential ansatz for Eq. (3.52), we find the solution as

$$\bar{c}_\mathrm{in}(y) = 2A \cosh(y/\lambda_\mathrm{in}) + c_\mathrm{in}^0 \tag{3.53a}$$

$$\bar{c}_\mathrm{out}(y) = 2Be^{L/\lambda_\mathrm{out}} \cosh\left[(y-L)/\lambda_\mathrm{out}\right] + c_\mathrm{out}^0 \tag{3.53b}$$

together with the constants

$$A = \frac{\Delta c}{2} \frac{1}{1 + \frac{\lambda_\mathrm{out}}{\lambda_\mathrm{in}} \frac{\tanh(y/\lambda_\mathrm{in})}{\tanh[(y_\mathrm{I}-L)/\lambda_\mathrm{out})]}} \frac{1}{\cosh\left(\frac{y_\mathrm{I}}{\lambda_\mathrm{in}}\right)} \tag{3.54a}$$

$$B = \frac{\Delta c}{2} e^{-L/\lambda_\mathrm{out}} \frac{1}{1 + \frac{\lambda_\mathrm{in}}{\lambda_\mathrm{out}} \frac{\tanh[(L-y_\mathrm{I})/\lambda_\mathrm{out}]}{\tanh(y_\mathrm{I}/\lambda_\mathrm{in})}} \frac{1}{\cosh[(y_\mathrm{I} - L/)\lambda_\mathrm{out}]}. \tag{3.54b}$$

The morphogen concentration profile is therefore given by an hyperbolic cosine that smoothly interpolates between a region of high and a region of low concentration (Fig. 3.9a).

Finally, by setting $y = y_\mathrm{I}$ in Eq. (3.53), we obtain the morphogen concentration $\bar{c}_\mathrm{I} = \bar{c}_i(y_\mathrm{I})$ at the position of the interface:

$$\bar{c}_\mathrm{I}(y_\mathrm{I}) = \frac{\Delta c}{1 + \frac{\lambda_\mathrm{in}}{\lambda_\mathrm{out}} \frac{\tanh\left(\frac{L-y_\mathrm{I}}{\lambda_\mathrm{out}}\right)}{\tanh\left(\frac{y_\mathrm{I}}{\lambda_\mathrm{in}}\right)}} + c^0_\mathrm{out} \tag{3.55}$$

Note that we have omitted the labels "in" and "out" that indicate the respective gut region, since at the position $y = y_\mathrm{I}$ the concentrations $\bar{c}_\mathrm{in}$ and $\bar{c}_\mathrm{out}$ are equal.

The stationary interface position $\bar{y}_\mathrm{I}$ (an consequently the branch thickness) is defined by the stationary solution of Eq. (3.49a). We require $\partial_t \bar{y}_\mathrm{I} = 0$ and find that the stationary solution satisfies

$$\frac{v_0}{\gamma} = \bar{c}_\mathrm{I}(\bar{y}_\mathrm{I}). \tag{3.56}$$

By choosing Δc as a characteristic concentration value, we thus find that the ratio of interface growth tendency v_0 and inhibition strength $\gamma \Delta c$ determine the stationary interface position and consequently branch thickness. Due to the nonlinearity of $\bar{c}_\mathrm{I}$, this constitutes an implicit relation that determines $\bar{y}_\mathrm{I}$. The steady-state solution $\bar{y}_\mathrm{I}$ exists if $v_0/\gamma \leq c^0_\mathrm{in}$ (assuming that $c^0_\mathrm{in} > c^0_\mathrm{out}$). In general, we need to solve Eq. (3.56) numerically to obtain $\bar{y}_\mathrm{I}$.

However, we can determine approximations for $\bar{y}_\mathrm{I}$ in different limiting regimes (Fig. 3.9b). In the regime of narrow branches ($L \ll \lambda_i$ and thus $y_\mathrm{I} \ll \lambda_i$), we find the approximation

$$\frac{\bar{y}_\mathrm{I}}{L} = \frac{1}{1 - \left(\frac{\lambda_\mathrm{out}}{\lambda_\mathrm{in}}\right)^2 \frac{\frac{v_0}{\gamma} - c_\mathrm{in}}{\frac{v_0}{\gamma} - c_\mathrm{out}}}. \tag{3.57}$$

In this regime, we therefore find that $\bar{y}_\mathrm{I} \sim L$. Interestingly, the stationary interface position is independent of any diffusion-degradation length if $\lambda_\mathrm{in} = \lambda_\mathrm{out}$. In the regime of thin branches ($(L - y_\mathrm{I})/\lambda_\mathrm{out} \gg 1$), we find that the stationary interface position is given by

$$\frac{\bar{y}_\mathrm{I}}{\lambda_\mathrm{in}} = \operatorname{arctanh}\left(-\frac{\lambda_\mathrm{in}}{\lambda_\mathrm{out}} \frac{\frac{v_0}{\gamma} - c_\mathrm{out}}{\frac{v_0}{\gamma} - c_\mathrm{in}}\right). \tag{3.58}$$

Finally, we find that in the regime of thick branches ($\bar{y}_\mathrm{I} \gg \lambda_\mathrm{in}$), the stationary interface

position is governed by

$$\frac{L-\bar{y}_{\mathrm{I}}}{\lambda_{\mathrm{out}}} = \operatorname{arctanh}\left(-\frac{\lambda_{\mathrm{out}}}{\lambda_{\mathrm{in}}}\frac{\frac{v_0}{\gamma}-c_{\mathrm{in}}}{\frac{v_0}{\gamma}-c_{\mathrm{out}}}\right). \tag{3.59}$$

These equations demonstrate how the diffusion-degradation lengths and the branch distance determine the branch thickness in the respective limits.

Next, we demonstrated the control of branch thickness in our simulations. To this end, we studied branched morphologies obtained from the instability of a flat moving interface, where we use Δc a control parameter for branch thickness (Fig. 3.10a). Apart from controlling branch thickness, the concentration difference Δc introduces additional changes to interface motion and instability. Recall that the concentration difference Δc influences interface velocity (Fig. 3.3b). We consider a wide range of Δc and as a consequence study the instability of interfaces with both positive and negative velocity. The concentration difference Δc additionally controls branch distance according to Eq. (3.35). To compensate the effect that varying values of Δc have on branch distance, we choose $\beta \propto \Delta c$, which maintains branch distance according to Eq. (3.35).

Finally, we compared the prediction of branch thickness from our minimal scenario with the branch thickness observed in simulations of the full model. We first quantified branch distance and confirmed that branch distance is constant in agreement with our prediction (Fig. 3.10b). Next, we quantified branch thickness and found good agreement between the predicted and observed values of branch thickness (Fig. 3.10c). Interestingly, we find that changes in branch thickness can result in changes in the topology of morphologies. For example, for small values of branch thickness, we find loose branches that lost contact with the main part of the network. By contrast, for large values of branch thickness, we find that branches form loops. Overall, we thus established a quantitative way to study branch thickness and identified Δc as a parameter to control branch thickness.

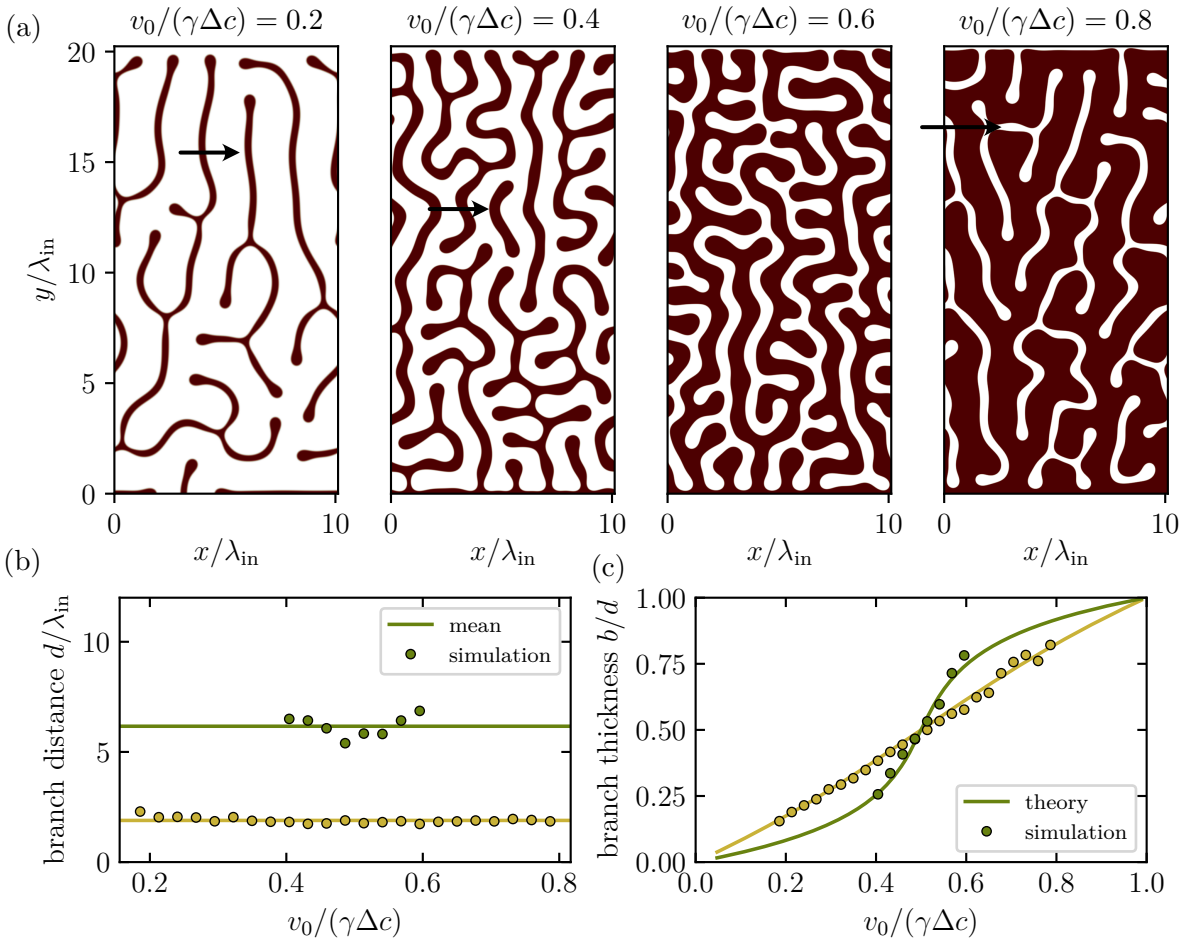

Figure 3.10: Control of branch thickness. (a) We show morphologies obtained from the instability of a flat moving interface for different values of Δc. To maintain branch distance as we vary Δc, we choose $\beta \sim \Delta c$ according to Eq. (3.35). The two left scenarios correspond to an interface that starts close to the top system boundary and moves downwards ($v < 0$), while the two right scenarios correspond to interfaces that start close to the bottom system boundary and move upwards ($v > 0$). v_0 denotes the tendency of interface growth, γ denotes the inhibition strength, and Δc denotes the difference of the offset concentration in the "in" and "out" region. (b) We show branch distance d (dots) as a function of the ratio $v_0/(\gamma\Delta c)$ for different values branch distance d. We additionally show the mean value in each case (line). To control branch distance, we considered the values $\beta/(\gamma\Delta c\lambda_{\text{in}}) = 0.005$ (yellow) and $\beta/(\gamma\Delta c\lambda_{\text{in}}) = 0.11$ (green). (c) We show the ratio b/d (dots) of branch thickness b and distance d as a function of $v_0/(\gamma\Delta c)$ for different values of branch distance.

3.5 Summary and discussion

In this chapter, we have studied morphogen-controlled growth of an interface as a model for branching morphogenesis. We show how branched morphologies arise from instabilities in the interface motion in a self-organized way and analyzed the geometrical and topological properties of the resulting morphologies.

At the center of our study, lies our continuum model for morphogen-controlled interface growth. In this model, we represent the outline of a hypothetical branched organ by an infinitely thin interface. We assume that the interface has a constant tendency to grow, which is inhibited by the concentration of a morphogen. Additionally, we introduce a curvature dependency into interface growth which reduces the growth of outward protrusions and increases growth of inward protrusions. Thus, the curvature dependency gives the interface a tendency to grow to a flat configuration and effectively stabilizes interface motion. We assume that the morphogen diffuses in the system and undergoes region-dependent degradation and production. In particular, we consider a case where morphogen production takes place predominantly inside the organ and forms gradients from inside to the outside of the organ. Overall, we think that this model captures key features of branched organ morphogenesis.

To understand if an instability can occur for this system, we first study the motion of a flat interface in an infinitely long system. We perform a linear stability analysis for this scenario and determine the corresponding growth rate spectrum. Additionally, we consider the limit of quasistatic morphogen dynamics in which the morphogen concentration adapts instantaneously to any perturbations of the interface position. This limit allows us to discuss several key features of the pattern formation in our model. In the quasistatic limit, we can show that a transition from stable to unstable interface behavior occurs for increasing inhibition strength through the morphogen. The formation of a protrusion from the interface results in a reduction of morphogen concentration and thus in growth inhibition at the protrusion. In the unstable regime, the reduction in growth inhibition is large enough (or conversely, the stabilization from the curvature dependency of interface growth is small enough) that the protrusion grows further. The growth of a protrusion results in a further reduction in morphogen concentration and thus growth inhibition. We thus find a positive feedback between protrusion growth and morphogen reduction that results in unstable interface growth. When the quasistatic limit is violated, retardation effects further enhance the instability in the interface motion. The morphogen field lags behind interface perturbations and, as a consequence, the morphogen concentration at protrusion tips is reduced, leading to an increase in protrusion growth.

Next, we studied pattern formation beyond the linear stability analysis. We use the phase field method for the numerical solution of the interface equations and show how complex, branched morphologies originate from the instability in interface motion. We identify branch distance and thickness as key parameters of the resulting branched morphologies and study idealized scenarios of interface motion to understand how model parameters control branch distance and thickness. We identify the fastest growing wavelength of an instability occurring in a flat moving interface as a measure for branch distance. We discuss how the mutual inhibition of branches controls branch thickness and show how branch thickness can be related to the stationary position of a flat interface in a system of finite size. We identify the concentration in the organ as a control parameter for branch thickness. Finally, our approach also allows us to study topological properties of resulting morphologies. In the limit of small branch thickness, we find that branches pinch off and in the limit of large branch thickness we find that neighboring branches merge and form loops. In the intermediate regime, we find tree-like morphologies characterized by the absence of loops or loose branches.

The continuum model presented in this chapter provides a complimentary approach to the lattice model from chapter 2. While our lattice model allows us to study the formation of branched morphologies in the limit of strong noise and zero surface tension, here we study the limit of finite surface tension and zero noise. Moreover, in this chapter we provide a further example for an interface growth rule that yields an instability.

In our model, we assume that branching morphogenesis is solely controlled by a morphogen. However, several other environmental factors contribute to the formation of branched structures that we have excluded in our approach for simplicity. For example, the overall appearance of morphologies can be influenced both by the geometry of the environment it grows in and the initial configuration of the network. The formation of the mouse mammary gland starts from initial placodes formed during embryogenesis and sensory neuron morphogenesis in the zebrafish fin takes place in an almost circular sector [20, 185]. Thus, our approach of initializing the instability from a flat moving interface in a rectangular system facilitates the analysis of the instability, but oversimplifies the scenarios encountered in organisms. Several extrinsic signals can influence branching morphogenesis. Sensory neurons in the zebrafish fin show a distinct radial orientation and it was proposed that chemical (e.g morphogen gradients) or mechanical cues influence this orientation [185, 186]. Finally, we also studied the formation of branched structures in a non-growing environment while branching morphogenesis can take place in a growing organism. For example, the planarian gut undergoes extensive remodeling and forms numerous new side branches as the organism increases in size [187]. While these points

have not been addressed in this chapter, we take them into account, when we study the branching morphogenesis of the planarian gut in chapter 5.

Chapter 4

Quantitative analysis of planarian gut branching morphology

In this chapter, we present the planarian gut as an example of a highly branched organ. We provide a detailed analysis of the geometrical and size-dependent properties of planarian gut morphologies along with an analysis of size and shape of the planarian body and pharynx.

We first introduce the experimental data that our collaborators Amrutha Palavalli and Baiqun An from the lab of Jochen Rink at the Max-Planck Institute for Multidisciplinary Sciences in Göttingen obtained. We explain the image processing and subsequent quantification procedure including the definition of the various quantities we consider in our analysis. We subsequently use our analysis to study shape and size of the planarian body and pharynx. Next, we study the size-dependent properties of the planarian gut. Overall, our analysis provides important insights of the organization of the planarian gut. Moreover, our findings from this chapter inform key aspects of a model for gut branching morphogenesis presented in the next chapter. We will use the tools for gut quantification presented here to quantify gut morphologies obtained from the model presented in the next chapter.

4.1 Quantification of the planarian gut

Our collaborators first imaged the planarian gut to quantify its geometrical as well as size-dependent properties. To this end, they collected cohorts consisting of ca. 10 size-matched animals in the range 1 to 11 mm and subsequently prepared the animals for imaging with a fixation process. Note that the fixation process changes the size of the organism. While an animal was labeled being of a certain size before fixation, the size after fixation typically

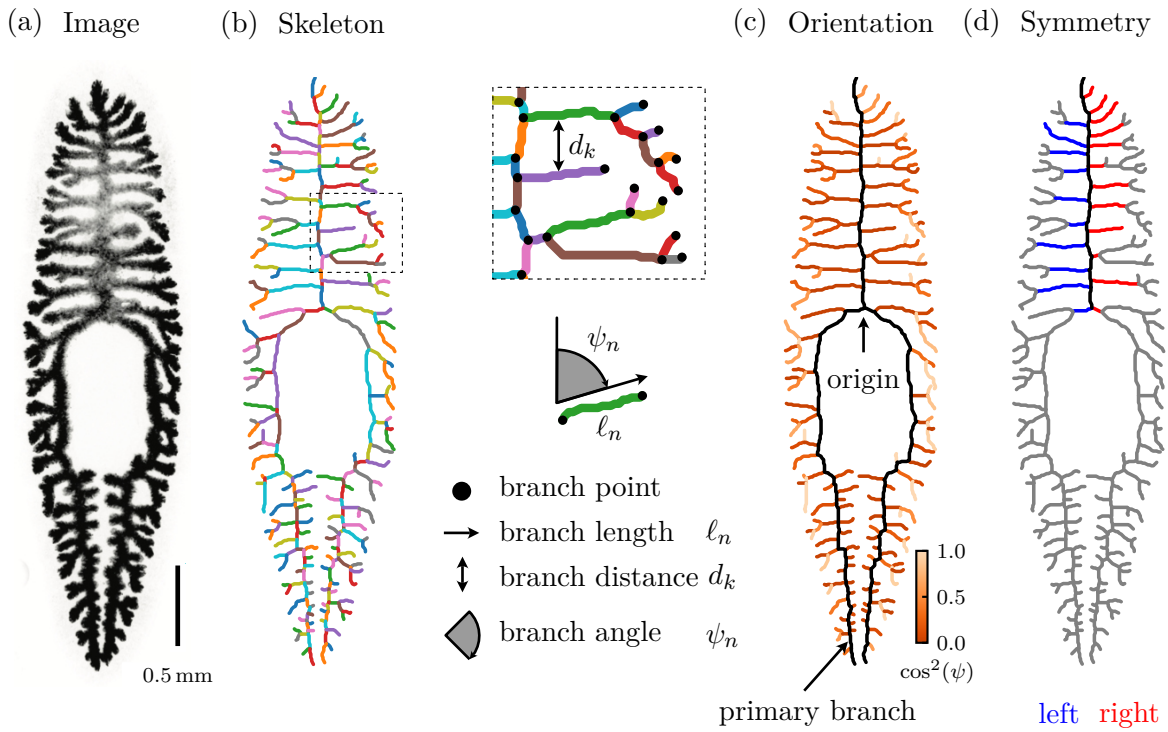

Figure 4.1: Quantifying planarians and the planarian gut. (a) *In-situ* hybridization of the planarian gut. Intensity is proportional to expression of a selected gene in inner intestinal cells. (b) Our collaborators used the segmentation of the raw data in (a) to determine the skeleton of the planarian gut. Inset: We define a branch e_n as the set of pixels that connect two branch points (black dots) in the skeleton. Colors indicate different branches and the index n labels branches. (c) We show the primary branch (black) and side branches (orange). The orange tone indicates the orientational order parameter $\cos^2(\psi)$, where ψ denotes branch angle. (d) We show side branches originating in the anterior part of the primary branch (black) that grow to the left (blue) and right (red) along with unclassified branches (gray). Raw image data as well as segmentation and skeleton obtained by Amrutha Palavalli.

slightly decreases. This explains why the size range displayed in parts of our analysis differs from 1 to 11 mm, but is slightly shifted a to range with smaller lower and upper bounds. Moreover, due to the grouping into size-matched animals, we find that our data is also grouped into roughly five clusters (cf. Fig. 4.4a). After size-matching and fixation, our collaborators performed *in-situ* hybridizations using a marker for inner intestinal cells (Fig. 4.1a). From a binarization of the raw data they determined a skeleton, i.e. a one pixel wide representation of the binarized data with the same connectivity as the original data. The skeletonized gut structures are the cornerstone of our analysis and allow us to quantify various properties of gut organization. Note, however, that the employed gut marker only labels inner but not outer intestinal cells and thus we can faithfully reconstruct the skeleton of the gut, but we (so far) lack information about the branch thickness.

At the center of our gut skeleton analysis lies the identification of branch points ("vertices") and branches ("edges") (Fig. 4.1b). We define pixels as branch points based on properties of a local, 3×3 neighborhood around them (see appendix C for details) and branches as the set of pixels

$$e_n = \{(i_1, j_1), \ldots, (i_M, j_M)\} \tag{4.1}$$

that connect two branch points (i_1, j_1) and (i_M, j_M). We denote the total number of branches by N, the total number of pixels in a branch by M, and use the index n to label individual branches. Note that the connection of two branch points is unique as we consider tree-like (loopless) structures. We additionally distinguish between the primary branch and side branches. The primary branch is determined as the union of the three longest paths of branches that each originate at the origin of the gut (Fig. 4.1c). We call any remaining branches side branches.

Branch length, thickness, and distance

Based on the definition of an branch in Eq. (4.1), we define several geometrical branch properties (Fig. 4.1b). We define branch length ℓ_n of an individual branch as

$$\ell_n = \sum_{m=1}^{M-1} \Delta\ell_m, \tag{4.2}$$

where $\Delta\ell_m = \sqrt{(i_{m+1} - i_m)^2 + (j_{m+1} - j_m)^2}$ denotes the Euclidean distance of a branch segment between two pixels (i_m, j_m) and (i_{m+1}, j_{m+1}). We define the mean branch length

ℓ of the organism as the mean

$$\ell = \frac{1}{N} \sum_{n=1}^{N} \ell_n \tag{4.3}$$

of individual branch lengths. Finally, we define total gut length $L_{\text{gut}} = \sum_n \ell_n$ as the total length of all branches and find $L_{\text{gut}} = N\ell$.

Even though we (so far) lack the data to faithfully estimate branch thickness, we provide the necessary definitions and use them in chapter 5 to analyze the respective properties of simulated gut structures. To estimate branch thickness, we use the so-called distance transform [168]. The distance transform is applied to binarized images and returns for every foreground pixel (i, j) of the image the distance r_{ij} to the nearest background pixel. The distance transform r_{ij} at the position of the branch skeleton (i.e. branch midline) provides a measure for the distance to the branch boundary and thus can be used to determine branch thickness. We define the thickness of an individual branch b_n as the averaged distance transform along a branch e_n according to

$$b_n = \frac{1}{M} \sum_{(i,j) \in e_n} 2r_{ij}, \tag{4.4}$$

where the factor of 2 is needed as branch thickness represents the distance betweeen branch boundaries. We define the mean branch thickness of the organism as the mean

$$b = \frac{1}{N} \sum_{n=1}^{N} b_n. \tag{4.5}$$

of individual branch thickness.

Apart from branch length and thickness, branch distance d is another key property of gut morphologies. To determine branch distance, we consider each column of the image in turn and determine the distance d_k of subsequent side branches. We then define the mean branch distance of a morphology as the mean

$$d = \frac{1}{N_d} \sum_{k=1}^{N_d} d_k, \tag{4.6}$$

of individual side branch distances, where N_d denotes the total number of side branch distances in the entire image. Note that we exclude distances d_k that span the pharynx to prevent the distance calculation to be biased.

Branch orientation

To quantify branch orientation, we use the mean branch angle ψ_n. The mean branch angle ψ_n is defined as the circular mean of the local branch angles ψ_{nm} of individual branch segments. The local branch angles ψ_{nm} represent the inclination of an individual segment m of a branch e_n to a vertical axis and are obtained from

$$x_{nm} = \cos\psi_{nm} \tag{4.7a}$$
$$= \frac{i_{m+1} - i_m}{h_m} \tag{4.7b}$$
$$y_{nm} = \sin\psi_{nm} \tag{4.8a}$$
$$= \frac{j_{m+1} - j_m}{h_m}, \tag{4.8b}$$

where the tuple (x_{nm}, y_{nm}) represents the position on the unit circle corresponding to the local branch angle ψ_{nm}. To determine the mean branch angle from the set of local angles, we determine the arithmetic mean $(\bar{x}_n, \bar{y}_n)$ of the corresponding unit circle positions. Taking the arithmetic mean of unit circle positions ensures the correct averaging of angles as compared to directly averaging angles. We then obtain the mean branch angle ψ_n from

$$\tan(\psi_n) = \frac{\bar{y}_n}{\bar{x}_n}. \tag{4.9}$$

The average angle $\bar{\psi}_n$ is then $\bar{\psi}_n = \mathrm{atan2}(\bar{y}_n, \bar{x}_n)$, where atan2 denotes the two argument arctan. Note that atan2 returns angles in the range $[-\pi, \pi]$ and therefore has the advantage to unambiguously determine the angle. By contrast, the atan function returns angles in the range $[-\pi/2, \pi/2]$ which requires to determine the corresponding quadrant manually. Overall, this constitutes a robust measure for branch orientation. Compared to other methods (e.g. inclination of branch end-to-end vector to vertical axis) this method robustly characterizes branch orientation also for the curved branches we find in the gut (Fig. 4.1c).

Branch symmetry

Finally, we quantify the symmetry of gut morphologies (Fig. 4.1d). We determine the symmetry of a gut structure as the mismatch of branch points along the anterior part of the primary branch (Fig. 4.1d, black line). We call a gut structure symmetric if branches that grow into the left and right organism side originate at the same position on the primary branch and antisymmetric otherwise. To quantify the mismatch between branch points, we introduce the indicator functions $v_{i,m}$ for the left ($i = l$) and right ($i = r$) organism side, where $m = 1, \ldots, M_{\mathrm{pb}}$ indicates the position along the primary branch that consists of M_{pb} pixels and N_{pb} individual branches. The indicator function has $v_{l,m} = 1$

if at the respective position a branch grows into the left organism side and similarly for $v_{r,m}$. We determine the integrated indicator function

$$V_{i,m} = \sum_{\tilde{m}=1}^{m} v_{i,\tilde{m}}, \tag{4.10}$$

which has a stair-like function. For symmetric gut structures, branch points along the primary branch and thus also the stair-like integrated indicator function matches. By contrast, for antisymmetric structures, a mismatch between branch points and thus the integrated indicator function exists. We quantify the mismatch by the normalized integrated squared difference

$$\Delta V = \frac{1}{N_{\mathrm{pb}}} \sum_{m=1}^{M_{\mathrm{pb}}} (V_{l,m} - V_{r,m})^2. \tag{4.11}$$

We find the value $\Delta V = 13.71$ (averaged over $n = 11$ worms with 1 mm), which indicates that the gut operates in an intermediate regime away from being either symmetric or antisymmetric.

Gut morphology

We use the provided skeletons to quantify size and shape of planarians (Fig. 4.3a). We determine the convex hull of the gut skeleton and use it as a measure of the worm outline that we characterize by its center of mass $(x_{\mathrm{w}}, y_{\mathrm{w}})$ as well as its length L_y, width L_x, and area A_{w}. The convex hull is the smallest convex polygon that encloses all elements of a given set and can be visualized as a the configuration of a rubber band that contracts until no further contraction is possible. We extract the pharynx outline in a similar manner by employing an algorithm that expands a shape until no further expansion is possible. We characterize the pharynx outline by its center of mass $(x_{\mathrm{p}}, y_{\mathrm{p}})$ as well as its length l_y, width l_x, and area A_{p}. We further define the branched area A_{b} as the difference $A_{\mathrm{b}} = A_{\mathrm{w}} - A_{\mathrm{p}}$ between worm and pharynx area. Thereby the branched area denotes the size of region that the gut can expand into.

Our collaborators imaged gut morphologies in the range from 1 to 11 mm and provided the corresponding gut skeletons (Fig. 4.2). Next, we employ this data to study size-dependent properties of planarians and in particular the planarian gut.

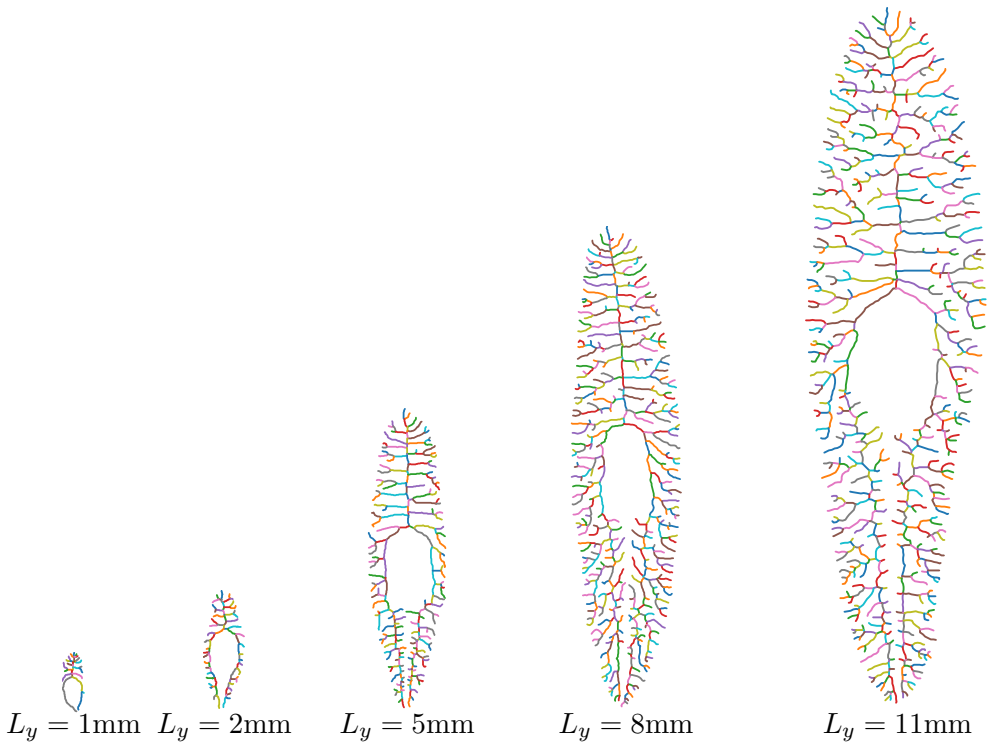

Figure 4.2: Size-dependent changes of organism and gut morphology. We illustrate size-dependent changes in organism and gut morphology based on gut skeletons for the five different body sizes quantified by our collaborators. We consider organisms with length L_y in the range 1 mm to 11 mm, thus spanning a more than 10 fold increase in organism length and a more than 100 fold increase in branched area. Segmentation and skeletonization performed by Amrutha Palavalli.

4.2 Size and shape of flatworms and their pharynx

We first quantify the shape of flatworms and their pharynx (Fig. 4.3). To this end, we determine the worm and pharynx outlines from the convex hull of worm and pharynx. We position the outlines at the center of the coordinate system by subtracting the organism center of mass $(x_\mathrm{w}, y_\mathrm{w})$ or the pharynx center of mass $(x_\mathrm{p}, y_\mathrm{p})$ from the respective outline. We further rescale the outlines with their respective width and length. We present the rescaled outlines along with an ellipse given by the equation $x^2 + y^2 = 1$ and find good agreement. This indicates that an ellipse is an approximation for worm and pharynx outline. To further support this finding, we perform a least-squares fit of the equation $x^r + y^r = 1$ of a generalized ellipse to the rescaled worm and pharynx outlines. We obtain the values $r_\mathrm{w} = 1.85 \pm 0.12$ and $r_\mathrm{p} = 1.99 \pm 0.16$ from the fit which are close to the value $r = 2$ of an ideal ellipse. We therefore adopt ellipses as a minimal approximation for worm and pharynx shape.

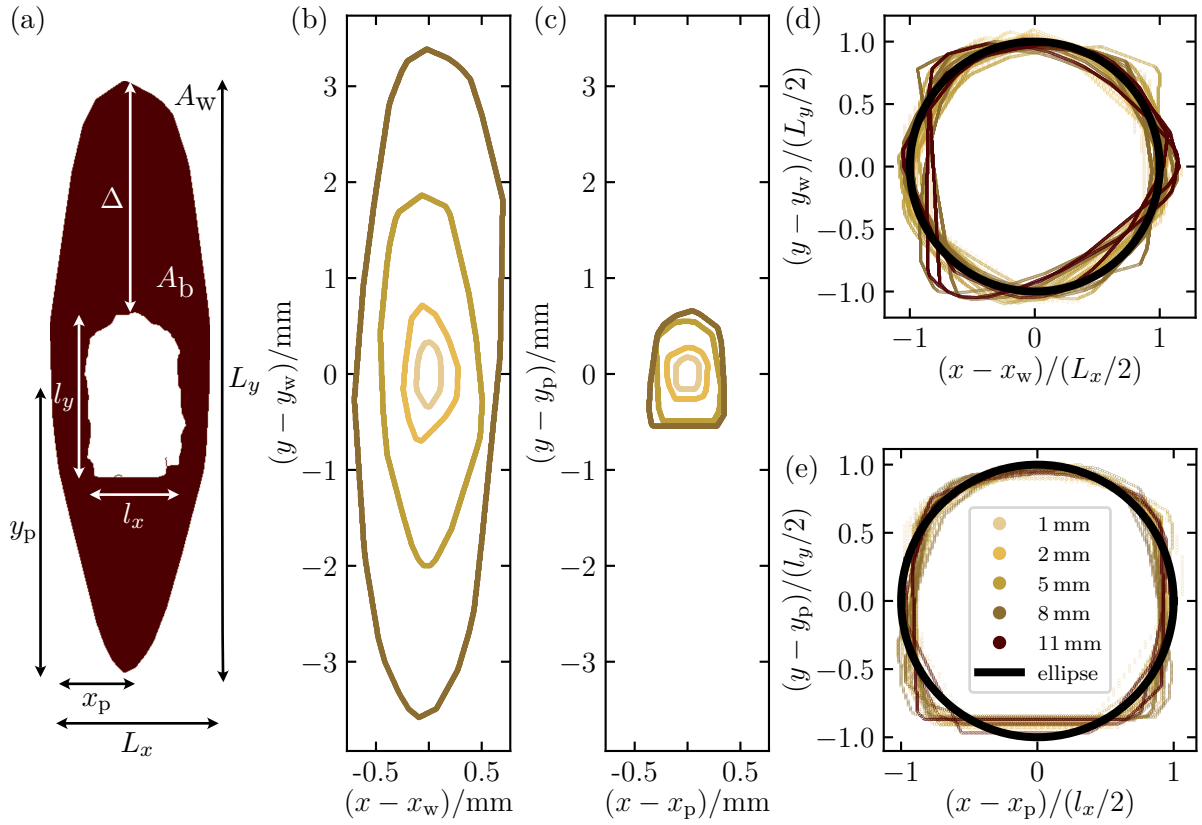

Figure 4.3: Quantification of organism size and shape. (a) We show the worm outline together with the pharynx outline. We characterize the worm outline obtained from a convex hull of gut skeletons by its length L_y, width L_x, and area A_w. Likewise, we characterize the pharynx outline by its length l_y, width l_x, and area A_p. Additionally, we quantify its center of mass (x_p, y_p) as well the distance Δ between the top of organism and pharynx. (b,c) We show the organism and pharynx outline centered at their respective center of mass (x_w, y_w) and (x_p, y_p). (d,e) We show the worm and pharynx outlines rescaled by the respective length. Additionally, we show an ellipse of the form $x^r - y^r = 1$ with $r = 2$ (black line).

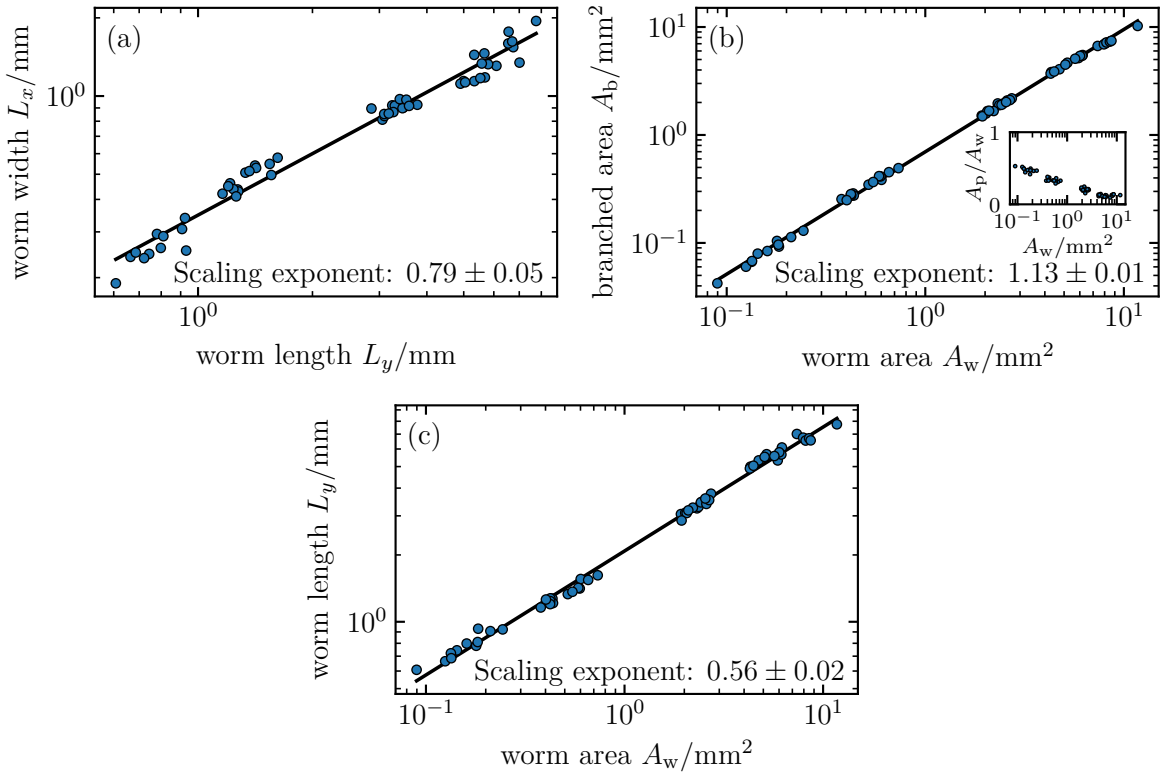

Figure 4.4: Quantification of body size and aspect ratio of planarians. We present different measures for body size and how they are related. (a) We show organism width L_x as a function of worm length L_y (dots) and a fit of the form $y = ax^b$ (line). (b) We show branched area A_b as a function of worm area A_w (dots) together with a fit of the form $y = ax^b$ (line). The inset shows the relative pharynx area $A_\mathrm{p}/A_\mathrm{w}$ as a function of worm area. (c) We show the worm length L_y as a function of worm area A_w (dots) together with a fit of the form $y = ax^b$ (line). Note that in all cases the power law fit was obtained from a linear fit to logarithmized data.

Since our aim is to study size-dependent properties of the planarian gut, we next examine different measures for worm size (Fig. 4.4). We first study the relationship between worm width L_x and worm length L_y and find a power law with scaling exponent < 1. This scaling law indicates that worm length increases faster than worm width which we can confirm visually (Fig. 4.2). Likewise, we study the relationship between organism area A_w and the branched area A_b. We find that a power law with scaling exponent > 1 relates organism area and branched area, indicating that branched area increases faster than worm area. We attribute this non-isometric scaling to the decreasing relative size of the pharynx (see next section for more details). Finally, we examine the relation between worm length L_y and area A_w. We find that a power law with scaling exponent close to 0.5 relates worm length and worm area as expected from dimensional considerations. Note that this scaling exponent is in agreement with previous studies where the power law $L_y \propto A_\mathrm{w}^{0.55}$ was reported [65]. We have therefore presented an ensemble of size quantifications. We have established scaling relations between different measures of size and can therefore convert different size measurements into each other. We choose A_b as a measure for worm size.

We can employ the scaling relation $L_x \propto L_y^{0.79}$ between worm length L_y and worm width L_x to determine the ratio g_x/g_y of organism growth rate g_x and g_y. An organism that grows with constant rate in each direction $i \in \{x, y\}$ obeys $L_i(t) = L_{i,0}e^{g_i t}$, where t denotes time and $L_{i,0}$ denotes the length at time $t = 0$. This implies the scaling relation $L_x \propto L_y^{g_x/g_y}$ between worm width and length. From a comparison with the measured scaling relation (Fig. 4.4a) we therefore find $g_x/g_y = 0.79$ for the ratio of growth rates.

We next present a quantification of size and position of the planarian pharynx (Fig 4.5). The pharynx is located along the organism midline ($x_\mathrm{p}/L_x \approx 0.5$) in the lower semihalf of the worm ($y_\mathrm{p}/L_y < 0.5$). While the distance Δ between organism tip and the top part of the pharynx is independent of organism size, the pharynx position y_p shows a slight increase for larger organism sizes. From this we conclude that the organism exhibits slight anisotropic growth, i.e. the tail region grows faster than the head region. Clearly, the relative pharynx size decreases for increasing organism size. For small organism size the pharynx spans almost the entire organism in terms of width ($l_x/L_x \to 1$) and half of the organism in terms of length ($l_y/L_y \approx 0.5$). By contrast, for a large organism the pharynx spans half of the organism in width ($l_x/L_x \approx 0.5$) and a quarter in terms of length ($l_y/L_y \approx 0.25$). This decrease of the relative pharynx size is also confirmed visually (Fig. 4.2).

We present the data obtained from the quantification of pharynx size and position together with different interpolation functions (Fig. 4.5). We show the relative position x_p/L_x and the relative distance Δ/L_y along with their average value (Fig. 4.5a,c line).

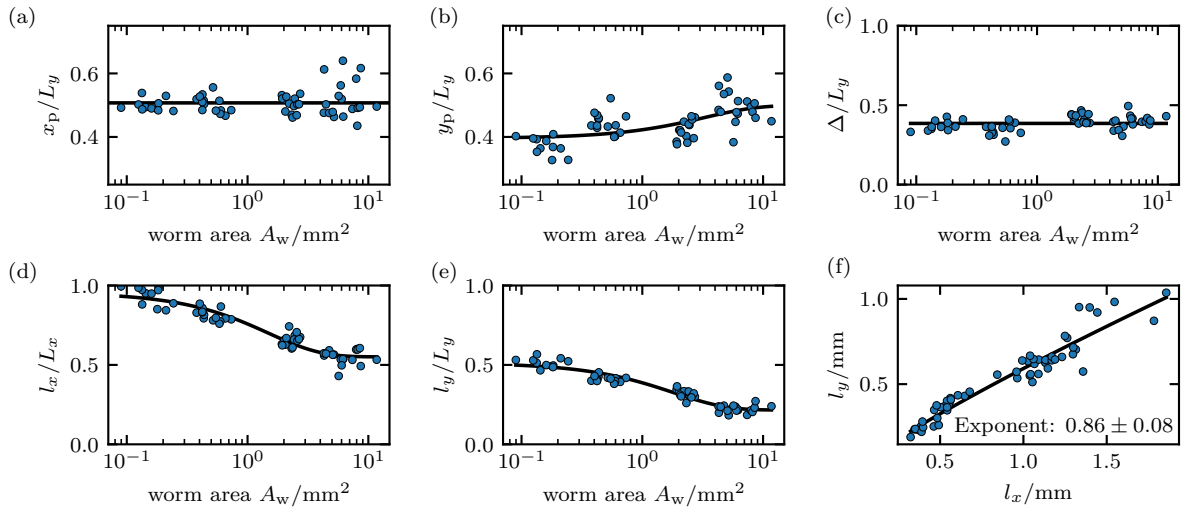

Figure 4.5: Position, size, and aspect ratio of the pharynx. (a) We show the measured horizontal component x_p of the pharynx center of mass (dots) along with its mean $\bar{x}_p/L_x = 0.51 \pm 0.04$ (line). (b) We display the relative vertical position y_p/L_y of pharynx center of mass (dots) along with with a fit to Eq. (4.12) (line). (c) We show the difference Δ from the organism tip to the top part of the pharynx along with its mean value $\bar{\Delta}/L_y = 0.39 \pm 0.04$ (line). (d,e) We show the relative pharynx width l_x/L_x and length l_y/L_y (dots) along with a fit to Eq. (4.12) (line). (f) We display the pharynx length l_y as a function of pharynx width l_x (dots) along with a fit of the form $y = ax^b$ (line). We performed a linear fit to the logarithmized data.

We show the relative position y_p/L_y as well as the pharynx size l_x/L_x and l_y/L_y together with the interpolation function

$$f(x) = ae^{-x/b} + c, \tag{4.12}$$

where a,b, and c are fit parameters determined for each of the aforementioned quantities (Fig. 4.5). We will use these interpolation function later in our model to correctly position and size the model pharynx.

4.3 Size-dependent properties and scaling laws of the planarian gut

We identify four complementary scaling relationships that characterize the size-dependent properties of the planarian gut. We first analyze the total length of the gut and find the

key scaling relationship

$$L_{\mathrm{gut}} \propto A_{\mathrm{b}}^{\eta} \tag{4.13}$$

with scaling exponent $\eta = 0.75 \pm 0.01$. Thereby the massive increase of total gut length over two orders of magnitude of organism size is well described by a power law with a single scaling exponent. Interestingly, the scaling exponent η is different from 1/2 and thereby does not follow from simple dimensional considerations.

The non-isometric scaling of the total gut length is related to the non-isometric scaling of branch distance. To see this, we note that the scaling relationship Eq. (4.13) relates the total gut length with an area and thereby implicitly defines a length. This implicitly defined length provides a measure for the distance of branches and we can infer from Eq. (4.13) that it scales with branched area with scaling exponent 0.25. To confirm this observation, we independently quantified the distance d of side branches. We find that $d \propto A_{\mathrm{b}}^{\alpha_y}$ with $\alpha_y = 0.24 \pm 0.04$ confirming our prediction. Thus, branch distance increases with organism length in a non-isometric manner.

To investigate whether the increase in total gut length originates from an increase in branch length ℓ or the number of branches we further analyzed the size dependency of N and ℓ. We obtain that mean branch length obeys $\ell \propto A_{\mathrm{b}}^{\alpha_x}$ with $\alpha_x = 0.19 \pm 0.08$ and that the number of branches obeys $N \propto A_{\mathrm{b}}^{\zeta}$ with $\zeta = 0.59 \pm 0.05$. Thus, the massive increase in the total gut length stems from both an increase in the number of branches as well as an increase of mean branch length. We obtain the reported scaling exponents from a least-squares fit of a linear function to the logarithmic data. Moreover, to determine the scaling exponents of N and ℓ, we excluded points with $A_{\mathrm{b}} < 2 \cdot 10^4\,\mathrm{mm}^2$ corresponding to the 1 mm cohort. We exclude the 1 mm cohort since for small organism sizes mean branch length is heavily biased by the length of branches belonging to the primary branch. We also show the mean branch length where branches belonging to the primary branch are excluded and find a better agreement.

Besides the scaling of branch length, branch distance, and the number of branches, we also characterize branch orientation (Fig. 4.7). Given the vertical orientation of the elements of the primary branch, we focused our analysis on side branches. We use the mean branch angle ψ_n introduced in Eq. (4.9) and study the probability distribution $p[\cos^2(\psi_n)]$ of the orientational order parameter $\cos^2(\psi_n)$ of side branches. The orientational order parameter respects the organismal symmetry and allows us to detect horizontal ($\cos^2(\psi_n) = 0$), vertical ($\cos^2(\psi_n) = 1$), and diagonal ($\cos^2(\psi_n) = 1/2$) branches in a simplified manner. We find that independent of organism size the distribution of the orientational order parameter shows a strong peak at $\cos^2(\psi) = 0$ indicating the mostly

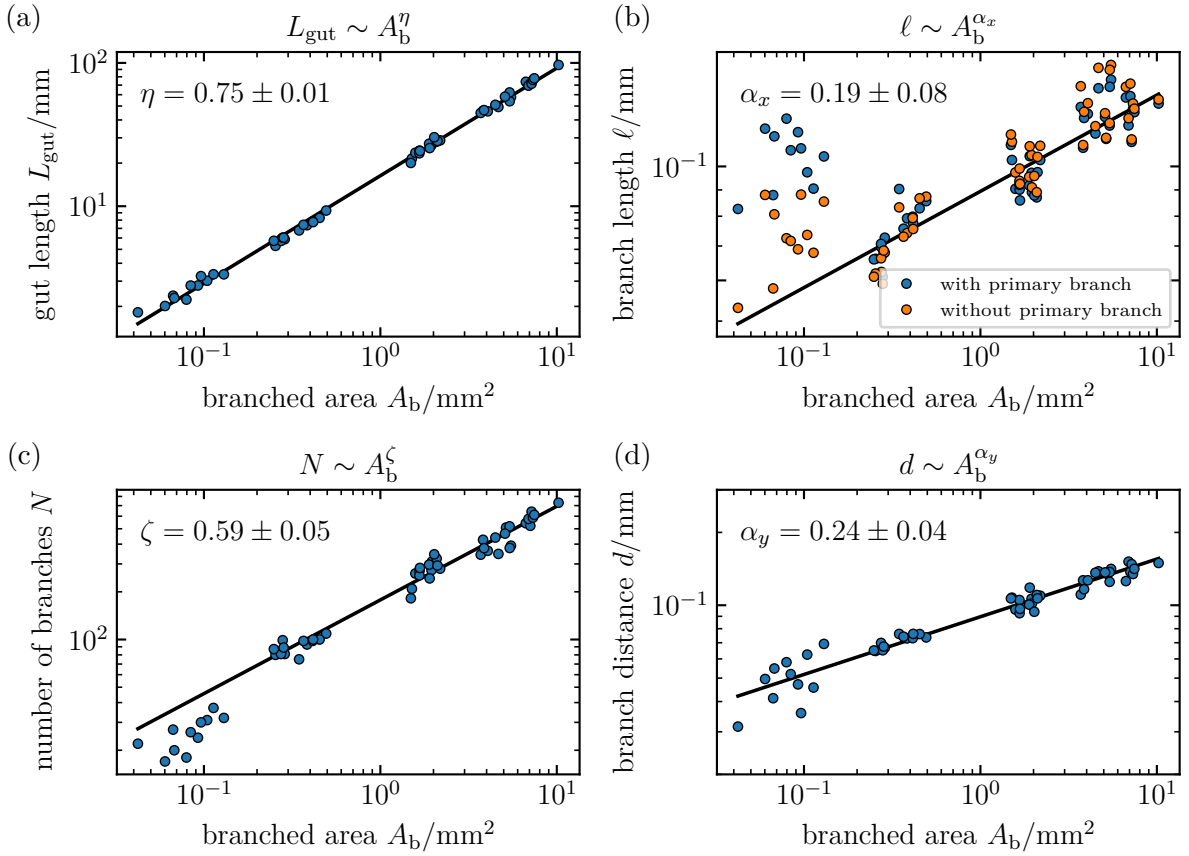

Figure 4.6: Scaling of the planarian gut. (a) We show the total gut length L_{gut} as a function of the branched area A_{b} (dots) along with a fit of the form $L_{\mathrm{gut}} = L_{\mathrm{gut}}^0 A_{\mathrm{b}}^{\eta}$ (line). (b) We display the mean branch length ℓ (blue dots) as a function of branched area A_{b} along with a fit of the form $\ell = \ell_0 A_{\mathrm{b}}^{\alpha_x}$ (line) for values $A_{\mathrm{b}} > 0.2\,\mathrm{mm}^2$. To illustrate how the primary branch biases ℓ towards larger values for small organism sizes, we additionally display the mean branch length without the primary branch (orange dots). (c) We show the total number of branches N as a function of the branched area A_{b} (dots) along with a fit of the form $N = N_0 A_{\mathrm{b}}^{\eta}$. As for ℓ, the fit was obtained for the range $A_{\mathrm{b}} > 0.2\,\mathrm{mm}^2$. (d) We show branch distance d as a function of branched area A_{b} (dots) along with the fit $d = d_0 A_{\mathrm{b}}^{\alpha_y}$ (line). In each case, the a linear fit to logarithmized data was performed.

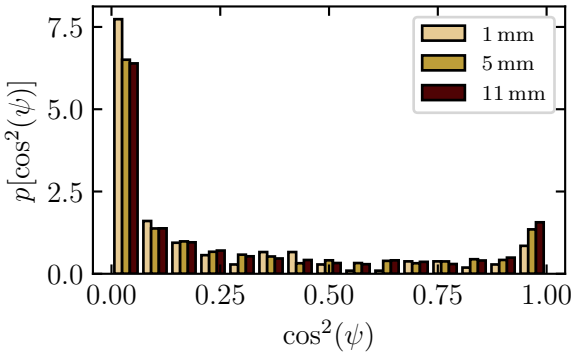

Figure 4.7: Quantification of branch orientation. We show the probability distribution $p[\cos^2(\psi)]$ of the orientational order parameter $\cos^2(\psi)$ of branch orientation ψ for differently sized animals (color). The displayed distribution corresponds to side branches from $n = 11$ (1 mm), $n = 14$ (5 mm), $n = 6$ (11 mm) animals.

horizontal orientation of side branches. Since branches originate from other branches with a non-zero angle and branches are oriented towards the curved organismal boundary in the head and tail region of the organism, branch orientation shows in general large variation. As a consequence, we find that apart from the peak at $\cos^2(\psi) = 0$ the orientational order parameter has a mostly uniform distribution away from $\cos^2(\psi) = 0$.

4.4 Summary and discussion

In this chapter, we have introduced the planarian gut as an example of a highly branched organ. We have quantified the geometrical and size-dependent properties of gut morphologies as well as the size and shape of planarians and their pharynx. The findings presented here form the basis of chapter 5, where we theoretically study gut branching morphogenesis.

We first introduced the experimental data provided by our collaborators and its quantification. They performed *in-situ* hybridization of in total $n = 57$ planarians in the size range from 1 to 11 mm. Next, they binarized the raw data and determined a skeleton on basis of the binarization. The skeleton is a one-pixel wide connectivity-preserving representation of the binarized data and serves as the basis of our quantitative analysis. We identify individual branches in the skeleton and quantify their mean length ℓ, distance d, thickness b, and angle ψ as well as the total number of branches N and the total gut length L_{gut}. Additionally, we use the mismatch of branch points along the primary branch as a measure for the symmetry of gut morphologies. Even though the provided data fails to

robustly label the gut outline, we explain the quantification of branch thickness b, which we will apply to our simulated gut structures. On the basis of gut skeletons, we further quantified worm and pharynx shape. In each case, we use a convex hull to extract the respective outline. We use the convex hull area as a measure for worm area A_{w} and pharynx area A_{p}, respectively. We use the major and minor axis length as a measure for organism length L_y and width L_y as well as pharynx length l_y and width l_x. The center of mass provides a measure for the horizontal x_{p} and vertical pharynx position y_{p}.

We then used our analysis to discuss various aspects regarding the size and shape of worm and pharynx outline. Interestingly, we find that worm length and width are related by the scaling relation $L_x \propto L_y^{0.79}$ indicating that the aspect ratio of the organism is size-dependent. In particular, the organism length increases more rapidly than organism width with a growth rate ratio of $g_x/g_y = 0.79$. We find that worm and pharynx shape are approximately described by an ellipse. In particular, we find that the pharynx is located along the organism midline ($x_{\mathrm{p}}/L_x \approx 1/2$) and shifts its relative position y_{p}/L_y in anterior direction for larger organism sizes while its relative size $A_{\mathrm{p}}/A_{\mathrm{w}}$ decreases. The aspect ratio of pharynx shows also shows a size-dependent behavior with a similar trend as the organism aspect ratio.

Finally, we used our analysis to study geometrical and in particular size-dependent properties of the planarian gut. We find that side branches are aligned towards the organismal boundary and that the gut exhibits neither a symmetric nor antisymmetric, but an intermediate configuration. Interestingly, key characteristics of the gut show power law scaling as a function of body size with scaling exponents that lack a simple geometrical interpretation. The scaling laws reveal that the total gut length displays a tremendous increase with organism size which stems from both an increase in mean branch length and the total branch number.

Let us also discuss shortcomings and limitations of our analysis. We have focused on analyzing 2D projections of 3D gut images and thus neglected features of the 3D architecture of the gut. For example, with increasing organism size branches occasionally grow above each other (Jochen Rink, personal communication). It might also be interesting to analyze 3D properties such as total gut surface area and total gut volume. The gut is the planarian organ responsible for delivery of nutrients to cells and it might be thus related to Kleiber's law scaling of metabolic rate in planarians [65].

Overall, we developed a set of versatile tools to analyze various aspects of the planarian body and gut. We apply our analysis tools in the next chapter to gut morphologies obtained from a gut branching model and thus they allow us to compare scaling laws from model and experiment. Moreover, our detailed analysis of worm and pharynx outline

informs the choice of boundary conditions in our gut branching model.

Chapter 5

Morphogen-controlled growth and scaling of the planarian gut

In this chapter, we present a model for morphogen-controlled growth and scaling of the planarian gut. In this model, we reconsider our continuum model presented in chapter 3 and combine it with novel ideas and concepts to understand planarian gut morphogenesis. At the center of our model is again the growth of an interface subject to the concentration of a morphogen. As opposed to previous chapters, we now account for details of the organism shape and study the formation of branched structures emerging from a primary branch in an elliptic, worm-like geometry. Moreover, inspired by the orientation of branches in the planarian gut, we take into account external guiding cues that align branches to predefined axes in addition to the purely morphogen-controlled gut growth. Finally, to account for the massive body size fluctuations of planarians, we include organism growth in our description allowing us to study size-dependent properties of branching morphologies.

To systematically understand the formation of branched patterns in this model, we proceed in three steps. After defining the model, we first consider a system without organism growth and discuss key determinants for the formation of branched structures in this scenario. We demonstrate the alignment of branches with different external guiding cues and discuss how morphogen-mediated interaction between branches in the left and right organism half determine the symmetry of branching morphologies. By using findings from chapter 3, we demonstrate the control of branch distance and thickness of gut branching morphologies. As a second step, we present two scenarios for generating gut morphologies for different organism sizes. In a first approach (branching model), we study the *de-novo* formation of morphologies in a systems of different sizes. In a second approach (branching model with organism growth), we study the continuous remodeling of a morphology subject to organism growth. In both cases, we analyze the size-dependent

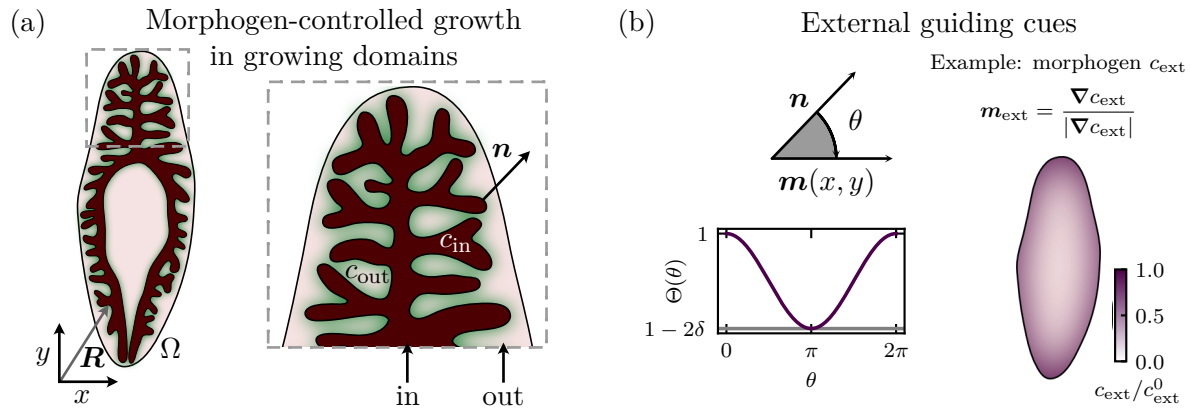

Figure 5.1: Model for morphogen-controlled growth and scaling of the planarian gut. (a) We represent the gut outline by an infinitely thin interface $\boldsymbol{R}$ with normal vector $\boldsymbol{n}$. This interface separates the growing domain Ω into a region inside ("in") and outside the gut ("out"). We consider morphogen-controlled growth of the interface $\boldsymbol{R}$, where c_i denotes the morphogen concentration in the region $i \in \{\text{in}, \text{out}\}$. (b) We take into account the effect of external guiding cues on interface growth by an external orientation field $\boldsymbol{m}$. As an example, we show the orientation field $\boldsymbol{m}_{\text{ext}}$ derived from the concentration c_{ext} of a second morphogen with constant concentration c^0_{ext} at the organism boundary.

properties of resulting morphologies and find power law scaling of various gut features as a function of organism size. In a third step, we rationalize the observed scaling relations by simple scaling arguments. Throughout this chapter, we compare the value of quantities from simulations and experiments to provide a parameter regime which yields realistic gut morphologies in the model.

5.1 Morphogen-controlled interface growth in growing domains

We now present a minimal model to study morphogen-controlled branching morphogenesis and growth of the planarian gut (Fig. 5.1). In our minimal approach, we represent the gut outline by an infinitely thin interface $\boldsymbol{R}$ and study the dynamics of $\boldsymbol{R}$ in a 2D domain Ω. The gut outline separates the domain Ω into a region inside and outside of the gut, where the respective region is labeled by the index $i \in \{\text{in}, \text{out}\}$.

The motion of $\boldsymbol{R}$ and therefore gut growth takes place in normal direction $\boldsymbol{n}$ with

velocity v_n according to

$$\partial_t \boldsymbol{R} = v_n \boldsymbol{n} \tag{5.1a}$$

$$v_n = \chi(c, \boldsymbol{m}) - \beta\kappa + \boldsymbol{u} \cdot \boldsymbol{n} + a\Xi. \tag{5.1b}$$

The normal velocity v_n captures key contributions to interface growth in a coarse-grained way and is therefore at the center of our model. We assume that growth depends on interface curvature κ, where according to our convention κ is positive for outward protrusions (concave shapes) and negative for inward protrusions (convex shapes). Due to the curvature dependency of interface growth, outward protrusions experience a negative and inward protrusions a positive velocity. As a result, the interface has a tendency to grow to a flat configuration and is effectively stabilized, where the parameter β determines the strength of the curvature dependency and thus the strength of the stabilization. The advection term $\boldsymbol{u}\cdot\boldsymbol{n}$ takes into account that the interface is carried along with the organism as the organism grows, where $\boldsymbol{u}$ denotes the velocity field corresponding to organism growth. A hypothetical gut structure of circular shape subject to only the advection term deforms to an ellipse with a total area larger than before (assuming anisotropic organism growth $g_x \neq g_y$). Additionally, we assume that the interface is subject to uniform distributed noise $\Xi \in [-1/2, 1/2]$ with noise amplitude a. Finally, the term χ represents the influence of different signals on gut growth. We assume that a morphogen with concentration c is present in the organism that controls interface growth and thus χ depends on morphogen concentration. Additionally, we assume that gut growth is guided by external cues such as planar cell polarity or a second morphogen originating at the organism boundary. We represent external guiding cues in a coarse grained way with an external orientation field $\boldsymbol{m}$ that guides interface growth. The term χ lies at the heart of our model and we will explain its precise form now in more detail.

The term χ depends on both the morphogen concentration c and on the external orientation field $\boldsymbol{m}$. We assume that these dependencies can be separated into the form

$$\chi(c, \boldsymbol{m}) = \Gamma(c)\Theta(\boldsymbol{m}), \tag{5.2}$$

where Γ takes into account the dependency on the morphogen concentration c and Θ takes into account the direction dependency of growth. A further motivation to employ this separation ansatz comes from studies of solidification, where this approach is used to include anisotropy arising from molecular structure [183]. In chapter 3, we identified the

function

$$\Gamma(c) = v_0 - \gamma c(\boldsymbol{R}) \tag{5.3}$$

as a minimal example that yields self-organized branched structures and therefore employ it here again. The parameter v_0 denotes a basic growth tendency that is inhibited with strength γ by the presence of morphogen at the interface. We assume for the direction dependency Θ of growth

$$\Theta(\boldsymbol{m}) = 1 - 2\delta \sin^2(\theta/2) \tag{5.4a}$$

$$\theta = \sphericalangle(\boldsymbol{n}, \boldsymbol{m}), \tag{5.4b}$$

where δ denotes the coupling strength between interface growth and external orientation field and lies in the range $\delta \in [0, 1/2]$ to ensure $\chi > 0$ (Fig. 5.1b). θ denotes the angle between the interface normal vector $\boldsymbol{n}$ and the external orientation field $\boldsymbol{m}$ and is crucial to understand the influence of $\boldsymbol{m}$ on interface growth. For growth directions $\boldsymbol{n}$ parallel to $\boldsymbol{m}$ ($\sin^2(0) = 0$), the morphogen-controlled growth term $\chi(c, \boldsymbol{m}) = \Gamma(c)$ reduces to only its morphogen dependency. However, for growth directions $\boldsymbol{n}$ orthogonal to $\boldsymbol{m}$ ($\sin^2(\pi/2) = 1$), the morphogen-controlled growth term gives $\chi(c, \boldsymbol{m}) = \Gamma(c)(1 - 2\delta)$, i.e. growth is suppressed by a factor of $1 - 2\delta$ in the direction orthogonal to $\boldsymbol{m}$. As a result, we have a preferred growth in the direction of orientation vector $\boldsymbol{m}$ while growth orthogonal to $\boldsymbol{m}$ is suppressed.

We study morphogen-controlled growth of the planarian gut and therefore the morphogen concentration c_i is another important ingredient in our model. The dynamics of the morphogen concentration c_i in each region i is determined by the advection-diffusion equation

$$\partial_t c_i + \boldsymbol{u} \cdot \boldsymbol{\nabla} c_i = D\nabla^2 c_i - (k_i + g_x + g_y)c_i + s_i. \tag{5.5}$$

We take into account the diffusive motion of morphogen with effective diffusion constant D as well as effective degradation with rate k_i and a production with rate s_i. Moreover, due to organism growth, morphogen concentrations c_i are subject to dilution with rate $g_x + g_y$ and advection with velocity $\boldsymbol{u}$. At the interface $\boldsymbol{R}$, we enforce the boundary conditions

$$c_{\text{in}}(\boldsymbol{R}) = c_{\text{out}}(\boldsymbol{R}) \tag{5.6a}$$

$$\boldsymbol{n} \cdot \boldsymbol{\nabla} c_{\text{in}}(\boldsymbol{R}) = \boldsymbol{n} \cdot \boldsymbol{\nabla} c_{\text{out}}(\boldsymbol{R}), \tag{5.6b}$$

where we have used the interface normal vector $\boldsymbol{n}$. Therefore, we require that the con-

centrations and the normal components of the concentration gradients at the interface position $\boldsymbol{R}$ match.

Since the morphogenesis of the planarian gut takes place in a growing organism, we study the dynamics of $\boldsymbol{R}$ in a growing domain Ω. Every point $\boldsymbol{x} \in \Omega$ undergoes the dynamics

$$\partial_t \boldsymbol{x} = \boldsymbol{u} \tag{5.7a}$$

$$\boldsymbol{u} = g_x x \boldsymbol{e}_x + g_y y \boldsymbol{e}_y, \tag{5.7b}$$

where $\boldsymbol{u}$ is a velocity field and g_x and g_y denote the organism growth rates in the respective direction. Throughout this chapter, we assume constant growth rates g_i leading to an exponential increase of the dimensions of Ω. This allows us to study the scaling of observed structures over a wide range of sizes. Note that we consider periodic growth rates in the last section of this chapter, when we study the robustness of observed structures with respect to periodic growth and degrowth.

We consider two options for the orientation field $\boldsymbol{m}$. First, we consider an orientation field of the form

$$\boldsymbol{m}_y = \boldsymbol{e}_y \theta(x - L_x/2) - \boldsymbol{e}_y \theta(L_x/2 - x) \tag{5.8}$$

and thus enforce growth along mediolateral axis of the organism. In a different approach, we employ an "external" morphogen that has a source on the organism boundary and forms gradients to the organism center to guide gut growth. We refer to this morphogen as external, since it is produced at the organism boundary and not in the gut. For this case, we define the orientation field

$$\boldsymbol{m}_{\text{ext}} = \frac{\boldsymbol{\nabla} c_{\text{ext}}}{|\boldsymbol{\nabla} c_{\text{ext}}|}, \tag{5.9}$$

as the normalized gradient of c_{ext}, which enforces growth in direction of steepest increase of external morphogen concentration.

For all $\boldsymbol{x} \in \Omega$ the external (or second) morphogen concentration c_{ext} is subject to the advection-diffusion equation

$$\partial_t c_{\text{ext}} + \boldsymbol{u} \cdot \boldsymbol{\nabla} c_{\text{ext}} = D^x_{\text{ext}} \partial_x^2 c_{\text{ext}} + D^y_{\text{ext}} \partial_y^2 c_{\text{ext}} - (k_{\text{ext}} + g_x + g_y) c_{\text{ext}}, \tag{5.10}$$

together with the boundary condition $u|_{\partial\Omega} = \text{const}$. In Eq. (5.10), D^x_{ext} and D^y_{ext} denote effective diffusion constants and k_{ext} denotes the effective degradation constant of the external morphogen. The diffusion-degradation length $\lambda^x_{\text{ext}} = \sqrt{D^x_{\text{ext}}/k_{\text{ext}}}$ and $\lambda^y_{\text{ext}} =$

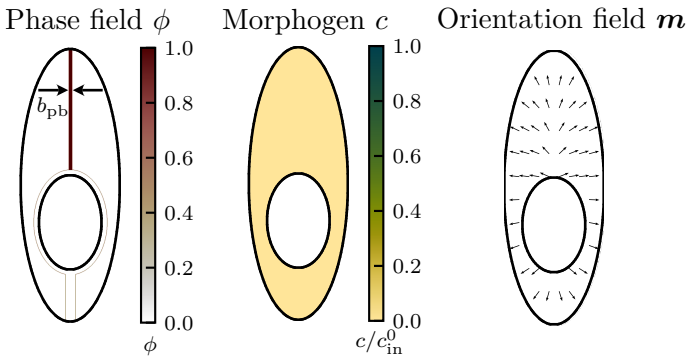

Figure 5.2: Numerical solution of the model for morphogen-controlled growth and scaling of the planarian gut. We use the phase field method presented in chapter 3 to study the interface dynamics numerically. For the phase field ϕ we impose a primary branch consisting of a straight line in the head region, an elliptic part around the pharynx, and two parallel straight lines as a boundary condition. The straight line in the head region has thickness b_{pb}, while the remaining parts are infinitely thin corresponding to the width of one pixel in the discretization. Details of boundary conditions are provided in appendix A.

$\sqrt{D^y_{\mathrm{ext}}/k_{\mathrm{ext}}}$ provide a characteristic length scale for the gradient generated by the external morphogen along the x and y direction, respectively. Note that by adapting the diffusion-degradation length scales λ^x_{ext} and λ^y_{ext} we can align growth of branches predominantly in x- ($\lambda^x_{\mathrm{ext}} \ll \lambda^y_{\mathrm{ext}}$) or y-direction ($\lambda^y_{\mathrm{ext}} \ll \lambda^x_{\mathrm{ext}}$) of the organism.

The morphogen dynamics defined by Eq. (5.10) describes the general scenario of a morphogen forming gradients towards the organism center and provides rich possibilities to direct the growth of branches. For simplicity, we consider a special case of this dynamics in the rest of this chapter. Instead of solving the time-dependent dynamics of Eq. (5.10), we consider the quasistatic limit and find the solution of $\partial_t c_{\mathrm{ext}} = 0$. Motivated by the orientation of planarian gut branches, we consider the case of branch alignment in horizontal direction ($\lambda^x_{\mathrm{ext}} \ll \lambda^y_{\mathrm{ext}}$). To ensure that this choice is maintained throughout organism growth, we consider the case $\lambda^x_{\mathrm{ext}} \propto L_x$ and $\lambda^y_{\mathrm{ext}} \propto L_y$.

We employ the phase field method to numerically study the interface dynamics of our model (Fig. 5.2). We refer the reader to section 3.3 of chapter 3 for a brief introduction to the phase field method and present the phase field model corresponding to Eqs. (5.1) in appendix B. The shape of the boundary employed in the phase field model is motivated by our analysis of organism shape. We determine the solution of phase field ϕ and morphogen concentration c in the domain $\Omega = \Omega_{\mathrm{w}} \setminus \Omega_{\mathrm{p}}$, which corresponds to an organism described by an ellipse Ω_{w} with an empty region Ω_{p} for the pharynx. The regions Ω_{w} and Ω_{p} are

defined by

$$\Omega_{\mathrm{w}} = \{(x,y)| \left|\frac{x-x_0}{L_x/2}\right|^2 + \left|\frac{y-y_0}{L_y/2}\right|^2 \leq 1\} \tag{5.11a}$$

$$\Omega_{\mathrm{p}} = \{(x,y) \left|\frac{x-x_{\mathrm{p},0}}{\ell_x/2}\right|^2 + \left|\frac{y-y_{\mathrm{p},0}}{\ell_y/2}\right|^2 \leq 1\}, \tag{5.11b}$$

where L_x and L_y denote organism width and length and l_x and l_y denote pharynx width and length. We use (x_0, y_0) and $(x_{\mathrm{p},0}, y_{\mathrm{p},0})$ to denote the position of the respective ellipse. We study the dynamics of the external morphogen in the domain Ω_{w}. To study the system dynamics numerically, we transform the phase field equations from a growing to a non-growing reference frame. In this reference frame, we enforce no-flux boundary conditions for both phase field and morphogen concentration on $\partial\Omega$ and additionally implement the primary branch as a boundary condition for the phase field ϕ with $\phi = 1$ (details see appendix A). In all our simulations, we use $\phi(x,y) = 0$, $c_i(x,y) = 0$, and $c_{\mathrm{ext}}(x,y) = 0$ as initial condition. We provide details on the numerical solution of the resulting phase field equations in appendix A.

5.2 Determinants of gut geometry in the model gut

To understand the formation of branched structures in our model, we first study the model dynamics in a non-growing domain. In particular, we consider a worm-like domain Ω reminiscent of a 1 mm worm and systematically study and compare the geometrical features of simulated and experimental gut structures.

5.2.1 Alignment of branching in the presence of guiding cues

The alignment of branches with an external orientation field $\boldsymbol{m}$ constitutes a key feature of our model. We here study the formation of simulated gut structures with respect to the orientation field $\boldsymbol{m}_{\mathrm{y}}$ and $\boldsymbol{m}_{\mathrm{ext}}$. We provide qualitative arguments for why $\boldsymbol{m}_{\mathrm{ext}}$ constitutes a more realistic orientation field for branch alignment and then quantitatively compare branch orientation in simulated and experimental structures. Note that in this section we include a non-zero noise amplitude a to obtain branch orientation statistics. By contrast, the data presented in the remaining sections were obtained without noise.

We first qualitatively study the formation of gut structures subject to the orientation field $\boldsymbol{m}_{\mathrm{y}}$ (Fig. 5.3a). The orientation field $\boldsymbol{m}_{\mathrm{y}}$ provides a simple scenario for guiding gut growth and many features of the resulting patterns can be discussed here already. In

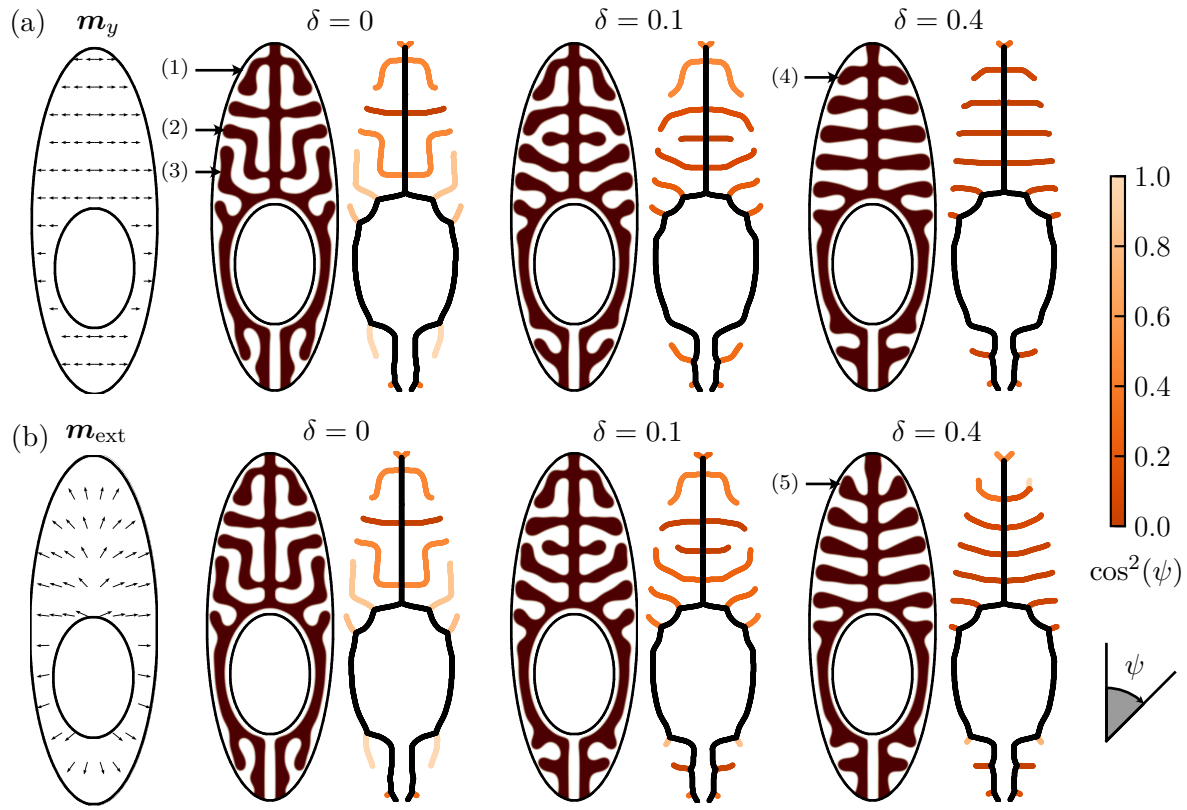

Figure 5.3: Alignment of branches with guiding cues. We show gut morphologies obtained with orientation field $\boldsymbol{m}_{\text{y}}$ (a, orientation in horizontal direction) and $\boldsymbol{m}_{\text{ext}}$ (b, orientation towards organism boundary). For both cases, we show the resulting gut morphologies (brown) along with their skeleton for increasing values of the orientation strength δ. In the skeletons, we indicate the primary branch (black) and side branches (orange). For side branches the color code indicates the value of $\cos^2(\psi)$, where ψ denotes the average branch angle measured with respect the y-axis.

particular, this scenario allows us to qualitatively discuss the transition from an irregular to a more regular gut morphology depending on the value of coupling δ between gut growth and orientation field. We first consider the case without a coupling between gut growth and orientation field ($\delta = 0$) as a reference case. Here, we observe an irregular overall gut morphology. For example, the branches labeled (1) and (3) start with a right angle with respect to the primary branch, but then undergo a sharp turn and grow along the organism boundary. Even more strikingly, branch (2) undergoes two turns at a right angle. This behavior can be understood by knowing the time evolution of the interface. Branch (3) starts growing prior to branch (2) and blocks its motion. Thus, branch (2) is forced to make a sharp turn. Upon increasing the value of the coupling δ, the gut morphology becomes more regular. Already for small coupling values ($\delta = 0.1$), turns with a right

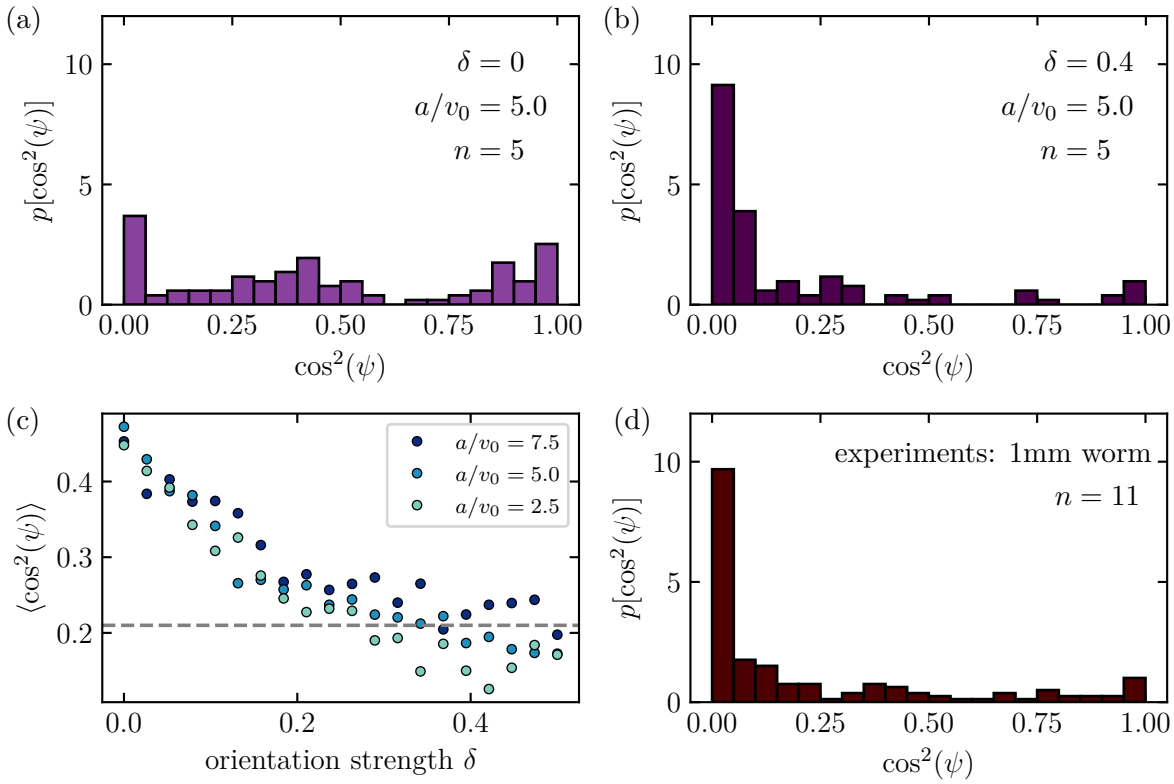

Figure 5.4: Statistics of orientational order parameter. (a,b) We show the probability distribution of the orientational order parameter $\cos^2(\psi)$ for zero (a) and non-zero (b) coupling strength δ. (c) Average orientational order parameter $\langle\cos^2(\psi)\rangle$ as a function of coupling strength δ for different noise amplitudes a. We additionally show the experimentally measured average orientation parameter for worms of length 1 mm (gray dashed line). (d) Probability distribution of the orientational order parameter obtained from worms of length 1 mm.

angle are lacking and for $\delta = 0.4$ almost all branches are parallel to each other and grow in horizontal direction. The transition from irregular to regular gut morphology is supported by the value of the orientational order parameter (color code of branches).

We also studied gut growth guided by the orientation field $\boldsymbol{m}_{\text{ext}}$ and found a qualitatively similar behavior (Fig. 5.3b). Without coupling between gut growth and orientation field ($\delta = 0$), we find irregular gut morphologies with branches that grow along the organism boundary and take sharp turns. For increasing values of coupling, the gut morphology becomes more regular and for large values of coupling ($\delta = 0.4$) branches are parallel to each other. Again, this transition is supported by the values of the orientational order parameter (color code of edges). Note that we found one key difference between the morphologies formed by $\boldsymbol{m}_{\text{y}}$ and $\boldsymbol{m}_{\text{ext}}$. While morphologies formed by $\boldsymbol{m}_{\text{y}}$ grow in horizontal

direction, morphologies formed by $\boldsymbol{m}_{\text{ext}}$ point towards the organism boundary. A striking example of this are branches marked (4) and (5). Branch (4) grows under the influence of $\boldsymbol{m}_{\text{y}}$ initially in horizontal direction, but once it reaches the boundary it grows along the boundary. By contrast, branch (5) grows towards the boundary. Since no evidence exists for growth of branches along the organism boundary and growth appears to be oriented towards the organism boundary in the experimental data, we consider gut growth guided by $\boldsymbol{m}_{\text{ext}}$ from now on only.

The transition from an irregular to a regular gut morphology is also reflected by the value of the orientational order parameter $\cos^2(\psi)$. We quantified the average angle ψ of individual branches and calculated the orientational order parameter $\cos^2(\psi)$ (Fig. 5.3, color code). From this, we determine the $\cos^2(\psi)$ distribution, which allows us to characterize gut morphologies in detail. In the case without coupling between gut growth and orientation field ($\delta = 0$), the value of the orientational order parameter is broadly distributed in the range $[0, 1]$ with three mildly pronounced peaks at $0, 1/2, 1$ (Fig. 5.4a). This indicates that branches are oriented in vertical, horizontal, or a direction that is a multiple of 45°. By contrast, for the case of large coupling, we find that orientational order parameter values are mostly localized around $\cos^2(\psi) = 1$ showing that most branches are oriented horizontally (Fig. 5.4b). This is further supported by our finding that the average orientational order parameter $\langle\cos^2(\psi)\rangle$ shows a monotonic decrease from $\langle\cos^2(\psi)\rangle \simeq 0.5$ to $\langle\cos^2(\psi)\rangle \simeq 0.2$ (Fig. 5.4c). Additionally, we find that this result is independent of the chosen noise level demonstrating that this transition is a robust feature of our model.

Finally, we employed our quantification of the average orientational order parameter to determine a range of coupling parameter δ that yields gut morphologies with branch orientations statistics similar to the ones from experimental gut morphologies. To this end, we indicate the experimentally determined average orientational order parameter in Fig. 5.4c (gray horizontal line). We find that irrespective of the noise level the parameter range $\delta \in [0.3, 0.5]$ gives reasonable agreement between average orientation parameter from simulation and experiment. Additionally, we find that the histogram of $\cos^2(\psi)$ agrees well both in terms of absolute numbers and shape (Fig. 5.4d). Thus, our model is able to give key features of gut morphologies. From now on, we consider the parameter $\delta = 0.4$ only.

5.2.2 Symmetry of gut branching morphologies

The symmetry of simulated gut branching morphologies with respect to the vertical organismal midline is another important feature of simulated gut structures. In particular, we observe that branches in the left and the right organism half arrange in an antisymmetric

way to each other. A branch in the right half corresponds to a gap between branches in the left half and vice versa. Here, we now discuss the origin of this transition from symmetric to antisymmetric branch arrangement and demonstrate the control of branch arrangement symmetry.

We first qualitatively study how an antisymmetric branch arrangement arises during the formation of gut structures. We consider a system with a thin primary branch and additionally make sure that primary branch and the pharynx are centered at $x = L_x/2$. The correct positioning of primary branch and pharynx are important to make sure that no asymmetries enter the system via the boundary conditions. As the system gets unstable, small protrusions and eventually branches originate from the primary branch. At this stage, the symmetry along the vertical midline is still maintained. However, after the system enters a space filling configuration and a sufficiently long time has passed, the system transitions from a symmetric to an antisymmetric branch arrangement involving extensive branch rearrangements.

This transition originates from morphogen-mediated interactions between branches in the left and right organism sides. First, the transition is initiated by the spontaneous up- or downwards motion by one of the side branches due to noise (noise is part of the model or originates from numerical inaccuracies). To illustrate how the transition takes place, we now focus on the spontaneous upwards motion of a branch in the right body half. The spontaneous upwards motion of a side branch has two effects. First, the side branch is now misaligned with its corresponding branch on the left organism side. As a result, morphogen produced from a branch in the left organism half spreads in the right organism half and prevents the side branch from moving to its original position. Second, due to the spontaneous upwards motion of a side branch the distance between side branch and its upper neighbor decreases. This results in an increase of morphogen concentration between both branches and a mutual repulsion. The downwards motion of the side branch is blocked and hence it moves upwards. This triggers a chain reaction in which side branches on the right organism side move upwards and side branches on the left organism side move downwards. Overall, we find that the symmetric branch arrangement is unstable, whereas the antisymmetric branch arrangement is stable.

Morphogen-mediated interactions between branches on the left and right organism sides destabilize symmetric gut branching morphologies. Conversely, we can stabilize symmetric gut morphologies by preventing spreading of morphogens between both body sides. To this end, we introduce a primary branch with finite thickness b_{pb} and obtain the steady state configuration of a simulated gut for various values of b_{pb} (Fig. 5.5a). With increasing primary branch thickness, the mismatch between branch points along the primary branch

decreases and thus symmetry increases. To quantify this observation, we used our quantification procedure presented in chapter 4. We first determine the indicator functions v_i that signal whether a branch grows towards the left or right organism half (Fig. 5.5b,c). Next, we find the integrated indicator function V_i which has a characteristic stair-like shape and calculate the normalized integrated squared difference ΔV of indicator functions given in Eq. (4.11). In agreement with our observation for simulated gut structures, we find a clear decrease of ΔV with increasing thickness of the primary branch b_{pb} (Fig. 5.5d). We compare the value of ΔV obtained in simulations and experiment and find for $b_{\mathrm{pb}}/\lambda_{\mathrm{in}} = 1/2$ reasonable agreement between simulation and experiment.

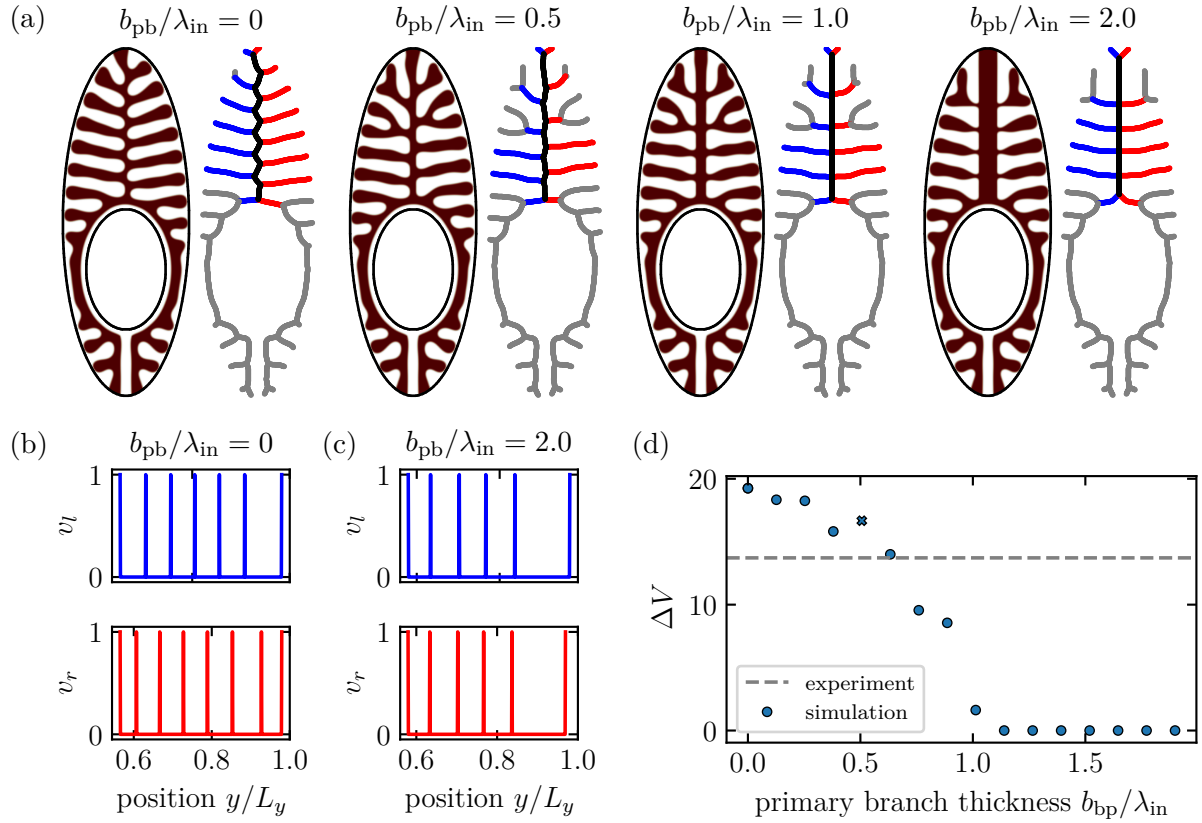

Figure 5.5: Symmetry of gut branching morphologies. (a) We show gut morphologies (brown) along with their skeleton for different values of primary branch thickness b_{pb}. We indicate the anterior part of the primary branch (black), branches originating from this to the left (blue) and the right (red) and the remaining side branches (gray). (b,c) We show indicator functions v_i for zero (b) and non-zero (c) primary branch thickness. y denotes the position at which a branch grows to the left or right. (d) We show the integrated squared difference ΔV of the normalized integrated indicator function as a measure for the mismatch of branches as a function of primary branch thickness b_{pb}. We indicate the experimentally measured value of the asymmetry (gray dashed line) and a realistic parameter value (cross).

5.2.3 Control of branch distance

In our discussion of simulated gut morphologies, we have so far focused on branch arrangement. This included the branch arrangement with respect to an orientation field and the (anti)symmetric branch arrangement between left and right organism body sides. Apart from branch arrangement, it is crucial to discuss the effect of varying branch distance and branch thickness on gut morphologies. Here, we now discuss the effect of varying branch distance on gut morphologies and in the next section we present a similar analysis for the effect of varying branch thickness.

To study the influence of branch distance on gut morphologies, we make use of key results from chapter 3. There we have studied the instability of a flat moving interface in an infinitely long system. We have identified the ratio $\gamma\Delta c/\beta$ between characteristic inhibition strength $\gamma\Delta c$ and the strength β of curvature dependency of gut growth as a key determinant of branch distance. In particular, with Eq. (3.35) we provided an analytical relation for branch distance in an idealized scenario. Even though the assumptions of this scenario are not entirely applicable here, the relation for branch distance still provides qualitative analytical insight into the dependency of branch distance on system parameters. In particular, it allows us to generate morphologies with different values of branch distance (Fig. 5.6a).

To understand the effect of different values of branch distance in detail, we carefully quantified gut morphologies. We first quantified branch distance d and confirmed our earlier observation of a strong increase of branch distance with increasing β (Fig. 5.6b). We next quantified branch thickness b and find that an increase in branch distance results in an increase in branch thickness (Fig. 5.6c). Clearly, an increase in branch distance results in a decrease of morphogen concentration between branches. This promotes branch growth and results in an increased branch thickness. Interestingly, we find that an increase in branch distance results in an increase in the mean branch length ℓ (Fig. 5.6d). This can be understood by considering branches in head and tail region of the organism separately. In the head region, branches originate from the primary branch and grow towards the organism boundary. Thus, irrespective of branch thickness or distance, branches in the head region have length $\ell \simeq L_x/2$ of roughly half the organism width L_x. By contrast, the presence of branches in the tail region strongly depends on the value of branch distance. For small branch distance and consequently small branch thickness, many short branches form in the tail region and thus the overall branch length is smaller than $L_x/2$. By contrast, for large branch distance and branch thickness, side branches are lacking in the tail region since the primary branch occupies all available space. Thus, the overall mean

branch length satisfies $\ell \simeq L_x/2$.

Apart from branch distance, thickness, and length we also quantified global gut properties. For example, we find that the branch number N decreases for increasing branch distance (Fig. 5.6e). Clearly, given that the organism length is fixed, more branches fit in the system as branch distance decreases. We also quantified the influence of branch distance on the total gut length L_{gut} and found a decrease of gut length with increasing branch distance (Fig. 5.6f). With increasing branch distance, less branches are present in the system and thus total gut length decreases. Note that this finding is consistent with the relation $L_{\mathrm{gut}} = N\ell$ for gut length. The strong decrease of branch number overcompensates a mild increase in branch length and thus overall gives an increase in gut length. Apart from qualitative insights on the influence of branch distance on gut length, we can also discuss the range of possible values L_{gut} can take. For small branch distance, the total gut length is in principle unbounded and can take arbitrarily large values. As branch distance increases, branches get less numerous until eventually no side branches appear and the gut is composed only of the primary branch. Thus, gut length is bounded from below by the primary branch length $L_{\mathrm{pb}} \simeq 2fL_y + (1-f)L_y$, where $f = y_{\mathrm{o}}/L_y$ denotes the relative position y_{o} of the primary branch origin. Finally, we also quantified gut area and find that gut area is not affected by changes in branch distance (Fig. 5.6g). Given the approximate relation $A_{\mathrm{gut}} \simeq L_{\mathrm{gut}}b$, we find that the branch distance independent gut area comes from the compensation of gut length decrease by an increase in branch thickness. Overall, branch distance serves as a key parameter to control gut morphology as it allows us to go from highly ramified morphologies to morphologies with only a few side branches by increasing β.

To find a parameter range for β, where gut properties in simulation and experiments coincide, we compare simulated and experimental gut properties. We first relate branched areas from simulation and experiment by the relation

$$A_{\mathrm{b}}^{\mathrm{exp}} = A_{\mathrm{b}}^{\mathrm{sim}} \left(\frac{L_{y,0}^{\mathrm{exp}}}{L_{y,0}^{\mathrm{sim}}} \right)^2 , \tag{5.12}$$

where the subscript "sim" and "exp" indicate the respective quantities for simulations and experiments. This relation allows us to determine the branched area $A_{\mathrm{b}}^{\mathrm{exp}}$ in experiments corresponding to the branched area $A_{\mathrm{b}}^{\mathrm{sim}}$ used in simulations. We can use $A_{\mathrm{b}}^{\mathrm{exp}}$ and the scaling relations provided in Fig. 4.6 to determine the gut properties of an experimental system corresponding to the system size studied in simulations (Fig. 5.6, gray dashed lines). We find reasonable agreement for total gut length L_{gut} in simulations and experiments for

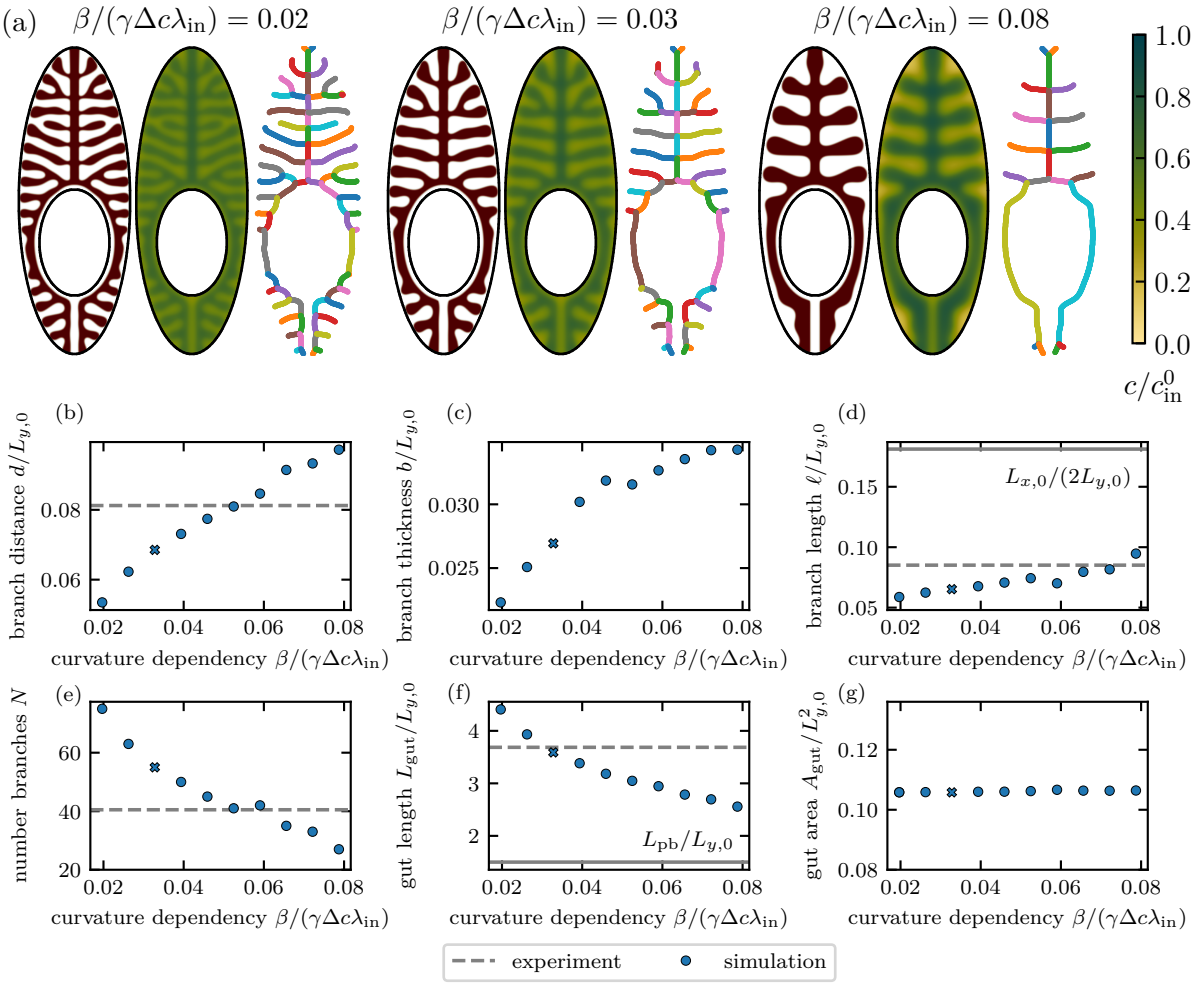

Figure 5.6: Control of branch distance. (a) We show gut morphologies (brown) together with the corresponding morphogen concentration c (green tone) and skeleton for different values of the curvature dependency β of interface growth. Different colors in the skeleton indicate different branches. (b-g) We show various gut features as a function of the curvature dependency β. $L_{y,0}$ denotes the organism length. In cases (b,d,e,f), we provide the experimentally measured value of the respective quantity (dashed gray line) along with a realistic parameter value (cross). For the branch length in (d) we show half the organism width $L_x/2$ as an upper bound (solid gray line). For the total gut length in (f) we show the primary branch length $L_{\rm pb}$ as a lower bound (solid gray line).

$\beta/(\gamma\Delta c\lambda_{\text{in}}) \simeq 0.03$. In this regime, the total number of branches and mean branch length deviate form their experimentally measured value due to the shape of the primary branch in our simulations. While in the actual organism the primary branch in the posterior region is given by two diagonal lines approaching each other, we use two parallel lines with a fixed distance in the simulations. As a result, we find more branches in the organism posterior region in the simulations than in the experimental system. The additional small, posterior branches lead to a smaller mean branch length in simulations than in experiments.

5.2.4 Control of branch thickness

Having discussed the influence of branch distance on simulated gut morphology, we now provide a similar discussion for the influence of branch thickness on gut morphology. In particular, we generate gut morphologies for different values of branch thickness while maintaining branch distance and analyze the corresponding changes in gut morphology.

To generate gut morphologies with different values of branch thickness, but the same value of branch distance, we again use findings from chapter 3. There, we demonstrated branch thickness control from mutual branch inhibition. In particular, we presented a minimal model that allowed us to provide Eq. (3.56) as relation for branch thickness. According to this relation, the interplay between gut growth tendency v_0 and the characteristic inhibition strength $\gamma\Delta c$ determine branch thickness. While an increase in v_0 promotes gut growth and therefore increases branch thickness, an increase in $\gamma\Delta c$ inhibits gut growth and therefore decreases branch thickness. Even though we here consider a more complex scenario than considered in the minimal model, the findings from the minimal model still provide guidance for the influence of model parameters on branch thickness. Here, we use Δc to control branch thickness. To ensure that branch distance stays constant as branch thickness is varied, we need to compensate an increase in Δc with an appropriate increase in β with $\Delta c \sim \beta$ as required by Eq. (3.35). We use this strategy to generate gut morphologies and find that all gut morphologies have a remarkably similar skeleton and thus overall structure while at the same time morphologies occupy more of the available space in the organism due to increased branch thickness (Fig. 5.7a).

We next quantified the resulting gut morphologies to first confirm that our approach of changing branch thickness while maintaining branch distance works. We quantified branch distance d and found that branch distance stays as predicted approximately constant (Fig. 5.7b). We quantified branch thickness b and find a roughly 2fold increase in b with decreasing value of Δc (Fig. 5.7c). These two observations confirm that as predicted branch distance is constant for all morphologies while an increase in branch thickness is observed

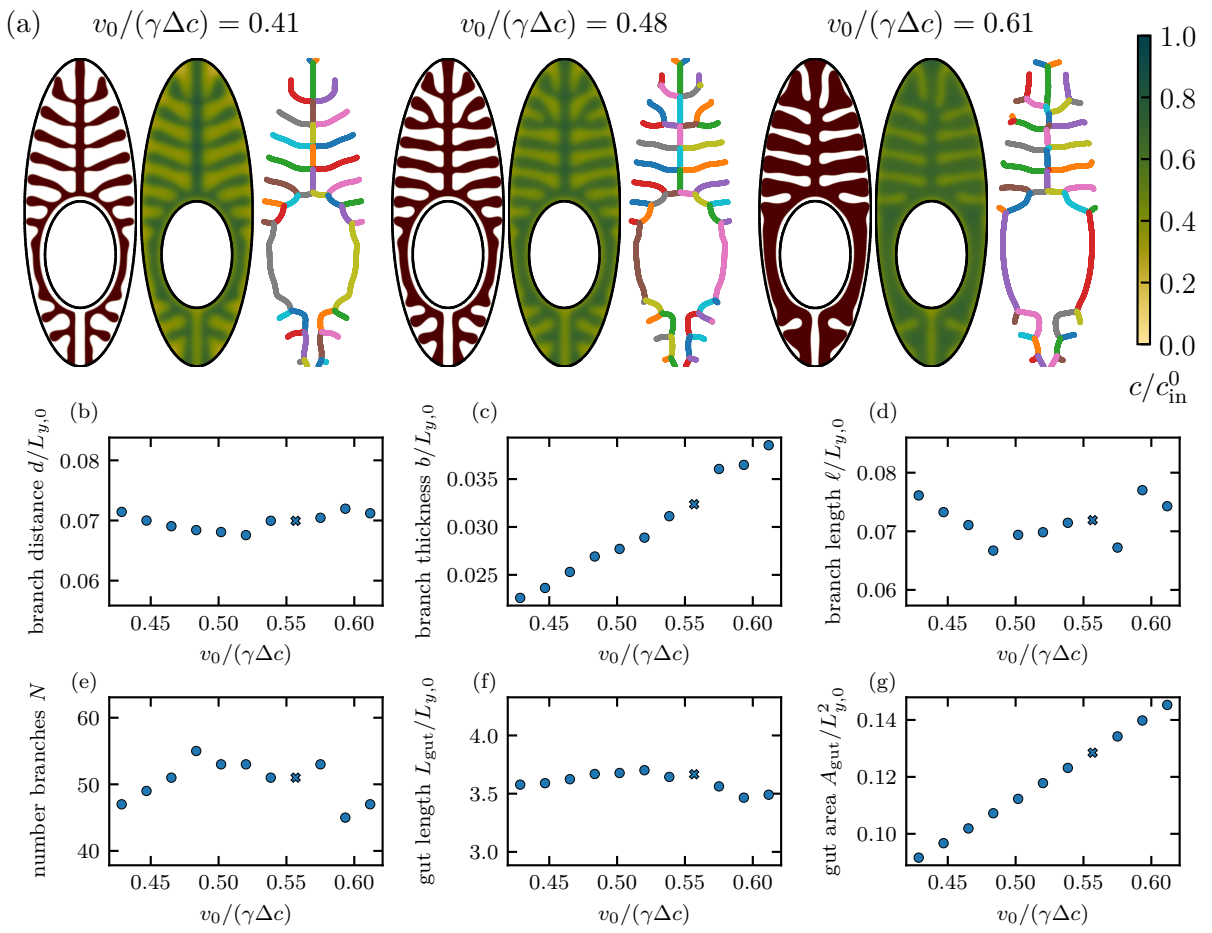

Figure 5.7: Control of branch thickness. (a) We show gut morphologies (brown) together with the corresponding morphogen concentration c (green tone) and skeleton for different values of $v_0/(\gamma\Delta c)$. Different colors in the skeleton indicate different branches. (b-g) We show various gut quantities as a function of the ratio $v_0/(\gamma\Delta c)$. $L_{y,0}$ denotes organism length. We indicate the parameter value used in the rest of this chapter (cross).

as Δc decreases. Note that this is in agreement with the qualitative predictions from the simple scenarios we studied in chapter 3 and thus further highlights their usefulness. We studied the effect of branch thickness changes on the remaining gut properties and find that overall gut structure stays constant as neither branch length ℓ, total branch number N, or total gut length L_{gut} show any significant change (Fig. 5.7d-f). We finally studied total gut area A_{gut} and find that gut area increases with branch thickness which can be rationalized from the approximation $A_{\text{gut}} \simeq L_{\text{gut}} b$ together with the branch thickness independent gut length (Fig. 5.7g).

Overall, we have identified branch thickness as a further key parameter to control gut morphology. Once our collaborators generate gut images that allow us to reliably extract

branch thickness, we can use the approach presented here to choose model parameters to account for the observed branch thickness. In combination with our previous approaches, where we studied branch orientation, distance and also overall gut symmetry, we have overall demonstrated control over the geometrical properties of simulated gut structures in a non-growing domain. Next, we employ the so far generated structures (using the parameter value indicated by the "cross" in figures) and study their size-dependent properties.

5.3 Size-dependent properties and scaling laws

Massive size increases are a key feature of planarian biology. Depending on food availability, planarians can grow and even shrink over massive size ranges. The species *S. mediterranea*, for example, can adjust their body length 20fold [65]. This massive increase in body size is also reflected in the organization of the planarian gut. During organism growth, the gut undergoes extensive remodeling of existing branches and *de-novo* formation of new branches [187]. We studied the size-dependent properties of the planarian gut in chapter 4 and found that despite the complexity of this reorganization process various gut properties obey power laws. This naturally rises the questions about size-dependent properties of gut morphologies in the model and if scaling laws arise here as well.

To study the size-dependent properties of gut morphologies in our model, we consider two approaches to generate gut morphologies of different sizes. In our first approach (branching model), we study the *de-novo* formation of gut morphologies from a primary branch in differently sized worm-like geometries. In a second approach (branching model with growth), we consider an already established gut morphology as initial condition and subsequently study its remodeling subject to organism growth. In both cases, we quantify size-dependent properties of the resulting morphologies and find that various gut properties are described by power laws of the form $y = y_0 x^{\alpha}$. In particular, we demonstrate control of intercept y_0 and scaling exponent α.

5.3.1 Quantitative study of the branching model

We first employed the branching scenario to generate gut morphologies in differently-sized worm-like geometries and find that irrespective of size, branching takes place robustly and leads to gut morphologies that fill the entire available space. As a way to alter gut morphologies and thus potentially observed scaling exponents, we consider gut morphogenesis for different organism aspect ratios. To this end, we study the formation of simulated

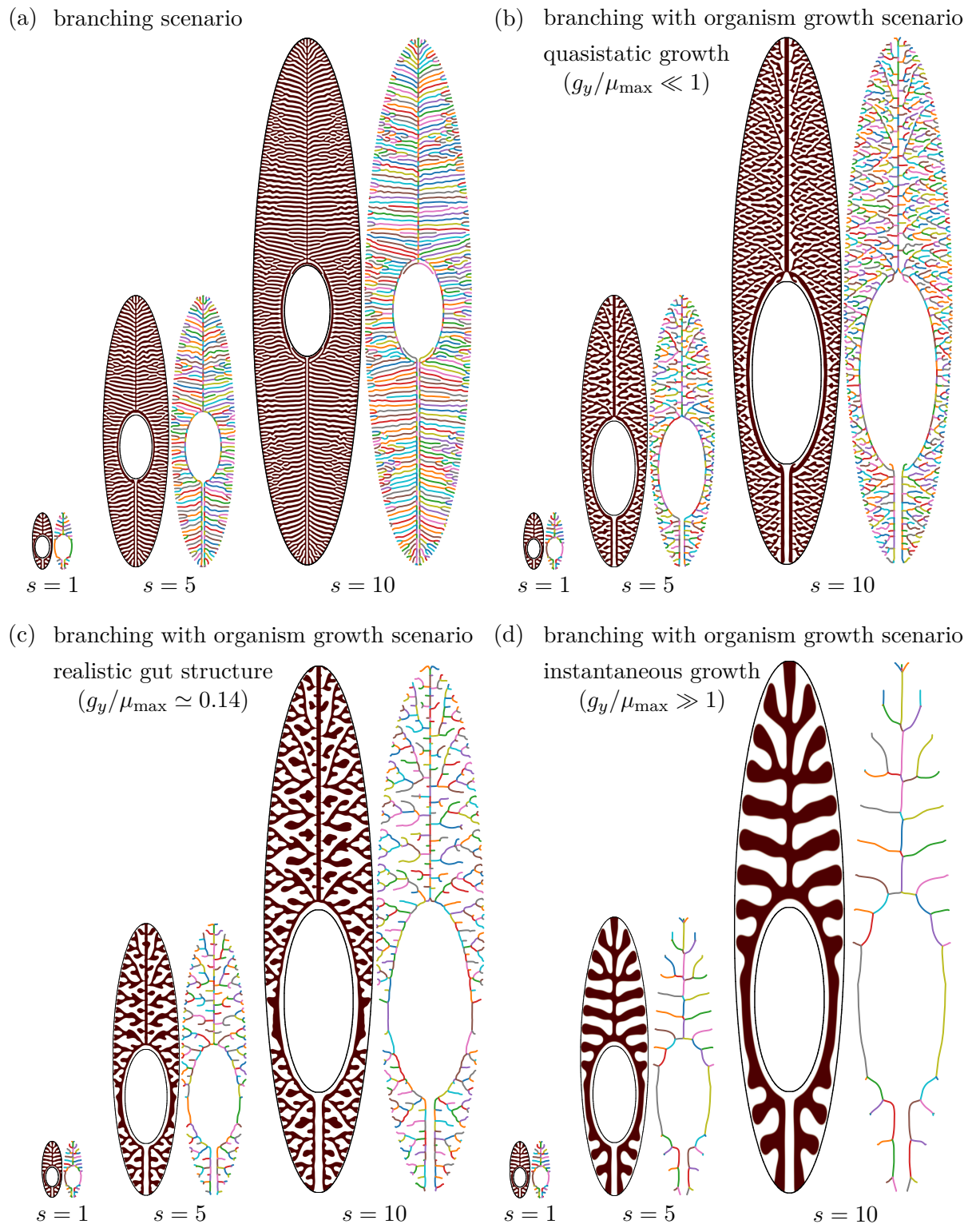

Figure 5.8: Simulated gut morphologies for different system sizes.. We show simulated gut morphologies for different relative size increases $s = L_y/L_{y,0}$, where L_y denotes the organism length and $L_{y,0}$ denotes the initial organism length. (a) We show simulated gut morphologies generated with the branching scenario. (b-d) We show simulated gut morphologies sizes generated with the branching and growth scenario with different values of $g_y/\mu_{\max}$, where g_y denotes the organism growth rate and we employ $\mu_{\max}$ as a measure for gut growth rate.

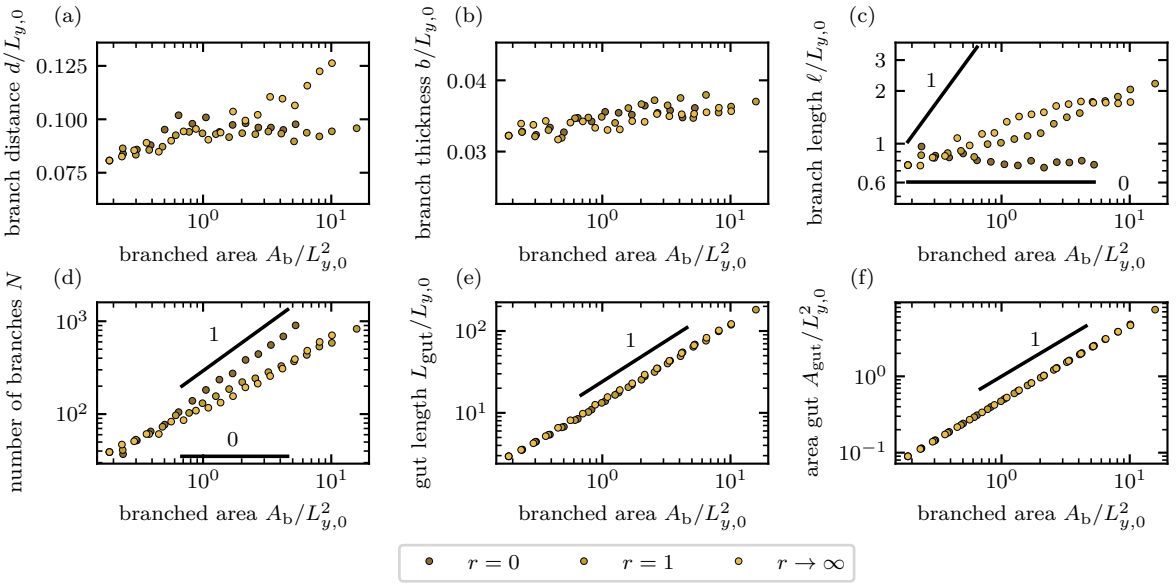

Figure 5.9: Gut scaling in the branching scenario. We show various gut features as a function of branched area A_b for different values of anisotropy parameter r, where $L_x \propto L_y^r$. $L_{y,0}$ denotes the initial organism length. We indicate scaling laws obtained from a scaling argument (black lines).

gut structures in worm-like geometries with different anisotropy parameter r defined in $L_x \propto L_y^r$. As the organism aspect ratio is in principle fixed in the real organism, this approach might appear artificial at first. However, it allows us to discuss important features of gut organization.

Discussion of scaling exponents

We quantified gut morphologies obtained from the branching model to understand their size-dependent properties. We first quantified branch distance d and find that branch distance is approximately constant with respect to organism size (Fig. 5.9a). Despite the tremendous increase in organism size of two orders of magnitude, we find only a mild increase in branch distance. This size-independent behavior of branch distance is expected and in agreement with earlier observations. In chapter 3, we have used the scenario of a flat moving interface and revealed several determinants of branch distance (e.g. strength β of curvature dependency of interface growth). As the determinants of branch distance are size-independent, we also find that branch distance is size-independent. We next quantified branch thickness b and found that branch thickness and distance display similar size-dependent behavior (Fig. 5.9b). In particular, also branch thickness

shows only a slight increase despite the massive increase of branched area. The similarity in the size-dependent behavior between branch distance and thickness can be understood in the light of our branch thickness discussion from chapter 3. There, we identified branch distance as a key determinant of branch thickness. Thus, given that branch distance is constant, a constant branch thickness is not surprising. Next, we studied branch length ℓ and found that branch length depends on the organism aspect ratio and shows different size-dependent behavior for small and large organism sizes (Fig. 5.9c). For small organism sizes, branch length is constant since the value of the mean branch length is dominated by two long branches next to the pharynx. These branches are extraordinarily long since they lack further side branches due to space limitations imposed by the pharynx. An abrupt change in the size-dependency of mean branch length occurs once a critical system size is reached. For increasing organism sizes, the relative size of the pharynx decreases and space for side branches next to the pharynx becomes available. Thus, for large organism sizes the mean branch length is no longer dominated by two long branches next to the pharynx. For large organism sizes, we find that the size-dependent behavior of branch length depends on the anisotropy parameter r. We find for an organism with size increase in y-direction only ($r = 0$) constant branch length. In this case, organism width is fixed and branches of the same length emerge from the primary branch. As a result, we find size-independent branch length. We find size-dependent branch length for an organism with size increase in x-direction only ($r \to 0$). In this case, organism length is fixed and branches invade an organism with increasing width. As a result, we find size-dependent branch length.

Having discussed the size-dependent behavior of branch properties, we can now also discuss the size-dependency of global gut properties. We first quantified the total branch number and found qualitatively a similar behavior to branch length. We observe that for large organism sizes the size-dependent behavior is influenced by the anisotropy parameter r (Fig. 5.9d). For an organism with size increase in y-direction only, more branches of the same length are added along the primary branch and we find $N \propto L_y$ and thus $N \propto A_\mathrm{b}$. For any other system size increases, the increase in branch number is less strong as additional side branches appear. The size-dependent behavior of total gut length is captured by the scaling relation $L_\mathrm{gut} \propto A_\mathrm{b}$ (Fig. 5.9e). This can be easily rationalized by recalling that for total gut length $L_\mathrm{gut} = N\ell$ holds. The scaling exponents of branch length and number of branches simply combine to a linear scaling of total gut length with branched area. Finally, we study the size-dependent behavior of total gut area and find that it is captured by $A_\mathrm{gut} \propto A_\mathrm{b}$ (Fig. 5.9f). In this case, we can use $A_\mathrm{gut} \simeq L_\mathrm{gut} b$ as a simple approximation to understand size-dependent behavior. Clearly, since the branch

thickness is independent of organism size, we find that total gut area and total gut length exhibit the same size dependency.

5.3.2 Quantitative study of the branching model with organism growth

As a second example for how gut morphologies of different sizes can be generated, we now consider the branching model with organism growth. In this model, we include organism growth in the dynamics ($g_x \neq 0, g_y \neq 0$) and study the remodeling of gut morphologies as organism size continuously increases. Note that this approach is in strong contrast to the branching model, where we studied the *de-novo* formation of gut morphologies in a discrete set of differently sized worm-geometries. The presence of organism growth and, in particular, the competition between organism growth and gut growth leads to drastic changes in overall gut morphology, which we analyze in this section.

The focus of our analysis will be again the size-dependency of gut morphologies. To generate gut morphologies of different sizes, we follow a two-step approach in which we first specify an initial gut structure and subsequently study the remodeling of this structure subject to organism growth. For simplicity, we use gut morphologies generated with the branching model (i.e. in a small worm-geometry without organism growth) as an initial condition. Our understanding of the branching model allows us to control various features of the initial condition and thus initialize the growth process in a controlled way. As a second step, we then study the remodeling of the initial gut morphology subject to growth rates g_x and g_y, where we keep the ratio of growth rates $r = g_x/g_y$ constant. Maintaining the ratio of growth rates ensures the scaling $L_x \propto L_y^r$ of length L_y and width L_x, as observed in the experimental data. Overall, this two-step approach allows us to generate gut morphologies of different sizes in a controlled way.

To understand the influence of organism growth on gut morphologies, we studied the remodeling of gut morphologies for a range of organismal growth rates g_i (Fig. 5.8b-d). We find that the interplay of organismal growth and gut growth has a striking influence on overall gut morphology. While organism growth is characterized by the rates g_i, we use the growth rate of the fastest growing mode from the instability of a flat moving interface $\mu_{\max}$ given in Eq. (3.33) as a measure for gut growth. In the limit of quasistatic organism growth ($g_i \ll \mu_{\max}$), we observe highly ramified structures which a uniform branch density irrespective of size. By contrast, we find that in the limit of instantaneous organism growth ($g_i \gg \mu_{\max}$) the branch density decreases. In this case, gut morphologies are simply scaled up as the organism grows.

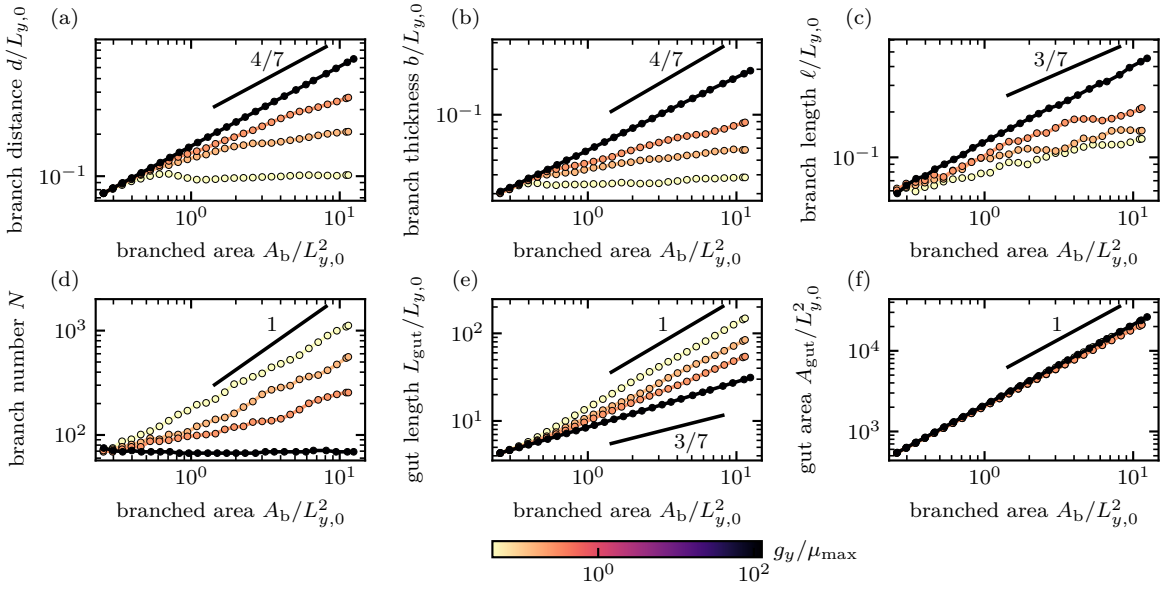

Figure 5.10: Gut scaling in the branching with growth scenario. We show various gut features as a function of branched area A_b for different values of organismal growth rate g_i. $L_{y,0}$ denotes the initial organism length. In all simulations, we maintain the ratio of growth rates $r = g_x/g_y$ as g_y is varied. We indicate scaling laws obtained from a scaling argument (black lines).

We subsequently quantified the gut morphologies obtained from the branching model with organism growth. We find that the size-dependency of various features is governed by power laws of the form $y = y_0 x^\alpha$. In particular, we find that for large enough organism sizes the competition between organism growth and gut growth determines the scaling exponent. To understand how this competition gives rise to different scaling exponents, we now discuss the behavior of length scales such as branch distance, branch thickness, and branch length. From this, we can then also understand the behavior of branch number and the total gut length and area.

Discussion of scaling exponents

Many of the key features introduced by the competition between organism and gut growth can be discussed already for the behavior of branch distance (Fig. 5.10a). For example, we find that branch distance exhibits qualitatively different behaviors depending on the organism size - or equivalent to that - depending on how long the organism has been subject to organism growth already. For a small organism ($A_b/L_{y,0}^2 < 1$), we find that branch distance scales with organism area as $d \propto A_b^{4/7}$ irrespective of the applied growth rate. In this regime, the distance of branches increases along with the organism length

resulting in the scaling $d \propto L_y$ and thus $d \propto A_\mathrm{b}^{1/(1+r)}$ with $1/(1+r) = 4/7$ ($r = 3/4$). This type of behavior continues until a critical branch distance has been reached and branch interfaces get unstable again. New branches form along the primary branch and also from tip splitting of already existing branches.

For a large organism ($A_\mathrm{b}/L_{y,0}^2 > 1$), we find that branch distance scales with branched area as $d \propto A_\mathrm{b}^{\alpha_y}$, where the scaling exponent α_y depends on the particular growth rate. In this regime, the behavior of branch distance is characterized by the competition of organism growth and gut growth. While organism growth continuously increases branch distance, gut growth leads to emergence of new branches and thus decreases branch distance. We can illustrate how this competition gives rise to different scaling exponents for two limiting regimes. In the limit of instantaneous growth, organism growth takes place at a much faster pace than gut growth ($g_i \gg \mu_\mathrm{max}$). As a result, gut morphologies are simply scaled up and lack any morphological changes. We find that branch distance d scales as $d \propto L_y$ and thus $d \propto A^{1/(1+r)}$ with $1/(1+r) = 4/7$ ($r = 3/4$). By contrast, in the limit of quasistatic organism growth, gut growth rate is much larger than the organism growth rate ($g_i \ll \mu_\mathrm{max}$). In this limit, the gut has enough time to adapt to any morphological changes caused by organism growth. As a result, we find that the branch distance is constant. Note that from now on we will focus on the regime of large organisms and discuss the different observed scaling exponents.

The size-dependent behavior of branch thickness b resembles the behavior of branch distance (Fig. 5.10b). In the limit of instantaneous growth, we find that branch thickness scales with branched area as $b \propto A_\mathrm{b}^{4/7}$. In this limit, organism growth proceeds much faster than gut growth. No additional branches form and the gut is simply scaled up. As a result, branch thickness scales as $b \propto L_y$ and thus as $b \propto A_\mathrm{b}^{1/(1+r)}$ with $1/(1+r) = 4/7$ ($r = 3/4$). In the limit of quasistatic growth, we already found that branch distance is constant with respect to branched area. As branch distance determines branch thickness, we also find that branch thickness is constant.

Finally, also the mean branch length ℓ displays power law scaling for large organism sizes with a range of different exponents that depends on the organism growth rate (Fig. 5.10c). In the limit of instantaneous growth, the mean branch length approximately scales with branched area as $\ell \propto A_\mathrm{b}^{3/7}$. To rationalize this, we consider a simple scenario in which all branches are aligned horizontally. In this idealized scenario, branch length obeys $\ell \propto L_x$ and thus $\ell \propto A_\mathrm{b}^{r/(1+r)}$ with $r/(1+r) = 3/7$ ($r = 3/4$), which is in good agreement with the finding from simulations. Note that the exponent from simulations slightly deviates from the predicted exponent towards larger values since our assumption of horizontal branch

alignment breaks down. Some branches display vertical alignment with branch length scaling of $\ell \propto L_y$ corresponding to $\ell \propto A_\mathrm{b}^{1/(1+r)}$ with $1/(1+r) = 4/7$ ($r = 3/4$). Thus, branches with vertical orientation bias the scaling exponent towards higher values. In the quasistatic limit, the mean branch length shows only a slight increase with organism size. To understand this, we can again invoke the simplified scenario in which all side branches are oriented horizontally. Due to extensive side branching in the quasistatic limit, branches in the simplified scenario have a tendency to maintain a constant length. However, this idealized argument again breaks down as some branches in the simulations display vertical alignment and bias the observed scaling exponent to larger values.

The scaling of branch distance, thickness, and length now allow us to understand the size-dependent behavior of total branch number, total gut length, and total gut area. In all cases, we again find power law scaling for large organism sizes with a range of scaling exponents determined by the competition between organism growth and gut growth. We now start by discussing the size-dependency of branch number as from this the behavior of total gut length and area follows (Fig. 5.10d). In the limit of instantaneous growth, the branch number is independent of organism size. In this limit gut, morphologies are simply scaled up along with the organism without any morphological changes. Thus, the number of branches is independent of organism size. By contrast, the number of branches increases strongly in the limit of quasistatic growth, where we find the scaling $N \propto A_\mathrm{b}^{0.75}$ indicating an (almost) constant branch density achieved by the extensive formation of new branches in this limit.

The size-dependent behavior of the total gut length can be understood from the behavior of mean branch length and the number of branches as for the total gut length holds $L_\mathrm{gut} = N\ell$. Since the number of branches and the mean branch length display power law scaling for large organism sizes, the total gut length also displays power law scaling as a consequence (Fig. 5.10e). In the limit of instantaneous growth, we find $L_\mathrm{gut} \propto A_\mathrm{b}^{3/7}$. In this limit, the branch number is constant and therefore the total gut length increases primarily due to an increase in mean branch length. Thus, the total gut length displays the same scaling behavior as mean branch length. In the limit of quasistatic growth, we find the scaling $L_\mathrm{gut} \propto A_\mathrm{b}$. In this limit, the mean branch length only displays a slight increase and thus total gut length primarily increases due to an increase of branch number. The scaling of mean branch length and branch number combines to a linear scaling.

Finally, the size-dependent behavior of total gut area can be understood from the behavior of total gut length and branch thickness. To this end, we use the relation $A_\mathrm{gut} \simeq L_\mathrm{gut} b$ as a simple approximation for total gut area. From this relation it is clear that total gut area exhibits power law scaling since both branch thickness and total gut length exhibit

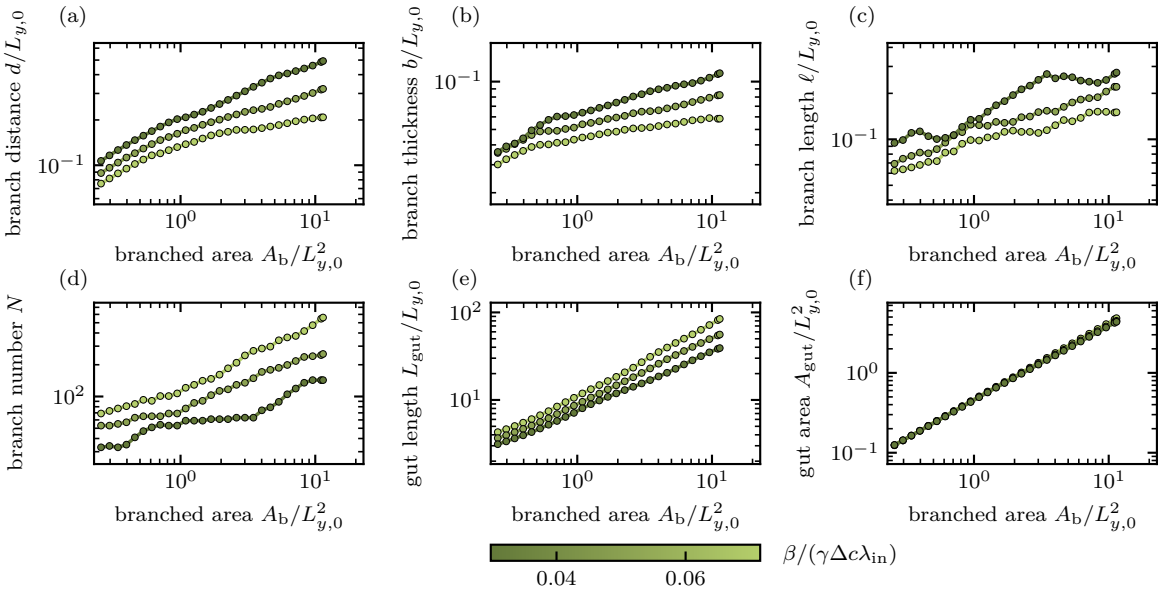

Figure 5.11: Influence of curvature dependency on gut scaling in the branching with growth scenario. We show various gut features as a function of branched area A_b for the growth rate $g_y/\mu_{\max} = 0.06$. $L_{y,0}$ denotes the initial organism length. Note that β controls branch distance of gut morphologies and thus we effectively study the influence of branch distance on gut scaling laws.

power law scaling. Interestingly, total gut area scales as $A_{\mathrm{gut}} \propto A_\mathrm{b}$ irrespective of the organism growth rate indicating a constant gut density (Fig. 5.10f). In the limit of instantaneous growth, gut morphologies are simply scaled up and lack any morphological changes. Clearly, this results in the scaling $A_{\mathrm{gut}} \propto A_\mathrm{b}$. This manifests itself also in the behavior of total gut length and branch thickness. A mild increase in total gut length is compensated by a strong increase in branch thickness overall giving rise to a constant gut density. Conversely, in the limit of quasistatic growth, branch thickness is constant and the increase of total gut area arises from the high degree of ramification of gut morphologies.

Discussion of offset

So far, we have established that various gut features display power law scaling of the form $y = y_0 x^\alpha$ and demonstrated how to change the scaling exponent α for a given value of intercept y_0. Now we demonstrate how to change the intercept y_0 for a given value of the scaling exponent α. To change the intercept of the resulting power laws, we alter properties of initial gut morphologies. Clearly, changing the value y_r of the power law at a reference organism size x_r, must correspond to a change in intercept y_0 given the scaling exponent is approximately constant.

As an example, we discuss the influence of branch distance of initial gut morphologies on the intercept of power law scaling. We use the gut morphologies presented in Fig. 5.6a as initial condition and study their size-dependent behavior. Again, we find that irrespective of branch distance gut features show power law scaling with a scaling exponent determined by the interplay between gut growth and organism growth. Most importantly, we find that the intercept y_0 of power laws depends on the chosen initial branch distance (Fig. 5.11).

5.4 Scaling argument for branching and growing networks

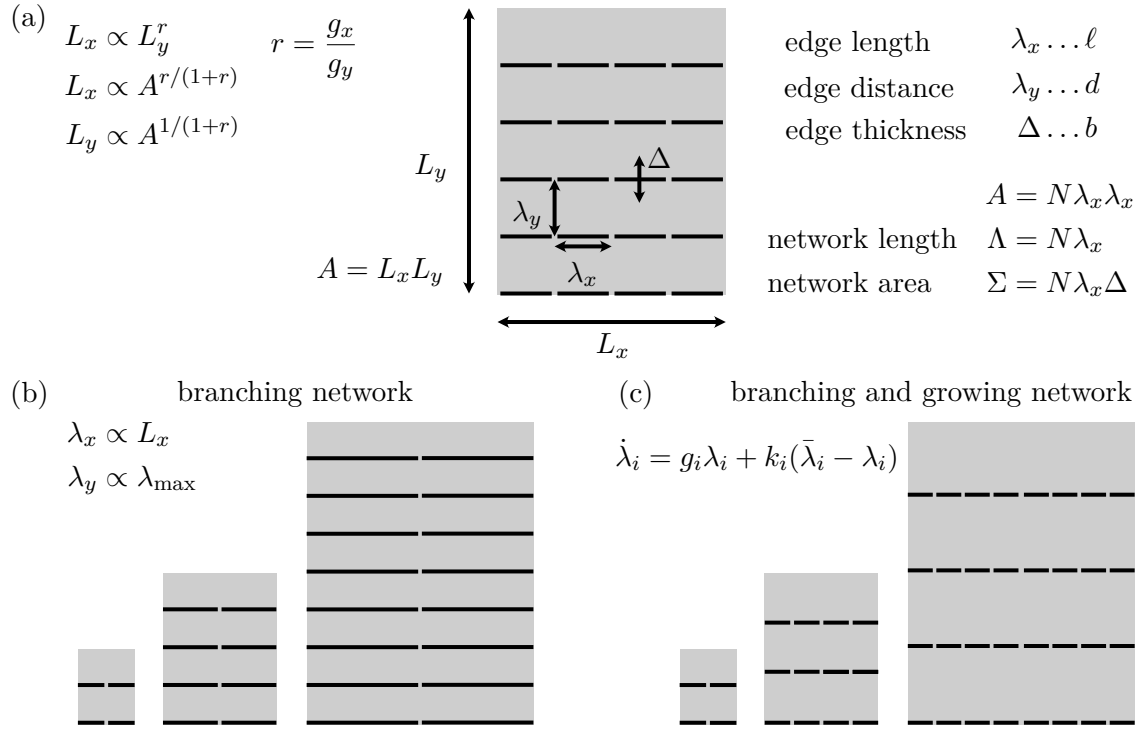

Figure 5.12: Scaling argument for minimal network geometry. (a) Instead of considering the full complexity of simulated gut morphology and worm-like boundary, we study a simplified scenario. We consider a rectangular system of length L_y, width L_x and thus area $A = L_x L_y$. We reduce the full complexity of the gut to a system of horizontal line segments of length λ_x, distance λ_y, and thickness Δ. (b) According to our scaling argument for branching networks, the line segments reach from the system center to the system boundary ($\lambda_x \propto L_x$) and maintain a preferred distance ($\lambda_y \propto \lambda_{\max}$) irrespective of system size. (c) According to our scaling argument for branching with growth, networks are subject to rescaling with organism growth rate g_i and relaxation to a preferred length $\bar{\lambda}_i$ with rate k_i, where $i \in \{x, y\}$.

In the previous section, we have discussed size-dependent properties and in particular

the scaling of gut morphologies in a model for branching and a model for branching with organism growth. To understand how scaling relations for different aspects of gut morphologies are related and how scaling laws emerge in principle, we now provide a simple scaling argument. In this argument, we reduce the full complexity of the simulated gut morphologies to a minimal network geometry (Fig. 5.12a). We simplify branches to horizontal line segments of length λ_x, vertical distance λ_y, and thickness Δ that constitute a network with in total N line segments with total length Λ and total area Σ. Note that we use characters from a different alphabet to distinguish properties of our minimal network geometry (Greek letters) and the morphologies observed in simulation and experiments (Latin letters). We approximate the elliptical organism shape by a rectangular domain and neglect the presence of the pharynx. The rectangular domain is characterized by its width L_x, length L_y, and area $A = L_x L_y$. Width and length are not independent, but related by $L_x \propto L_y^r$, where the exponent $r = g_x/g_y$ is given by the ratio of organism growth rates and quantifies the anisotropy of size changes of the domain. While for $r = 1$ width and length change isometrically, for $r < 1$ the length L_y increases faster than the width L_x and vice versa for $r > 1$. We relate area A to width L_x and length L_y by $L_x \propto A^{r/(1+r)}$ and $L_y \propto A^{1/(1+r)}$.

From the definition of the local quantities edge length, distance, and thickness, we define the overall number of edges in the network as well as total network length and area. The arrangement of edges constitutes a space filling network that satisfies $A = N\lambda_x\lambda_y$ (Fig. 5.12a). From this we find for the number of edges

$$N = \frac{A}{\lambda_x \lambda_y}. \tag{5.13}$$

We define the total network length Λ as

$$\Lambda = N\lambda_x. \tag{5.14}$$

Finally, the total network area Σ is obtained from

$$\Sigma = N\lambda_x\Delta. \tag{5.15}$$

Clearly, in all cases local quantities define total network properties.

We now make use of the correspondence between local and total network properties to understand how in general the scaling of local quantities determine scaling of total network properties. We define scaling exponents according as

$$\lambda_x \propto A^{\alpha_x} \qquad \lambda_y \propto A^{\alpha_y} \qquad \Delta \propto A^{\rho} \tag{5.16}$$

$$N \propto A^{\zeta} \qquad \Lambda \propto A^{\eta} \qquad \Sigma \propto A^{\nu} \tag{5.17}$$

For consistency, we have defined the scaling exponents in a similar fashion as for the data analysis presented so far. From the definitions of network properties Eqs. (5.13) to (5.15), we easily find

$$\begin{aligned} \zeta &= 1 - \alpha_x - \alpha_y \\ \eta &= \zeta + \alpha_x \\ \nu &= \zeta + \alpha_x + \rho. \end{aligned} \tag{5.18}$$

These relations emphasize again how local network properties determine total network properties in our scaling argument and conclude our discussion of how local and total network quantities are related. Overall, we have reduced the complexity of gut morphologies to a minimal network geometry and discussed how in this geometry different network properties and their size-dependencies are related. Next, we provide simple arguments for the value of scaling exponents of local network properties and compare scaling exponents obtained from the scaling argument with scaling exponents obtained from simulations.

5.4.1 Scaling exponents for branching networks

We use characteristic features of morphologies in the branching model to provide scaling exponents for local network properties in this scenario. We found that branch distance and thickness are constant with respect to organism size (Fig. 5.9a,b) and morphologies show little side branching (Fig 5.8a). These findings motivate us to assume

$$\lambda_y = \text{const} \qquad \Delta = \text{const} \qquad \lambda_x \propto L_x \tag{5.19}$$

for the scaling argument of the branching model. According to these assumptions, we consider an idealized network geometry with edges that extend from the system center to the system boundary and are characterized by distance and thickness that is constant with respect to system size (Fig. 5.12b).

The scaling exponents for network properties follow in straightforward way. We can read off the scaling exponents for edge distance and thickness directly from Eq. (5.19) and find the scaling exponent of edge length by using the relation between system width and

area:

$$\alpha_y = 0 \qquad \rho = 0 \qquad \alpha_x = \frac{r}{1+r} \tag{5.20}$$

Since we assumed that edge distance and thickness are lacking a size-dependency, their scaling exponents are zero. By contrast, we assumed that edge length is proportional to system width and thus edge length shows in general a size-dependency with the corresponding scaling exponent determined by the anisotropy parameter r. In the limit of system size changes in x-direction only ($r \to \infty$), edges are elongated with system width. In this limit, changes in system width and length are related by $L_x \propto A$ and thus we find $\alpha_x = 1$. In the limit of system size changes in y-direction only ($r = 0$), edges maintain their length and consequently edge length lacks a size dependency and we find $\alpha_x = 0$. We determine the scaling exponents for total network properties by combining the relation between local and total network properties Eq. (5.18) and the so far established local network properties Eq. (5.20):

$$\zeta = \frac{1}{1+r} \qquad \eta = 1 \qquad \nu = 1 \tag{5.21}$$

The total number of edges is defined in terms of edge distance and length and thus its size-dependency can be understood with the help of the size-dependencies of λ_y ad λ_x. In the limit of system size changes in y-direction only ($r = 0$), edges maintain their distance and length and thus the number of edges increases with system size as indicated by $\zeta = 1$. By contrast, in the limit of system size changes in x-direction only ($r \to \infty$), edges increase their length in proportion to system size and thus the number of edges is constant, and we find $\eta = 0$. Interestingly, we find that the scaling of total network length is independent of the anisotropy parameter r. To understand this, we combine Eq. (5.13) and Eq. (5.14) to find that total network length is only dependent on edge distance according to $\Lambda = A/\lambda_y$. Since network area is proportional to total network length (given constant edge thickness) we find $\nu = 1$.

We next compared the scaling exponents obtained from the scaling argument with exponents extracted from simulations and find overall a reasonable agreement (Fig 5.13). Our scaling argument correctly predicts that the size-dependency of gut properties is captured by power laws. In particular, our argument correctly predicts the scaling exponent for branch distance, thickness as well as total gut length and area. Even though our scaling argument fails to capture the scaling exponent α_x for the mean branch length and the total number of branches ζ, it correctly predicts that α_x and ζ depend on the anisotropy

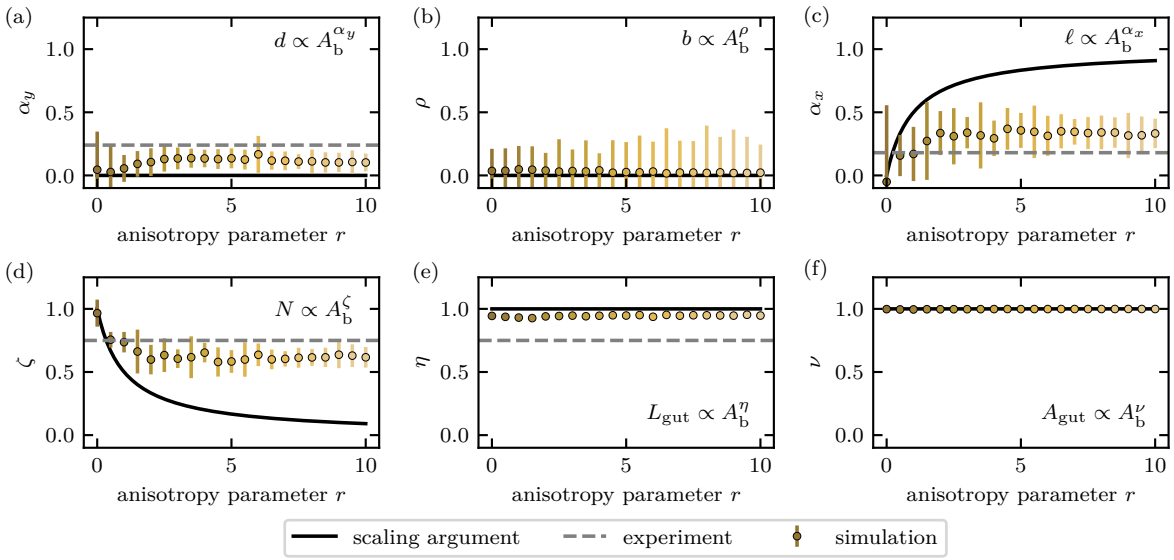

Figure 5.13: Scaling exponents in the branching model. We show scaling exponents from simulations (dots) along with predictions from our scaling argument (black line) given by Eq. (5.20) and Eq. (5.21) as a function of the anisotropy parameter r. We show scaling exponents obtained from a linear fit to the logarithmized data presented in Fig. 5.9 along with an error bar that represents the standard deviation of the obtained scaling exponent. Additionally, we show the scaling exponents determined in experiments (gray dashed line).

parameter r including the correct trend of how r influences the respective scaling exponents.

Deviations between predicted and extracted scaling exponents stem from the failure of assumptions in the scaling argument. In the scaling argument, we assumed that branches are oriented horizontally and extend from the system center to the system boundary without side branching. Clearly, this is an oversimplification as branches show side branching in the simulated structures (Fig. 5.8a). Since branches undergo side branching in the simulation, their mean branch length increases less with system size than assumed in the scaling argument. As a consequence, we find that the scaling exponent extracted from simulations is smaller than the exponent from the scaling argument. In relation to this, we find that due to side branching the number of branches in the simulations increases stronger with system size than predicted with the scaling argument. As a consequence, we find that the scaling exponent extracted from simulations is larger than the exponent from the scaling argument.

We provide an overview of scaling exponents obtained from simulations and scaling argument along with exponents determined from experiments in table 5.1. Note that

irrespective of the anisotropy parameter r the branching model fails to capture the scaling exponents determined in experiments.

5.4.2 Scaling exponents for branching and growing networks

In the scenario with branching and growth, the interplay between branch growth and organism growth controls overall gut morphology. For example, branch distance increases due to organism growth, but reduces when the separation of branches is large enough and new side branches emerge. We employ our minimal network geometry to study this interplay and derive the resulting scaling exponents in this case.

We consider a scenario in which the size of edges λ_i evolves in a growing domain of length L_i, where $i \in \{x, y\}$ (Fig. 5.12c). Size L_i and length λ_i undergo the dynamics

$$\frac{dL_i}{dt} = g_i L_i \tag{5.22a}$$

$$\frac{d\lambda_i}{dt} = g_i \lambda_i + k_i(\bar{\lambda}_i - \lambda_i), \tag{5.22b}$$

where g_i denotes the organismal growth rate, k_i denotes a relaxation rate and $\bar{\lambda}_i$ denotes a characteristic length scale. This dynamics takes into account key features of the branching process in a minimal way. We found that the interplay between organism growth and gut growth determines branch distance and length. To account for this interplay in our scaling argument, we assume that edge size is rescaled due to organism growth and at the same time has a tendency to relax back to a preferred length $\bar{\lambda}_i$ due to formation of new branches. Additionally, system size L_i is constantly rescaled with rate g_i due to organism growth. The dynamics is complemented by the initial conditions $\lambda_i(t = 0) = \lambda_{i,0}$ for edge size, $L_i(0) = L_{i,0}$ for domain length and thus $A_0 = L_{x,0}L_{y,0}$ for domain area. Motivated by our finding that branch thickness scaling follows branch distance scaling, we assume $\Delta \propto \lambda_y$ for the scaling argument.

To understand the size-dependency of λ_i, we solve the dynamics given by Eq. (5.22) and express edge size λ_i as a function of area A. We easily find that the dynamics of λ_i and L_i as a function of time are

$$A(t) = A_0 e^{(g_x+g_y)t} \tag{5.23a}$$

$$\lambda_i(t) = \bar{\lambda}_i \frac{\frac{k_i}{g_i}}{\frac{k_i}{g_i} - 1} + e^{g_i t(1-\frac{k_i}{g_i})} \left[\lambda_{i,0} - \bar{\lambda}_i \frac{\frac{k_i}{g_i}}{\frac{k_i}{g_i} - 1} \right]. \tag{5.23b}$$

We solve Eq. (5.23a) for t and use the result to eliminate the time dependency of λ_i in

Eq. (5.23b) in favor of an area dependency and find:

$$\lambda_i(A) = \bar{\lambda}\frac{\frac{k_i}{g_i}}{\frac{k_i}{g_i}-1} + \left(\frac{A}{A_0}\right)^{\frac{g_i-k_i}{g_x+g_y}}\left[\lambda_{i,0} - \bar{\lambda}\frac{\frac{k_i}{g_i}}{\frac{k_i}{g_i}-1}\right]. \tag{5.24}$$

This expression constitutes the general size-dependency of edge size λ_i and allows us to identify regimes in which λ_i displays scaling.

We find that the ratio k_i/g_i of relaxation and growth rate determines the size-dependent behavior of the edge sizes λ_i. For large organism sizes ($A/A_0 \gg 1$), we find the three qualitatively different size-dependencies

$$\lambda_i(A) = \begin{cases} \bar{\lambda}_i \frac{\frac{\nu_i}{g_i}}{\frac{\nu_i}{g_i}-1} & g_i < k_i \\ \nu_i \bar{\lambda}_i \frac{1}{g_x+g_y} \log\frac{A}{A_0} & g_i = k_i \\ \left[\lambda_{i,0} - \bar{\lambda}_i \frac{\frac{\nu_i}{g_i}}{\frac{k_i}{g_i}-1}\right]\left(\frac{A}{A_0}\right)^{\frac{g_i-\nu_i}{g_x+g_y}} & g_i > k_i. \end{cases} \tag{5.25}$$

For small organism growth rates ($g_i < k_i$), organism growth is slower than branch growth and thus branches manage to invade any free spaces and relax back to their preferred configuration. As a consequence, we find that edge size reaches a constant value in this limit. By contrast, for large organism growth rates ($g_i > k_i$), organism growth is faster than branch growth and thus branches never manage to invade free spaces. As a consequence, edge length increases as a function of time and therefore also size. Between these two regimes we find that edge length increases logarithmically with area as a special case.

From the scaling relation of lengths λ_i given by Eq. (5.25), we can read off the scaling exponents:

$$\alpha_x = \begin{cases} 0 & g_x < k_x \\ \frac{g_x-k_x}{g_x+g_y} & g_x > k_x \end{cases} \tag{5.26}$$

$$\alpha_y = \begin{cases} 0 & g_y < k_y \\ \frac{g_y-k_y}{g_x+g_y} & g_y > k_y \end{cases} \tag{5.27}$$

For the case $k_i = g_i$, no power scaling is found as edge size increases logarithmically with area. The exponents for the remaining network properties then follow by Eq. (5.18).

We subsequently compared the scaling exponents obtained from the scaling argument and the simulations. To this end, we determined the scaling exponents in the simulation data by performing a linear fit to the respective logarithmized gut property for large organism sizes ($A/A_0 > 2$). Overall, we find reasonable agreement between predicted and measured scaling exponents (Fig. 5.14). Our scaling argument correctly predicts the overall trend in scaling exponents from quasistatic to instantaneous growth for six

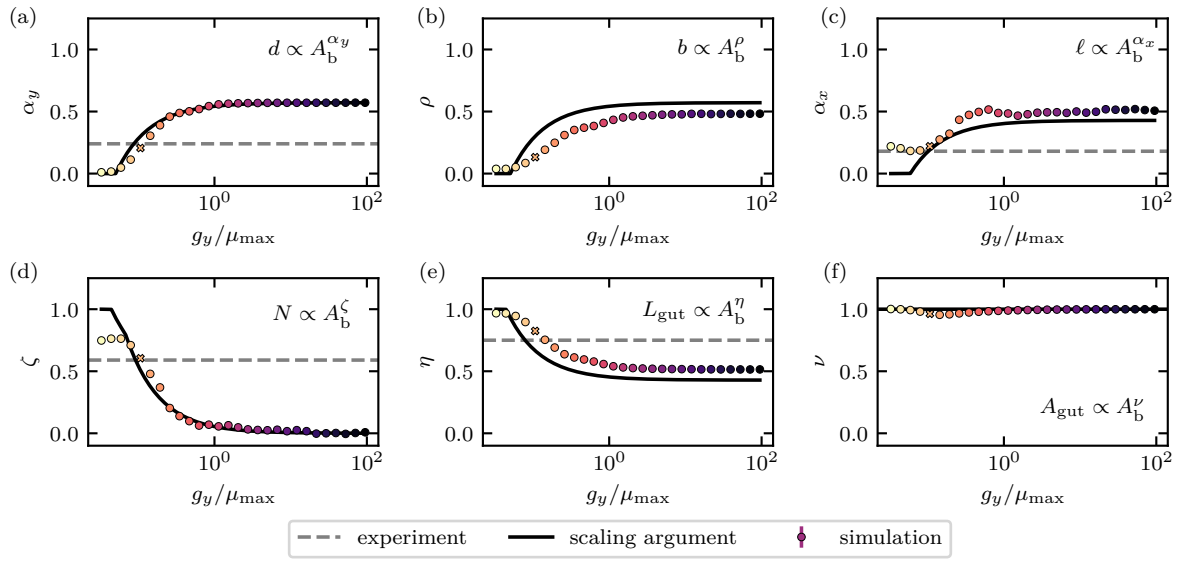

Figure 5.14: Scaling exponents in the branching model with growth. We show scaling exponents from simulations (dots) along with predictions from the scaling argument given by Eq. (5.26), (5.27), and Eq. (5.18) (black line) for different values of organism growth rate g_y. Scaling exponents for simulations were determined from a linear fit of the respective logarithmized quantity shown in Fig. 5.10 for sizes $A_\mathrm{b}/A_\mathrm{b}(t=0) > 2$. Additionally, we show the scaling exponents determined in experiments (gray dashed line) and highlight the set of scaling exponents in simulations that are closest to the experimental exponents (cross).

observables simultaneously.

We find deviations between predicted and extracted scaling exponents due to the failure of assumptions in our scaling argument. In the scaling argument, we assumed that the simulated gut structures consist of horizontally aligned branches and excluded the primary branch from the argument. However, branches display a slight deviation from horizontal alignment causing a deviation between extracted and predicted scaling exponents. While edge length is subject to rescaling only in x-direction in the scaling argument, edge length is subject to rescaling in both x and y-direction in the simulation. This results in a measured scaling exponent that is larger than the predicted exponent. In a similar way, edge thickness is subject to rescaling in y-direction in the scaling argument, but subject to rescaling in both x and y-direction in the simulation. As a consequence, the measured scaling exponents are smaller than the predicted exponents. The exclusion of the primary branch from the scaling argument can cause additional deviations between measured and predicted scaling exponents. In the limit of quasistatic organism growth, the numerous almost horizontal edges that originate from the primary branch contribute a major part

of the total gut length and the exclusion of the primary branch from the scaling argument is well justified. However, in the limit of instantaneous organism growth, the primary branch contributes a major part of the total gut length and excluding the primary branch from our argument leads to deviations between measured and predicted exponents. In the scaling argument, we assume that total gut length stems from horizontal edges and thus is rescaled only in x-direction. However, in the simulation the primary branch contributes significantly to total gut length and thus total gut length is rescaled both in x and y-direction. As a result, we find that measured scaling exponents are larger than predicted scaling exponents in the limit of instantaneous growth.

We provide an overview of scaling exponents derived from the scaling argument for the branching with growth scenario in table 5.1. Interestingly, we find that scaling exponents obtained experimentally lie within the range predicted by the scaling argument. To understand whether the scenario of branching with organism growth can generate the scaling relations of the real organism, we next provide a detailed comparison of the size-dependent behavior of gut properties found in the model and the organism.

5.5 Comparison with experimental data

After systematically identifying a parameter regime in which gut properties from simulations and experiments share features in a small organism size (section 5.2) and during organism growth (section 5.3), we next compared the gut properties for the identified regime in detail with experimental data. We show gut structure properties obtained from the branching with growth scenario together with experimental data by using the organism length $L_{y,0}$ of the smallest organism taken into account as a length unit (Fig. 5.15). Most importantly, we find reasonable agreement between gut properties in simulation and experiments. In both cases, gut properties show (approximately) power law behavior characterized by similar intercept and scaling exponents. Let us further highlight that the scaling behavior of the four experimentally quantified gut properties are captured simultaneously by our model. The model additionally predicts the scaling of branch length b and total gut area A_{gut}. Currently, experiments are ongoing to determine these gut properties which then eventually provide a further test of our model.

Deviations between simulated and experimental gut structures can have different sources. Deviations between gut properties from simulations and experiments can occur due to the finite resolution of our systematic parameter scan. Both intercept and scaling exponent can be further improved by performing a parameter scan with a higher resolution. Devi-

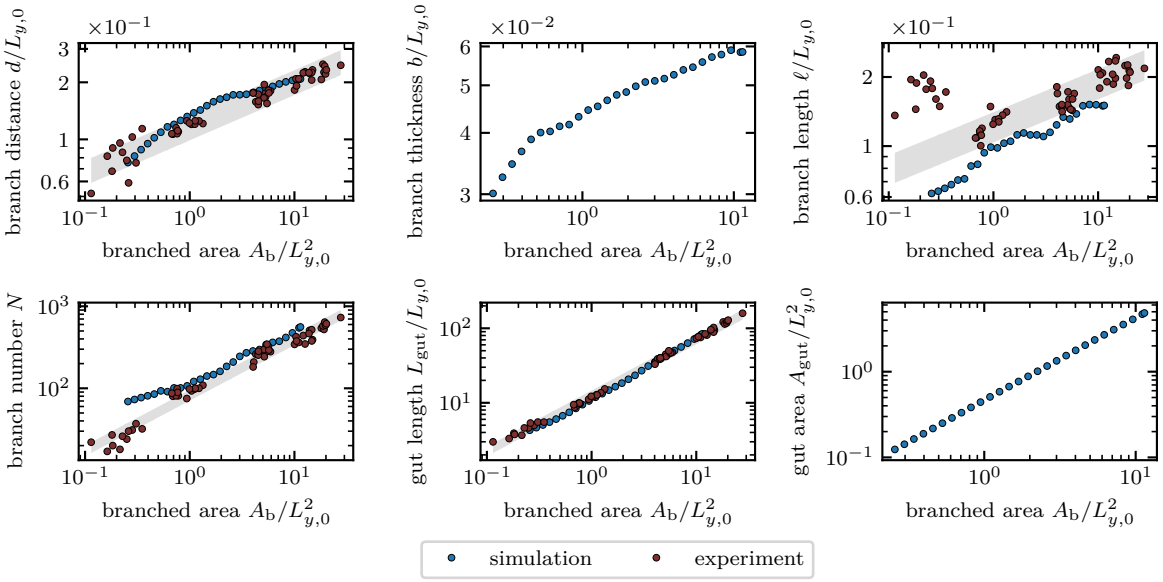

Figure 5.15: Comparison of gut scaling laws from experiment and theory. We show various gut features obtained in simulations (blue dots) and experiments (brown dots) as a function of branched area A_{b}. $L_{y,0}$ denotes the smallest organism length taken into account in simulation and experiment. The gray area corresponds ±15% of the power law fit to the respective experimental gut property and serves as a reference to estimate deviations between gut properties in simulation and experiment. The gut structures corresponding to the simulation data presented here can be found in Fig. 5.8c.

ations can occur also due to a mismatch of structures from simulations and experiments at small sizes already. For example, we find a deviation between mean branch length ℓ and total branch number N for small organism sizes. In the experimental gut structures, the two posterior parts of the primary branch (Fig. 4.2) lack side branches in 1 mm organisms and bias the mean branch length towards large values. As the organism size increases, side branches appear along the anterior parts of the primary branch leading to a sudden reduction of mean branch length. By contrast, in our simulation, the anterior part already carries side branches in a small organism (Fig. 5.6a) and thus lacks a sudden jump in mean branch length. Finally, our choice to use the smallest organism length $L_{y,0}$ taken into account as a length unit also causes deviations. In experiments, $L_{y,0}$ can be obtained only approximately and thus introduces deviations into our comparison. In our comparison of simulated and experimental gut properties, we show ±15% of power law fits of experimental gut properties as a reference to estimate deviation between gut properties in simulation and experiment.

We finally provide the scaling exponents for gut properties from simulations presented

Table 5.1: Overview of scaling exponents in experiments and simulations. We show scaling exponents for anisotropy parameter $r = 3/4$. The format $[\cdot, \cdot]$ indicates a range of exponents. ND denotes not determined. For details on how exponents were obtained, we refer the reader to the corresponding sections.

Exponent	Experiments	branching		branching and growth	
		simulation	scaling argument	simulation	scaling argument
α_x	0.19 ± 0.08	0.29 ± 0.06	$3/7 \simeq 0.43$	0.22 ± 0.01	$[0, 3/7]$
α_y	0.24 ± 0.04	0.01 ± 0.24	0	0.21 ± 0.01	$[0, 4/7]$
ζ	0.59 ± 0.05	0.68 ± 0.04	$4/7 \simeq 0.57$	0.60 ± 0.01	$[1, \ 0\ ]$
η	0.75 ± 0.01	0.96 ± 0.01	1	0.82 ± 0.01	$[1, 3/7]$
ρ	ND	0.01 ± 0.46	0	0.13 ± 0.01	$[1, 3/7]$
ν	ND	1.00 ± 0.01	1	0.96 ± 0.01	$[1, 3/7]$

in Fig. 5.15 in table 5.1 and thereby complete our overview of gut scaling behavior in simulation and experiment.

5.6 Effect of periodic organism (de)growth on morphologies

Inspired by the fascinating ability of planarians to grow and degrow their body and thus also their gut, we finally studied the behavior of gut properties in our model with respect to cycles of growth and degrowth. In particular, we wondered whether our model in principle can account for the growth and degrowth of gut structures and if so whether this process shows signs of irreversibility.

To study the effect of cycles of growth and degrowth on gut morpholgies, we initialized our model with an already established gut morphology and studied its time evolution subject to a periodic growth rate $g_i(t)$ for $i \in \{x, y\}$ with period T. We choose T such that after half a period the organism length has increased by a factor s irrespective of growth rate, i.e. $L_y(t = T/2) = sL_{y,0}$. For simplicity, we consider a sinusoidal growth rate $g_i(t) = g_{i,0} \sin(2\pi t/T)$, where $g_{i,0}$ denotes the growth amplitude. For a sinusoidal growth rate, organism length undergoes the dynamics

$$L_i(t) = L_{i,0} e^{G_i(t)} \qquad G_i(t) = \int_0^t g(\tilde{t}) d\tilde{t} = \frac{g_{i,0} T}{2\pi} \left[1 - \cos\left(2\pi \frac{t}{T}\right)\right]. \tag{5.28}$$

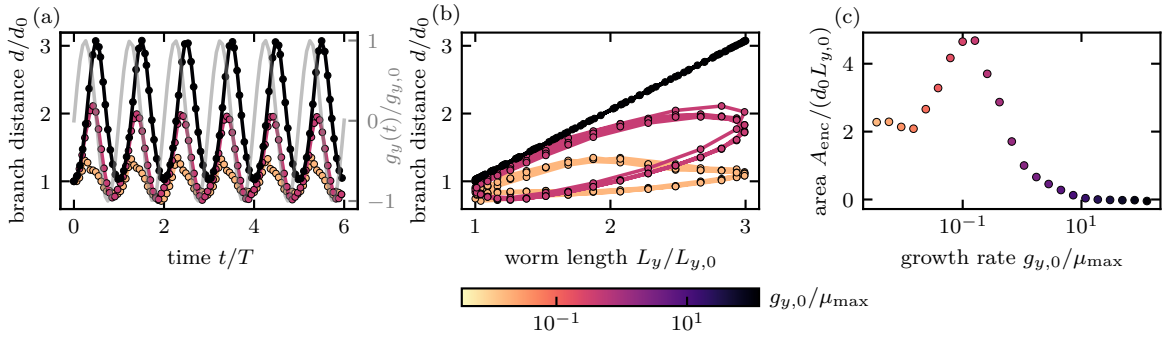

Figure 5.16: Periodic organism (de)growth of gut structures. (a) We show branch distance as a function of time t for different values of growth rate $g_{y,0}$. We denote the branch distance at time $t = 0$ by d_0. We additionally show the sinusoidal growth rate $g(t)$ with period T and amplitude $g_{y,0}$ that we use to grow the organism (gray line). (b) We show branch distance d as a function of organism length L_y for the same values of growth rate $g_{y,0}$ as in (a). $L_{y,0}$ denotes initial organism length. (c) We show the enclosed area A_{enc} of orbits as a function of growth rate $g_{y,0}$. The area was determined according to Eq. (5.32) for orbits from simulation data using the trapezoidal rule for $n = 6$ and $m = 2$ (last four periods).

and according to this the organism length L_y satisfies $L_y(T/2) = sL_{y,0}$ for the period

$$T = \frac{\pi}{g_{y,0}} \log(s). \tag{5.29}$$

This type of scenario allows us to study the effect of periodic organism growth on gut morphologies.

We track several gut properties as a function of time and discuss the behavior of branch distance d as an example gut property. Most importantly, we find that morphologies can undergo numerous rounds of growth and degrowth while maintaining their overall branched morphology. After an initial transient behavior, gut properties reach a periodic behavior with an amplitude and phase determined by the organismal growth rate (Fig. 5.16a). Note that amplitude and phase of the periodic dynamics have important consequences for the reversibility of this process and thus will be the focus of our discussion.

The time-dependent behavior of gut morphologies can be understood with the help of the scaling argument presented in section 5.4 of this chapter. In our scaling argument, we studied the dynamics of the edge distance λ_y in a simple network geometry as an idealized scenario for the dynamics of branch distance d during organism growth. In this scenario, edge distance λ_y is subject to rescaling due to organism growth with rate g_y and relaxation towards a preferred length scale $\bar{\lambda}_y$ with rate k_y due to the growth of additional

side branches. In the limit of quasistatic organism growth ($g_i \ll k_i$), we find that

$$\lambda_y(t) = \bar{\lambda}_y \left(1 + \frac{g_y(t)}{k_y}\right) + \mathcal{O}\left(\left(\frac{g_{y,0}}{k_y}\right)^2\right) \tag{5.30}$$

satisfies Eq. (5.22b) to linear order in $g_{y,0}/k_y$ for a periodic growth rate. According to this, the length scale λ_y oscillates in phase with the periodic growth rate and thus with a phase difference ($\Delta\phi = \pi/2$) to organism length L_y with an amplitude determined by the growth amplitude $g_{y,0}$. Note that these findings are in agreement with the behavior of branch distance d observed in simulations (Fig. 5.16a). To understand the limit of instantaneous growth ($g_y \gg k_y$), we consider a special case of Eq. (5.22b), where no relaxation to a preferred length takes place ($k_y = 0$). For a periodic growth rate we find the solution

$$\lambda_y(t) = \lambda_{y,0} e^{G_y(t)} \tag{5.31}$$

for edge distance. In this limit, organism growth dominates the dynamics of edge distance and no side branches emerge. As a consequence, λ_y follows the behavior of system size with $\lambda_y \propto L_y$. Edge distance oscillates in phase with the organism length ($\Delta\phi = 0$) and in each period of growth and degrowth changes its length by a factor of s. Again, the predictions from the scaling argument are in agreement with the behavior of branch distance in the simulation data (Fig. 5.16a).

To understand the reversibility of gut properties subject to periodic organism growth, we next studied the behavior of branch distance as a function of organism length. Clearly, if growth and degrowth are reversible then growth and degrowth trajectories in the (d, L_y) plane follow along the same path and branch distance is a function of size only. By contrast, different paths for growth and degrowth in the (d, L_y) plane indicate the irreversibility of growth and degrowth. We show the values of branch distance depicted in Fig. 5.16a now as a function of organism length L_y and find that after a short transient behavior the trajectories settle into a closed orbit (Fig. 5.16b). In the limit of quasistatic growth ($g_i \ll \mu_{\max}$), we find that orbits enclose a non-zero enclosed area indicating irreversibility. In this limit, we found that branch distance lags behind organism length with a non-zero phase difference, thus giving orbits with non-zero area. By contrast, in the limit of instantaneous growth ($g_i \gg \mu_{\max}$), we found zero phase difference between branch distance and organism length and thus orbits enclose zero area indicating the reversibility in this limit.

To quantify the irreversibility of periodic growth and degrowth, we use the area A_{enc} enclosed by the orbit of the nth and mth growth and degrowth cycle as a measure. The

enclosed area is defined by

$$A_{\mathrm{enc}} = \frac{1}{n-m} \int_{L_m}^{L_n} d(L)\, \mathrm{d}L, \tag{5.32}$$

where we used $L_n = L(t = nT)$ as an abbreviation and $n - m$ denotes the amount of growth and degrowth cycles taken into account for the irreversibility quantification. We find a growth rate dependent enclosed area with finite value in the limit of quasistatic growth, a maximum in the intermediate regime, and a vanishing enclosed area for the limit of instantaneous growth (Fig. 5.16c). To understand this non-monotonic behavior, we again employ our scaling argument. In the limit of quasistatic organism growth, we find by combining Eq. (5.30) and Eq. (5.32) that $A_{\mathrm{enc}} \propto g_{y,0}$. With increasing growth rate the amplitude of oscillations in edge distance and thus the enclosed area and irreversibility of growth and degrowth increases. Note that this calculation fails to account correctly for the plateau in enclosed area for small values of the growth rate due to an oversimplification of the branching process in the scaling argument. While in the scaling argument the amplitude of edge distance oscillations can vanish for $g_y \to 0$, they will always be finite in the simulations as branch distance needs to pass a critical threshold for branching to occur. In the limit of instantaneous organism growth, the phase difference between organism length and branch distance vanishes with increasing organism growth rate and thus enclosed area and the irreversibility vanish with increasing organism growth rate.

Note that we also considered a periodic rectangular function (reminiscent of a feeding and starvation period of the organism) and found that the main findings of this section qualitatively still hold.

5.7 Summary and discussion

In this chapter, we have presented a model for morphogen-controlled growth and scaling of the planarian gut. In this model, we combine ideas presented in chapter 3 with novel concepts needed to account for the organization of the planarian gut. At the center of our approach is again the idea that a morphogen controls the growth of a complex branched organ. In addition, we consider external guiding cues that can alter the orientation of branches. We take into account the organism shape and study branching morphogenesis in a realistic worm-like geometry. To account for the massive body size increase of planarians, we include organism growth in our description.

Summary

In our model, we consider a 2D system and describe the outline of the planarian gut by an infinitely thin interface. The dynamics of this interface lies at the center of our model and captures key processes responsible for the morphogenesis of the planarian gut in a coarse grained way. As in chapter 3, the interface has a constant tendency to grow which is inhibited by the concentration of a morphogen. We have established this as a minimal growth rule that yields self-organized branched structures and thus employ it here again. As before, we consider a curvature dependency of interface growth that results in the stabilization of interface motion. Motivated by the orientation of branches in the planarian gut, we take into account external guiding cues that can alter branch orientation. Finally, we account for the overall growth of the organism by an advection term in the interface growth equation. We describe the morphogen dynamics by a minimal reaction-advection-diffusion system. According to this, the morphogen spreads in the organism via diffusion and also by advection due to organism growth. Morphogen undergoes region-dependent degradation and production with a constant rate and is additionally subject to an effective degradation rate due to the dilution by organism growth. We consider a scenario in which morphogen is produced in the gut region and no production takes place outside the gut region. Inspired by our quantitative analysis of planarian body shape we study the coupled dynamics of interface and morphogen in an elliptic growing domain with an empty space in its center to account for the region the pharynx resides in. Overall, we think that this model captures key effects responsible for the morphogenesis of the planarian gut in a coarse grained fashion.

To systematically understand the growth of branched structures in this model, we first considered a non-growing domain as a simple scenario of pattern formation. Most importantly, we find that irrespective of organism shape or external guiding cues the interface robustly undergoes an instability leading to the formation of branched structures. We first studied the influence of different external orientation fields on gut morphologies. We considered the external orientation field $\boldsymbol{m}_{\mathrm{y}}$ (orientation in horizontal direction) and $\boldsymbol{m}_{\mathrm{ext}}$ (orientation towards organism boundary) and demonstrated that for both cases branches align in direction of orientation field for increasing values of coupling strength δ. We find that $\boldsymbol{m}_{\mathrm{ext}}$ captures qualitative features of gut morphologies in planarians well and we therefore focus our discussion on this case of orientation field. We further showed how morphogen-mediated interactions between branches in the left and right organism half influence gut morphology symmetry and how the thickness of the primary branch can be used to control these interactions and thus symmetry. In the limit of an infinitely

thin primary branch, gut morphologies display an antisymmetric configuration, where a branch in the left system half corresponds to a gap between branches in the right system half and vice versa. In this limit, branches spontaneously leave a symmetric arrangement and morphogen from the opposite organism half prevents branch motion to the original symmetric arrangement. We demonstrated that for increasing primary branch thickness this effect is suppressed and a transition from antisymmetric to symmetric configuration takes place. Finally, we used the findings presented in chapter 3 to discuss the control of branch distance and thickness. We use the strength of curvature dependency of interface growth to control branch distance and show that increasing the dependency of interface growth on curvature increases branch distance. We use the morphogen inhibition strength to control branch thickness and show how decreasing inhibition strength leads to an increase in branch thickness. Overall, we have systematically discussed various aspects of pattern formation and demonstrated the generation of an entire family of worm structures. We quantified key features of the planarian gut in both simulations and experiments and identify a parameter regime in which the structures in our model share key features with the gut in small organism sizes (1 mm).

Next, we proposed two different scenarios to generate gut morphologies of different sizes and discussed their size-dependent properties. In a first approach (branching scenario), we study the *de-novo* formation of gut morphologies in systems of different sizes. Overall, morphologies show a relatively simple organization with branches extending from the primary branch to the organism boundary with almost no further side branching. We find that size-dependent gut properties show power law scaling as a function of system size and demonstrate how the control of the scaling exponent of branch length and number by organism aspect ratio.

In an alternative approach (branching with growth scenario), we study the continuous remodeling of an already established structure subject to organism growth. In strong contrast to the branching scenario, we find that depending on the ratio of gut growth to organism growth morphologies can exhibit highly branched shapes with numerous side branches. In the limit of quasistatic growth, gut growth is much faster than organism growth and thus any empty spaces in morphologies can be invaded by new branches. As a result, we find highly ramified morphologies with numerous side branches. By contrast, in the limit of instantaneous growth, gut growth is much slower than organism growth and spaces in morphologies remain empty. As a result, we find a simple gut architecture in which morphologies are simply scaled up during organism growth. The transition from a simple to complex gut organization is also reflected in the size-dependent properties. We find that size-dependent gut properties are captured by power laws with scaling exponents

that are determined by the ratio of gut growth rate to organism growth rate.

To understand how scaling relations of different gut properties are related and originate, we next used a simple scaling argument. We reduce the complexity of morphologies to a minimal network geometry in which branches are represented by straight horizontal edges. Motivated by our quantification of morphologies in the simulation, we propose an ansatz for the scaling of edge length, distance, and thickness and from this determine the scaling of total network length, area, and total edge number. For the branching scenario, we assume that edges extend from the system center to the boundary and maintain a size-independent distance and thickness. This ansatz is in agreement with the scaling of branch length and distance and captures the aspect ratio dependence of branch length. It further allows us to correctly predict the scaling of total gut length and area as well as the aspect ratio-dependent scaling of total branch number. For the scenario of branching with growth, we propose a dynamics for edge length and distance that captures the interplay between gut growth and organism growth. We assume that edge length and distance are constantly rescaled due to organism growth and have a tendency to relax to a preferred length scale due to growth of new branches. Motivated by the observation that branch distance determines branch thickness, we assume that edge thickness scales linearly with edge distance. Our scaling argument for the branching with growth scenario, correctly predicts the transition from highly branched networks in the limit of quasistatic growth to scaled up networks in the limit of instantaneous growth. Deviations between our scaling argument and observed scaling exponents in simulations originate from oversimplifications in the model assumptions.

Having analyzed two different scenarios to generate differently sized morphologies, we next compared properties of simulated and experimental gut structures. While the branching scenario disagrees with the experimental gut properties, we find that the branching with growth scenario captures the four experimentally determined gut properties well. This highlights the importance of organism growth in our description.

Inspired by the ability of flatworms to both grow and degrow, we finally studied the behavior of simulated gut structures subject to periodic organism growth. We use a sinusoidal growth rate as a simple scenario to study periodic body size changes and study branch distance as an example gut property. Most importantly, we find that simulated gut structures can undergo numerous rounds of growth and degrowth without loosing their branched structure. In addition, we find that the amplitude and phase of branch distance oscillations depend on the ratio of gut growth rate to organism growth rate. In the limit of quasistatic growth, we find that branch distance oscillations are in phase with sinusoidal growth rate and exhibit a phase difference with organism length. By contrast, in the limit

of instantaneous growth, gut growth is much slower than organism growth, and branch formation is lacking. As a result, branch distances are periodically scaled along with the organism length and branch distance oscillations have zero phase difference

Overall, we have thus presented a novel theoretical framework to study the self-organized growth and scaling of the planarian gut. Our framework provides a range of qualitative and quantitative predictions on the organization of the planarian gut which we next use as a basis to discuss experimental tests of the model. Additionally, we discuss limitations of our approach, outline the wider implications of our findings and give an outlook on future work.

Discussion

Our model provides various experimentally testable predictions. Most importantly, we predict the scaling of six different gut properties as a function of organism size. We compared the scaling of branch length and distance as well as total branch number and total gut length obtained from simulations and experiments and found good agreement for both intercept and exponents of scaling relations. Currently, experiments with a marker for outer intestinal cells are ongoing, which will allow us to extract branch outlines. From this, we can determine branch thickness and total gut area and test our model prediction for the respective quantity.

In our model, the formation of branched structures crucially relies on the guidance of a morphogen that is produced on the gut. Thus, naturally the question arises how already formed gut structures change for altered morphogen production. According to our model, a decrease in morphogen production for an already formed structure results in an increase in branch thickness as mutual branch inhibition is reduced. Even more strikingly, the complete removal of morphogen would result in a sheet-like morphology, where all branches have merged. Currently, RNAi experiments are ongoing to inhibit the production of several morphogens candidates and to eventually test our prediction. Once a morphogen has been identified, features of the morphogen gradient in model and experiment can be compared such as for example the size-independent gradient length scale predicted according to the model.

The existence of guiding cues that control the orientation of branches is a further key assumption of our approach. In this chapter, we have presented a second morphogen that is produced on the organismal boundary and forms gradients towards the organism center as an example of such a cue. The removal of this guiding cue results in branches that, in general, are less oriented towards the organism boundary and can also undergo sharp

turns. In planarians, *wnt5* is a candidate for such a morphogen as it is expressed along the mediolateral axis and the inhibition of *wnt5* expression constitutes another test of our model [103, 108, 134]. Note that in this chapter we have focused on a second morphogen originating from the organism boundary as a guiding cue. However, many other factors can contribute to the alignment of branches. For example, planar cell polarity as well as mechanical cues from muscle fiber orientation might contribute to branch orientation [115, 188]. Our framework takes into account external guiding cues in a coarse grained way via the external orientation field and can in principle take into account other guiding cues as well.

Finally, we studied the periodic (de)growth of gut morphologies in the model and demonstrated the irreversibility of gut properties under (de)growth. For example, we showed that gut morphologies of a growing organism are characterized by a larger branch distance than in a shrinking organism. An experimental way to test this prediction might be to grow a set of small (e.g. 1 mm) worms to a medium size (e.g. 5 mm) and conversely starve a set of large worms (e.g. 11 mm) to the same medium size and subsequently measure their gut properties.

Our model is based on a set of simplifying assumptions that might limit the applicability of our results. To reduce the computational complexity of our problem, we presented a 2D model. However, planarians are 3D organisms and their gut shows distinct features of 3D organization. For example, in large organisms branches occasionally grow over each other (Jochen Rink, personal communication). To account for the 3D organization of the gut, the model needs to be studied in 3D. Note, however, that our key findings remain unaffected by the dimensionality of the problem. Given the existence of an instability in 3D, we also expect the mutual inhibition of branches, the invasion of empty regions by branches, the organization of branch orientation by external guiding cues, and also the emergence of scaling relations due to interplay of gut growth and organism growth. Another simplification of our approach lies in the assumption that morphogen is produced *on* the gut. As the gut is a hollow tube a more realistic approach would be to assume morphogen production only at the gut outline. Note that this can be easily implement with the phase field method by using a morphogen production term with $s_{\text{in}} \propto \phi(1-\phi)$ instead of $s_{\text{in}} \propto \phi$.

Let us finally discuss future research directions. A key result of our model is the emergence of scaling relations from the interplay of gut growth and organism growth. In our model, a range of exponents arises, but our model fails to provide an explanation for why a particular organism growth rate and thus a set of gut scaling exponents is chosen in the organism. We envision that by implementing a feedback between organism growth and

gut growth a particular exponent can be chosen.

Chapter 6

Summary and discussion

In this thesis, we have theoretically studied the self-organized growth and scaling of branched organs. In our approach, we represent the organ outline by an infinitely thin interface and study the morphogen-controlled motion of this interface in growing domains. We demonstrate the formation of highly branched morphologies from an instability in interface motion and show how the interplay between interface motion, morphogen dynamics, and domain growth control the geometrical, topological, and size-dependent properties of the resulting structures.

Summary

In the first part of this thesis (chapter 2 and 3), we consider different scenarios of morphogen-controlled interface motion in non-growing domains and study how geometrical and topological properties arise from the interplay of interface motion and morphogen dynamics. To this end, we first present a stochastic lattice model for morphogen-controlled interface growth in chapter 2. In this model, the state of lattice sites (occupied, unoccupied) indicates the presence or absence of an organ cell. The set of all occupied lattice sites constitutes the organ and we refer to this set as "aggregate". State changes occur in a stochastic manner controlled by a morphogen gradient and represent organ growth. We assume that a minimal reaction-diffusion system governs morphogen dynamics. According to this dynamics, morphogen shows an effective diffusion and undergoes region-dependent degradation and production. In particular, we consider a setting with strong morphogen production on the aggregate with morphogen gradients forming towards the system boundary. As a simple scenario for pattern formation, we consider a single occupied lattice site in a square system as an initial condition. We numerically study the dynamics of this scenario and find that highly branched morphologies occur from an instability in interface motion. The formation of an interface protrusion leads to a decrease of morphogen

gradients at the protrusion and consequently protrusion growth is enhanced. A positive feedback between increase in protrusion growth and decrease in morphogen gradient length sets in, which leads to the formation of highly branched morphologies. The characteristic morphogen gradient length scales control the geometry of the resulting structures. Depending on the morphogen gradient length scale, we find structures ranging from highly branched morphologies with self-similar properties to almost circular structures with only a few branches. Finally, we present the Euler characteristic as an example of a topological invariant and use it to introduce topological constraints into interface motion. As a result, we find tree-like (loopless) aggregates with otherwise similar statistical properties. Overall, chapter 2 serves as a first example for the formation of branched structures from an instability in interface growth and how the geometrical and topological properties can be controlled.

In chapter 3, we study a continuum model of morphogen-controlled interface motion. This model serves as a complementary approach to our lattice model and provides a further example of morphogen-controlled interface motion that forms branched morphologies from an instability. We again represent an organ outline by an infinitely thin interface. As opposed to the lattice model, where a morphogen gradient determines interface motion, here we study a scenario, where the interface has an intrinsic tendency to grow, but growth is inhibited by the morphogen concentration at the interface. Additionally, we consider a curvature-dependency of interface growth that results in a negative velocity of outward protrusions and a positive velocity of inward protrusions. As a consequence, the interface has a tendency to grow to a flat configuration and interface motion is stabilized on small length scales. As before, we assume that morphogen undergoes effective diffusion along with a region-dependent degradation and production and again focus on a scenario in which morphogen is dominantly produced within the interface and a gradient forms to the outside. To understand if an instability can occur in interface motion, we perform a linear stability analysis of a flat moving interface. Additionally, we consider the limit of quasistatic morphogen dynamics in which the morphogen concentration instantaneously follows any interface perturbations. This limit allows us to understand key features of the instability in detail. Most importantly, we find that a flat moving interface can exhibit an instability. The formation of an outward protrusion results in a reduction of morphogen concentration and thus in a reduction of growth inhibition at the protrusion. As a consequence, the protrusion growth is enhanced and a positive feedback between protrusion growth and morphogen reduction leads to complex branched morphologies. To understand the geometrical and topological properties of the resulting morphologies, we studied the formation of unstable interface patterns in this model beyond the linear stability anal-

ysis. In particular, we combine analytically solvable scenarios of interface motion with the numerical solution of the model to understand how branch distance and thickness are controlled. We use the wavelength of the fastest growing mode in the instability of a flat moving interface as a measure for branch distance and relate branch distance regulation to the interplay of stabilization from the curvature dependency and destabilization from morphogen inhibition. To understand branch thickness regulation, we reduce the complexity of mutual branch inhibition to studying the stationary position of a flat interface. We identify the stationary position of a flat interface as a measure for branch thickness and explain branch thickness regulation from the interplay of interface growth tendency and morphogen inhibition.

In the first part of this thesis (chapter 2 and 3), we demonstrated that branched morphologies can originate from instabilities in morphogen-controlled interface motion and discussed how the interplay of interface motion and morphogen dynamics determines the geometry and topology of the resulting structures. By considering different scenarios of morphogen-controlled interface growth, we demonstrated the robustness and versatility of our approach. So far, however, we have considered only idealized scenarios of interface motion where only morphogen concentration determines interface motion and thus organ growth. In many organisms, however, several other environmental cues influence the growth of branched organs. For example, constraints imposed by the organism shape can influence the overall morphology of branched organs [20, 185]. Moreover, chemical and mechanical cues affect the growth of branched organs and can lead to a orientation of branches along a certain organismal axes [185, 186]. Most importantly, we neglected the influence of organism growth and thus the role of body size for the morphogenesis of branched organs [187]. In the second part of this thesis (chapter 4 and 5), we address these questions in our study of planarian gut branching morphogenesis.

In chapter 4, we present the planarian gut as an example of a highly branched organ that grows and scales along with organism size. We provide a quantitative analysis of the geometrical and size-dependent properties of the planarian gut as well as the shape and size of the planarian body. Our collaborators from the MPINAT in Göttingen (Amrutha Palavalli, Baiqun An, Jochen Rink) performed *in-situ* hybridizations of the planarian gut. They extract a skeleton, i.e. a one pixel wide connectivity-preserving representation of the original data, from their raw data that allows us to extract various quantitative features of planarian gut and body. First, we analyzed the shape and size of the planarian body. We use the convex hull of the skeleton as a measure for the organism outline and show that planarians have a size-dependent aspect ratio with the length increasing faster than the organism width and that planarian body outline is approximately captured by

an ellipse. We perform a similar analysis for the gut-devoid region, where the planarian pharynx resides. We find that this region increases with a similar size-dependent aspect ratio as the organism and its shape can also be approximately captured by an ellipse. These findings inform our choice of boundary conditions in our theoretical study of the planarian gut. Additionally, we studied several geometrical gut properties and in particular their size-dependent behavior. We distinguish primary branch and side branches. The primary branch is the union of the three longest paths of branches starting at the pharynx and we call any remaining branches side branch. We study the symmetry of gut branching morphologies and find that morphologies neither exhibit a symmetric (side branches projecting to the left and right organism half originate at identical positions) nor anti-symmetric configuration (side branches projecting to left and right organism side alternate), but exhibit an intermediate configuration. Moreover, we study branch orientation and show that side branches exhibit a strong orientation towards the organism boundary. Most importantly, we demonstrate the power law scaling of several gut properties (e.g. branch distance or total branch number) with system size. The findings and quantification tools presented in this chapter serve as a basis for our theoretical study of planarian gut branching morphogenesis presented in the next chapter.

To theoretically study the growth and scaling of the planarian gut, we reconsider our continuum model for morphogen-controlled growth and include novel features that are needed to account for the organization of the planarian gut. In contrast to our previous approaches, we take into account the organism shape. Motivated by our quantitative study of planarian and pharynx shape, we study interface motion in a domain of elliptical shape. As a second novelty, we take into account that interface growth can be influenced by external guiding cues. As an example, we consider a second morphogen that forms gradients from the organism boundary to the organism center and assume that interface growth takes place preferably into direction of this morphogen gradient. Most importantly, we include organism growth in our model. The interface is now moved along as the organism grows in addition to its intrinsic tendency to grow, the inhibition through a morphogen, and its curvature dependency.

To understand the formation of branched structures in this model, we first consider a non-growing system and study the *de-novo* formation of gut structures from a primary branch. This minimal, hypothetical scenario allows us to study basic pattern formation principles of this model. Most importantly, irrespective of boundary-related constraints or influences from external guiding cues, the interface robustly undergoes an instability and forms highly branched morphologies. In the absence of external guiding cues, the morphologies are disordered with branches growing along the organism boundary and

undergoing sharp turns. By contrast, for increasing values of coupling between external guiding cue and interface growth, morphologies become ordered and branches increasingly orient towards the organism boundary. Morphology symmetry is controlled by morphogen-mediated interactions between branches in the left and right organism half. Branches initially form in a symmetric configuration, but then transition spontaneously to an anti-symmetric configuration. The reverse transition is prevented by morphogen concentration spreading between the two organism halves. For increasing primary branch thickness, this interaction is suppressed, leading to the formation of symmetric morphologies. Overall, we present a range of simulated gut structures and demonstrate control over its geometrical properties. In particular, we can provide a parameter regime where simulated gut structures share key features with experimental ones.

Next, we employed two scenarios to study the size-dependent properties of the planarian gut. In our first scenario (branching scenario), we study the *de-novo* formation of gut structures from a primary branch in differently sized systems. We a find simple gut organization with side branches extending from the primary branch to the organism boundary without any further side branches. Various gut properties are captured by scaling relations, but as the observed scaling exponents disagree with the experimentally measured ones, we conclude that the branching scenario fails to account for size-dependent planarian gut organization. In an alternative approach (branching with growth scenario), we consider an already formed simulated gut morphology and study its continuous remodeling as organism size increases. Depending on the ratio of gut growth rate to organism growth rate, we find a set of structures ranging from highly branched morphologies with numerous side branches to morphologies that are simply scaled up as organism size increases. Gut properties are described by scaling relations with scaling exponents depending on the ratio of gut growth to organism growth rate. In particular, this range includes a set of exponents in agreement with experimentally measured exponents.

Discussion

Overall, we have provided a novel theoretical framework to study the self-organized growth and scaling of branched organs in biology. Our framework is based on the generation of branched interface morphologies from instabilities and thus has parallels with other unstable interface growth phenomena such as viscous fingering or solidification. For example, in solidification, the interface between liquid and solid region moves under the influence of a temperature field which is governed by the diffusion equation [136]. The formation of interface protrusions results in unstable interface growth due to a positive feedback between

protrusion growth and temperature reduction at the protrusion. Additionally, intrinsic (e.g. molecular structure) and extrinsic cues (e.g. properties of surrounding medium) can alter the morphology of structures [139, 149]. In our approach, the formation of unstable structures is governed by similar principles. The interface representing the organ outline moves under the influence of a morphogen concentration field which is also governed by the diffusion equation. In a similar way to solidification, the formation of a protrusion leads to unstable interface growth and external cues (e.g. second morphogen) can influence organ growth.

Inspired by the formation of branched structures in biology, our approach complements and extends existing studies of unstable interface growth phenomena. While heat and thus the temperature field in solidification is a conserved quantity, morphogen concentration constitutes a non-conserved quantity as it can be produced and undergo degradation. The non-zero degradation rate of morphogen leads to additional length scales that can drastically alter morphologies. For example, we find that the degradation length can suppress the instability (lattice model) or can serve as a control parameter for branch distance and thickness (continuum model). Motivated by the importance of branched organ topology, we established concepts to quantify and control the topology of resulting morphologies. In the lattice model, we use the Euler characteristic to introduce topological constraints into interface growth that lead to the formation of tree-like structures. In the continuum model, we demonstrate the regulation of branch thickness by mutual branch inhibition and use this to generate morphologies with loops (limit of large branch thickness) and with loose branches (limit of small branch thickness). Most importantly, branched organs need to adapt their size and proportion as organism size increases. We include organism growth in our description and demonstrate its drastic effect on branched morphology. In particular, we relate the emergence of scaling relations with the interplay between organism growth and gut growth.

In contrast to other theories of branching morphogenesis, our approach provides instabilities as a physical mechanism for the generation of branched structures and can also be tested experimentally. For example, in a recent approach, branched organs are represented by a set of line segments with active tips. Branch growth is taken into account by a branching and annihilating random walk of active tips and additionally tips become inactive when they are in close proximity to other tips [20]. While this can explain the large scale organization of branched networks, an explanation for the *de-novo* formation of branches and tip termination is lacking. In our approach, branches are formed from an instability and tip termination results from mutual branch inhibition. Size-dependent network properties and, in particular, the scaling of networks is often considered as an

optimization problem [75, 189, 190]. For example, scaling relations of network geometries can be derived from minimizing the energy dissipation of fluid transport [75]. While this predicts scaling relations for various systems correctly, a clear picture of network formation is lacking which makes experimental tests difficult. By contrast, our approach provides a clear physical picture of network formation and, on the basis of this, predicts various experimentally testable scenarios.

Outlook

As a future research direction, we envision to relate gut scaling with the organismal energy budget to study metabolic scaling. The metabolic rate P, defined as the heat production of an organism in a resting state, is a key quantity that characterizes organismal metabolic activity. Interestingly, in numerous organisms (including planarians) the metabolic rate shows power law scaling with body mass M according to $P \propto M^{3/4}$ known as Kleiber's law [65, 74]. As Kleiber's law is found in various animals across an enormous size range, it indicates a fundamental organization principle in animal metabolism. According to a prominent hypothesis, Kleiber's law results from transport limitations that constrain nutrient delivery and thus metabolism [75, 77]. Given the role of the planarian gut for nutrient delivery to the planarian body and the massive available size range, planarians constitute an ideal system to study metabolic scaling. We aim to combine a set of experimental and theoretical approaches to test the transport limitation hypothesis and understand the role of transport limitations for planarian metabolism. For example, we envision to employ our understanding of gut morphogenesis to alter gut structure and monitor for related changes in organism metabolism. Additionally, we can combine existing energy balance models with our continuum model of gut branching morphogenesis to develop a spatial energy balance model. We can include a nutrient field into our description with a source on the gut to identify scenarios in which metabolic scaling can emerge. Overall, our study of gut branching morphogenesis can inspire new experiments and approaches to advance our understanding of metabolic scaling.

Appendix A

Numerical solution of the phase field model

In this appendix, we provide details for the numerical solution of the phase field model presented in chapter 3 and 5. We first state the equations of the phase field model again for completeness. To simplify the numerical solution of the model, we transform the model equations from a growing to non-growing domain. We present the finite-difference discretization of the transformed equation and finally introduce an adaptive step size scheme that we employ to drastically reduce the number of time steps needed. Overall, we present a versatile numerical scheme that allows to study interface dynamics using the phase field method for various geometries in an efficient way.

A.1 Model equations in growing reference frame

The dynamics of the phase field ϕ and the morphogen concentration c is governed by the set of equations

$$\tau\left(\frac{\partial\phi}{\partial t}+\boldsymbol{u}\cdot\boldsymbol{\nabla}\phi\right)=\xi^2\nabla^2\phi+r(\phi) \tag{A.1a}$$

$$\frac{\partial c}{\partial t}+\boldsymbol{u}\cdot\boldsymbol{\nabla}c=D\nabla^2c-[k(\phi)+g_x(t)+g_y(t)]c+s(\phi). \tag{A.1b}$$

To abbreviate the model equations, we introduced the source term r of the phase field model as

$$r(\phi)=2a^2\phi(1-\phi)\left(\phi-\frac{1}{2}+\frac{\hat{\chi}}{2a^2}\right), \tag{A.2}$$

where the energetic bias is defined by $\hat{\chi} = \hat{\Gamma}\hat{\Theta} + \hat{a}\Xi$ together with

$$\hat{\Gamma}(c) = \hat{v}_0 - \hat{\gamma}c(x,y) \tag{A.3a}$$

$$\hat{\Theta} = 1 - \delta\left[1 - \frac{(-\boldsymbol{\nabla}\phi)}{|\boldsymbol{\nabla}\phi|} \cdot \boldsymbol{m}\right]. \tag{A.3b}$$

The noise term Ξ denotes a uniform distribution in the range $[-1/2, 1/2]$. The degradation rate k and the source term s of the morphogen concentration are defined by

$$k(\phi) = k_{\text{in}}\phi + k_{\text{out}}(1-\phi) \tag{A.4a}$$

$$s(\phi) = s_{\text{in}}\phi + s_{\text{out}}(1-\phi). \tag{A.4b}$$

For a detailed discussion of the model parameters we refer the reader to chapter 3 and 5.

A.2 Model equations in non-growing reference frame

To simplify Eq. (A.1), we transform the system dynamics from a growing to a non-growing reference frame by using the transformation

$$\begin{aligned}(x,y,t) &\rightarrow (\tilde{x},\tilde{y},\tilde{t})\\ \tilde{x} &= xe^{-G_x(t)}\\ \tilde{y} &= ye^{-G_y(t)}\\ \tilde{t} &= t.\end{aligned} \tag{A.5}$$

We indicate quantities in the non-growing domain by a $\sim$ symbol and abbreviate the integrated growth rate $G_i(t)$ by

$$G_i(t) = \int_0^t g_i(s)\, ds. \tag{A.6}$$

The transformation from growing to non-growing reference frame in Eq. (A.5) is also commonly used for studying the scaling of morphogen gradients or Turing instabilities in growing domains [191, 192].

According to the transformation given by Eq. (A.5), the phase field ϕ in the growing domain and the phase field $\tilde{\phi}$ in the non-growing domain are related by

$$\begin{aligned}\phi(x,y,t) &= \phi(\tilde{x}e^{G_x(t)}, \tilde{y}e^{G_y(t)}, t)\\ &= \tilde{\phi}(\tilde{x},\tilde{y},\tilde{t}).\end{aligned} \tag{A.7}$$

By using the chain rule, we find that the time-derivative of the phase field ϕ transforms as

$$\frac{\partial \phi}{\partial t} = -g_x x e^{-G_x(t)} \frac{\partial \tilde{\phi}}{\partial \tilde{x}} - g_y y e^{-G_y(t)} \frac{\partial \tilde{\phi}}{\partial \tilde{y}} + \frac{\partial \tilde{\phi}}{\partial \tilde{t}}. \tag{A.8}$$

Likewise, we find for the transformation of first and second spatial derivative of the phase field

$$\frac{\partial \phi}{\partial x} = e^{-G_x(t)} \frac{\partial \tilde{\phi}}{\partial \tilde{x}} \qquad \frac{\partial}{\partial x}\frac{\partial \phi}{\partial x} = e^{-2G_x(t)} \frac{\partial^2 \tilde{\phi}}{\partial \tilde{x}^2}. \tag{A.9}$$

By combining the relations for the transformed derivatives Eq. (A.7) to Eq. (A.9) with the model in the growing reference frame given by Eq. (A.1), we find that the phase field model equations in the non-growing reference frame are given by

$$\tau \frac{\partial \phi}{\partial t} = \xi^2 e^{-2G_x(t)} \frac{\partial^2 \phi}{\partial x^2} + \xi^2 e^{-2G_y(t)} \frac{\partial^2 \phi}{\partial y^2} + r(\phi) \tag{A.10a}$$

$$\frac{\partial c}{\partial t} = D e^{-2G_x(t)} \frac{\partial^2 c}{\partial x^2} + D e^{-2G_y(t)} \frac{\partial^2 c}{\partial y^2} - [k(\phi) + g_x(t) + g_y(t)]c + s(\phi). \tag{A.10b}$$

Most importantly, we find that in the non-growing reference frame the advection term vanishes and time-dependent diffusion constants appear. Thus, we changed the problem from the solution of an advection-diffusion equation to the solution of a diffusion equation, which drastically reduces the problem complexity. Note that the descriptions in growing and non-growing domains are equivalent, but correspond to two different point of views. In the growing reference frame, intrinsic length scales (e.g. reaction-diffusion lengths) maintain their length, but the system size increases. By contrast, in the non-growing reference frame, intrinsic length scales decrease, but the system size increases. As a result, intrinsic length scales and the system size show the same relative behavior irrespective of the chosen reference frame.

In this thesis, we studied interface and thus phase field dynamics in various geometries with different boundary conditions. Since we use the model equations in the non-growing reference frame for their numerical solution, we also define the boundary conditions in the non-growing reference frame. In chapter 3, we studied interface dynamics without organism growth ($g_x = g_y = 0$) in the rectangular geometry

$$\Omega_\mathrm{r} = \{(x, y) | x \in [0, L_y], y \in [0, L_y]\}. \tag{A.11}$$

We used the no-flux boundary conditions

$$\partial_y \phi(x,0) = 0 \qquad \partial_y c(x,0) = 0 \tag{A.12a}$$

$$\partial_y \phi(x,L_y) = 0 \qquad \partial_y c(x,L_y) = 0 \tag{A.12b}$$

at the bottom ($y = 0$) and top ($y = L_y$) boundary along with the periodic boundary conditions

$$\phi(0,y) = \phi(L_x,y) \qquad c(0,y) = c(L_x,y) \tag{A.13}$$

at the left ($x = 0$) and right ($x = L_x$) boundary. In chapter 5, we studied interface and thus phase field dynamics in an elliptic domain Ω_w with a hole Ω_p in it as defined by

$$\Omega_\mathrm{w} = \{(x,y)| \left|\frac{x-x_0}{L_x/2}\right|^2 + \left|\frac{y-y_0}{L_y/2}\right|^2 \leq 1\} \tag{A.14a}$$

$$\Omega_\mathrm{p} = \{(x,y) \left|\frac{x-x_{\mathrm{p},0}}{\ell_x/2}\right|^2 + \left|\frac{y-y_{\mathrm{p},0}}{\ell_y/2}\right|^2 \leq 1\}. \tag{A.14b}$$

We used no-flux boundary conditions for phase field and morphogen concentration on the domain boundaries $\partial\Omega_\mathrm{w}$ and $\partial\Omega_\mathrm{p}$. Additionally, we defined a region Ω_pb where $\phi = 1$ holds in order to model the primary branch. In all cases, we use $\phi(x,y) = 0$ and $c(x,y) = 0$ as initial condition at $t = 0$.

A.3 Finite difference discretization

We employ the finite difference method for the numerical solution of the model equations in the non-growing reference frame [193–195]. We discretize positions x, y, and time t by using the grid

$$x_i = i\Delta x \qquad i = 0,\cdots,N_x - 1 \tag{A.15a}$$

$$y_j = j\Delta y \qquad j = 0,\cdots,N_y - 1 \tag{A.15b}$$

$$t_n = n\Delta t \qquad n = 0,\cdots,N_t - 1, \tag{A.15c}$$

where $\Delta x = L_x/N_x$, $\Delta y = L_y/N_y$, and $\Delta t = T/N_t$ denote the grid spacing and N_x, N_y, and N_t denote the number of grid points used for the discretization. We further introduce

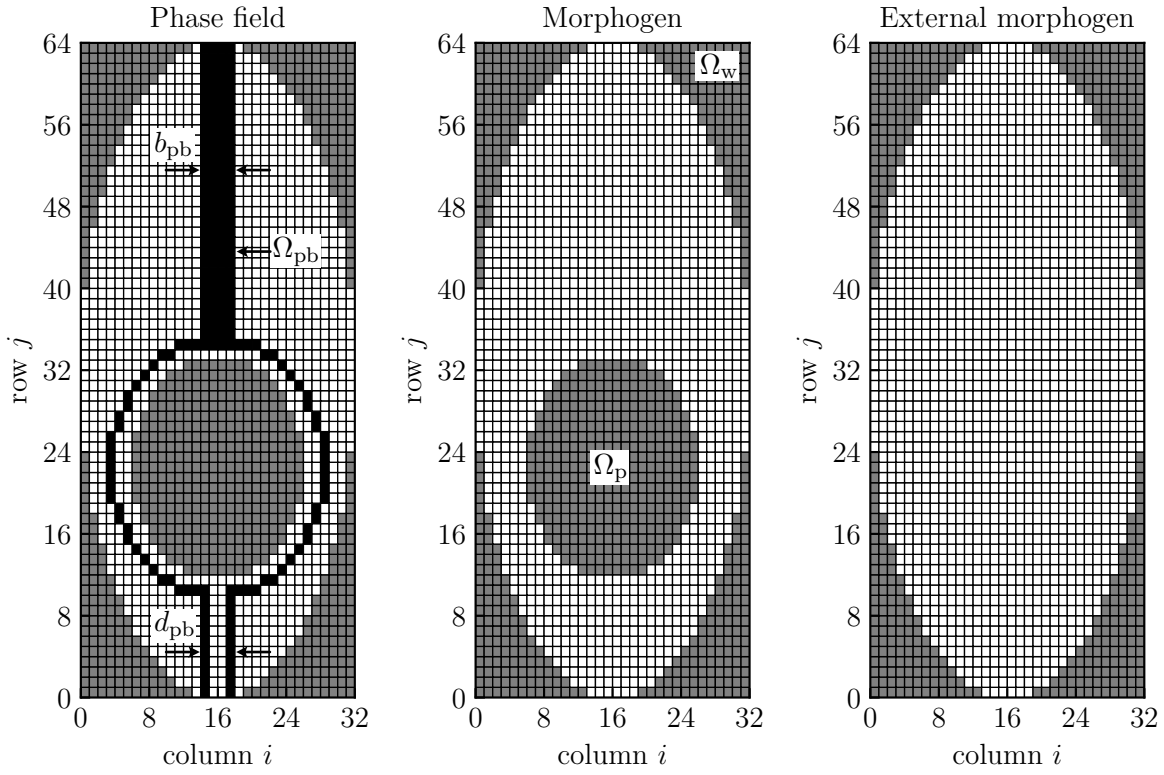

Figure A.1: Computational domain of the discretized equations. We show the computational domains employed for the phase field, morphogen concentration, and external morphogen concentration in chapter 5. We show the primary branch domain Ω_{pb}, the worm domain Ω_{w} (large white ellipse), the pharynx domain Ω_{p} (small gray domain), and the simulation domain $\Omega = \Omega_{\mathrm{w}} \setminus \Omega_{\mathrm{p}}$.

the abbreviations

$$\phi(x_i, y_j, t_n) = \phi_{i,j}^n \qquad\qquad c(x_i, y_j, t_n) = c_{i,j}^n \tag{A.16}$$

for the values of phase field and morphogen concentration at grid points.

To discretize derivatives, we use forward, backwards, and also centered finite difference discretizations [195]. For time derivatives we employ both the forward difference approximation

$$\frac{\partial \phi}{\partial t}(x_i, y_j, t_n) = \frac{\phi_{i,j}^{n+1} - \phi_{i,j}^n}{\Delta t} + \mathcal{O}(\Delta t) \tag{A.17}$$

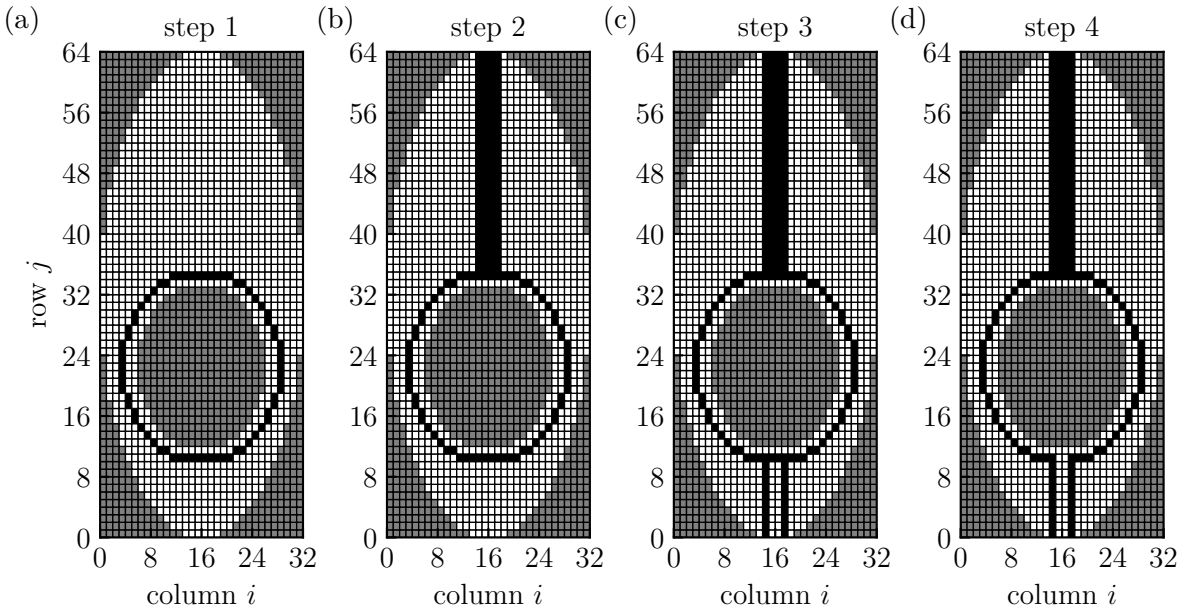

Figure A.2: Construction of primary branch domain $\Omega_{\mathbf{pb}}$. The construction of the primary branch domain proceeds in four steps. (a) We first draw an ellipse around $(x_{\mathrm{p},0}, y_{\mathrm{p},0})$ with minor axis $l_{\mathrm{p},x}$ length and major axis length $l_{\mathrm{p},y}$ that serves as the part of the primary branch enclosing the pharynx region. (b) Next, we draw a straight line with width b_{pb} from the top of the system to the intersection pharynx enclosing ellipse. (c) We draw two parallel straight lines with distance d_{pb} from the bottom of the system to the pharynx enclosing ellipse. (d) Finally, we remove the part of the pharynx-enclosing ellipse between the previously drawn parallel lines.

and the backward difference approximation

$$\frac{\partial \phi}{\partial t}(x_i, y_j, t_n) = \frac{\phi_{i,j}^n - \phi_{i,j}^{n-1}}{\Delta t} + \mathcal{O}(\Delta t). \tag{A.18}$$

We use the the backward difference approximation for first order spatial derivatives

$$\frac{\partial \phi}{\partial x}(x_i, y_j, t_n) = \frac{\phi_{i+1,j}^n - \phi_{i,j}^n}{\Delta x} + \mathcal{O}(\Delta x) \tag{A.19}$$

and the centered difference approximation for the second order spatial derivatives

$$\frac{\partial^2 \phi}{\partial x^2}(x_i, y_j, t_n) = \frac{\phi_{i+1,j}^n - 2\phi_{i,j}^n + \phi_{i-1,j}^n}{\Delta x^2} + \mathcal{O}(\Delta x^2). \tag{A.20}$$

To derive the discretized versions of the coupled partial differential equations, we replaced derivatives with their respective finite difference approximations. Using the forward difference in time and centered difference in space we find for the discretized phase field

equation

$$\phi_{i,j}^{n+1} - \phi_{i,j}^{n} = F_{\phi,x}^{n}(\phi_{i+1,j}^{n} - 2\phi_{i,j}^{n} + \phi_{i-1,j}^{n}) + F_{\phi,y}^{n}(\phi_{i,j+1}^{n} - 2\phi_{i,j}^{n} + \phi_{i,j-1}^{n}) + \frac{1}{\tau} r(\phi_{i,j}^{n}), \tag{A.21}$$

where we have introduced the dimensionless Fourier numbers [195]

$$F_{\phi,x}^{n} = \frac{\xi^2}{\tau}\frac{\Delta t}{\Delta x^2} e^{-2G_x(t_n)} \qquad F_{\phi,y}^{n} = \frac{\xi^2}{\tau}\frac{\Delta t}{\Delta x^2} e^{-2G_y(t_n)}. \tag{A.22}$$

Note that Eq. (A.21) constitutes an explicit scheme since it provides an explicit relation for the calculation of phase field values at time t_{n+1} from phase field values at times t_n. Using the backward difference in time and the centered difference in space we find the discretized morphogen concentration equations

$$\begin{aligned} c_{i,j}^{n+1} - c_{i,j}^{n} = F_{c,x}^{n+1}(c_{i+1,j}^{n+1} - 2c_{i,j}^{n+1} + c_{i-1,j}^{n+1}) + F_{c,y}^{n+1}(c_{i,j+1}^{n+1} - 2c_{i,j}^{n+1} + c_{i,j-1}^{n+1}) \\ -k(\phi_{i,j}^{n+1})\Delta t c_{i,j}^{n+1} + s(\phi_{i,j}^{n+1})\Delta t \end{aligned} \tag{A.23}$$

together with the dimensionless Fourier numbers

$$F_{c,x}^{n} = D\frac{\Delta t}{\Delta x^2} e^{-2G_x(t_n)} \qquad F_{c,y}^{n} = D\frac{\Delta t}{\Delta x^2} e^{-2G_y(t_n)}. \tag{A.24}$$

This constitutes an implicit scheme since Eq. (A.23) provides a set of coupled linear equations that we need to solve to obtain concentration values at time step t_{n+1}. We use an explicit scheme for the phase field equations since explicit schemes are simple also for nonlinear equations. However, as we will see below this comes with the disadvantage that the step size Δt can not be chosen arbitrarily large. Implicit schemes are unconditionally stable, but have the disadvantage that a set of coupled equations needs to be solved.

The rectangular and worm-like computational domains along with the respective boundary conditions can be addressed with the finite difference method in a straightforward way. To study the model dynamics in the rectangular domain Ω_r, we use the grid introduced in Eq. (A.15). We replace grid points in the finite difference schemes that lie outside the grid by using a discretized version of the respective boundary conditions [195]. For example, we use the discretized no-flux boundary conditions

$$\frac{\phi_{0,j}^{n} - \phi_{-1,j}^{n}}{\Delta x} = 0 \qquad \frac{\phi_{N_y,j}^{n} - \phi_{N_y-1,j}^{n}}{\Delta x} = 0 \tag{A.25}$$

of the phase field at the bottom and top boundary to eliminate grid points $\phi_{-1,j}$ and

$\phi_{N_y-1,j}$ and likewise for the morphogen concentration. We use the discretized version of the periodic boundary conditions

$$\phi_{i,-1} = \phi_{i,N_y-1} \qquad \phi_{i,N_y} = \phi_{i,0} \tag{A.26}$$

to eliminate grid points $\phi_{i,-1}$ and ϕ_{i,N_y} and likewise for the morphogen concentration. To study model dynamics in the worm like domain, we again employ the grid introduced in Eq. (A.15). We use the finite difference schemes for grid points in Ω along with the respective replacements at the boundaries. We enforce the value $\phi_{i,j} = 1$ for grid points in Ω_{pb}.

We construct the primary branch domain Ω_{pb} in a four-step procedure. We first draw the boundary of an ellipse centered at $(x_{\mathrm{p},0}, y_{\mathrm{p},0})$ with minor axis length $l_{\mathrm{p},x}$ and major axis length $l_{\mathrm{p},y}$ (Fig. A.2a) This ellipse serves as the part of the primary branch that encloses the pharynx region. Next, we draw a straight line with thickness b_{pb} from the top of the computational domain to its intersection with the pharynx enclosing part of the primary branch (Fig. A.2b). Next, we draw two parallel straight lines with distance d_{pb} from the bottom of the system to the pharynx enclosing part of the primary branch (Fig. A.2c). Finally, we remove the pharynx enclosing part of the primary branch between the two parallel straight lines (Fig. A.2d).

To efficiently implement the numerical solution of the model equations, we rewrite the finite difference schemes in vector form. While the update scheme for the phase field dynamics is easily implemented, the update scheme for the morphogen concentration constitutes an implicit equation, which we solve by using the conjugate gradient method [162].

A.4 Numerical stability and non-uniform step size scheme

We now discuss the numerical stability of the finite difference schemes Eq. (A.21) and Eq. (A.23). This provides us with criteria for choosing step size Δt and grid resolution Δx and Δy. Moreover, it will allow us to propose an adaptive step size scheme that satisfies the constraints imposed by numerical stability, but also reduces the number of time steps needed.

To understand the numerical stability of the finite difference scheme Eq. (A.21) for the phase field, we study the (reduced) scheme

$$\phi_{i,j}^{n+1} - \phi_{i,j}^{n} = F_{\phi,x}(\phi_{i+1,j}^{n} - 2\phi_{i,j}^{n} + \phi_{i-1,j}^{n}) + F_{\phi,y}(\phi_{i,j+1}^{n} - 2\phi_{i,j}^{n} + \phi_{i,j-1}^{n}), \tag{A.27}$$

where we consider the time-independent Fourier numbers F_ϕ and neglected the source term r to simplify analysis. Even though we consider only a reduced finite difference scheme, the analysis of its numerical stability will still provide useful qualitative predictions. We employ the Neumann analysis as a basic tool for studying the numerical stability of linear finite difference schemes with constant coefficients [195]. According to this analysis, we study the time dependence of the solutions $\phi_{i,j}^n$ by making the ansatz

$$\phi_{l,j}^n = A^n e^{iq_x l\Delta x} e^{iq_y j\Delta y}, \tag{A.28}$$

where A denotes the amplification factor[1]. A numerical scheme is called stable if $|A| < 1$ holds for all Fourier modes. By inserting the ansatz into Eq. (A.27) and solving for A, we find

$$A = 1 - 4F_{\phi,x}\sin^2\left(\frac{q_x\Delta x}{2}\right) - 4F_{\phi,y}\sin^2\left(\frac{q_y\Delta y}{2}\right) \tag{A.29}$$

and conclude that the reduced numerical scheme is stable if $F_{\phi,x} + F_{\phi,y} < \frac{1}{2}$ holds. Due to the dependency of the Fourier numbers on the step size and grid spacing, this relation constitutes a constraint for the chosen discretization. Note that this finding is in qualitative agreement with our observations for the full finite difference scheme. There we found heuristically that for numerical stability $F_{\phi,x} + F_{\phi,y} < c$ needs to hold, where c is a constant that depends on the model parameters and was found to be $c < 1/2$.

To understand the stability of the numerical scheme of the morphogen concentration, we proceed in a similar way. We use the (reduced) scheme

$$\begin{aligned} c_{i,j}^{n+1} - c_{i,j}^n = F_{c,x}(c_{i+1,j}^{n+1} - 2c_{i,j}^{n+1} + c_{i-1,j}^{n+1}) + F_{c,y}(c_{i,j+1}^{n+1} - 2c_{i,j}^{n+1} + c_{i,j-1}^{n+1}) \\ -k(\phi_{i,j}^{n+1})\Delta t c_{i,j}^{n+1}, \end{aligned} \tag{A.30}$$

where we assumed time-independent Fourier numbers F_c and neglected the concentration-independent source term s as it is irrelevant for the numerical stability. We insert the ansatz

$$c_{l,j}^n = A^n e^{iq_x l\Delta x} e^{iq_y j\Delta y}, \tag{A.31}$$

into Eq. (A.30) and determine the amplification factor A:

$$A = \frac{1}{1 + 4F_{c,x}\sin^2\left(\frac{q_x\Delta x}{2}\right) + 4F_{c,y}\sin^2\left(\frac{q_y\Delta y}{2}\right) + k\Delta t} \tag{A.32}$$

[1]Note that the superscript indicates a power, not the time step.

According to this, the numerical scheme is stable irrespective of grid resolution Δx, Δy, and temporal step size Δt.

The conditions for numerical stability and the interface properties presented in chapter 3 inform our choices of step size Δt and grid spacing Δx and Δy. We choose the grid spacing such that an interface of width w can be resolved ($\Delta x = \Delta y \approx w$). In the case of a growing organism the interface width decreases and we ensure that the smallest encountered interface width is resolved. For given grid spacing Δx and Δy, the numerical stability of the explicit Euler scheme employed for the phase field equation determines the allowed step size Δt. For a given grid spacing, we choose step size Δt such that the sum of Fourier numbers is smaller than an empirically found threshold c at every time step.

An important constraint of our numerical scheme is the limitation on Fourier numbers and thus the time step Δt introduced by the explicit scheme used to discretize the phase field equation. For a given grid spacing the time step Δt needs to be chosen small enough to ensure numerical stability. However, we can relax the constraint imposed on time steps for simulations with non-zero growth rate due to the time-dependency of Fourier numbers in this case. For example, for simulations including constant growth rates g_i, the Fourier number decreases exponentially in time and the time step Δt can be increased exponentially in time without affecting numerical stability. In general, we can choose the time step

$$\Delta t = F^0_{\phi,x} \frac{\tau}{\xi^2} \Delta x^2 e^{2G(t_n)} \tag{A.33}$$

for simulations with non-zero growth rate g_i, where we introduced $G = \min(G_x, G_y)$ and also assumed a square grid ($\Delta x = \Delta y$). The corresponding sequence of time points t_n at which we obtain the solution then reads

$$t_{n+1} = F^0_{\phi,x} \frac{\tau}{\xi^2} \Delta x^2 e^{2G(t_n)} + t_n \tag{A.34}$$

and we find for the Fourier numbers at every time step

$$F^n_{\phi,x} = F^0_{\phi,x}\, e^{2(G(t_n) - G_x(t_n))t_n} \qquad F^n_{\phi,y} = F^0_{\phi,y}\, e^{2[G(t_n) - G_y(t_n)]}, \tag{A.35}$$

where we used $G = \min(G_x, G_y)$. Given that numerical stability holds for the initial Fourier numbers, our adaptive step size scheme maintains numerical stability throughout the simulation while drastically reducing the number of time steps employed.

Appendix B

Sharp-interface limit of the phase field equations

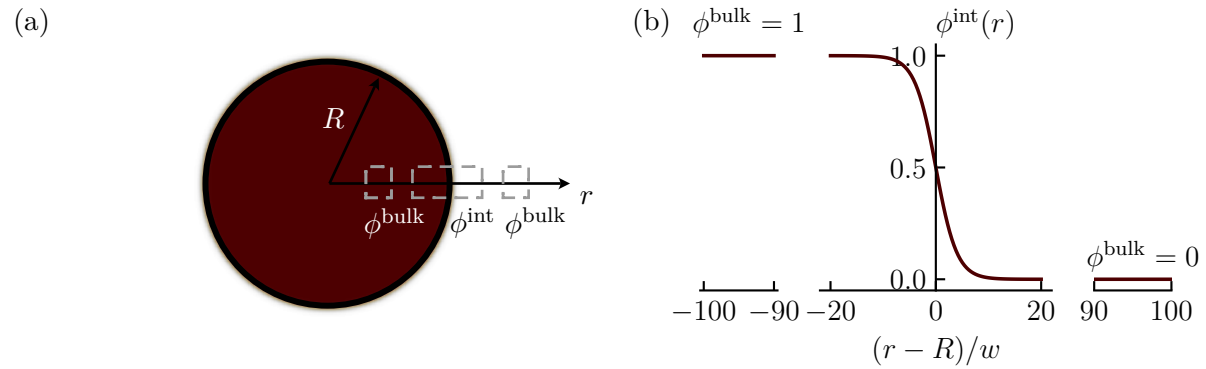

Figure B.1: Sharp interface limit of the phase field method. (a) We show a circular structure obtained with the phase field method (brown) along with its interface (black). We denote the radial coordinate by r and the interface position by R. ϕ^{int} and ϕ^{bulk} denote the phase field value near and far away from the interface, respectively. (b) Radial cross section of the phase field profile shown in (a). We use w to denote the interface width.

In this section, we establish the connection between the phase field model given by Eq. (A.1) presented in the previous section and the corresponding sharp interface limit presented in the main text by following the approach presented in Refs. [144, 196, 197]. We consider a radially symmetric phase field profile $\phi(r, t)$ with an interface located at position R. We study the limit of small interface width $w \to 0$ while the mobility μ and the surface tension σ are held constant. In particular, we assume that the interface width is small compared to the radius R ($w/R \ll 1$) and to the diffusion degradation lengths λ_i ($w/\lambda_i \ll 1$). Moreover, we assume that for an interface moving with a velocity v the diffusive timescale $t_{\text{d}} = w^2\mu$ is much smaller than the advective time scale $t_{\text{a}} = v/w$ of

the phase field equation, i.e. we assume the interface Péclet number $vw\mu$ is small. We derive an approximation ϕ^{bulk} for the phase field ϕ that is valid for regions far away from the interface. Likewise, we derive an approximation ϕ^{int} of the phase field ϕ that is valid near the interface. We then use these approximations and relate them to Eq. (5.1) of the sharp interface limit and derive boundary conditions between the different regions.

Bulk region

We first derive the approximations ϕ^{bulk} and c^{bulk} for the phase field and morphogen concentration in the bulk region, i.e. in regions far away from the interface. We rewrite the phase field equation from Eq. (A.1a) in the form

$$\mu w^2 \left[\partial_t \phi + \boldsymbol{u} \cdot \boldsymbol{n}\, \partial_r \phi\right] = w^2 \partial_r^2 \phi + \frac{w}{r} \partial_r \phi + \frac{1}{2} f_{\text{s}}'(\phi) + \frac{w}{6\sigma} \frac{\hat{\chi}}{6} f_{\text{t}}'(\phi), \tag{B.1}$$

where we have expressed all parameters in terms of the interface width w and otherwise constant parameters. We used polar coordinates to express gradients and the Laplacian and employed the symmetric part f_{s} and tilting f_{t} of the bulk energy contribution defined in Eq. (3.38). In the limit of small interface width w, gradients in the phase field dynamics in Eq. (B.1) can be neglected far away from the interface and the phase field equation reads

$$f_{\text{s}}'(\phi^{\text{bulk}}) = 0. \tag{B.2}$$

The symmetric part f_{s} of the bulk energy contribution has minima at $\phi = 0, 1$ and therefore we find that far away from the interface, the phase field takes the values

$$\phi^{\text{bulk}} = 0, 1. \tag{B.3}$$

Using the bulk values ϕ^{bulk} and inserting them into Eq. (A.1b), we find

$$\partial_t c^{\text{bulk}} + \boldsymbol{u} \cdot \boldsymbol{\nabla} c^{\text{bulk}} = D \nabla^2 c^{\text{bulk}} - [k(\phi^{\text{bulk}}) + g_x + g_y] c^{\text{bulk}} + s(\phi^{\text{bulk}}). \tag{B.4}$$

For $\phi^{\text{bulk}} = 1$, this gives the dynamics for the "in" and for $\phi^{\text{bulk}} = 0$, we recover the dynamics for the "out" region.

Interface region

To examine the behavior of morphogen concentration and phase field near the interface, we use the coordinate transformation

$$\tilde{r} = \frac{r - R}{w}. \tag{B.5}$$

With this transformation we move to a reference frame that is comoving with an interface located at position R. Moreover, the rescaling ("stretching") of $\tilde{r}$ with the interface width allows us to study the phase field and morphogen profiles near the interface. We first apply this transformation to the phase field dynamics in Eq. (B.1) and find

$$\mu w^2 \left[\partial_t \phi - v_n \frac{1}{w}\partial_{\tilde{r}}\phi + \boldsymbol{u}(w\tilde{\boldsymbol{r}} + \boldsymbol{R}) \cdot \boldsymbol{n}\frac{1}{w}\partial_{\tilde{r}}\phi\right] = \partial_{\tilde{r}}^2\phi + \frac{w}{w\tilde{r} + R}\partial_{\tilde{r}}\phi + \frac{1}{2}f_{\mathrm{s}}'(\phi) + \frac{w}{6\sigma}\frac{\hat{\chi}}{6}f_{\mathrm{t}}'(\phi), \tag{B.6}$$

where we have used $v_n = \dot{R}$. In the limit $w \to 0$, we find that near the interface the behavior of ϕ is governed by

$$0 = \partial_{\tilde{r}}^2\phi^{\mathrm{int}} + \frac{1}{2}f_{\mathrm{s}}'(\phi^{\mathrm{int}}). \tag{B.7}$$

To ensure that the solution ϕ^{int} approaches the values of values of the phase field in the bulk region for the limit $\phi^{\mathrm{int}}(\tilde{r} \pm \infty)$, we solve this equation using the boundary conditions $\phi^{\mathrm{int}}(-\infty) = 1$ and $\phi^{\mathrm{int}}(\infty) = 0$. The phase field profile near the interface is given by

$$\phi^{\mathrm{int}}(\tilde{r}) = \frac{1}{2}\left[1 - \tanh\left(\frac{\tilde{r}}{2}\right)\right]. \tag{B.8}$$

Note that this is a rescaled version of the 1D phase field profile Eq. (3.42) with $v = 0$. Thus, we find that the phase field profile of a weakly curved interface is locally given by a 1D phase field profile.

To study the morphogen concentration near the interface, we apply the transformation Eq. (B.5) to Eq. (A.1b) and find

$$\frac{w^2}{D}\left[\partial_t c - v_n \frac{1}{w}\partial_{\tilde{r}}c + \boldsymbol{u}(w\tilde{\boldsymbol{r}} + \boldsymbol{R}) \cdot \boldsymbol{n}\frac{1}{w}\partial_{\tilde{r}}c\right] = \partial_{\tilde{r}}^2 c + \frac{w}{\tilde{r}w + R}\partial_{\tilde{r}}c - \frac{w^2}{D}[k(\phi) + g_x + g_y]c + \frac{w^2}{D}s(\phi). \tag{B.9}$$

In the limit $w \to 0$ we find that the morphogen concentration c^{int} near the interface is

governed by

$$\partial_{\tilde{r}}^2 c^{\text{int}} = 0. \tag{B.10}$$

From this, it follows that $c^{\text{int}}(\tilde{r}) = A\tilde{r} + B$, where A, B are integration constants. Since the morphogen concentration c^{int} has to be bounded for $\tilde{r} \to \infty$, we conclude that $A = 0$ and obtain $c^{\text{int}}(\tilde{r}) = \text{const}$, i.e. that the morphogen concentration near the interface is constant.

Interface velocity and boundary conditions at the interface

We calculate the interface velocity v_n by performing an integration of the governing equation of ϕ in a neighborhood of size ℓ around the interface. We choose the neighborhood such that $w \ll \ell \ll \lambda_i$. The governing equation of ϕ at the interface position R reads

$$\mu w^2 \left[-v_n \partial_r \phi - \boldsymbol{u}(\boldsymbol{R}) \cdot \boldsymbol{n} \partial_r \phi - \boldsymbol{u}(\boldsymbol{r}) \cdot \boldsymbol{n} \partial_r \phi\right] = w^2 \left[\partial_r^2 \phi + \frac{1}{r+R} \partial_r \phi\right] + \frac{w}{6\sigma} f'(\phi). \tag{B.11}$$

We multiply both sides by $\partial_r \phi$ and integrate over $R - \ell \ll r \ll R + \ell$ and find

$$\mu w^2 \frac{1}{6w} \left[-v_n - \boldsymbol{u}(\boldsymbol{R}) \cdot \boldsymbol{n}\right] = w^2 \frac{1}{6w} \frac{1}{R} + \frac{w}{6\sigma} \frac{\hat{\chi}}{6}, \tag{B.12}$$

where we have used $\int (\partial_r \phi)^2 = 1/(6w)$. We then arrive at the relation for interface velocity

$$v_n = \frac{1}{\mu} \left[\frac{\hat{\chi}}{6\sigma} - \frac{1}{R}\right] + \boldsymbol{u}(\boldsymbol{R}) \cdot \boldsymbol{n} \tag{B.13}$$

and recall that $\hat{\chi} = \hat{\Gamma}\hat{\Theta} + \hat{a}\Xi$ with

$$\hat{\Gamma}(c) = \hat{v}_0 - \hat{\gamma} c(x, y) \tag{B.14a}$$

$$\hat{\Theta} = 1 - \delta \left[1 - \frac{(-\boldsymbol{\nabla}\phi)}{|\boldsymbol{\nabla}\phi|} \cdot \boldsymbol{m}\right]. \tag{B.14b}$$

This relation Eq. (B.13) for interface velocity is central as it allows us to relate quantities in the phase field model (with hat) to quantities in the continuum model (without hat).

To relate parameters in the phase field and continuum model, we first recall the interface dynamics in the continuum model

$$v_n = \Gamma\Theta - \beta\kappa + \boldsymbol{u} \cdot \boldsymbol{n} + a\Xi \tag{B.15}$$

together with

$$\Gamma = v_0 - \gamma c \tag{B.16a}$$

$$\Theta = 1 - 2\delta \sin^2(\theta/2) \tag{B.16b}$$

By comparing Eq. (B.13) and Eq. (B.15), we make the identifications $v_0 = \frac{\xi/a}{\tau}\hat{v}_0$, $\gamma = \frac{\xi/a}{\tau}\hat{\gamma}$, and $\beta = \frac{\xi^2}{\tau}$. For the case of a non-zero noise amplitude $\hat{a}$ that is added to $\hat{\chi}$, we find $a = \frac{\xi/a}{\tau}\hat{a}$. We can derive the dependency of interface growth on external orientation field by using the relation [196]

$$\frac{(-\boldsymbol{\nabla}\phi)}{|\boldsymbol{\nabla}\phi|} = \boldsymbol{n}, \tag{B.17}$$

which holds for $w \to 0$. We use $\boldsymbol{n}\cdot\boldsymbol{m} = \cos(\theta)$ together with the trigonemetric identity $1 - \cos(\theta) = 2\sin^2(\theta/2)$ and obtain $\Theta = 1 - 2\delta\sin^2(\theta/2)$. Since the morphogen concentration near the interface is constant, the boundary conditions Eq. (5.6) follow trivially.

Appendix C

Morphometry of branched patterns

In this appendix, we present details on various quantifications of branched structures that we used in the main text.

C.1 Quantifying branch distance and branch thickness

To determine the branch distance and thickness in phase field simulations of systems with rectangular geometry, we first obtain the binarized phase field $\bar{\phi}$ and its skeleton (Fig. C.1a). The binarized phase field is defined on the basis of the phase field ϕ by

$$\bar{\phi} = \begin{cases} 1 & \phi > 1/2 \\ 0 & \phi \leq 1/2 \end{cases}. \tag{C.1}$$

The skeleton is a one-pixel wide representation of the binarized phase field $\bar{\phi}$ with the same conncectivity as $\bar{\phi}$ and was obtained with the skeletonization algorithm implemented in the scikit package [198, 199]. The binarized phase field and its skeleton are central to our analysis and allow us to determine branch distance and thickness in a simplified manner.

For the quantification of branch distance and thickness, we consider each row j of the discretized and binarized phase field $\bar{\phi}_{ij}$ and skeleton separately (Fig. C.1bc) Considering each row in turn, we determined the distance d_k of subsequent peaks in the skeleton and the length b_k of regions of consecutive 1s. The branch distance d and thickness b corresponding to the entire phase field configuration is then determined from the arithmetic mean

$$d = \frac{1}{N_d} \sum_k d_k \qquad\qquad b = \frac{1}{N_b} \sum_k b_k \tag{C.2}$$

of the respective quantity, where N_d denotes the total number of all regions between peaks

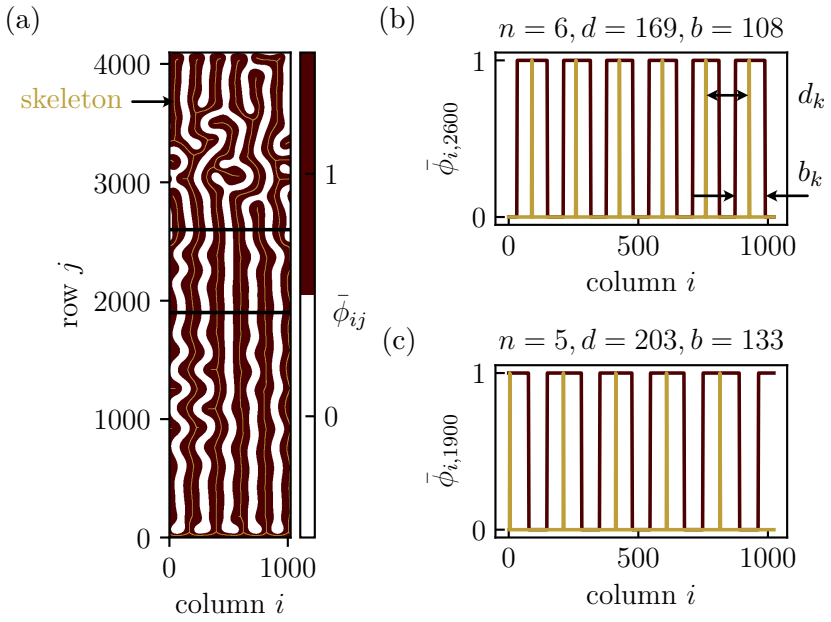

Figure C.1: Quantification of branch distance d and thickness b in a rectangular geometry. (a) We show the binarized phase field $\bar{\phi}_{ij}$ resulting from a simulation of the model presented in chapter 3. (b,c) We show the binarized phase field $\bar{\phi}_{ij}$ (brown) and skeleton (yellow) for two example rows from the image shown in (a). We indicate the distance d_k of two peaks of the skeleton and the length b_k of a region of consecutive 1s in the binarized phase field. In each case, we show the number n of periods in the respective row, the mean branch distance d, and mean branch thickness b for the row.

in the skeleton and N_b denotes the total number of regions of consecutive 1s. The error shown along with the mean in the main text corresponds to the standard deviation of d_k and b_k. Note that our method takes into account periodic boundary conditions. To demonstrate this, we applied our method to a row corresponding to a branch configuration with and without overlap at the system boundary (Fig. C.1b,c). In both cases, the number n of periods in the row is correctly estimated.

C.2 Definition of branch points

The identification of branch points in the skeleton of gut structures obtained from experiments and simulations is a central element of our analysis. The classification of a lattice site (i, j) as branch point or tip is based on local 3×3 neighborhood around the respective lattice site (Fig. C.2). An occupied lattice site ($n_{ij} = 1$) is called a threefold branch point if it has more than two occupied neighbors and the local neighborhood has three unoccupied non-connected regions. Similarly, we call an occupied lattice site a fourfold branch point if

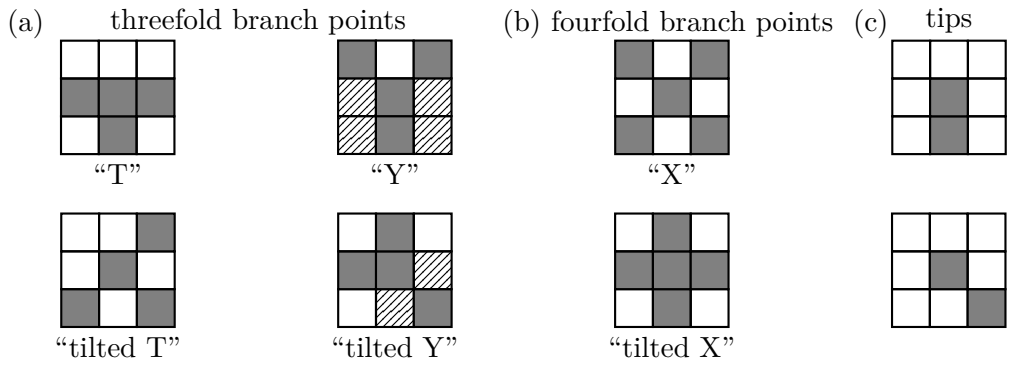

Figure C.2: Definition of branch points and tips. The definition of branch points and tips is based on local, 3×3 neighborhoods that contain occupied ($n_{ij} = 1$) and unoccupied ($n_{ij} = 0$) sites. (a) Threefold branch points are occupied lattice sites with more than two occupied neighbors and a neighborhood with three unoccupied non-connected regions. (b) Fourfold branch points are occupied lattice sites with more than two occupied neighbors and a neighborhood with four unoccupied non-connected regions. (c) Tips are occupied lattice sites with exactly one occupied neighbor.

it has more than two occupied neighbors, but the local neighborhood is divided into four unoccupied non-connected regions. Finally, we call an occupied lattice site a tip if it has exactly one occupied neighbor. Thus, the local neighborhood of a tip has one unoccupied connected region. We identify the local neighborhoods satisfying these criteria (Fig. C.2) and label tips and branch points accordingly in the skeleton (Fig. C.3).

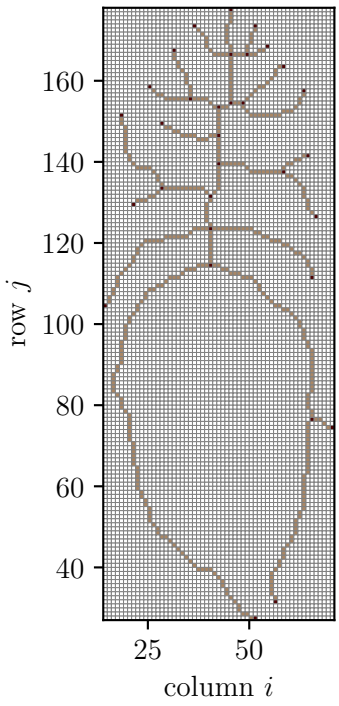

Figure C.3: Identification of vertices. We show the branch points and tips (dark brown) obtained in a skeleton of an experimental gut structure from the vertex definitions shown in Fig. C.2

Appendix D

Parameter values used in this thesis

In this chapter, we provide parameter values and additional information that is needed to generate the data used in this thesis.

In Fig. 5.9, we used the following procedure to generate differently sized organisms. We first choose $g_y = 1$ and $g_x = r g_y$, where r is the anisotropy parameter. We choose organism size according to $L_i = L_{i,0} e^{g_i t}$ with $t \in [0, \frac{1}{g_x + g_y} \log(s_A)]$, where s_A denotes the relative area increase and was $s_A = 65$. In Fig. 5.8a, we adopt a similar strategy, but choose $L_i = L_{i,0} e^{g_i t}$ with $t \in [0, \frac{1}{g_y} \log(s_L)]$, where s_L denotes the relative length increase. In both cases, we adapt the relative pharynx size l_x/L_x, l_y/L_y, and pharynx position y_p/L_y to organism size as follows. We found that relative pharynx size and position obey the function

$$f(s) = a e^{-s_L/b} + c, \tag{D.1}$$

where the parameter values for the respective cases are

l_x/L_x :	$a = 0.22$	$b = 1.23$	$c = 0.20$
l_y/L_y :	$a = 0.16$	$b = 1.52$	$c = 0.07$
y_p/L_y :	$a = -0.21$	$b = 5.24$	$c = 0.59.$

These parameters were initially determined from a fit of the corresponding data with respect to system length using Eq. (D.1), but afterwards adjusted, as for example the pharynx region in small worms was found to be too large and almost collided with the organism boundary. We additionally employed $l_{\mathrm{p},x} = 1.15 l_x$ and $l_{\mathrm{p},y} = 1.15 l_y$ for the elliptical part of the primary branch around the pharynx in both figures. In both figures, we additionally employed the rescaling $\tilde{D}^i_\mathrm{ext} = (L_i/L_{i,0})^2 D^i_\mathrm{ext}$, where $\tilde{D}^i_\mathrm{ext}$ denotes the diffusion constant of the external morphogen in a system of increased size. This rescaling adjusts the degradation length of the second morphogen with system size.

Table D.1: Parameters used in chapter 2.

Symbol	Unit	Fig. 2,6	Fig. 3,7c	Fig. 3,7d	Fig. 8
N	/	250	512	512	100
a	a	1	1	1	1
M	/	7500	10000	10000	1000
k_+^0	k_+^0	1	1	1	1
k_-^0	k_+^0	0	0	0	-1
D	$a^2 k_+^0$	1	1	$[1, 10^{12}]$	1
k_{in}	k_+^0	10000	10000	10000	10000
k_{out}	k_+^0	$1.6 \cdot 10^{-9}$	$[3.81 \cdot 10^{-1}, 3.82 \cdot 10^{-11}]$	$[4 \cdot 10^{-10}, 3.81 \cdot 10^{2}]$	$1.6 \cdot 10^{-9}$
s_{in}	k_+^0	10000	1	1	10000
s_{out}	k_+^0	0	0	0	0

In Fig. 5.10 and Fig. 5.11 we used the following procedure to generate differently sized organisms. Given a range of growth rates g_y, we determined $g_x = r g_y$ and run the simulation for $T = \frac{1}{g_y} \log(s_L)$ with $s_L = 9.5$.

Table D.2: Parameters used in chapter 3. Note that in the last column we used L as a length unit and L/v as a time unit.

Parameter	Unit	Fig. 2a	Fig. 2b	Fig. 3a	Fig. 3b	Fig. 4a	Fig. 4b
L_x	λ_{out}	/	/	/	/	0.63	1
L_y	λ_{out}	/	/	/	/	/	/
T	$1/k_{\text{out}}$	/	/	/	/	/	/
v_0	$\lambda_{\text{out}} k_{\text{out}}$	/	/	/	[0.46,3.21]	/	/
γ	$\lambda_{\text{out}} k_{\text{out}}$	/	/	0.61	0.61	$[31.6, 0, -6.32] \cdot 10^5$	2.5
β	$\lambda_{\text{out}}^2 k_{\text{out}}$	/	/	/	/	$2 \cdot 10^5$	0.25
v	$\lambda_{\text{out}} k_{\text{out}}$	$[7.07, 1.41, 0.014]$	[-10.61,10.61]	[-9.18,9.18]	/	$1.26 \cdot 10^6$	1
y_{I}	λ_{out}	/	/	/	/	/	/
D	$\lambda_{\text{out}}^2 k_{\text{out}}$	1	1	1	1	1	[1.67,5,25]
k_{in}	k_{out}	1	[0.25,1,4]	1	1	1	[0.67,2,10]
k_{out}	k_{out}	1	1	1	1	1	[0.67,2,10]
s_{in}	k_{out}	3	$3 \cdot [1/4, 1, 4]$	[3.27,6.54,13.07]	[5.23,6.54,7.84]	3	[2,6,30]
s_{out}	k_{out}	0	0	0	0	0	0
ξ/a	λ_{out}	/	/	/	/	/	/
$\frac{\xi/a}{\tau}$	$\lambda_{\text{out}} k_{\text{out}}$	/	/	/	/	/	/

Table D.3: Parameters used in chapter 3 (continued).

Parameter	Unit	Fig. 6	Fig. 7	Fig. 9a	Fig. 9b	Fig. 10
L_x	λ_{out}	20.24	20.24	/	/	10.12
L_y	λ_{out}	80.95	80.95	5	[0.1,5,10]	20.24
T	$1/k_{\text{out}}$	$1.25 \cdot 10^6$	$1.25 \cdot 10^6$	/	/	$1.25 \cdot 10^6$
v_0	$\lambda_{\text{out}} k_{\text{out}}$	$2.98 \cdot 10^{-4}$	$2.98 \cdot 10^{-4}$	/	$[0, 4.70 \cdot 10^{-4}]$	$2.98 \cdot 10^{-4}$
γ	$\lambda_{\text{out}} k_{\text{out}}$	$1.56 \cdot 10^{-4}$	$1.56 \cdot 10^{-4}$	/	$1.57 \cdot 10^{-4}$	$1.57 \cdot 10^{-4}$
β	$\lambda_{\text{out}}^2 k_{\text{out}}$	$2.54 \cdot 10^{-5}$	$[1.08 \cdot 10^{-5}, 4 \cdot 10^{-5}]$	/	/	$[1.72, 7.28] \cdot 10^{-5}$
v	$\lambda_{\text{out}} k_{\text{out}}$	/	/	/	/	/
y_{I}	λ_{out}	/	/	$[0.75, 2.5, 4.25]$	/	/
D	$\lambda_{\text{out}}^2 k_{\text{out}}$	1	1	1	1	1
k_{in}	k_{out}	1	1	1	1	1
k_{out}	k_{out}	1	1	1	1	1
s_{in}	k_{out}	3	3	3	3	$[2.42, 10.24]$
s_{out}	k_{out}	0	0	0	0	0
ξ/a	λ_{out}	$3.58 \cdot 10^{-2}$	$3.58 \cdot 10^{-2}$	/	/	$[0.03, 0.12]$
$\frac{\xi/a}{\tau}$	$\lambda_{\text{out}} k_{\text{out}}$	$1.19 \cdot 10^{-3}$	$1.19 \cdot 10^{-3}$	/	/	$1.19 \cdot 10^{-3}$

Table D.4: Parameters used in chapter 5. In all simulations, we used $l_x/L_x = 0.64$, $l_y/L_y = 0.34$, $x_{\mathrm{p},0}/L_x = 0.5$, and $y_{\mathrm{p},0}/L_y = 0.36$. The ellipse we use to construct the primary branch has $l_{\mathrm{p},x}/L_x = 0.74$ and $l_{\mathrm{p},y}/L_y = 0.38$.

Parameter	Unit	Fig. 3	Fig. 4	Fig. 5	Fig. 6	Fig. 7
L_x	λ_{out}	15.18	15.18	15.18	15.18	15.18
L_y	λ_{out}	41.89	41.89	41.89	41.89	41.89
T	$1/k_{\mathrm{out}}$	$2.5 \cdot 10^6$	$2.5 \cdot 10^6$	$1.25 \cdot 10^6$	$2.5 \cdot 10^6$	$2.5 \cdot 10^6$
v_0	$\lambda_{\mathrm{out}} k_{\mathrm{out}}$	$2.39 \cdot 10^{-4}$	$2.39 \cdot 10^{-4}$	$2.39 \cdot 10^{-4}$	$2.39 \cdot 10^{-4}$	$2.39 \cdot 10^{-4}$
γ	$\lambda_{\mathrm{out}} k_{\mathrm{out}}$	$1.57 \cdot 10^{-4}$	$1.57 \cdot 10^{-4}$	$1.49 \cdot 10^{-4}$	$1.49 \cdot 10^{-4}$	$1.49 \cdot 10^{-4}$
β	$\lambda_{\mathrm{out}}^2 k_{\mathrm{out}}$	$2.13 \cdot 10^{-5}$	$2.13 \cdot 10^{-5}$	$1.45 \cdot 10^{-5}$	$[8.8, 35.2] \cdot 10^{-6}$	$[1.12, 1.59] \cdot 10^{-5}$
δ	/	$[0, 0.5]$	$[0, 0.5]$	0.4	0.4	0.4
a_{noise}	$\lambda_{\mathrm{out}} k_{\mathrm{out}}$	0	$[0.60, 1.19, 1.79] \cdot 10^{-3}$	0	0	0
D	$\lambda_{\mathrm{out}}^2 k_{\mathrm{out}}$	1	1	1	1	1
k_{in}	k_{out}	1	1	1	1	1
k_{out}	k_{out}	1	1	1	1	1
s_{in}	k_{out}	3	3	3.3	3.3	$[2.4, 3.9]$
s_{out}	k_{out}	0.1	0.1	0	0	0
g_x	k_{out}	0	0	0	0	0
g_y	k_{out}	0	0	0	0	0
D_{ext}^x	$\lambda_{\mathrm{out}}^2 k_{\mathrm{out}}$	$3.28 \cdot 10^{-4}$	$3.28 \cdot 10^{-4}$	$3.28 \cdot 10^{-4}$	$3.28 \cdot 10^{-4}$	$3.28 \cdot 10^{-4}$
D_{ext}^y	$\lambda_{\mathrm{out}}^2 k_{\mathrm{out}}$	$4 \cdot 10^{-5}$	0	0	0	0
k_{ext}	k_{out}	$5 \cdot 10^{-4}$	10^{-3}	10^{-3}	10^{-3}	10^{-3}
b_{pb}	λ_{out}	1	1	$[0, 2]$	1	1
d_{pb}	λ_{out}	0.76	0.76	0.76	0.76	0.76
ξ/a	λ_{out}	$3.58 \cdot 10^{-2}$	$3.58 \cdot 10^{-2}$	$3.58 \cdot 10^{-2}$	$3.58 \cdot 10^{-2}$	$[1.71, 2.79] \cdot 10^{-2}$
$\frac{\xi/a}{\tau}$	$\lambda_{\mathrm{out}} k_{\mathrm{out}}$	$1.19 \cdot 10^{-3}$	$1.19 \cdot 10^{-3}$	$1.19 \cdot 10^{-3}$	$1.19 \cdot 10^{-3}$	$1.19 \cdot 10^{-3}$

Table D.5: Parameters used in chapter 5 (continued).

Parameter	Unit	Fig. 8a	Fig. 9	Fig. 10	Fig. 11	Fig. 16
$L_{x,0}$	λ_{out}	15.18	15.18	15.18	15.18	15.18
$L_{y,0}$	λ_{out}	41.89	37.95	41.89	41.89	41.89
r	/	3/4	$[0, 10]$	0.75	0.75	0.75
T	$1/k_{\text{out}}$	$1.25 \cdot 10^6$	$1.25 \cdot 10^6$	$[6.52 \cdot 10^5, 2.25 \cdot 10^3]$	$[6.52 \cdot 10^5, 2.25 \cdot 10^3]$	$[7.38 \cdot 10^7, 2.07 \cdot 10^3]$
v_0	$\lambda_{\text{out}} k_{\text{out}}$	$2.39 \cdot 10^{-4}$	$2.39 \cdot 10^{-4}$	$2.39 \cdot 10^{-4}$	$2.39 \cdot 10^{-4}$	$2.39 \cdot 10^{-4}$
γ	$\lambda_{\text{out}} k_{\text{out}}$	$1.49 \cdot 10^{-4}$	$1.49 \cdot 10^{-4}$	$1.49 \cdot 10^{-4}$	$1.49 \cdot 10^{-4}$	$1.49 \cdot 10^{-4}$
β	$\lambda_{\text{out}}^2 k_{\text{out}}$	$1.47 \cdot 10^{-5}$	$2.23 \cdot 10^{-5}$	$1.47 \cdot 10^{-5}$	$[1.47, 2.35, 3.52] \cdot 10^{-5}$	$1.47 \cdot 10^{-5}$
δ	/	0.4	0.4	0.4	0.4	0.4
a_{noise}	$\lambda_{\text{out}} k_{\text{out}}$	0	0	0	0	0
D	$\lambda_{\text{out}}^2 k_{\text{out}}$	1	1	1	1	1
k_{in}	k_{out}	1	1	1	1	1
k_{out}	k_{out}	1	1	1	1	1
s_{in}	k_{out}	3.3	3.3	3.3	3.3	3.3
s_{out}	k_{out}	0	0	0	0	0
g_x	k_{out}	0	0	$0.75 \cdot [3.46 \cdot 10^{-6}, 10^{-2}]$	$4.68 \cdot 10^{-6}$	$0.75 \cdot [2.81 \cdot 10^{-7}, 10^{-2}]$
g_y	k_{out}	0	0	$[3.46 \cdot 10^{-6}, 10^{-2}]$	$6.24 \cdot 10^{-6}$	$[2.81 \cdot 10^{-7}, 10^{-2}]$
D_{ext}^x	$\lambda_{\text{out}}^2 k_{\text{out}}$	$10^{-3} \cdot [3.28, 96.12]$	$10^{-3} \cdot [3.28, 96.12]$	$3.28 \cdot 10^{-3}$	$3.28 \cdot 10^{-3}$	$3.28 \cdot 10^{-4}$
D_{ext}^y	$\lambda_{\text{out}}^2 k_{\text{out}}$	0	0	0	0	0
k_{ext}	k_{out}	10^{-3}	10^{-3}	10^{-3}	10^{-3}	10^{-3}
b_{pb}	λ_{out}	0.5	1	0.5	0.5	0.5
d_{pb}	λ_{out}	0.76	0.76	0.76	0.76	0.76
ξ/a	λ_{out}	$3.58 \cdot 10^{-2}$	$3.74 \cdot 10^{-2}$	$3.58 \cdot 10^{-2}$	$3.58 \cdot 10^{-2}$	$3.58 \cdot 10^{-2}$
$\frac{\xi/a}{\tau}$	$\lambda_{\text{out}} k_{\text{out}}$	$1.19 \cdot 10^{-3}$	$1.19 \cdot 10^{-3}$	$1.19 \cdot 10^{-3}$	$1.19 \cdot 10^{-3}$	$1.19 \cdot 10^{-3}$

Bibliography

[1] L. Wolpert, C. Tickle, A. Martinez Arias, P. A. Lawrence, and J. Locke. *Principles of Development*. Oxford University Press, Oxford, 6th edition, 2019 (cited on pages 1–5).

[2] S. F. Gilbert. *Developmental Biology*. Sinauer Associates, Sunderland, MA, 9th edition, 2010 (cited on pages 1, 4, 5).

[3] J. M. W. Slack. *Essential Developmental Biology*. Blackwell Science, Malden, MA, 2001 (cited on pages 1, 2, 4).

[4] C. Collinet and T. Lecuit. Programmed and self-organized flow of information during morphogenesis. *Nature Reviews Molecular Cell Biology*, 22(4):245–265, 2021 (cited on pages 2–4).

[5] P. Lu and Z. Werb. Patterning Mechanisms of Branched Organs. *Science*, 322(5907): 1506–1509, 2008 (cited on pages 2, 10).

[6] A. Ochoa-Espinosa and M. Affolter. Branching Morphogenesis: From Cells to Organs and Back. *Cold Spring Harbor Perspectives in Biology*, 4(10):a008243–a008243, 2012 (cited on pages 2, 10, 11).

[7] E. Hannezo, J. Prost, and J.-F. Joanny. Instabilities of Monolayered Epithelia: Shape and Structure of Villi and Crypts. *Physical Review Letters*, 107(7):078104, 2011 (cited on page 2).

[8] A. E. Shyer, T. Tallinen, N. L. Nerurkar, Z. Wei, E. S. Gil, D. L. Kaplan, C. J. Tabin, and L. Mahadevan. Villification: How the Gut Gets Its Villi. *Science*, 342(6155):212–218, 2013 (cited on page 2).

[9] T. Tallinen, J. Y. Chung, J. S. Biggins, and L. Mahadevan. Gyrification from constrained cortical expansion. *Proceedings of the National Academy of Sciences*, 111(35):12667–12672, 2014 (cited on pages 2, 4).

[10] T. Tallinen, J. Y. Chung, F. Rousseau, N. Girard, J. Lefèvre, and L. Mahadevan. On the growth and form of cortical convolutions. *Nature Physics*, 12(6):588–593, 2016 (cited on pages 2, 4).

[11] C. Tan, P. R. Norden, W. Yu, T. Liu, N. Ujiie, S. K. Lee, X. Yan, Y. Dyakiv, K. Aoto, S. Ortega, I. G. De Plaen, V. Sampath, and T. Kume. Endothelial FOXC1 and FOXC2 promote intestinal regeneration after ischemia–reperfusion injury. *EMBO reports*, 24(7):e56030, 2023 (cited on page 2).

[12] E. Katifori, G. J. Szöllősi, and M. O. Magnasco. Damage and Fluctuations Induce Loops in Optimal Transport Networks. *Physical Review Letters*, 104(4):048704, 2010 (cited on pages 2, 3).

[13] K. Ishihara, A. Mukherjee, E. Gromberg, J. Brugués, E. M. Tanaka, and F. Jülicher. Topological morphogenesis of neuroepithelial organoids. *Nature Physics*, 2022 (cited on page 2).

[14] J. R. Banavar, F. Colaiori, A. Flammini, A. Maritan, and A. Rinaldo. Topology of the Fittest Transportation Network. *Physical Review Letters*, 84(20):4745–4748, 2000 (cited on page 3).

[15] M. Durand. Structure of Optimal Transport Networks Subject to a Global Constraint. *Physical Review Letters*, 98(8):088701, 2007 (cited on page 3).

[16] S. Bohn and M. O. Magnasco. Structure, Scaling, and Phase Transition in the Optimal Transport Network. *Physical Review Letters*, 98(8):088702, 2007 (cited on page 3).

[17] F. Corson. Fluctuations and Redundancy in Optimal Transport Networks. *Physical Review Letters*, 104(4):048703, 2010 (cited on page 3).

[18] A. Bailles, E. W. Gehrels, and T. Lecuit. Mechanochemical Principles of Spatial and Temporal Patterns in Cells and Tissues. *Annual Review of Cell and Developmental Biology*, 38(1):321–347, 2022 (cited on page 3).

[19] J. Howard, S. W. Grill, and J. S. Bois. Turing's next steps: the mechanochemical basis of morphogenesis. *Nature Reviews Molecular Cell Biology*, 12(6):392–398, 2011 (cited on page 3).

[20] E. Hannezo, C. L. Scheele, M. Moad, N. Drogo, R. Heer, R. V. Sampogna, J. van Rheenen, and B. D. Simons. A Unifying Theory of Branching Morphogenesis. *Cell*, 171(1):242–255.e27, 2017 (cited on pages 3, 71, 137, 140).

[21] S. Kondo and T. Miura. Reaction-Diffusion Model as a Framework for Understanding Biological Pattern Formation. *Science*, 329(5999):1616–1620, 2010 (cited on page 3).

[22] A. M. Turing. The chemical basis of morphogenesis. *Philosophical Transactions of the Royal Society of London. Series B, Biological Sciences*, 237(641):37–72, 1952 (cited on page 3).

[23] A. Gierer and H. Meinhardt. A Theory of Biological Pattern Formation. *Kybernetik*, 12(1):30–39, 1972 (cited on page 4).

[24] H. Meinhardt and A. Gierer. Applications of a theory of biological pattern formation based on lateral inhibition. *Journal of Cell Science*, 15(2):321–346, 1974 (cited on page 4).

[25] H. Meinhardt and A. Gierer. Pattern formation by local self-activation and lateral inhibition. *BioEssays*, 22(8):753–760, 2000 (cited on page 4).

[26] R. Sheth, L. Marcon, M. F. Bastida, M. Junco, L. Quintana, R. Dahn, M. Kmita, J. Sharpe, and M. A. Ros. *Hox* Genes Regulate Digit Patterning by Controlling the Wavelength of a Turing-Type Mechanism. *Science*, 338(6113):1476–1480, 2012 (cited on page 4).

[27] A. Nakamasu, G. Takahashi, A. Kanbe, and S. Kondo. Interactions between zebrafish pigment cells responsible for the generation of Turing patterns. *Proceedings of the National Academy of Sciences*, 106(21):8429–8434, 2009 (cited on page 4).

[28] L. Wolpert. Morphogens: History. In *Encyclopedia of Neuroscience*, pages 975–979. Elsevier, Berlin, 2009 (cited on page 4).

[29] O. Wartlick, A. Kicheva, and M. Gonzalez-Gaitan. Morphogen Gradient Formation. *Cold Spring Harbor Perspectives in Biology*, 1(3):a001255–a001255, 2009 (cited on pages 4, 5, 8).

[30] K. W. Rogers and A. F. Schier. Morphogen Gradients: From Generation to Interpretation. *Annual Review of Cell and Developmental Biology*, 27(1):377–407, 2011 (cited on pages 4, 7, 8).

[31] T. H. Morgan. "Polarity" considered as a phenomenon of gradation of materials. *Journal of Experimental Zoology*, 2(4):495–506, 1905 (cited on page 4).

[32] T. H. Morgan. *Regeneration*. The Macmillan Company, New York, NY, 1901 (cited on page 4).

[33] C. M. Child. Studies on the dynamics of morphogenesis and inheritance in experimental reproduction. I. The axial gradient in planaria dorotocephala as a limiting factor in regulation. *Journal of Experimental Zoology*, 10(3):265–320, 1911 (cited on page 4).

[34] H. Spemann and H. Mangold. Über Induktion von Embryonalanlagen durch Implantation artfremder Organisatoren. *Archiv für Mikroskopische Anatomie und Entwicklungsmechanik*, 100(3-4):599–638, 1924 (cited on page 4).

[35] K. Sander and P. E. Faessler. Introducing the Spemann-Mangold organizer: experiments and insights that generated a key concept in developmental biology. *The International Journal of Developmental Biology*, 45(1):1–11, 2001 (cited on page 4).

[36] E. M. De Robertis. Spemann's organizer and self-regulation in amphibian embryos. *Nature Reviews Molecular Cell Biology*, 7(4):296–302, 2006 (cited on page 4).

[37] E. M. De Robertis. Spemann's organizer and the self-regulation of embryonic fields. *Mechanisms of Development*, 126(11-12):925–941, 2009 (cited on page 4).

[38] Created with biorender.com. 2023. URL: `https://www.biorender.com` (visited on 07/11/2023) (cited on page 5).

[39] E. M. De Robertis and H. Kuroda. Dorsal-ventral patterning and neural induction in *Xenopus* embryos. *Annual Review of Cell and Developmental Biology*, 20(1):285–308, 2004 (cited on page 5).

[40] L. Wolpert. Positional Information and the Spatial Pattern of Cellular Differentiation. *Journal of Theoretical Biology*, 25(1):1–47, 1969 (cited on page 5).

[41] K. S. Stapornwongkul and J.-P. Vincent. Generation of extracellular morphogen gradients: the case for diffusion. *Nature Reviews Genetics*, 22(6):393–411, 2021 (cited on pages 6, 7).

[42] C. Nüsslein-Volhard and E. Wieschaus. Mutations affecting segment number and polarity in *Drosophila*. *Nature*, 287(5785):795–801, 1980 (cited on page 5).

[43] H. G. Frohnhöfer and C. Nüsslein-Volhard. Organization of anterior pattern in the *Drosophila* embryo by the maternal gene *bicoid*. *Nature*, 324(6093):120–125, 1986 (cited on page 5).

[44] C. Nüsslein-Volhard, H. G. Frohnhöfer, and R. Lehmann. Determination of Anteroposterior Polarity in *Drosophila*. *Science*, 238(4834):1675–1681, 1987 (cited on page 5).

[45] W. Driever and C. Nüsslein-Volhard. A Gradient of *bicoid* Protein in Drosophila Embryos. *Cell*, 54(1):83–93, 1988 (cited on pages 5, 7).

[46] W. Driever and C. Nüsslein-Volhard. The *bicoid* Protein Determines Position in the Drosophila Embryo in a Concentration-Dependent Manner. *Cell*, 54(1):95–104, 1988 (cited on page 5).

[47] A. Kicheva and J. Briscoe. Control of Tissue Development by Morphogens. *Annual Review of Cell and Developmental Biology*, 39(1):91–121, 2023 (cited on pages 6–8).

[48] T. Lecuit, W. J. Brook, M. Ng, M. Calleja, H. Sun, and S. M. Cohen. Two distinct mechanisms for long-range patterning by Decapentaplegic in the Drosophila wing. *Nature*, 381(6581):387–393, 1996 (cited on page 6).

[49] D. Nellen, R. Burke, G. Struhl, and K. Basler. Direct and Long-Range Action of a DPP Morphogen Gradient. *Cell*, 85(3):357–368, 1996 (cited on page 6).

[50] A. A. Teleman and S. M. Cohen. Dpp Gradient Formation in the *Drosophila* Wing Imaginal Disc. *Cell*, 103(6):971–980, 2000 (cited on page 6).

[51] M. Strigini and S. M. Cohen. A Hedgehog activity gradient contributes to AP axial patterning of the *Drosophila* wing. *Development*, 124(22):4697–4705, 1997 (cited on page 6).

[52] T. Tabata and T. B. Kornberg. Hedgehog Is a Signaling Protein with a Key Role in Patterning Drosophila Imaginal Discs. *Cell*, 76(1):89–102, 1994 (cited on page 6).

[53] C. Kiecker and C. Niehrs. A morphogen gradient of Wnt/β-catenin signalling regulates anteroposterior neural patterning in *Xenopus*. *Development*, 128(21):4189–4201, 2001 (cited on page 6).

[54] M. Kondo. Bone morphogenetic proteins in the early development of zebrafish. *FEBS Journal*, 274(12):2960–2967, 2007 (cited on page 6).

[55] G. Schwank and K. Basler. Regulation of Organ Growth by Morphogen Gradients. *Cold Spring Harbor Perspectives in Biology*, 2(1):a001669, 2010 (cited on page 6).

[56] O. Wartlick, P. Mumcu, A. Kicheva, T. Bittig, C. Seum, F. Jülicher, and M. González-Gaitán. Dynamics of Dpp Signaling and Proliferation Control. *Science*, 331(6021):1154–1159, 2011 (cited on page 6).

[57] O. Wartlick, P. Mumcu, F. Jülicher, and M. González-Gaitán. Understanding morphogenetic growth control — lessons from flies. *Nature Reviews Molecular Cell Biology*, 12(9):594–604, 2011 (cited on page 6).

[58] O. Wartlick, F. Jülicher, and M. González-Gaitán. Growth control by a moving morphogen gradient during *Drosophila* eye development. *Development*, 141(9):1884–1893, 2014 (cited on page 6).

[59] R. Mateus, L. Holtzer, C. Seum, Z. Hadjivasiliou, M. Dubois, F. Jülicher, and M. Gonzalez-Gaitan. BMP Signaling Gradient Scaling in the Zebrafish Pectoral Fin. *Cell Reports*, 30(12):4292–4302.e7, 2020 (cited on page 6).

[60] P. Müller, K. W. Rogers, S. R. Yu, M. Brand, and A. F. Schier. Morphogen transport. *Development*, 140(8):1621–1638, 2013 (cited on pages 7, 8).

[61] P. K. Mattila and P. Lappalainen. Filopodia: molecular architecture and cellular functions. *Nature Reviews Molecular Cell Biology*, 9(6):446–454, 2008 (cited on page 7).

[62] F. Crick. Diffusion in Embryogenesis. *Nature*, 225(5231):420–422, 1970 (cited on page 8).

[63] S. R. Yu, M. Burkhardt, M. Nowak, J. Ries, Z. Petrášek, S. Scholpp, P. Schwille, and M. Brand. Fgf8 morphogen gradient forms by a source-sink mechanism with freely diffusing molecules. *Nature*, 461(7263):533–536, 2009 (cited on page 8).

[64] A. Kicheva, P. Pantazis, T. Bollenbach, Y. Kalaidzidis, T. Bittig, F. Jülicher, and M. González-Gaitán. Kinetics of Morphogen Gradient Formation. *Science*, 315(5811):521–525, 2007 (cited on page 8).

[65] A. Thommen, S. Werner, O. Frank, J. Philipp, O. Knittelfelder, Y. Quek, K. Fahmy, A. Shevchenko, B. M. Friedrich, F. Jülicher, and J. C. Rink. Body size-dependent energy storage causes Kleiber's law scaling of the metabolic rate in planarians. *eLife*, 8:e38187, 2019. Published under CC BY 4.0 license, `https://creativecommons.org/licenses/by/4.0/` (cited on pages 8, 12, 82, 87, 106, 141).

[66] A. M. Makarieva, V. G. Gorshkov, B.-L. Li, S. L. Chown, P. B. Reich, and V. M. Gavrilov. Mean mass-specific metabolic rates are strikingly similar across life's major domains: Evidence for life's metabolic optimum. *Proceedings of the National Academy of Sciences*, 105(44):16994–16999, 2008 (cited on page 8).

[67] R. Sears and W. F. Perrin. Blue Whale: Balaenoptera musculus. In W. F. Perrin, B. Würsig, and J. G. M. Thewissen, editors, *Encyclopedia of Marine Mammals*, pages 120–124. Academic Press, London, 2nd edition, 2009 (cited on page 8).

[68] J. Gayon. History of the Concept of Allometry. *American Zoologist*, 40(5):748–758, 2000 (cited on page 8).

[69] S. J. Gould. Allometry and size in ontogeny and phylogeny. *Biological Reviews*, 41(4):587–638, 1966 (cited on page 8).

[70] A. W. Shingleton. Allometry: The Study of Biological Scaling. *Nature Education Knowledge*, 3(10):2, 2010 (cited on pages 8, 9).

[71] R. H. Peters. *The Ecological Implications of Body Size*. Cambridge University Press, Cambridge, United Kingdom, 1st edition, 1983 (cited on pages 8, 9).

[72] K. Schmidt-Nielsen. *Scaling, why is animal size so important?* Cambridge University Press, Cambridge, United Kingdom, 1984 (cited on page 9).

[73] T. Dawson and A. Hulbert. Standard metabolism, body temperature, and surface areas of Australian marsupials. *American Journal of Physiology-Legacy Content*, 218(4):1233–1238, 1970 (cited on page 9).

[74] M. Kleiber. Body size and metabolism. *Hilgardia*, 6(11):315–353, 1932 (cited on pages 9, 141).

[75] G. B. West. A General Model for the Origin of Allometric Scaling Laws in Biology. *Science*, 276(5309):122–126, 1997 (cited on pages 9, 141).

[76] G. B. West, J. H. Brown, and B. J. Enquist. A general model for the structure and allometry of plant vascular systems. *Nature*, 400(6745):664–667, 1999 (cited on page 9).

[77] B. Kooijman. *Dynamic Energy Budget Theory For Metabolic Organisation*. Cambridge University Press, Cambridge, United Kingdom, 3rd edition, 2009 (cited on pages 9, 141).

[78] C. Samakovlis, N. Hacohen, G. Manning, D. C. Sutherland, K. Guillemin, and M. A. Krasnow. Development of the *Drosophila* tracheal system occurs by a series of morphologically distinct but genetically coupled branching events. *Development*, 122(5):1395–1407, 1996 (cited on page 11).

[79] N. Gjorevski and C. M. Nelson. Integrated morphodynamic signalling of the mammary gland. *Nature Reviews Molecular Cell Biology*, 12(9):581–593, 2011 (cited on page 11).

[80] J. A. Davies, editor. *Branching Morphogenesis*. Molecular Biology Intelligence Unit. Landes Bioscience/Eurekah.com, Georgetown, TX and Springer Science+Business Media, New York, NY, 2006 (cited on page 9).

[81] J. A. Davies. Do different branching epithelia use a conserved developmental mechanism? *BioEssays*, 24(10):937–948, 2002 (cited on page 9).

[82] C. M. Nelson, M. M. VanDuijn, J. L. Inman, D. A. Fletcher, and M. J. Bissell. Tissue Geometry Determines Sites of Mammary Branching Morphogenesis in Organotypic Cultures. *Science*, 314(5797):298–300, 2006 (cited on pages 10, 12).

[83] C. M. Nelson. Geometric control of tissue morphogenesis. *Biochimica et Biophysica Acta - Molecular Cell Research*, 1793(5):903–910, 2009 (cited on pages 10, 11).

[84] R. J. Metzger and M. A. Krasnow. Genetic Control of Branching Morphogenesis. *Science*, 284(5420):1635–1639, 1999 (cited on page 10).

[85] M. Affolter, R. Zeller, and E. Caussinus. Tissue remodelling through branching morphogenesis. *Nature Reviews Molecular Cell Biology*, 10(12):831–842, 2009 (cited on page 10).

[86] M. Affolter and E. Caussinus. Tracheal branching morphogenesis in *Drosophila* : new insights into cell behaviour and organ architecture. *Development*, 135(12):2055–2064, 2008 (cited on page 10).

[87] A. Uv. *Drosophila* tracheal morphogenesis: intricate cellular solutions to basic plumbing problems. *Trends in Cell Biology*, 13(6):301–309, 2003 (cited on page 10).

[88] A. Ghabrial, S. Luschnig, M. M. Metzstein, and M. A. Krasnow. Branching Morphogenesis of the *Drosophila* Tracheal System. *Annual Review of Cell and Developmental Biology*, 19(1):623–647, 2003 (cited on page 10).

[89] D. Sutherland, C. Samakovlis, and M. A. Krasnow. *branchless* Encodes a Drosophila FGF Homolog That Controls Tracheal Cell Migration and the Pattern of Branching. *Cell*, 87(6):1091–1101, 1996 (cited on page 10).

[90] C. Klämbt, L. Glazer, and B. Z. Shilo. *breathless*, a *Drosophila* FGF receptor homolog, is essential for migration of tracheal and specific midline glial cells. *Genes & Development*, 6(9):1668–1678, 1992 (cited on page 10).

[91] A. S. Ghabrial and M. A. Krasnow. Social interactions among epithelial cells during tracheal branching morphogenesis. *Nature*, 441(7094):746–749, 2006 (cited on page 10).

[92] M. Llimargas. The *Notch* pathway helps to pattern the tips of the *Drosophila* tracheal branches by selecting cell fates. *Development*, 126(11):2355–2364, 1999 (cited on page 10).

[93] T. Ikeya and S. Hayashi. Interplay of Notch and FGF signaling restricts cell fate and MAPK activation in the *Drosophila* trachea. *Development*, 126(20):4455–4463, 1999 (cited on page 10).

[94] M. D. Sternlicht, H. Kouros-Mehr, P. Lu, and Z. Werb. Hormonal and local control of mammary branching morphogenesis. *Differentiation*, 74(7):365–381, 2006 (cited on page 11).

[95] C. W. Daniel, S. Robinson, and G. B. Silberstein. The Role of TGF-β in Patterning and Growth of the Mammary Ductal Tree. *Journal of Mammary Gland Biology and Neoplasia*, 1(4):331–341, 1996 (cited on page 11).

[96] C. W. Daniel, G. B. Silberstein, K. Van Horn, P. Strickland, and S. Robinson. TGF-β1-Induced Inhibition of Mouse Mammary Ductal Growth: Developmental Specificity and Characterization. *Developmental Biology*, 135(1):20–30, 1989 (cited on page 11).

[97] G. B. Silberstein and C. W. Daniel. Reversible Inhibition of Mammary Gland Growth by Transforming Growth Factor-β. *Science*, 237(4812):291–293, 1987 (cited on page 11).

[98] G. B. Silberstein, K. C. Flanders, A. B. Roberts, and C. W. Daniel. Regulation of Mammary Morphogenesis: Evidence for Extracellular Matrix-Mediated Inhibition of Ductal Budding by Transforming Growth Factor-β1. *Developmental Biology*, 152(2):354–362, 1992 (cited on page 12).

[99] H. Macias, A. Moran, Y. Samara, M. Moreno, J. E. Compton, G. Harburg, P. Strickland, and L. Hinck. SLIT/ROBO1 Signaling Suppresses Mammary Branching Morphogenesis by Limiting Basal Cell Number. *Developmental Cell*, 20(6):827–840, 2011 (cited on page 12).

[100] D. F. Pierce, M. D. Johnson, Y. Matsui, S. D. Robinson, L. I. Gold, A. F. Purchio, C. W. Daniel, B. L. Hogan, and H. L. Moses. Inhibition of mammary duct development but not alveolar outgrowth during pregnancy in transgenic mice expressing active TGF-β1. *Genes & Development*, 7(12a):2308–2317, 1993 (cited on page 12).

[101] S.-Y. Liu, C. Selck, B. Friedrich, R. Lutz, M. Vila-Farré, A. Dahl, H. Brandl, N. Lakshmanaperumal, I. Henry, and J. C. Rink. Reactivating head regrowth in a regeneration-deficient planarian species. *Nature*, 500(7460):81–84, 2013 (cited on page 12).

[102] L. Drees and J. C. Rink. The planarian flatworm *Schmidtea mediterranea*. *Nature Methods*, 20(1):3–5, 2023 (cited on page 12).

[103] M. Ivankovic, R. Haneckova, A. Thommen, M. A. Grohme, M. Vila-Farré, S. Werner, and J. C. Rink. Model systems for regeneration: planarians. *Development*, 146(17):dev167684, 2019 (cited on pages 12, 14–16, 133).

[104] J. G. Dalyell. *Observations on Some Interesting Phenomena in Animal Physiology, Exhibited by Several Species of Planarieae: Illustrated by Coloured Figures of Living Animals*. Archibald Constable & Co., Edinburgh, 1814 (cited on page 12).

[105] R. Sluys and M. Riutort. Planarian Diversity and Phylogeny. In J. C. Rink, editor, *Planarian Regeneration*. Volume 1774, pages 1–56. Springer New York, New York, NY, 2018. Series Title: Methods in Molecular Biology (cited on pages 12, 13).

[106] J. Dickmann, J. C. Rink, and F. Jülicher. Long-range morphogen gradient formation by cell-to-cell signal propagation. *Physical Biology*, 19(6):066001, 2022 (cited on page 13).

[107] S. Werner, T. Stückemann, M. Beirán Amigo, J. C. Rink, F. Jülicher, and B. M. Friedrich. Scaling and Regeneration of Self-Organized Patterns. *Physical Review Letters*, 114(13):138101, 2015 (cited on page 13).

[108] D. J. Forsthoefel and P. A. Newmark. Emerging patterns in planarian regeneration. *Current Opinion in Genetics & Development*, 19(4):412–420, 2009 (cited on pages 13, 15, 133).

[109] P. Garcia-Corrales and J. Gamo. The Ultrastructure of the Gastrodermal Gland Cells in the Freshwater Planarian *Dugesia gonocephala* s.l. *Acta Zoologica*, 67(1):43–51, 1986 (cited on page 13).

[110] P. Garcia-Corrales and J. Gamo. Ultrastructural changes in the gastrodermal phagocytic cells of the planarian Dugesia gonocephala s.l. during food digestion (Platthelminthes). *Zoomorphology*, 108(2):109–117, 1988 (cited on page 13).

[111] S. Ishii and T. Sakurai. Food ingestion by planarian intestinal phagocytic cells - a study by scanning electron microscopy. In S. Tyler, editor, *Turbellarian Biology*, pages 179–185. Springer Netherlands, Dordrecht, 1991 (cited on page 13).

[112] C. T. Fincher, O. Wurtzel, T. De Hoog, K. M. Kravarik, and P. W. Reddien. Cell type transcriptome atlas for the planarian *Schmidtea mediterranea*. *Science*, 360(6391):eaaq1736, 2018 (cited on page 13).

[113] H. Orii, H. Ito, and K. Watanabe. Anatomy of the Planarian Dugesia japonica I. The Muscular System Revealed by Antisera against Myosin Heavy Chains. *Zoological Science*, 19(10):1123–1131, 2002 (cited on page 13).

[114] J. N. Witchley, M. Mayer, D. E. Wagner, J. H. Owen, and P. W. Reddien. Muscle Cells Provide Instructions for Planarian Regeneration. *Cell Reports*, 4(4):633–641, 2013 (cited on page 15).

[115] M. L. Scimone, L. E. Cote, and P. W. Reddien. Orthogonal muscle fibres have different instructive roles in planarian regeneration. *Nature*, 551(7682):623–628, 2017 (cited on pages 15, 133).

[116] P. Rompolas, R. S. Patel-King, and S. M. King. Schmidtea mediterranea. In *Methods in Cell Biology*. Volume 93, pages 81–98. Elsevier, 2009 (cited on page 15).

[117] J. C. Rink. Stem Cells, Patterning and Regeneration in Planarians: Self-Organization at the Organismal Scale. In J. C. Rink, editor, *Planarian Regeneration*. Volume 1774, pages 57–172. Springer New York, New York, NY, 2018. Series Title: Methods in Molecular Biology (cited on page 15).

[118] P. W. Reddien and A. S. Alvarado. Fundamentals of Planarian Regeneration. *Annual Review of Cell and Developmental Biology*, 20(1):725–757, 2004 (cited on page 15).

[119] J. Baguñà and R. Romero. Quantitative analysis of cell types during growth, degrowth and regeneration in the planarians *Dugesia mediterranea* and *Dugesia tigrina*. *Hydrobiologia*, 84(1):181–194, 1981 (cited on page 15).

[120] J. Baguñà. Dramatic mitotic response in planarians after feeding, and a hypothesis for the control mechanism. *Journal of Experimental Zoology*, 190(1):117–122, 1974 (cited on page 15).

[121] J. Baguñà. Mitosis in the intact and regenerating planarian *Dugesia mediterranea* n.sp. I. Mitotic studies during growth, feeding and starvation. *Journal of Experimental Zoology*, 195(1):53–64, 1976 (cited on page 15).

[122] P. A. Newmark and A. Sánchez Alvarado. Bromodeoxyuridine Specifically Labels the Regenerative Stem Cells of Planarians. *Developmental Biology*, 220(2):142–153, 2000 (cited on page 15).

[123] C. R. Bardeen and F. H. Baetjer. The inhibitive action of the Roentgen rays on regeneration in planarians. *Journal of Experimental Zoology*, 1(1):191–195, 1904 (cited on page 15).

[124] P. W. Reddien, A. L. Bermange, K. J. Murfitt, J. R. Jennings, and A. Sánchez Alvarado. Identification of Genes Needed for Regeneration, Stem Cell Function, and Tissue Homeostasis by Systematic Gene Perturbation in Planaria. *Developmental Cell*, 8(5):635–649, 2005 (cited on page 15).

[125] D. E. Wagner, I. E. Wang, and P. W. Reddien. Clonogenic Neoblasts Are Pluripotent Adult Stem Cells That Underlie Planarian Regeneration. *Science*, 332(6031):811–816, 2011 (cited on page 15).

[126] T. Stückemann, J. P. Cleland, S. Werner, H. Thi-Kim Vu, R. Bayersdorf, S.-Y. Liu, B. Friedrich, F. Jülicher, and J. C. Rink. Antagonistic Self-Organizing Patterning Systems Control Maintenance and Regeneration of the Anteroposterior Axis in Planarians. *Developmental Cell*, 40(3):248–263.e4, 2017 (cited on page 15).

[127] K. A. Gurley, J. C. Rink, and A. S. Alvarado. β-Catenin Defines Head Versus Tail Identity During Planarian Regeneration and Homeostasis. *Science*, 319(5861):323–327, 2008 (cited on page 15).

[128] M. Iglesias, M. Almuedo-Castillo, A. A. Aboobaker, and E. Salo. Early planarian brain regeneration is independent of blastema polarity mediated by the Wnt/β-catenin pathway. *Developmental Biology*, 358(1):68–78, 2011 (cited on page 15).

[129] M. Iglesias, J. L. Gomez-Skarmeta, E. Salo, and T. Adell. Silencing of *Smed-β catenin1* generates radial-like hypercephalized planarians. *Development*, 135(7):1215–1221, 2008 (cited on page 15).

[130] C. P. Petersen and P. W. Reddien. *Smed-β catenin-1* Is Required for Anteroposterior Blastema Polarity in Planarian Regeneration. *Science*, 319(5861):327–330, 2008 (cited on page 15).

[131] M. A. Gaviño and P. W. Reddien. A Bmp/Admp Regulatory Circuit Controls Maintenance and Regeneration of Dorsal-Ventral Polarity in Planarians. *Current Biology*, 21(4):294–299, 2011 (cited on page 15).

[132] P. W. Reddien, A. L. Bermange, A. M. Kicza, and A. Sánchez Alvarado. BMP signaling regulates the dorsal planarian midline and is needed for asymmetric regeneration. *Development*, 134(22):4043–4051, 2007 (cited on page 15).

[133] F. Cebrià, T. Guo, J. Jopek, and P. A. Newmark. Regeneration and maintenance of the planarian midline is regulated by a slit orthologue. *Developmental Biology*, 307(2):394–406, 2007 (cited on page 15).

[134] K. A. Gurley, S. A. Elliott, O. Simakov, H. A. Schmidt, T. W. Holstein, and A. S. Alvarado. Expression of secreted Wnt pathway components reveals unexpected complexity of the planarian amputation response. *Developmental Biology*, 347(1):24–39, 2010 (cited on pages 15, 133).

[135] P. Meakin. *Fractals, scaling and growth far from equilibrium*, number 5 in Cambridge Nonlinear Science Series. Cambridge University Press, Cambridge, United Kingdom, 1st edition, 1998 (cited on pages 16, 17, 33).

[136] J. S. Langer. Instabilities and pattern formation in crystal growth. *Reviews of Modern Physics*, 52(1):1–28, 1980 (cited on pages 16–18, 59, 139).

[137] T. Vicsek and J. Kertész. Laplacian Pattern Formation. *Europhysics News*, 19(2):24–27, 1988 (cited on page 16).

[138] T. Vicsek. *Fractal Growth Phenomena*. World Scientific Publishing, Singapore, 2nd edition, 1992 (cited on pages 16, 25, 58).

[139] S. Ohta and H. Honjo. Growth Probability Distribution in Irregular Fractal-Like Crystal Growth of Ammonium Chloride. *Physical Review Letters*, 60(7):611–614, 1988 (cited on pages 17, 19, 140).

[140] P. G. Saffman and S. G. Taylor. The penetration of a fluid into a porous medium or Hele-Shaw cell containing a more viscous liquid. *Proceedings of the Royal Society of London. Series A. Mathematical and Physical Sciences*, 245(1242):312–329, 1958 (cited on pages 17, 19).

[141] M. Matsushita, M. Sano, Y. Hayakawa, H. Honjo, and Y. Sawada. Fractal Structures of Zinc Metal Leaves Grown by Electrodeposition. *Physical Review Letters*, 53(3):286–289, 1984 (cited on pages 17, 20, 44).

[142] L. Niemeyer, L. Pietronero, and H. J. Wiesmann. Fractal Dimension of Dielectric Breakdown. *Physical Review Letters*, 52(12):1033–1036, 1984 (cited on pages 17, 21, 44).

[143] D. Komarechka (Wikimedia Commons). Snowflake. 2021. URL: `https://w.wiki/84Hr` (visited on 06/11/2023). This work is licensed under the CC0 1.0 Deed license. To view a copy of this license, visit `https://creativecommons.org/publicdomain/zero/1.0/deed.en`. (cited on page 17).

[144] C. Godrèche, editor. *Solids Far From Equilibrium*, number 1 in Collection Aléa-Saclay. Cambridge University Press, Cambridge, United Kingdom, 1991 (cited on pages 16, 60, 153).

[145] E. Ben-Jacob, I. Cohen, and H. Levine. Cooperative self-organization of microorganisms. *Advances in Physics*, 49(4):395–554, 2000 (cited on page 16).

[146] W. W. Mullins and R. F. Sekerka. Morphological Stability of a Particle Growing by Diffusion or Heat Flow. *Journal of Applied Physics*, 34(2):323–329, 1963 (cited on page 18).

[147] W. W. Mullins and R. F. Sekerka. Stability of a Planar Interface During Solidification of a Dilute Binary Alloy. *Journal of Applied Physics*, 35(2):444–451, 1964 (cited on page 18).

[148] R. Chuoke, P. Van Meurs, and C. Van Der Poel. The Instability of Slow, Immiscible, Viscous Liquid-Liquid Displacements in Permeable Media. *Transactions of the AIME*, 216(01):188–194, 1959 (cited on page 19).

[149] H. Honjo, S. Ohta, and M. Matsushita. Irregular Fractal-Like Crystal Growth of Ammonium Chloride. *Journal of the Physical Society of Japan*, 55(8):2487–2490, 1986 (cited on pages 19, 140).

[150] J.-D. Chen. Radial viscous fingering patterns in Hele-Shaw cells. *Experiments in Fluids*, 5(6):363–371, 1987 (cited on page 19).

[151] D. Grier, E. Ben-Jacob, R. Clarke, and L. M. Sander. Morphology and Microstructure in Electrochemical Deposition of Zinc. *Physical Review Letters*, 56(12):1264–1267, 1986 (cited on page 20).

[152] T. A. Witten and L. M. Sander. Diffusion-Limited Aggregation, a Kinetic Critical Phenomenon. *Physical Review Letters*, 47(19):1400–1403, 1981 (cited on pages 20, 31).

[153] T. A. Witten and L. M. Sander. Diffusion-limited aggregation. *Physical Review B*, 27(9):5686–5697, 1983 (cited on pages 20, 31).

[154] J. Nittmann and H. E. Stanley. Tip splitting without interfacial tension and dendritic growth patterns arising from molecular anisotropy. *Nature*, 321(6071):663–668, 1986 (cited on pages 21, 44).

[155] T. Vicsek. Pattern Formation in Diffusion-Limited Aggregation. *Physical Review Letters*, 53(24):2281–2284, 1984 (cited on pages 21, 44).

[156] R. Tao, M. A. Novotny, and K. Kaski. Diffusion-limited aggregation with surface tension. *Physical Review A*, 38(2):1019–1026, 1988 (cited on pages 21, 44).

[157] L. P. Kadanoff. Simulating Hydrodynamics: a Pedestrian Model. *Journal of Statistical Physics*, 39(3-4):267–283, 1985 (cited on pages 21, 44).

[158] S. Liang. Random-walk simulations of flow in Hele Shaw cells. *Physical Review A*, 33(4):2663–2674, 1986 (cited on pages 21, 44).

[159] D. T. Gillespie. Exact Stochastic Simulation of Coupled Chemical Reactions. *The Journal of Physical Chemistry*, 81(25):2340–2361, 1977 (cited on page 29).

[160] D. T. Gillespie. Stochastic Simulation of Chemical Kinetics. *Annual Review of Physical Chemistry*, 58(1):35–55, 2007 (cited on page 29).

[161] C. Broedersz and E. Frey. Lecture Notes in Stochastic Processes. Faculty of Physics at Ludwig Maximilian University of Munich, 2018 (cited on page 29).

[162] J. R. Shewchuk. An Introduction to the Conjugate Gradient Method Without the Agonizing Pain. Technical report, Carnegie-Mellon University, Department of Computer Science, Pittsburgh, PA, 1994. `https://www.cs.cmu.edu/~quake-papers/painless-conjugate-gradient.pdf` (visited on 5/11/2023) (cited on pages 29, 150).

[163] P. M. Chaikin and T. C. Lubensky. *Principles of condensed matter physics*. Cambridge University Press, Cambridge, United Kingdom, 1st edition, 1995 (cited on page 33).

[164] P. Meakin. Diffusion-controlled cluster formation in 2—6-dimensional space. *Physical Review A*, 27(3):1495–1507, 1983 (cited on page 33).

[165] K. Jänich. *Topologie*. Springer-Lehrbuch. Springer, Berlin, 8th edition, 2008 (cited on page 35).

[166] F. Toenniessen. *Topologie*. Springer, Berlin, 2017 (cited on page 35).

[167] G. Flegg. *From geometry to topology*. Dover Publications, Mineola, NY, 1st edition, 2001 (cited on page 35).

[168] W. K. Pratt. *Digital image processing: PIKS Scientific inside*. Wiley-Interscience, Hoboken, NJ, 4th edition, 2007 (cited on pages 35, 76).

[169] J.-D. Chen and D. Wilkinson. Pore-Scale Viscous Fingering in Porous Media. *Physical Review Letters*, 55(18):1892–1895, 1985 (cited on page 44).

[170] K. J. Måløy, J. Feder, and T. Jøssang. Viscous Fingering Fractals in Porous Media. *Physical Review Letters*, 55(24):2688–2691, 1985 (cited on page 44).

[171] M. A. Mainster. The Fractal Properties of Retinal Vessels: Embryological and Clinical Implications. *Eye*, 4(1):235–241, 1990 (cited on page 44).

[172] F. Family, B. R. Masters, and D. E. Platt. Fractal pattern formation in human retinal vessels. *Physica D: Nonlinear Phenomena*, 38(1-3):98–103, 1989 (cited on page 44).

[173] B. R. Masters. Fractal Analysis of the Vascular Tree in the Human Retina. *Annual Review of Biomedical Engineering*, 6(1):427–452, 2004 (cited on page 44).

[174] S. Shree, S. Sutradhar, O. Trottier, Y. Tu, X. Liang, and J. Howard. Dynamic instability of dendrite tips generates the highly branched morphologies of sensory neurons. *Science Advances*, 8(26):eabn0080, 2022 (cited on page 44).

[175] M. Liao, X. Liang, and J. Howard. The narrowing of dendrite branches across nodes follows a well-defined scaling law. *Proceedings of the National Academy of Sciences*, 118(27):e2022395118, 2021 (cited on page 44).

[176] M. Liao, A. D. Bird, H. Cuntz, and J. Howard. Topology recapitulates morphogenesis of neuronal dendrites. *Cell Reports*, 42(11):113268, 2023 (cited on page 44).

[177] J. Kertész and T. Vicsek. Diffusion-limited aggregation and regular patterns: fluctuations versus anisotropy. *Journal of Physics A: Mathematical and General*, 19(5):L257–L262, 1986 (cited on page 44).

[178] R. Kobayashi. A brief introduction to phase field method. *AIP Conference Proceedings*, 1270(1):282–291, 2010 (cited on pages 57–60).

[179] J. A. Sethian. *Level Set Methods and Fast Marching Methods: Evolving Interfaces in Computational Geometry, Fluid Mechanics, Computer Vision, and Materials Sciences*, number 3 in Cambridge Monographs on Applied and Computational Mathematics. Cambridge University Press, Cambridge, United Kingdom, 2nd edition, 2010 (cited on page 57).

[180] C. Hirt and B. Nichols. Volume of Fluid (VOF) Method for the Dynamics of Free Boundaries. *Journal of Computational Physics*, 39(1):201–225, 1981 (cited on page 57).

[181] A. J. Degregoria and L. W. Schwartz. A boundary-integral method for two-phase displacement in Hele-Shaw cells. *Journal of Fluid Mechanics*, 164:383–400, 1986 (cited on page 58).

[182] S. M. Allen and J. W. Cahn. A microscopic theory for antiphase boundary motion and its application to antiphase domain coarsening. *Acta Metallurgica*, 27(6):1085–1095, 1979 (cited on page 60).

[183] R. Kobayashi. A Numerical Approach to Three-Dimensional Dendritic Solidification. *Experimental Mathematics*, 3(1):59–81, 1994 (cited on pages 60, 91).

[184] J. S. Langer. Models of Pattern Formation in First-Order Phase Transitions. In *Series on Directions in Condensed Matter Physics*. Volume 1, pages 165–186. WORLD SCIENTIFIC, 1986 (cited on page 60).

[185] M. C. Uçar, D. Kamenev, K. Sunadome, D. Fachet, F. Lallemend, I. Adameyko, S. Hadjab, and E. Hannezo. Theory of branching morphogenesis by local interactions and global guidance. *Nature Communications*, 12(1):6830, 2021 (cited on pages 71, 137).

[186] J. Seo, W. Youn, J. Y. Choi, H. Cho, H. Choi, C. Lanara, E. Stratakis, and I. S. Choi. Neuro-taxis: Neuronal movement in gradients of chemical and physical environments. *Developmental Neurobiology*, 80(9-10):361–377, 2020 (cited on pages 71, 137).

[187] D. J. Forsthoefel, A. E. Park, and P. A. Newmark. Stem cell-based growth, regeneration, and remodeling of the planarian intestine. *Developmental Biology*, 356(2):445–459, 2011 (cited on pages 71, 106, 137).

[188] H. T.-K. Vu, S. Mansour, M. Kücken, C. Blasse, C. Basquin, J. Azimzadeh, E. W. Myers, L. Brusch, and J. C. Rink. Dynamic Polarization of the Multiciliated Planarian Epidermis between Body Plan Landmarks. *Developmental Cell*, 51(4):526–542.e6, 2019 (cited on page 133).

[189] J. R. Banavar, A. Maritan, and A. Rinaldo. Size and form in efficient transportation networks. *Nature*, 399(6732):130–132, 1999 (cited on page 141).

[190] P. S. Dodds. Optimal Form of Branching Supply and Collection Networks. *Physical Review Letters*, 104(4):048702, 2010 (cited on page 141).

[191] I. Averbukh, D. Ben-Zvi, S. Mishra, and N. Barkai. Scaling morphogen gradients during tissue growth by a cell division rule. *Development*, 141(10):2150–2156, 2014 (cited on page 144).

[192] E. Crampin. Reaction and Diffusion on Growing Domains: Scenarios for Robust Pattern Formation. *Bulletin of Mathematical Biology*, 61(6):1093–1120, 1999 (cited on page 144).

[193] R. J. LeVeque. *Finite Difference Methods for Ordinary and Partial Differential Equations*. Society for Industrial and Applied Mathematics, 2007 (cited on page 146).

[194] W. H. Press, S. A. Teukolsky, W. T. Vetterling, and B. P. Flannery. *Numerical Recipes in C: The Art of Scientific Computing*. Cambridge University Press, Cambridge, United Kingdom, 2nd edition, 1992 (cited on page 146).

[195] H. P. Langtangen and S. Linge. *Finite Difference Computing with PDEs: A Modern Software Approach*, volume 16 of *Texts in Computational Science and Engineering*. Springer International Publishing, Cham, Switzerland, 2017 (cited on pages 146, 147, 149, 151).

[196] K. R. Elder, M. Grant, N. Provatas, and J. M. Kosterlitz. Sharp interface limits of phase-field models. *Physical Review E*, 64(2):021604, 2001 (cited on pages 153, 157).

[197] N. Provatas and K. Elder. *Phase-Field Methods in Materials Science and Engineering*. Wiley-VCH Verlag GmbH & Co. KGaA, Weinheim, Germany, 2010 (cited on page 153).

[198] S. Van Der Walt, J. L. Schönberger, J. Nunez-Iglesias, F. Boulogne, J. D. Warner, N. Yager, E. Gouillart, and T. Yu. Scikit-image: image processing in Python. *PeerJ*, 2:e453, 2014 (cited on page 159).

[199] T. Y. Zhang and C. Y. Suen. A Fast Parallel Algorithm for Thinning Digital Patterns. *Communications of the ACM*, 27(3):236–239, 1984 (cited on page 159).

Versicherung

Hiermit versichere ich, dass ich die vorliegende Arbeit ohne unzulässige Hilfe Dritter und ohne Benutzung anderer als der angegebenen Hilfsmittel angefertigt habe; die aus fremden Quellen direkt oder indirekt übernommenen Gedanken sind als solche kenntlich gemacht. Die Arbeit wurde bisher weder im Inland noch im Ausland in gleicher oder ähnlicher Form einer anderen Prüfungsbehörde vorgelegt. Die vorliegende Arbeit wurde unter der Betreuung von Prof. Dr. Frank Jülicher am Max-Planck-Institut für Physik komplexer Systeme in Dresden angefertigt.

Christian Hanauer
Dresden, Dezember 2023